Universidad de Granada

A Dissertation for the Degree of Doctor of Philosophy

HYDRODYNAMICS AND MIXING AT RIVER CONFLUENCES:

ON THE INFLUENCE OF BUOYANCY AND TIDES

Hidrodinámica y mezcla en la confluencia de ríos:
influencia de los contrastes de densidad y de la marea

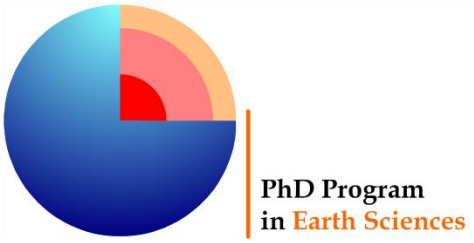

Cintia Luz Ramón Casañas

January 2016

Dissertation advisor: Francisco José Rueda Valdivia

Editor: Universidad de Granada. Tesis Doctorales
Autora: Cintia Luz Ramón Casañas
ISBN: 978-84-9125-890-2
URI: http://hdl.handle.net/10481/43718

Preface

The PhD candidate Cintia Luz Ramón Casañas and the dissertation advisor Francisco José Rueda Valdivia guarantee that the thesis is the work of the PhD candidate under the supervision of her advisor and except where acknowledged in the customary manner, the material presented in this thesis is, to the best of our knowledge, original and has not been submitted in whole or part for a degree in any university.

La doctoranda Cintia Luz Ramón Casañas y el director de la tesis Francisco José Rueda Valdivia garantizamos, al firmar esta tesis doctoral, que el trabajo ha sido realizado por la doctoranda bajo la dirección del director de la tesis y hasta donde nuestro conocimiento alcanza, en la realización del trabajo, se han respetado los derechos de otros autores a ser citados, cuando se han utilizado sus resultados o publicaciones.

Granada, January 20, 2016

Dissertation advisor	PhD candidate
Director de la Tesis	La doctoranda
	
Fdo.: Francisco José Rueda Valdivia	Fdo.: Cintia Luz Ramón Casañas

For many of us, water simply flows from a faucet, and we think little about it beyond this point of contact. We have lost a sense of respect for the wild river, for the complex workings of a wetland, for the intricate web of life that water supports.

Sandra Postel

This PhD thesis has been carried out at the Department of Civil Engineering and the Water Institute of the University of Granada. Work on the confluence between the Ebro and Segre rivers was funded through a collaborative agreement between the University of Barcelona and the University of Granada to work jointly in the project "*Gestión hidráulica y técnicas de detección remota aplicada al control de poblaciones mejillón cebra: el caso del embalse de Ribarroja y el tramo inferior del río Ebro*", funded by the Spanish Ministry of the Environment. Work on the Sacramento River was funded through the project "*North Delta Salmon Out-migration Study*", funded by the United States Department of Interior — Bureau of Reclamation (USBR), solicitation No. 09SS200013. The PhD student was supported by a PhD grant (*Programa Estatal de Promoción del Talento y su Empleabilidad, subprograma de Formación de Profesorado Universitario*) from the Spanish Government.

General abstract

River confluences are critical points in river networks where strong physical and chemical gradients develop, resulting in a wide range of distinctive environmental conditions (habitats) for biological growth. Large variations in water temperatures, organic matter, nutrients, for example, and in general, in water chemistry have been reported to occur at these sites. As a consequence of their high spatial and temporal heterogeneity of habitats and resources, river confluences behave as biological hotspots, where the number of species appears to increase very significantly in comparison with other river reaches. The effects of river confluences persist downstream, therefore, affecting biological communities and ecological processes at scales of river reaches and channel networks. The spatial extent of the reaches downstream of river junctions where heterogeneous habitat conditions persist, largely depends on the rate at which mixing between the mainstream and tributary waters occurs. The literature on mixing in river confluences is extensive, but still, our understanding of flow and mixing dynamics in these sites is far from complete. In particular, the effect of density contrast between the confluent streams on mixing has traditionally been neglected, which has been justified by differences in the inertia of the confluent flows being much higher than density differences. However, as the scale of the confluent channels increases, the probability of draining different geological terrains also increases which results in an increasing potential for significant differences in density.

In this work, we present results of a series of field experiments carried out in a confluence in Northern Spain where the presence of density contrast is important for both the spatial arrangement of the rivers once at the confluence and river mixing. The confluence presents seasonal variations in the river density contrast, which ranges from O (10^{-2}) kg m^{-3} in winter to O (1) kg m^{-3} during summer. Depending on the river density contrast, the confluent rivers flow side by side or one on top of the other. Through the use of three-dimensional numerical experiments, we illustrate that, despite being negligible from a dynamic point of view, the weak density contrasts observed in winter are able to distort the mixing layer between the rivers. This distortion changes the contact area

available for mixing, and ultimately affects mixing rates. Numerical experiments are also presented for the strong density contrast observed in summer, when the confluence is vertically stratified. We assess the factors controlling the location of the plunging zone and mixing rates. In particular, we focus on the interaction between inertial and buoyancy forces, the effect of wind forcing and the unsteady nature of the hydraulic forcing. It is shown that the steady-state location of the plunge zone is controlled by an inertia-buoyancy balance, which accounts for the relative magnitude of the buoyancy forcing associated with river density differences, and the magnitudes of both the main-stream and the tributary inertia. This has important consequences for river mixing since mixing rates increase as the plunging occurs at the confluence due to a combination of large mixing-interface surfaces and high diffusivities. Wind forcing, depending on its velocity and direction is able to affect mixing rates at this confluence through (1) altering the buoyancy-inertia equilibrium, (2) altering the patter of secondary circulation within the confluence and/or (3) increasing shear at the confluence. This work further shows that there is a time lag between a change in the equilibrium conditions of the inflows and the system response (movement of the plunge point) to this change.

River junctions where water may follow two or more alternative pathways (diffluences) are also critical points in river networks where aquatic migratory species select different migration routes. This is the case, for example, of the juvenile Chinook salmon (*Oncorhynchus tshawytscha*) in the Sacramento-San Joaquin River Delta. This work also presents preliminary results on a reach of the Sacramento River where juveniles may remain in the main Sacramento River or select other two migration routes that lead to the interior of the delta, where salmon survival is known to decrease. This river reach is affected by the tides, with flow reversal occurring during flood tides; and the entrances to the two migration routes that lead to the interior of the delta are located at the outside of a river bend, where secondary circulation is known to occur. Our results are consistent with previous studies that show that during the flood tide almost all the flow, and thus, all the salmon, are directed to the interior delta through these two migration routes. This work also suggests that, during ebb tides, fish entrainment rates into the interior of the delta are higher than those expected by flow entrainment alone due to the preference of salmon for migrating near surface (first four meters of the water column in

the Sacramento River), together with the effect of secondary circulation that pushes the surface-biased salmon towards the outside of the bend where the entrance of these two migration routes are located.

The work presented in Chapter 2 has been published in *Water Resources Research*, entitled "Mixing and circulation at the confluence of two rivers entering a meandering reservoir ", and authored by C. L. Ramón, A. B. Hoyer, J. Armengol, J. Dolz and F. J. Rueda. The work presented in Chapter 3 has been published in *Journal of Geophysical Research — Oceans*, entitled "Mixing dynamics at the confluence of two large rivers undergoing weak density variations", and authored by C. L. Ramón, J. Armengol, J. Dolz, J. Prats and F.J. Rueda. The work presented in Chapter 4 is currently under review in *Journal of Hydrology*, entitled "the influence of flow inertia, buoyancy, wind, and flow unsteadiness on mixing at the asymmetrical confluence of two large rivers", and authored by C. L Ramón, J. Prats and F. J. Rueda. Chapter 5 on the effect of the secondary circulation and fish entrance distribution on entrainment of juvenile salmon into the interior Sacramento-San Joaquin River Delta over a tidal cycle is in preparation for future submission. Two additional manuscripts are included as appendices. In Appendix A, we include a manuscript which contains a series of validation exercises through which we made sure that the 3D Cartesian primitive-equation hydrodynamic model, even if based on hydrostatic equations and using a simplified turbulence sub-model, is capable of reproducing key features in river hydraulics. This manuscript has been published in *International Journal of Computational Methods*, entitled, "Simulation of turbulent flows in river confluences and meandering channels with a Cartesian 3D free surface hydrodynamic model", and authored by C. L. Ramón, J. Prats and F. J. Rueda. Appendix B includes a second manuscript in which we propose and test a method to include inflow-outflow boundary conditions along arbitrary directions in Cartesian models. This approach has been used in the implementation of the model at the confluence between the Ebro and Segre rivers. The manuscript is cited in the literature as Ramón, C.L, A. Cortés, and F. J. Rueda (2015). Inflow-outflow boundary conditions along arbitrary directions in Cartesian lake models. *Computers & Geosciences*, 74(2015), 87-96, doi:10.1016/j.cageo.2014.10.002.

Resumen general

Las confluencias de ríos son nodos clave en la red hídrica en donde se producen fuertes gradientes físicos y químicos (ej.: gradientes en la temperatura del agua, en la materia orgánica, en la carga de nutrientes, etc.), que tienen como resultado la formación de un abanico amplio de condiciones ambientales (hábitats) para el crecimiento biológico. Debido a la heterogeneidad tanto espacial como temporal de los hábitats y recursos presentes en las confluencias, éstas se comportan como puntos calientes de biodiversidad, donde el número de especies puede aumentar de forma muy significativa en comparación con otros tramos de la red fluvial. Además, estos efectos persisten aguas abajo de las confluencias por lo que influyen sobre las comunidades biológicas y sobre los procesos ecológicos tanto a nivel de tramos de ríos, como a nivel de toda la red fluvial; si bien, la extensión del tramo de río, aguas abajo de una confluencia, con características heterogéneas depende, en gran medida, de las tasas de mezcla entre el agua de la corriente principal y la de su tributario. Aunque la literatura que versa sobre la mezcla de ríos aguas abajo de confluencias es extensa, todavía queda camino por recorrer en nuestro entendimiento sobre los procesos de mezcla en estas áreas. Concretamente, y debido a que se trata de ambientes dominados en gran medida por las diferencias inerciales de los ríos confluyentes, la literatura suele despreciar el efecto sobre la mezcla que podría tener la presencia de contrastes de densidad entre los ríos. Sin embargo, a medida que la escala de la confluencia aumenta, la probabilidad de que los ríos que confluyen en ella drenen cuencas de mayor tamaño también aumenta, y por tanto de que drenen territorios con distintas características geológicas, lo que potencialmente resultaría en diferencias significativas en las densidades de los ríos.

En esta tesis, se presentan los resultados de una serie de experimentos realizados en una confluencia en el norte de España donde los contrastes de densidad son importantes tanto para la distribución espacial de los ríos una vez confluyen como para las tasas de mezcla de los mismos aguas abajo de la confluencia. Estos contrastes de densidad varían de forma estacional, con valores que van desde los O (10^{-2}) kg m^{-3} en invierno hasta las diferencias de O (1) kg m^{-3} en verano, y la magnitud de estas

diferencias es responsable de que los ríos fluyan uno paralelo al otro o de que se dispongan uno encima del otro (estratificación vertical). Mediante el uso de modelación numérica, se mostrará que, a pesar de que podrían despreciarse desde un punto de vista dinámico, la existencia de pequeños contrastes de densidad (como los encontradas en invierno en esta confluencia) puede causar la deformación de la interfase de mezcla entre los dos ríos, la cual conlleva cambios en el área de contacto entre las dos masas de agua y, por tanto, tiene consecuencias sobre las tasas de mezcla. También se presentarán simulaciones con las que se evaluarán los factores que controlan la localización del punto de hundimiento así como las tasas de mezcla bajo las condiciones de fuertes contrastes de densidad típicas del verano, con particular foco sobre la interacción entre las fuerzas inerciales y de flotabilidad, el efecto del forzamiento del viento y sobre la naturaleza no estacionaria del forzamiento hidráulico. Esta tesis mostrará que la localización, en estado estacionario, del punto de hundimiento está controlada por un equilibrio entre las fuerzas inerciales (los ríos entran con distinta inercia a la confluencia) y de flotabilidad (los ríos tienen distinta densidad), lo cual tiene importantes consecuencias en la mezcla de los ríos ya que las tasas de mezcla aumentan a medida que el punto de hundimiento se produce en la confluencia en sí misma, debido a una combinación de una mayor interfase de mezcla y valores altos de difusividad. Por otro lado, el forzamiento del viento, dependiendo de su dirección y velocidad, también es capaz de afectar a las tasas de mezcla mediante (1) la alteración del equilibrio entre las fuerzas inerciales y de flotabilidad, (2) la alteración del patrón de recirculación lateral en la confluencia y/o (3) el aumento de los niveles de cizalla en la confluencia. Esta tesis también muestra que hay un desfase entre un cambio en las condiciones de entrada de los ríos (cambios en el caudal y/o densidad) y el desplazamiento del punto de hundimiento como respuesta del sistema a un cambio en las condiciones de equilibrio

Los nodos en la red hidrológica donde el agua puede seguir uno o más caminos alternativos (difluencias) son también puntos críticos en la red fluvial, en donde las especies migratorias acuícolas eligen distintas rutas migratorias. Este es el caso, por ejemplo, del salmón real (*Oncorhynchus tshawytscha*) en el delta formado por los ríos Sacramento y San Joaquín en California. Esta tesis también recoge los resultados preliminares de simulaciones realizadas en un tramo del río Sacramento donde los

juveniles del salmón real pueden o bien permanecer en la corriente principal, o bien elegir entre otras dos rutas migratorias que los dirigen al interior del delta, donde las tasas de supervivencia de los juveniles son inferiores. Este tramo del río Sacramento está afectado por el régimen mareal por lo que el agua fluye en sentido contrario durante la marea llenante, y la entrada a las dos rutas que dirigen a los salmones al interior del delta están situadas en el exterior de un meandro, donde se producen fenómenos de recirculación lateral del flujo. Los resultados preliminares son consistentes con estudios previos que muestran la importancia de las mareas, ya que durante la marea llenante casi todo el flujo, y por tanto los salmones, se dirigen hacia el interior del delta a través de estas dos rutas migratorias. Este trabajo también sugiere que, durante la marea vaciante el porcentaje de peces que entra en el interior del delta es mayor que el esperado en función del caudal redirigido hacia estas dos rutas, debido a la combinación de la preferencia de los salmones por nadar cerca de la superficie (en los primeros cuatro metros de la columna de agua en el río Sacramento) y de la presencia de recirculación lateral, que desplaza a los salmones hacia el exterior del meandro (donde se localizan las entradas a estas dos rutas migratorias) en las zonas cercanas a la superficie.

El trabajo presentado en el capítulo 2 ha sido publicado en *Water Resources Research* con el título “Mixing and circulation at the confluence of two rivers entering a meandering reservoir “, y sus autores son C. L. Ramón, A. B. Hoyer, J. Armengol, J. Dolz y F. J. Rueda. El trabajo presentado en el capítulo 3 ha sido publicado en *Journal of Geophysical Research – Oceans* con el título “Mixing dynamics at the confluence of two large rivers undergoing weak density variations”, y ha sido escrito por C. L. Ramón, J. Armengol, J. Dolz, J. Prats y F. J. Rueda. El trabajo presentado en el capítulo 4 está actualmente en revision en *Journal of Hydrology*, bajo el título “the influence of flow inertia, buoyancy, wind, and flow unsteadiness on mixing at the asymmetrical confluence of two large rivers”, y sus autores son C. L. Ramón, J. Prats y F. J. Rueda. El material del capítulo 5 que evalúa los efectos dentro del ciclo mareal de la recirculación lateral y de la distribución de los juveniles del salmón real sobre el porcentaje final de salmones que entran en el interior del delta formado por los ríos Sacramento y San Joaquín está en preparación para su futuro envío a una revista científica. Adicionalmente, se han incluido, como apéndices, dos manuscritos. En el apéndice A, incluimos un manuscrito que

contiene una serie de ejercicios de validación a través de los cuales se ha asegurado que el modelo hidrodinámico Cartesiano usado en esta tesis, aunque basado en las ecuaciones hidrostáticas y aunque haga uso de un submodelo de turbulencia simplificado, es capaz de reproducir características clave en la hidráulica de ríos. Este manuscrito ha sido publicado en *International Journal of Computational Methods*, bajo el título "Simulation of turbulent flows in river confluences and meandering channels with a Cartesian 3D free surface hydrodynamic model", y ha sido escrito por C. L. Ramón, J. Prats y F. J. Rueda. El apéndice B incluye un segundo manuscrito en el que se propone y se evalúa un método para incluir condiciones de frontera de entrada y salida de flujo a lo largo de direcciones arbitrarias en modelos Cartesianos. Esta aproximación se ha utilizado en la implementación del modelo en la confluencia entre los ríos Ebro y Segre. Este manuscrito se cita en la literatura como "Ramón, C. L, A. Cortés, y F. J. Rueda, 2015. Inflow-outflow boundary conditions along arbitrary directions in Cartesian lake models. *Computers & Geosciences*, 74(2015), 87-96, doi:10.1016/j.cageo.2014.10.002".

Acknowledgements

First and foremost, I would like to thank my advisor, Francisco Rueda, for his willingness to supervise this thesis, for his constant support and encouragement and for his guidance throughout the course of this work. He has shown continuous interest and has worked tirelessly to help solve all the arising problems. Thanks are also due to Jon Burau and Aaron Blake for kindly hosting me at the USGS California Water Science Center in Sacramento (California). Thanks Jon for kindly providing me with all field data that was needed and guiding me during the duration of this stay. Thanks to Bruce Rhoads, for accepting me into the University of Illinois in Champaign and introducing me to the world of turbulence and for allowing me to take part in the field experiments. But more importantly, thanks for all the insightful comments and revisions, which greatly improved the quality of the published papers. Thanks to Marco Toffolon and Oliver Fringer for kindly accepting to review this thesis and for their insightful comments during the review process. Thanks to Ben Hodges for his useful comments and suggestions.

Thanks to my colleagues in the *Instituto del Agua*: Anna, Andrea, Alicia and Mario, who have contributed to the development of this thesis. Thanks for all your feedback and coffee breaks!! Mario, thanks for leading the parallelization of the code. Andrea, thanks for the 3D version of the particle tracking code. Ali, thanks for letting me do some fieldwork with you and for all the talks and lunches. To Ali and Tere, for helping me with all the administration paperwork.

Thanks to all the people that participated and helped in the data collection campaigns: Javier Vidal, Karla Gleichauf, Gonzalo González, Ángel David Gutiérrez Barceló, Ana Silió, and Raúl Medina. Thanks to the USGS team in Sacramento. To Paul Stumpner for helping me in the analysis of the ADCP data (and, of course, for the bike). To Quinn Lewis for all his help and patience. To all the PhD students in the Department of Geography and GIScience in the University of Illinois, for allowing me to participate in their field/labwork. Thanks to Joan Armengol, Josep Dolz and Jordi Prats. Thanks to the personnel from ENDESA-Medio Ambiente and the Flumen Institute for making their data available to us. Thanks to Dennis Hubbard for kindly accepting to check and correct

my English in some sections of this thesis. To Trevor Violette for making me feel at home in California and introducing me to the IPA world.

To all my friends for their constant cheering up and friendship. Thanks Vane for your endless support. And, of course, thanks to my family, without whose love, support and encouragement I would not have been able to complete this work.

Contents

List of Tables

List of Figures

Nomenclature

The following symbols are used in this PhD thesis (appendices not included):

A	Kinematic eddy viscosity	$m^2\ s^{-1}$
b	Channel width	m
C	Numerical tracer concentration	ppm
C_p	Theoretical concentration after complete mixing	ppm
C_d	Bottom drag coefficient	
c	Ideal speed of a gravity current $(= g\,\Delta\rho/\rho_0 D)^{0.5}/2$	$m\ s^{-1}$
Co_0	Conductivity values	$\mu S\ cm^{-1}$
C_{dw}	Wind drag coefficient	
D	Channel depth	m
d	Particle size	m
E_P	Particle entrainment rates	
E_Q	Flow entrainment rates	
Fr	Froude number	
Fr_i	Internal Froude number	
F_b	Baroclinic forcing	$m\ s^{-2}$
F_c	Centrifugal forcing	$m\ s^{-2}$
F_p	Barotropic forcing	$m\ s^{-2}$
f	Frequency	Hz
f_p	Frequency peak	Hz
g	Gravitational acceleration	$m\ s^{-2}$
g'	Reduced gravity $(= g\,\Delta\rho/\rho_0)$	$m\ s^{-2}$
H	Depth of the upper layer in a two-layer system	m
Δh	Vertical displacement of the interface between rivers	m
I	Slope	
I_c	Longitudinal channel slope	
K	Diffusivity	$m^2\ s^{-1}$
L	Length	m
L_M	Mixing length	m
ME_{SS}	*Murphy and Epstein* [1989] skill score	
n_T	Particle computational step	
O	Order of magnitude	
P_{sk}	Wind stirring	$m^2\ s^{-3}$
P_s	Shear production of TKE	$m^2\ s^{-3}$
Q	River discharge	$m^3\ s^{-1}$

Ri_g	Gradient Richardson number	
R_D	Depth ratio	
R_q	Discharge ratio	
R_u	Velocity ratio	
R_m	Momentum flux ratio	
R_s	Radius of curvature	m
$R_{sk\text{-}sk0}$	Stirring-to-stirring ratio	
$R_{s\text{-}s0}$	Shear-to-shear ratio	
$R_{sk\text{-}s}$	Stirring-to-shear ratio	
S	Surface	m^2
$SC25$	Specific conductance (T = 25 ºC)	$\mu S\ cm^{-1}$
SG	Specific gravity of suspended solids	
SS	Suspended solid concentration	$mg\ L^{-1}$
t	Time	s
Δt	Time step	s
T	Water temperature	ºC
T_a	Average temperature of air	ºC
ΔT	Magnitude of temperature differences (T_N-T_W)	ºC
T_d	Time scales of deposition	s
T_e	Particle entrainment times	s
T_f	Flow time scales	s
T_b	Baroclinic adjustment time	s
T_p	Period	s
TM	Total mixing	%
TDS	Total dissolved solid concentration	$mg\ L^{-1}$
$Turb$	Turbidity	ntu
U	Inflow velocity	$m\ s^{-1}$
$\bar{U}_c$	Depth-averaged mixing layer centerline velocity	$m\ s^{-1}$
$\Delta\bar{U}$	Difference between the depth-averaged downstream velocities in the Ebro and Segre rivers	$m\ s^{-1}$
u,v,w	Velocity in the x, y and z direction	$m\ s^{-1}$
u_s,u_n	Velocity in the streamwise and transverse direction	$m\ s^{-1}$
U_{10}	Wind velocity at 10 m height	$m\ s^{-1}$
$\langle u_s \rangle$	Average streamwise velocity	$m\ s^{-1}$
u^*	Friction velocity	$m\ s^{-1}$
u_a^*	Shear velocity of air	$m\ s^{-1}$
$u_{n,c}$	Maximum transverse velocity as a result of the centrifugal acceleration	$m\ s^{-1}$
$u_{n,b}$	Transverse velocity magnitude due to buoyancy forces	$m\ s^{-1}$

$u_{s,b}$	Streamwise velocity magnitude due to buoyancy forces	m s^{-1}
u_p	Primary velocity (Rozovskii's method)	m s^{-1}
$\langle u_p \rangle$	Section-averaged primary velocity	m s^{-1}
u_{sec}	Secondary velocity (Rozovskii's method)	m s^{-1}
$u_{sec\text{-}rms}$	Root mean square secondary velocity	m s^{-1}
u_{EW}	E-W velocity	m s^{-1}
u_{NS}	N-S velocity	m s^{-1}
u_{PL}	Streamwise velocicity of the displacement of the plunge point	m s^{-1}
V	Volume	m^3
W	Wedderburn number	
w_0	Settling velocity	m s^{-1}
X	Hydrodynamic quantity	
x_c	Nondimensional distance downstream (= s/b_p)	
x_H	Nondimensional distance downstream where the mixing interface becomes horizontal	
$x_{c\text{-}PL}$	Nondimensional location of the plunge point	
x, y, z	Cartesian coordinate system	m
s, n	Streamwise and transverse coordinates	m
$\Delta x, \Delta y, \Delta z$	Size of grid cells in the x, y and z directions	m
Y	Non-dimensional cross-stream distance	

Greek Symbols

α	Thermal expansion coefficient	$^oC^{-1}$
β	Ratio of the scales for the vertical and horizontal variability of the flow	
Γ	Dilution rates	%
γ	Width of the shear layer	m
δ	Deviation from complete mixing	%
ε_t	Transverse mixing coefficient	m^2 s^{-1}
ζ	Water free surface elevation	m
θ_B	Shear layer thickness	m
Λ	Non-dimensional elapsed time	
λ	Scaling factor to transform conductivity into salinity	mg L^{-1}(μS cm^{-1})$^{-1}$
$\Delta\rho$	Magnitude of the density difference (generally it refers to $\rho_W - \rho_N$)	kg m^{-3}
ρ	Water density	kg m^{-3}
ρ_a	Air density	kg m^{-3}
$\Delta\rho_{SS}$	Density contribution due to suspended solids	kg m^{-3}
$\Delta\rho/\rho_0$*	Value of $\Delta\rho/\rho_0$ for maximal mixing rates	

ς	Ratio between the depth-integrated specific conductance of a given site and the specific conductance of the Ebro water	
σ	Standard deviation of tracer concentration	ppm
Φ	Wind direction	^{o}

Subscripts

0	Reference value
DCC	Delta Cross Channel
GEO	Georgiana Slough
N	Segre River
W	Ebro River
c	Confluence
m	Main stream
t	Tributary
z	Vertical direction
h	Horizontal direction
p	Post-confluence

Chapter 1

Introduction and objectives

1.1 General introduction

River confluences are characteristic of all river networks worldwide. However, their ubiquity has not prevented them from remaining highly ignored by the scientific community until very recently. The first body of literature of river confluences was developed in the 1980s, where studies ranged from interest in the confluence morphology, hydraulics and sedimentology [*Mosley*, 1976; *Best*, 1987; *Roy et al.*, 1988] to interest in the ecological [*Bruns et al.*, 1984; *Petts and Greenwood*, 1985] and structural [*Abrahams and Campbell*, 1976; *Flint*, 1980; *Abrahams and Updegraph*, 1987] role of tributaries at the scale of rivers and river networks. From that decade on, the body of work on river confluences has increased almost exponentially [*Rice et al.*, 2008], demonstrating the importance of river confluences in the hydraulics, geomorphology, sedimentology and ecology of river networks.

In terms of ecology, for example, river confluences have been shown to have an indubitable biological value at both the scale of river confluences and river networks. The supply of water, sediment and organic materials from tributaries introduces step-like changes in the river continuum, which can cause ecological impacts as it is a shift in fish and macroinvertebrate abundance and community composition [e.g., *Rice et al.*, 2001; *Knispel and Castella*, 2003; *Fernandes et al.*, 2004; *Kiffney et al.*, 2006; *Torgersen et al.*, 2008]. At local scales, river confluences could be regions of high productivity where the receiving main-stream is enriched with nutrients, drifts and detritus from its tributaries [e.g., *Fernandes et al.*, 2004; *Wipfli and Gregovich*, 2002]. As a result of two different water masses coming together, river confluences are also areas of high heterogeneity where abrupt changes in physical-chemical properties occur. Strong gradients in, for example, organic matter [*Benda et al.*, 2003; *Bigelow et al.*, 2007; *Macnab et al.*, 2006], nutrients [*Kiffney et al.*, 2006], temperature [*Milner and Petts*, 1994; *Knispel and Castella*, 2003; *Torgersen et al.*, 2008] and substrate characteristics [*Rice et al.*, 2001] may occur at these sites. As a result of this heterogeneity, a wide range of potential

habitats for biological growth can occur [*Benda et al.*, 2004; *Rice et al.*, 2006], and the contrasting environments can be usefully exploited by mobile species [*Power and Dietrich*, 2002] for breeding purposes [e.g., *Kupferberg*, 1996], or for example, for predator-, flow- or thermal-refugia use [*Scrivener et al.*, 1994; *Fraser et al.*, 1995; *Kaeding*, 1996; *Bramblett et al.*, 2002; *Power and Dietrich*, 2002; *Cairns et al.*, 2005]. Moreover, some organisms may take ecological advantage of the unusual morphology and hydraulics of river confluences [*Franks et al*., 2002].

The morphology and hydraulics of river confluences is certainly unique and characterized by its complexity. Confluence morphology is, in broad terms, characterized by the presence of a scour hole, bars (tributary-mouth, mid-channel and bank-attached bars) and a region of sediment accumulation near the upstream junction corner [*Best and Rhoads*, 2008]. In terms of hydraulics, Best's model [*Best*, 1987] identifies six distinct elements (which not necessarily occur in all river confluences) (Figure 1.1): (1) a zone of flow stagnation at the upstream junction corner (possibly associated with the region of sediment accumulation) where water surface super-elevation occurs, (2) flow deflection where the rivers meet, (3) a zone of flow separation downstream of the downstream junction corner (associated with the presence of bank-attached lateral bars), (4) an area of maximum velocity, (5) an area of flow recovery downstream of the flow-separation zone and (6) a highly turbulent shear/mixing layer between the confluent flows. Another element that is frequently observed is (7) the development of back-to-back helical cells (Figure 1.1) [*Mosley*, 1976; *Ashmore*, 1982; *Ashmore and Parker*, 1983; *Ashmore et al*., 1992; *Rhoads and Kenworthy*, 1995, 1998; *McLelland et al.*, 1996; *Rhoads*, 1996; *Richardson et al.*, 1996; *Bradbrook et al*., 2000; *Rhoads and Sukhodolov*, 2001, *Szupiany et al*., 2007, 2009; *Riley and Rhoads*, 2012; *Riley et al*., 2015]. These cells develop, in the transverse direction, on both sides of the mixing layer as a result of the development of water super-elevations where the two tributaries meet (mixing layer). Flow within these back-to-back helical cells is directed inwards (flow convergence) near surface and outwards (flow divergence) near bed (Figure 1.1). The occurrence, size and shape of each of these elements of hydraulics are controlled by the magnitude and interaction of different controlling variables (not yet completely understood), that include the junction angle and the discharge (or momentum flux) ratio [*Mosley*, 1976; *Best and Reid*, 1984; *Rhoads and Kenworthy*, 1995, 1998], the presence of bed discordance (difference in the depths of the confluent streams) [*Best and Roy*, 1991; *Biron et al.*, 1993, 1996a,b; *Gaudet*

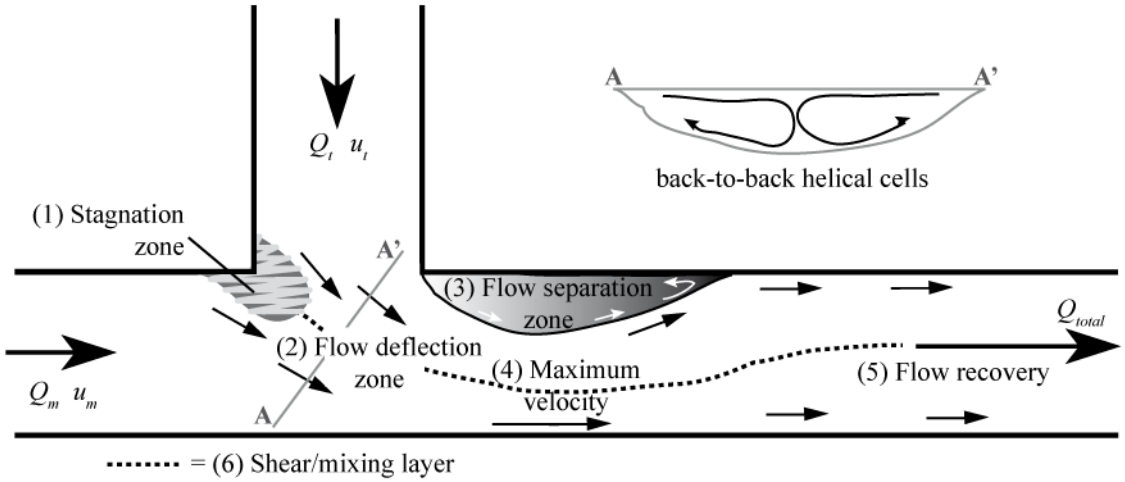

Figure 1.1 Best [1987]'s model of flow dynamics at river confluences and sketch of the back-to-back counter-rotating cells that commonly develop at river confluences in the transverse direction (section A-A').

and Roy, 1995; *De Serres et al.*, 1999; *Boyer et al.*, 2006], topographic effects, such as the presence of dunes [*Parsons et al.*, 2007]; and the confluence planform (e.g., curvature effects [e.g., *Ashmore and Parker*, 1983; *Riley et al.*, 2015] or symmetrical *vs.* asymmetrical shape of the confluence [*Bradbrook et al.*, 2000]). All this reflects the complexity associated with river confluences and probably explains the lag in knowledge of these systems with respect to the rest of the river network. This PhD thesis focuses on two particular processes/services of river confluences: (1) river mixing and (2) their role as nodes of the river network for migratory species, such as in the case of the juvenile Chinook salmon [*Oncorhynchus tshawytscha*] in their out-migration to the sea in the Sacramento-San Joaquin River Delta (California).

1.2 River mixing

Water masses joining at a river confluence are seldom similar and may, in fact exhibit large differences in physical-chemical characteristics. As a result, strong physical and chemical gradients develop in confluences, resulting in a wide range of distinctive environmental conditions (habitats) for biological growth. The spatial extent of the reaches downstream of river junctions where heterogeneous habitat conditions persist largely depends on the rate at which mixing between the mainstream and tributary waters occurs. Understanding flow mixing at confluences is, then, of key importance to understand river systems. Mixing between two confluent streams occurs mainly in the transverse direction, as a result of the two streams flowing parallel to each other with an

almost vertical mixing layer. *Fischer et al.* [1979] showed through a semi-theoretical analysis that transverse diffusion scales with the square of the channel width, and thus, mixing distances should increase significantly for large (post-confluence widths > 100 m) river confluences. Actually, mixing is commonly a relatively slow process and mixing distances downstream of river confluences are in the order of around 100 channel widths [*Mackay*, 1970; *Smith and Daish*, 1991; *Rutherford*, 1994; *Lane et al*., 2008, and references therein; *Campodonico et al*., 2015]. However, field studies in small and large river confluences have shown that, under some circumstances, rapid mixing may occur, with mixing lengths in the order of ≈ 10 channel widths [*Gaudet and Roy*, 1995; *Tao et al*., 1999; *Maurice-Bourgoin et al*., 2003; *Lane et al.*, 2008]. The distortion of the mixing layer has been identified as the cause of this rapid mixing, but the mechanisms leading to the distortion of the mixing layer are still unclear. Bed discordance and the presence of a channel-scale helical circulation have been identified as the two most important of these mechanisms. Laboratory [*Best and Roy*, 1991; *Biron et al*., 1996a,b] and field experiments [e.g., *Biron et al.*, 1993] have shown that, in the presence of bed discordance, a negative dynamic pressure develops at the lee of the tributary step and significant cross-stream pressure gradients may develop leading to flow separation, entrainment and upwelling of fluid from the deeper channel into the waters of the shallower, which result in significant reductions in mixing lengths [*Gaudet and Roy*, 1995]. *Gaudet and Roy* [1995], for example, reported mixing lengths of only ≈ 25 channel widths in a small (5-10 m in width) discordant confluence in Canada. When back-to-back helical cells develop at river confluences, differences in angular momentum between tributaries may cause helical motions to rapidly evolve into a single channel-width circulation cell [*Rhoads and Kenworthy*, 1995, 1998; *Rhoads*, 1996; *Bradbrook et al*., 2000], which appears to be very effective mechanisms for mixing [*Rhoads and Kenworthy*, 1995; *Rhoads and Sukhodolov*, 2001]. *Lane et al.* [2008], for example, found that the mixing length between the Paraná and Paraguay rivers in Argentina can vary from ca. 8 to 400 km depending on whether channel-scale helical motions develop or not.

Depth discordance, as reflected by small depth ratios ($R_D = D_t/D_m$, where t = tributary and m = main stream), often occurs in large river confluences, such as that of the Negro and Solimões rivers in Brazil ($R_D \approx 0.6$, *Laraque et al.* [2009]), that of the Paraguay and Paraná rivers ($R_D \approx 0.5$, *Lane et al.* [2008]) or that of the Ebro and Segre rivers in northern Spain — one of the study sites of this PhD thesis ($R_D \approx 0.4$, *Ramón et*

al. [2013], Figure 1.2). At large river confluences, however, avalanche faces and morphological steps due to bed discordance are typically very low-angle (see an example cross-section at the Ebro-Segre confluence in Figure 1.2), which prevent the formation of permanent flow separation [*Parsons et al.*, 2008]. Therefore, the three-dimensional distortion of the mixing layer often caused by discordance may be significantly less likely to occur in larger channel confluences. Since the rate of increase in width with discharge should be greater than the rate of increase in depth [*Leopold and Maddock*, 1953], in large river confluences the width-to-depth ratios are O (10^1) or larger (for example at the Ebro-Segre confluence it is ≈ 40), and, thus, topographic effects are expected to increase as well, limiting the development of helical motions [e.g., *Szupiany et al.*, 2009]. So, is there any other potential mechanism for distorting the mixing layer at large river confluences? Large rivers have a greater probability of draining different geological terrains, so the potential for significant differences in suspended sediment concentrations and/or conductivities (and so, in densities) between the confluent channels increases. River regulations (e.g., dams and weirs) upstream of river confluences can also cause changes in the thermal properties of the rivers being regulated [e.g., *Prats et al.*, 2010], which could result in temperature differences (and then, density differences) between the

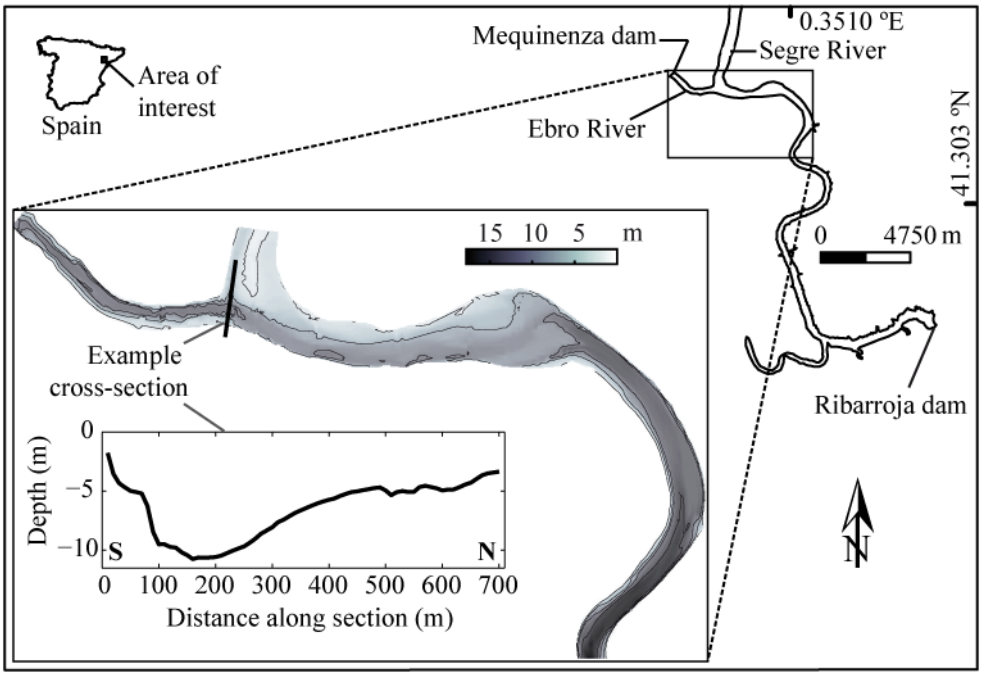

Figure 1.2 The Ribarroja reservoir. Location and bathymetry of the area of interest (the confluence between the Ebro and Segre rivers) and example cross-section illustrating the low angle slope of bed discordance.

confluent rivers [e.g., *Prats et al.*, 2010]. For example *Lane et al.* [2008] reported differences in density of O (10^{-1}) kg m^{-3} between the Paraná and Paraguay rivers due to the difference in suspended sediment loads. *Trevethan et al.* [2015] also reported differences in density of O (10^{-1}) kg m^{-3} between the Negro and Solimões rivers due to differences in suspended sediments, conductivities and temperatures [*Laraque et al.*, 2009]. *Ramón et al*. [2013] (this PhD thesis) reported density differences ranging from O (10^{-2}) (weak density differences) to O (1) (strong density differences) kg m^{-3} between the Ebro and Segre rivers due to differences in temperatures and conductivities. These small density differences can cause the denser river to flow below the less dense river [e.g., *Laraque et al.*, 2009], widening and distorting the mixing layer, with the potential of increasing river mixing. However, the influence that such density differences could have on confluence flow and mixing dynamics is currently unknown.

Even less studies published in the literature have focused on confluences of rivers with strong density contrasts (such it is the case of the O (1) kg m^{-3} density differences between the Ebro and Segre rivers in summer [*Ramón et al.*, 2013], this PhD thesis). Under those conditions, the denser river will plunge and flow below the less dense river and the interface separating the confluent rivers will tend to become nearly horizontal downstream of the plunge point [*Cook et al.*, 2006; *Ramón et al.*, 2013; *Lyubimova et al.*, 2014]. *Lyubimova et al.* [2014] further observed that the plunge point could be upstream of the confluence under strongly buoyant conditions, and low flow rates along the main river. Little is known beyond those facts and more detailed studies are needed to understand the behavior of river confluences under strong density contrasts. But, together with the presence of density differences, there are other mechanisms that could influence mixing at river confluences, and that, to our knowledge have not yet been evaluated before in the literature. This PhD thesis also focuses its attention on the evaluation of two mechanisms suggested by *Ramón et al*. [2013] (this PhD thesis) in their observations of their field experiments at the confluence between the Ebro and Segre rivers: The role of (1) wind forcing and (2) the time-variability of the inflows in river mixing.

The choice of the confluence between the Ebro and Segre rivers (Figure 1.2) was further (and originally) motivated by the presence of the invasive zebra mussels (*Dreissena polymorpha*, Figure 1.3a and Figure 1.3b) in the Ribarroja reservoir, where available records show that colonies of this species are well established since the

beginning of the XXI century [*Navarro et al.*, 2006]. In addition to their negative ecological impacts [e.g., *Strayer*, 2008, and references therein], zebra mussels also cause, among other economic impacts, damage to water-dependent electric power generation and drinking water treatment facilities by fouling intake pipes and other equipment, which results in severely impeded flows of water into these facilities. For example, according to the Ebro Water Confederation (www.chebro.es), investigation and preventive and plague-control actions only for the period of 2006-2009 amounted to a total of €11.6 million and it is predicted that the cumulative cost of battling against zebra mussels will have come to €105 million by 2025. The study of *Navarro et al.* [2006] near the Ribarroja dam, suggested that the distribution pattern of the zebra mussels in the water column during the stratification period was tightly linked to the density stratification in the reservoir, with epilimnetic waters acting as a "biological reactor". Given that stratification in the Ribarroja is hydraulically forced [e.g., *Prats et al.*, 2010], that is, stratification is the result of two water masses of different physical-chemical

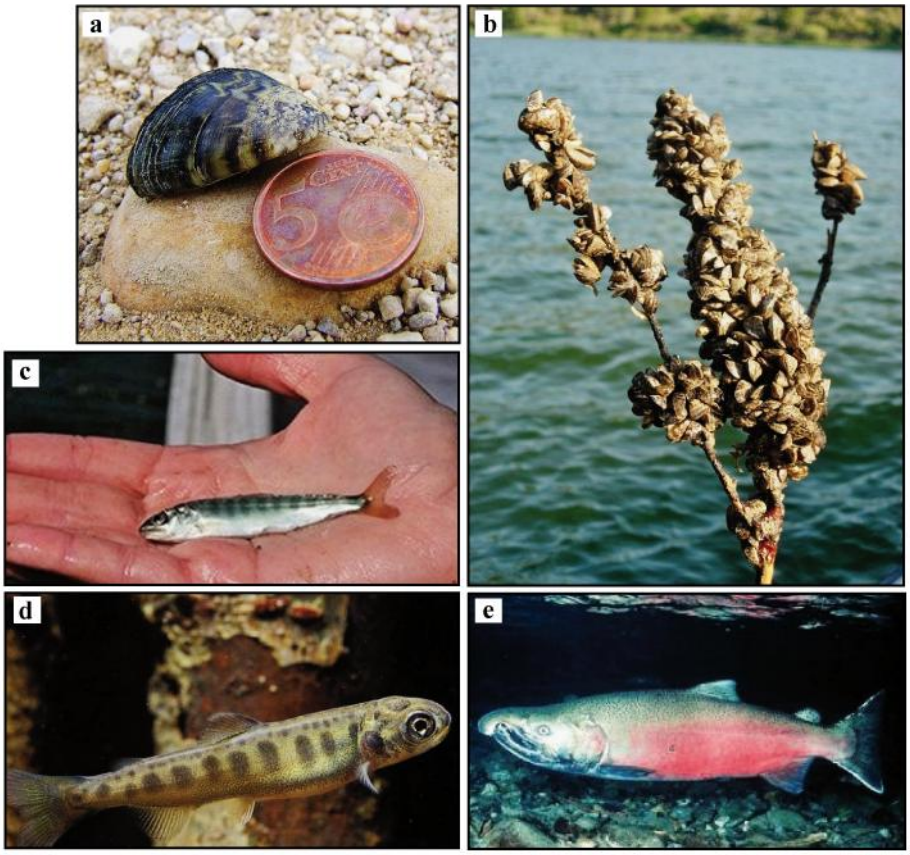

Figure 1.3 (a,b) zebra mussel (*Dreissena polymorpha*), (b) example of zebra-mussel colonization in the Ribarroja reservoir (www.chebro.es), and (c,d) juvenile and (e) adult Chinook salmon (*Oncorhynchus tshawytscha*) (ca.water.usgs.gov).

characteristics (the Ebro and Segre rivers) coming together at the tail of the reservoir; understanding mixing between the Ebro and Segre rivers is a necessary step to understand the distribution of the colonies of the zebra mussel in the reservoir.

1.3 River confluences/diffluences: important nodes in the river network

Together with their intrinsic and network-scale ecological value, confluences (and diffluences) also behave as critical nodes of the river network where aquatic migratory species select different migration routes. This is the case, for example, of the juvenile Chinook salmon (*Oncorhynchus tshawytscha*, Figure 1.3c and Figure 1.3d) in the Sacramento-San Joaquin River Delta (hereon, the Delta, Figure 1.4a). The Delta is characterized by its complexity, with many natural and man-made channels interconnected, and thus, with many confluences and diffluences. Due to the influence of tides, some of the nodes of the Delta can even behave as both confluences and diffluences depending on the tidal phase. Due to the complexity of the Delta, juveniles may take different migration routes on their way to the ocean [*Perry et al.*, 2010], which could result in different survival rates. So far, it is known that those migration routes that lead to the interior Delta have the lower survival rates [*Newman and Brandes*, 2010; *Perry*, 2010; *Perry et al.*, 2010, 2012; *Singer et al.*, 2013] with factors such as high predation rates, longer migration times and entrainment into the water pumping stations (located in the southern part of the Delta, Figure 1.4a) affecting salmon survival in those migration routes [*Brandes and Mclain*, 2001; *Newman and Rice*, 2002; *Newman*, 2003; *Kimmerer*, 2008; *Newman and Brandes*, 2010; *Perry et al.*, 2010]. But why do salmon select a given route? The answer to that question is not trivial, especially in the Delta, where recovery strategies for endangered salmon populations must coexist with the Delta's role in water management in California. The Delta supports California's trillion dollar economy (eighth largest in the world) and $27 billion agricultural industry [Delta Protection Commission, http://www.delta.ca.gov]. The two large pumping facilities located in the southern part of the Delta (Figure 1.4a) provide water for municipal, agricultural, and domestic purposes to more than 23 million people throughout central and southern California [*Newman and Brandes*, 2010]. Associated with the pumping projects, a man-made channel (the Delta Cross Channel, hereon DCC) was constructed to artificially connect the Sacramento River with the interior Delta (Figure 1.4) to reduce salinities at

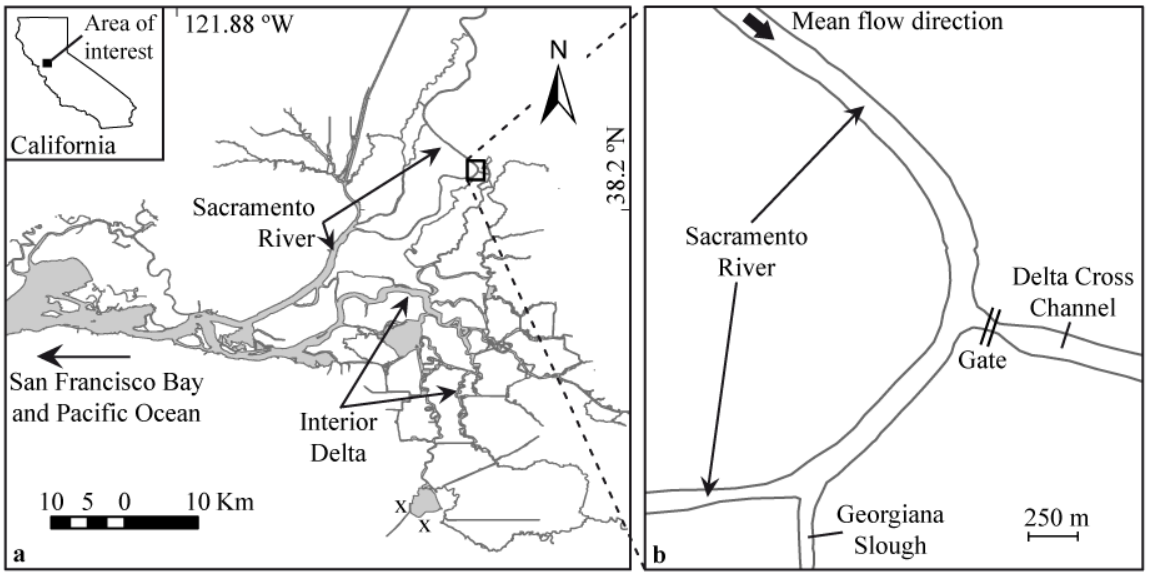

Figure 1.4 (a) The Sacramento-San Joaquin River Delta and (b) close-up view of the area of interest. The (X) symbols in (a) show the locations of the two pumping stations.

the pumping stations. And precisely the DCC together with Georgiana Slough (located downstream of DCC, Figure 1.4) are the two connections between the Sacramento River and the interior Delta, and are key parts of the two salmon migration routes in the Sacramento River that lead to the interior Delta (the lower-survival migration routes). To prevent fish from entering the interior Delta, the moveable gates in the DCC are closed during the emigration period of endangered winter-run juvenile Chinook salmon, assuming that fish entrainment into DCC is directly proportional to the mean fraction of river flow that is diverted to the interior Delta [*SWRCB*, 1995; *Low et al.*, 2006]. However, the validity of this assumption is not clear, and closing the DCC gates may result, for example, in a higher number of fish entering the interior Delta via Georgiana Slough (hereon GEO) [*Blake and Horn*, 2004]. The probability of fish entrainment into a given route will also depend on the hydraulic conditions that the fish encounter when migrating past each channel entrance, which varies with tides [*Blake and Horn*, 2004; *Steel et al*., 2013]. For example, fish tend to bypass the DCC on an ebb tide and to be advected into the DCC from the Sacramento River (both from locations upstream and downstream of the DCC entrance) on a flood tide [*Blake and Horn*, 2004]. In addition, although salmon route-selection is thought to be advection dominated [*Blake and Horn*, 2004; *Perry et al*., 2015], salmon behavior such as their preference for locations near surface (the first four meters of the water column in the Sacramento River [*Blake and Horn*, 2004]) may affect the final fate of the fish. This surface preference could be of

special importance in this reach of the Sacramento River, where the DCC and GEO junctions are located, for two reasons: (1) the DCC is shallower than the Sacramento River, with the DCC entrance located at ≈ 5 m depth; and (2) the two junctions are located at the outside of a river bend (Figure 1.4) where secondary circulation effects are expected to occur [e.g., *Rozovskii*, 1961]. As suggested by *Blake and Horn* [2004] and *Blake et al.* [2012] secondary circulation would tend to displace the surface-biased salmon towards the outer bank, and so, towards DCC and GEO. Thus, understanding the interaction of the tidal cycle with the development of secondary circulation in this reach of the Sacramento River, and fish distributions at the entrance of these junctions, is a key step in order to understand and quantify entrainment rates into these two migration routes, and to propose effective management strategies that maximize salmon survival and minimize economic losses.

1.4 Goals of this PhD thesis

The objectives of this thesis are:

I. To document and understand the effects of the weak density differences between rivers on the mixing dynamics in and downstream of large-scale river confluences;

II. To establish the factors that control the spatial arrangement of water masses and mixing rates across the contact interface, in river confluences under strong density contrasts;

III. To better understand the role of the physical processes of circulation in driving salmon migration-route selection in the Sacramento River. More specifically, we aim to answer two key questions in relation to juvenile salmon out-migration: (a) is fish entrainment higher than flow entrainment due to the presence of secondary circulation at the DCC-GEO bend?, and (b) is fish entrainment different to flow entrainment due to the non-uniform spatial distribution (surface-biased) of salmon at the entrance of both junctions?

For objectives (I) and (II), the junction of the Ebro and Segre rivers in Northern Spain was used as an example of a large confluence with strong asymmetry and a large junction angle (ca. 90°). To reach goals (I-II), first an experimental plan was laid out in which a

series of field campaigns were conducted near the confluence of the Ebro and Segre rivers. The field data collected in those campaigns was then interpreted using scaling arguments. Then, confluence hydrodynamics was modeled with the three-dimensional primitive-equation model of *Smith* [2006] where, in order to evaluate river mixing, numerical tracer experiments were conducted in which the main Ebro River was the river being traced. To reach goal (III) river hydrodynamics in the Sacramento-River reach was modeled with the three-dimensional primitive-equation model of *Smith* [2006] and the mechanistic-individual based model developed by *Hoyer et al.* [2014] was used to characterize salmon movements within the Sacramento-River reach.

1.5 Structure of this PhD thesis

This thesis is organized to reach goals (I-III) sequentially. First, in Chapter 2, the field data collected at the Ebro-Segre confluence is presented and interpreted using scaling arguments. Second, in Chapter 3, the transport and mixing simulations of the Ebro-Segre confluence are presented and the effect of weak river density differences on river mixing is evaluated. Next, Chapter 4 presents the transport and mixing simulations of the Ebro-Segre confluence under strong density differences and the factors controlling river arrangement and mixing are pinpointed and evaluated. Finally, in Chapter 5, the simulations of river hydrodynamics in the reach of the Sacramento River under study are presented and the effect on fish entrainment of the presence of secondary circulation and fish distribution upstream of river junctions are evaluated. The intention of this thesis is that each chapter can be read as a standalone article. This means that some of the information presented in each chapter is, especially that concerning the introduction and methods section, partially repetitive. The intention of this repetition is to provide the reader with all the necessary information to read each chapter independently.

Chapter 2

Mixing and circulation at the confluence of two rivers entering a meandering reservoir

Published in *Water Resour. Res.*, doi: 10.1002/wrcr.20131

Abstract

A field data set collected under different conditions is analyzed to characterize the spatial arrangement of two large inflows (Ebro and Segre) with distinct physical-chemical characteristics as they join at the upstream end of the Ribarroja reservoir in northern Spain. Given the short average residence time of water in the reservoir, the spatial arrangement of the rivers at their confluence and their mixing rates are likely the drivers of the stratification patterns observed near the dam. In winter, inflows have similar densities —$\Delta\rho/\rho_0$ ≈ O (10^{-5}) — and their spatial distribution is largely determined by inertial forces, and in particular, by the discharge ratio. Downstream of the confluence, both rivers flow side by side and largely unmixed over long distances. In summer, with $\Delta\rho/\rho_0$ of O (10^{-3}), the flow fields at the confluence are largely controlled by buoyancy forces. Atmospheric forcing during strong wind events and centrifugal forces caused by the meandering shape of the reservoir induce significant tilting of the isotherms, leading to localized high mixing rates. Mixing, in general, though is weak at this time of the year. In fall and early winter, density differences are largely controlled by conductivity differences between the incoming flows. The warmer Ebro water, with larger thermal inertia, flows beneath the colder Segre water. The spatial arrangement of the inflows is largely controlled by the discharge ratio and mixing between sources is strong, likely as a result of mixed water being denser than either of the incoming flows.

2.1 Introduction

Stratification in the water column provides one of the largest physical constraints for biological growth in lake ecosystems, controlling the vertical rate at which mass is transferred, and, hence, determining the environmental conditions in which

biogeochemical reactions occurs and biota develops. Stratification, for example, is tightly linked to the oxygen dynamics in lakes and reservoirs. Under stratified conditions, the vertical transfer of oxygen is reduced and oxygen levels in the deeper layers of eutrophic systems tend to decrease, getting even to levels close to zero. Under those conditions, the oxidation state of many water quality constituents change, modifying their physical and chemical behavior. Stratification develops as a result of a subtle balance between processes that alter the density of water over depth and other processes that mix parcels of fluid within the water column. In natural lakes, with negligible through flows, heat fluxes tend to warm up the surface layers, and, the mechanical energy imparted by the wind in the water column, either directly or through shear-generation will mix water parcels. Water flowing over a solid bottom may also introduce the necessary turbulent kinetic energy to mix the water column. Hence, one expects weaker stratifications in rivers and reservoirs with large throughflow rates [*Schräder*, 1958] or with small residence times. *Straškraba and Mauersberger* [1988], in fact, developed an empirical relationship between the average residence times and reservoir stratification characterized by the temperature difference between the surface and a depth of 30 m in summer (see also *Straškraba* [1999]). Hydraulic forcing can also be a source of stratification [*Tundisi*, 1984] when large inflows from rivers with different characteristics enter a lake or a reservoir. The Ribarroja reservoir, in northern Spain, is a case example of a reservoir that stratifies as a result of hydraulic forcing [*Prats et al*., 2010]. The two largest inflows into the reservoir (Ebro and Segre rivers) enter at its upstream end and have distinct physical-chemical characteristics that vary at seasonal, and even shorter, time scales. Given the short average residence time of water in the Ribarroja, stratification patterns observed near the dam are expected to be largely controlled by the relative magnitude of the inflows from the Ebro and Segre rivers and the rates at which these two sources mix as they travel downstream.

The extent to which basin scale stratification develops in hydraulically stratified reservoirs, in general, and the particular stratification patterns existing near the dam will depend on (1) the spatial distribution of the different sources of water as they enter the reservoir and (2) the rate at which they mix downstream of their confluence. The behavior of single inflows, in turn, critically depends on their density ρ relative to that of the surface of the reservoir ρ_0, ambient stratification and circulation, inflow rates [*Fischer et al*., 1979], and the particular geometry of the receiving basin near the inflow regions

[*Johnson et al.*, 1987; *Fleenor and Schladow*, 2000]. In long, narrow, straight, and quiescent basins with simple geometries in which lateral motions are restricted, the pathways of distribution of single inflows and their relevant time and spatial scales have been thoroughly studied in the literature through laboratory experiments [e.g., *Wells and Wettlaufer*, 2007; *Wells and Nadarajah*, 2009, and references therein], numerical simulations [e.g., *Chung and Gu*, 1998; *Bournet et al.*, 1999; *Kassem et al.*, 2003], and analysis of field data [e.g., *Fischer and Smith*, 1983; *Hebbert et al.*, 1979; *Dallimore et al.*, 2001]. According to these studies, an inflowing stream will push the stagnant ambient water until its inertia is arrested, at some distance from the inflow section, due to density differences. At this point, a stream having less density than the lake surface will separate from the bottom, riding on top of the water column as an overflow. The denser stream water will plunge, in turn, beneath the surface, and it will flow downward along the bottom as a gravity-driven density current, gradually entraining water until it reaches the level of neutral buoyancy where the densities of the flowing current and the ambient fluid are equal [*Stevens et al.*, 1995; *Ahlfeld et al.*, 2003]. The level of neutral buoyancy can even be the bottom of the basin [*Hebbert et al.*, 1979; *Finger et al.*, 2006]. Once the density currents reach their depth of neutral buoyancy, they will form intrusions that spread horizontally into the main body of the reservoir. The behavior of buoyant river inflows can be interpreted as the interplay between inertial and buoyancy forces, and hence can be parameterized in terms of the internal Froude number, $Fr_i = U/(g'D)^{0.5}$, where U represents the inflow velocity, D the depth of the channel, and g' ($= g\,\Delta\rho/\rho_0$) the reduced gravity calculated from the density differences between lake and river water. Upstream of the plunge/lift point, it is assumed that motion is dominated by inertial forces and $Fr_i >> 1$. Downstream, in turn, buoyancy forces dominate the motion and $Fr_i << 1$. At the plunge/lift point, Fr_i is O (1), and most expressions proposed to determine the location of the plunge/lift points are based on this condition.

Describing the pathways of distribution of river water under realistic conditions with more complex inflow geometries [*Rueda and MacIntyre*, 2010], with several inflows interacting [*Marti et al.*, 2011], or with strong circulation in the receiving basin, however, remains a major challenge in the study of inflows in reservoirs. The inflow of the Segre River into the upstream end of the Ribarroja reservoir (Figure 2.1) is a case example where those conditions hold. The reservoir is constructed on the Ebro River channel, has an elongated and meandering planform and typically exhibits large throughflow rates.

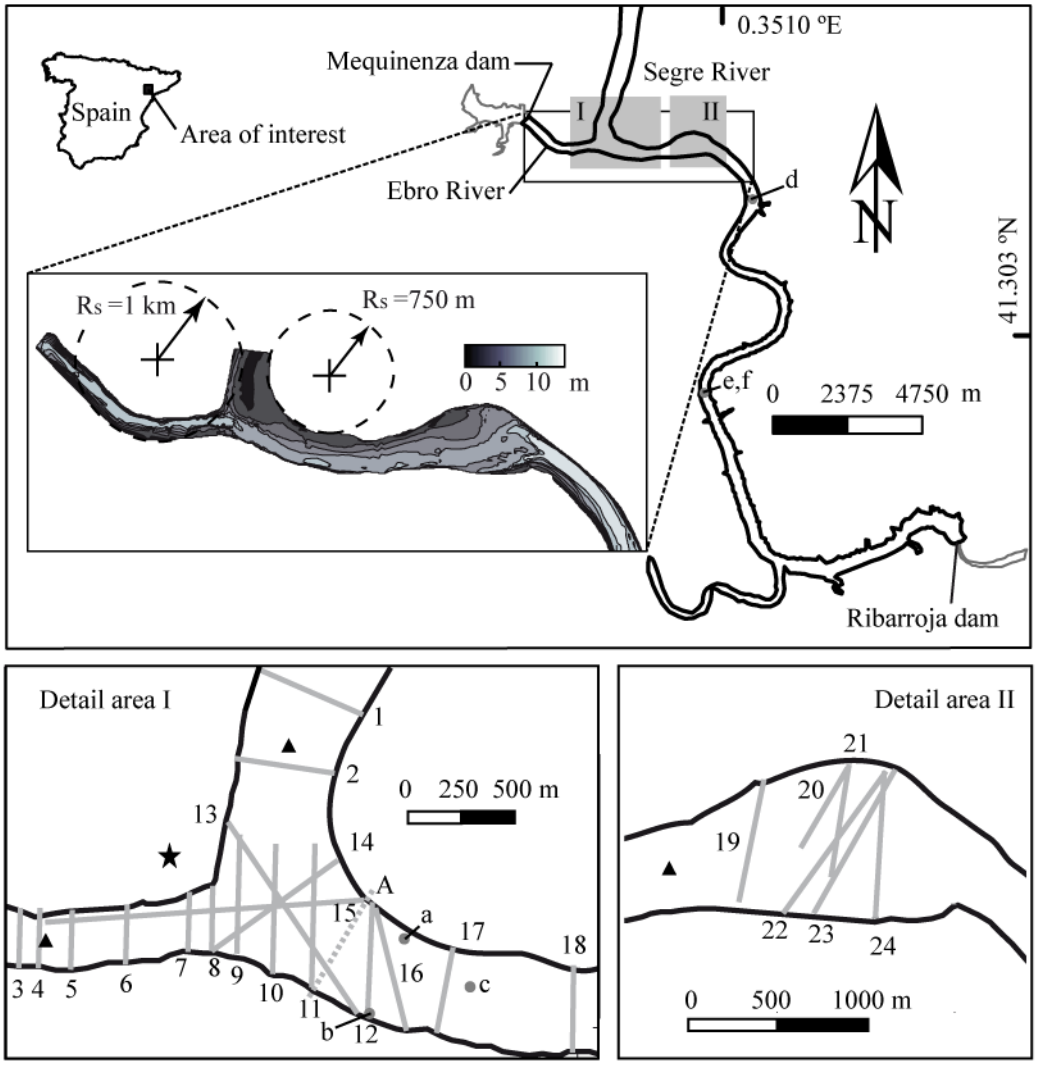

Figure 2.1 The Ribarroja reservoir (gray rectangle: area of study—the confluence between the Ebro and Segre rivers), bathymetry of the confluence and location of ADCP J*j*, F*j*, and N*j* transects (gray solid lines) for the 2009 campaign. Gray dashed line: location of cross-section A immediately downstream of the junction corner. Star: location where cameras were deployed during the July experiment; triangles: location of thermistor chains W, N, and C during the February experiment. Dots: locations where CTD profiles a-f were collected on day 50 (February experiment).

The Segre River enters the left margin of the reservoir shortly downstream of a dam that regulates the inflows from the Ebro River. Being able to describe and understand the spatial arrangement of the Ebro and Segre waters (the largest inflows) near their confluence and the mixing rates of both masses as they travel downstream appears to be the key to understanding stratification as observed near the dam and, hence, is important for water quality management. However, it is a challenging task for several reasons. First, because of the strong cross-flows along the Ribarroja reservoir, the rate of mixing

between the river and reservoir water may not conform to classical models for inflows into quiescent ambient waters. Second, the flow downstream of the confluence may be stratified, depending on the density difference between the rivers. Many studies exist that study circulation patterns of stratified flows within curved or meandering channels, but most of them are aimed at describing flows in laboratory settings [e.g., *Corney et al.*, 2006; *Chao et al.*, 2009; *Cossu and Wells*, 2010], estuarine environments [*Lacy and Monismith*, 2001], or in submarine channel bends [*Parsons et al*., 2010].

Our general goal in this work is to describe the spatial distribution of water from the Ebro (hereon western W-River) and Segre (hereon northern N-River) rivers as they enter the Ribarroja reservoir and to understand the physical processes controlling the rate of mixing between these two rivers at and downstream of their confluence, at the upstream end of the reservoir. Based on previous records collected in 1998, an experimental plan was laid out in which a series of field campaigns were conducted near the confluence of the N- and W-rivers (see Figure 2.1). The field data collected in those campaigns is presented and interpreted using scaling arguments.

2.2 Study site

The Ribarroja reservoir (41º 18' N, 0º 21' E) is the second of a chain of three reservoirs (Mequinenza-Ribarroja-Flix) constructed along the lower reaches of the W-River for hydroelectric power generation (Figure 2.1). It is warm, monomictic, and mesoeutrophic, and it is used for fishing, navigation, irrigation, and urban supply, in addition to being for hydropower. The basin is relatively shallow, with an average depth of 9.8 m, reaching values of up to 34 m near the dam. The free surface elevation is kept nearly constant and close to 69 m above sea level. Its area S and volume V when full are 2152 ha and 2.07×10^8 m^3, respectively. With an average throughflow Q of 300 m^3 s^{-1} (mean value from 1998), the nominal residence time of Ribarroja (= V/Q), is approximately 8 days. This value ranges from ≈ 3 days to less than a month [e.g., *Cruzado et al.*, 2002], depending on throughflow rates. Throughflows, in turn, typically vary from ≈ 200 m^3 s^{-1} in summer to nearly 800 m^3 s^{-1} in winter. Peak flows after storm events can be larger than 2000 m^3 s^{-1} [*Prats et al.*, 2010]. The reservoir has an elongated and meandering shape (Figure 2.1), with the two largest inflows (Segre N- and Ebro W-rivers) occurring at the Northwest end. Inflows from the W-River are regulated by the

Mequinenza dam, which discharges directly into the Ribarroja reservoir 3 km upstream of the confluence of the N-River into the W-River. Only the hydroelectric intakes, releasing deep hypolimnetic water with stable temperatures throughout the year, are operated on a regular basis [*Prats et al.*, 2010]. Inflows from the N-River, in turn, are largely unregulated and exhibit larger seasonal variations in temperature. Stratification in the reservoir, hence, is largely subject to hydraulic control exhibiting changes at seasonal scales.

The strongest stratification develops in summer, with a thermocline located between 5 and 10 m and a nearly anoxic hypolimnion, primarily formed by cold hypoxic waters released from the hypolimnion of the Mequinenza reservoir [*Prats et al.*, 2010]. Winds are highly variable with daily-averaged values ranging from 1 to nearly 10 m s^{-1}. Winds are strongly periodic (with 24-hr periods), predominantly from the Southeast during summer (from May to September), and from the East in the first 3 months of the hydrologic year. From January to March, winds are predominantly from the North and Northeast, veering to southeasterly winds in April. The strongest winds are commonly associated with southeasterly winds, but gusts of strong winds from the North and Northwest occasionally develop.

2.3 Material and Methods

2.3.1 Approach

Three different scenarios or modes for the behavior of the W- and N-rivers at their confluence were identified based on a preliminary analysis of existing information on river inflows and water temperatures, collected in 1998 (Figure 2.2). It was assumed in this analysis that water density would be largely controlled by its temperature, given that no other water properties had been observed at that time. Furthermore, this assumption is commonly used when studying freshwater bodies [e.g., *Horne and Goldman*, 1994; *Goudsmit et al.*, 2002; *Prats*, 2011]. Scenario 1 corresponds to the first few months of the year, when large inflow rates (average values of ≈ 200 m^3 s^{-1}) are observed both in the W- and N-rivers. Peak inflows in the N-River occur in December and May, probably associated with rainfall events and ice-off from the Pyrenees, respectively. Inflows from the W-River exhibit several peaks during this period of time, probably due to withdrawals

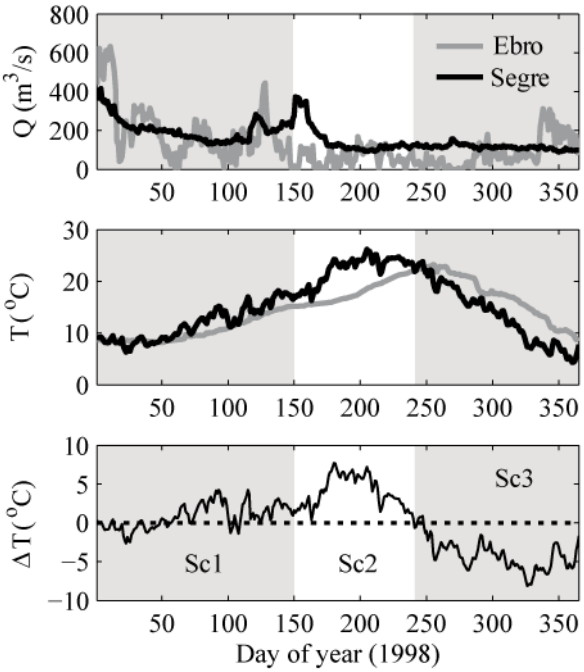

Figure 2.2 Scenarios (Sc) first proposed after analyzing daily inflow rates from the Ebro and Segre rivers, and water temperature in 1998. ΔT is the depth-averaged temperature difference between the Segre and Ebro rivers ($\Delta T = T_N - T_W$).

from Mequinenza after major rainfall events. The W- and N-temperatures are similar, especially during the first and coldest part of the year. N-temperatures tend to be warmer, though, toward the end of this period. In Scenario 2 (summer), inflow rates are lower (≈ 100 $m^3\ s^{-1}$) from both sources, and decreasing, in the case of the W-River. By the end of the period, the inflows from the W-River are negligible. Large temperature differences between the sources exist, with the warmer temperatures observed in the N-River. Finally, Scenario 3 corresponds to fall and beginning of winter conditions. The warmer temperatures are from the W-River and inflow rates are similar to those in Scenario 2. Other studies conducted in the Ribarroja already point to the existence of these three scenarios [e.g., *González*, 2007; *Prats*, 2011].

2.3.2 Field experiments

Three field experiments were conducted in 2009 to characterize the spatial distribution of the W- and N-waters at the confluence (see Table 2.1), under the three scenarios identified in the analysis of historical data. The first field experiment was conducted in late winter, from 18 February to 20 February (Julian days 49-51); the second in summer, on 21 and 22 July (Julian days 202-203); and the third, in late fall, on 25 and

26 November (Julian days 329-330). Wind (speed and direction), air temperature, relative humidity, and solar radiation records for the days of the three experiments were collected at a meteorological station existing on a floating platform deployed near the dam. Water velocity, temperature, conductivity, and turbidity were collected along several transects. Water velocity profiles were collected using a boat-mounted Acoustic Doppler Current Profiler (ADCP). Two ADCPs (1200 kHz and 600 kHz RDI-Workhorse) were used in the first experiment, and only one (1200 kHz) in all others. The 1200 kHz-ADCP was operated in two different working modes, depending on the depth of the reservoir along each transect. The high-resolution coherent mode 5 was used in the shallowest transects. The default Mode 1 was used in the deeper portions of the lake. The maximum bin size was 0.5 m in all cases. The ADCP transects will be referred to as F_j, J_j, and N_j for the February, July, and November campaigns, respectively, where j is the number of the transect in Figure 2.1. Temperature, conductivity, and turbidity profiles were collected at several points along the transects using Seabird SBE-19 conductivity-temperature-depth (CTD) profilers. SBE-19 recorded at a rate of 20 Hz while free falling through the water column, giving a vertical resolution of O (10^{-2}) m. The number of CTD profiles taken along each transect varied, and the distance between two consecutive profiles ranged from 100 to 300 m. The observations were mainly analyzed on a transect-by-transect mode. CTD data collected upstream of the confluence along the W- and N-rivers were used as references to characterize the properties of the sources (W- and N-water) in an end-member analysis of the mixed water downstream of the confluence. In this analysis, any given sample at and downstream of the confluence is assumed to be the result of a conservative mixture of two sources of water (end members) [e.g., *Boyle et al.*, 1974]. The bathymetry of the confluence was reconstructed from an existing bathymetry map of the upper midhalf of the reservoir (Figure 2.1), and additional data collected with the ADCP during the field experiments in 2009.

During the first experiment, three thermistor chains were deployed upstream of the W- (chain W) and N- (chain N) rivers and downstream of the confluence (chain C) to characterize daily changes in water temperature. Chains N, W, and C had 5, 13, and 14 HOBO H20-001 temperature loggers (resolution 0.02 ºC, accuracy ± 0.2 ºC), respectively, arranged at about ≈ 0.4-m intervals close to the surface and 1 m closer to the bottom, except for chain W, where a constant interval of 1 m was used. On the second campaign, several cameras were deployed near a high point located at the confluence to

Table 2.1 Summary of experiments conducted at the Ribarroja reservoir—Dates and measurements

Expe-riment	Day	Observation from boat	Day	Observations from autonomous instrumentation
Feb., 2009	49 50-51	▪ CTD profiles ▪ CTD profiles and ▪ Velocity profile observations with a RDI 1200 kHz and a RDI 600 kHz	49-51	▪Thermistor chains (Ebro, Segre and confluence) ▪ Wind, air temperature, relative humidity and solar radiation (meteorological station)
July, 2009	202-203	▪ CTD profiles and ▪ Velocity profile observations with a RDI 1200 kHz	202 202-203	▪ Photographs of the confluence ▪ Wind, air temperature, relative humidity and solar radiation (meteorological station)
Nov., 2009	329-330	▪ CTD profiles and ▪ Velocity profile observations with a RDI 1200 kHz	329-330	▪ Wind, air temperature, relative humidity and solar radiation (meteorological station)

the left of the W-River on day 202 (Figure 2.1). A series of photographs were taken from 11 A.M. to nearly 5 P.M.

The equation of state of *Chen and Millero* [1986], as reported by *Pawlowicz* [2008], was used to calculate density from temperature and salinity data. Salinity or total dissolved solids (TDS), in turn, was estimated from specific conductivity Co_0 (μS cm^{-1}) and temperature (ºC) records as follows [*Pawlowicz*, 2008]:

$$TDS = \lambda\left(\frac{Co_0}{1+0.0191\cdot(T-25)}\right). \qquad (2.1)$$

The scaling factor λ in equation (2.1), here set to 0.8, is known to vary between 0.55 and 0.9 mg L^{-1} (μS cm^{-1})$^{-1}$ in general usage, but can be as high as 1.4 mg L^{-1} (μS cm^{-1})$^{-1}$ in meromictic saline lakes [*Pawlowicz*, 2008]. The large variations (of up to 30%) in the value of the scaling factor are indicative of the extreme sensitivity of salinity values to changes in the ionic composition of water. Water samples collected in November 2009 were analyzed to determine their ionic composition. Using the results of that analysis, as

proposed by *Pawlowicz* [2008], the correlation between TDS and specific conductivity gives an average value of 0.8 ± 0.2 mg L^{-1} (μS cm^{-1})$^{-1}$ for the scaling factor, for both rivers, which makes the former assumption reasonable. No information was available on whether the ionic composition of the water from Mequinenza or the N-River changes in time. Hence, 0.8 is assumed valid for all the experiments. The contribution of suspended solid *SS* concentration in the density calculations was in all cases assumed negligible based on the observed turbidity differences (Table 2.2). The turbidity records *Turb* collected at the inflow sections were first converted to *SS* (mg L^{-1}) using the following empirical equation (r^2 = 0.97) developed for the study site

$$SS = 0.4785 \cdot Turb + 1.0904. \tag{2.2}$$

The contribution of *SS* to density ($\Delta\rho_{SS}$) was then calculated as follows [*Ford and Johnson*, 1983]:

$$\Delta\rho_{SS} = SS\left(1 - \frac{1}{SG}\right) \cdot 10^{-3}, \tag{2.3}$$

where *SG* is the specific gravity of suspended solids. Given that almost 95% of the suspended sediment load from the W-River [*Roura*, 2004] is retained upstream in Mequinenza, the N-River is the largest source of suspended sediments at the confluence, bringing mostly silt and clay with a particle size d < 25 mm and 9% of organic matter [*Flumen-Group*, 2009]. Assuming that $SG \approx 2.65$ (as in *Chen et al.* [2006]), the contribution of *SS* to density was always at least 1 order of magnitude lower than those caused by salinity and temperature differences. In February, for example, with the lowest temperatures (8 ºC) and the smallest differences in specific conductance (80 μS cm^{-1}, Table 2.2), the salinity driven-density contrast between the sources was O (10^{-2}) kg m^{-3}. Differences in turbidity of 10 nephelometric turbidity units (ntu) (Table 2.2), in turn, introduced density differences of O (10^{-3}) kg m^{-3}.

2.4 Results and Discussion

2.4.1 Density differences between sources

Specific conductance versus temperature for all records collected at all depths and spatial locations during the days of experiments for the three field campaigns are plotted in Figure 2.3. Density estimates are shown as isolines on these plots. Note that the records tend to form straight lines between two points representing the characteristics of the W- and N-rivers (end members), which is indicative of all water parcels at the confluence being the result of mixing between these two rivers.

Temperature differences between rivers in February were as much as 1 ºC. W-temperatures were nearly constant (≈ 8 ºC). N-temperatures, in turn, experienced diurnal oscillations with amplitudes that exceeded the average temperature differences between the two sources (Figure 2.3a and Figure 2.4). As a result of those changes, the records at the confluence also exhibited diurnal oscillations, forming straight lines between the end members. Conductivity differences between sources at this time of the year were of O (10) µS cm^{-1}, with the lower conductivities (718 µS cm^{-1}) observed in the N-River.

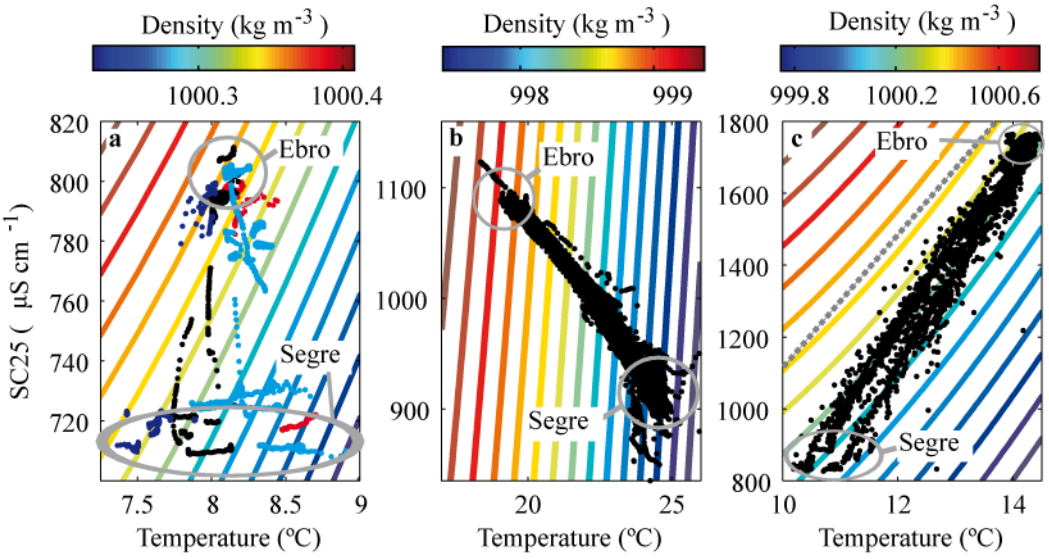

Figure 2.3 Distribution of specific conductance versus water temperature (dots) observed at different points at the confluence between the Ebro and Segre rivers in the Ribarroja reservoir. Colored lines in the background are lines with equal densities, calculated as *Chen and Millero* [1986] (see *Pawlowicz* [2008]). (a) February experiment. Dot color represents (1) red: day 49, (2) black: morning on day 50 (3) cyan: afternoon on day 50 and (4) blue: day 51; (b) July experiment; and (c) November experiment. The gray straight-dashed line in (c) shows the curvature of lines of equal density.

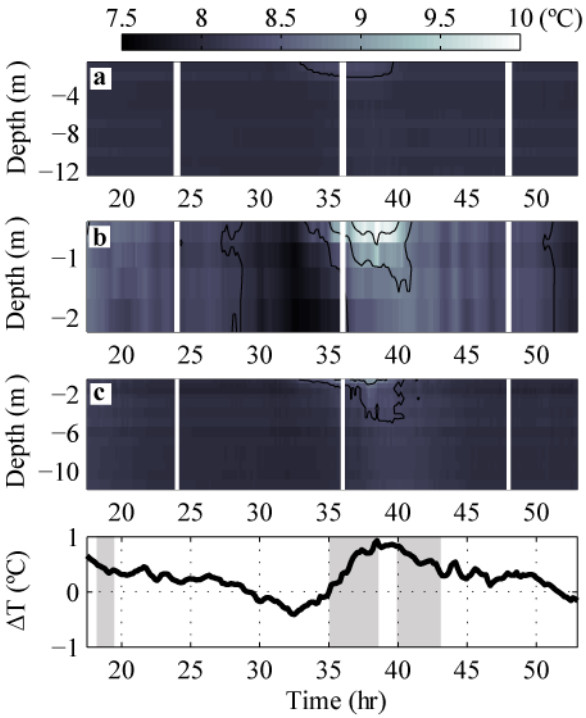

Figure 2.4 Temperature data from thermistor chains (triangles in Figure 2.1) located at (a) the Ebro River (chain-W), (b) the Segre River (chain-N), and (c) downstream of the confluence (chain-C), and differences between depth-averaged temperature ΔT for the Segre and Ebro rivers, $\Delta T = T_N - T_W$. White lines indicate 0000 hr, 1200 hr, and 2400 hr on day 50 [Time (hr) = 0 at 0:00 hr on day 49]. Shaded areas show time for CTD casts on days 49 and 50. CTD profiles on day 51 were collected between 1100 and 1330 hr.

Relative density differences $\Delta\rho/\rho_0$, driven both by differences in temperature and salinity between sources were of O (10^{-5}). As a result of the daily temperature variations, the N-water could be lighter or have similar density to the W-water. Maximum density differences $\Delta\rho/\rho_0$ occurred during the afternoon on day 50 with values of O (10^{-4}) (Figure 2.3a).

In contrast to the data from February, the data from July and November clusters along a unique straight line between the two end members (Figure 2.3b and Figure 2.3c). This is partly due to the large temperature and conductivity differences between sources at those times of the year, compared to the diurnal oscillations. In July, for example, temperature differences of up to 6 ºC (warmer in the N-River) were observed between the sources. Conductivity differences at this time were, in turn, weak, and approximately six times smaller than those observed in November. Hence, density differences between sources at this time were largely driven by temperature differences, and the isopycnals in

Figure 2.3b appear as steep lines compared to the other two periods. In November, in turn, temperature differences between sources were of up to 5 ºC and the differences in conductivity were ≈ 900 μS cm^{-1}. Inflow buoyancy was, at that time, controlled both by differences in temperature and salinity, and the W-water was, for example, denser than inflows from the N-River, despite being warmer. Note that all points tend to accumulate along two different lines, each one corresponding to data from the 2 days of the experiment (Figure 2.3c). While the water properties from the W-River were nearly constant during the experiment, the N-water was colder on the second day. Note also that water parcels formed by mixing between the two sources on the second day of the experiment should be denser than the end members, as a consequence of the curvature of the lines of equal density in Figure 2.3c. This interpretation, however, largely depends on the values of scaling factor used in equation (2.1). For $0.63 < \lambda < 0.8$ mg L^{-1} (μS cm^{-1})$^{-1}$, the mixed water is denser than both the W- and N-water. For $\lambda > 0.8$ mg L^{-1} (μS cm^{-1})$^{-1}$, in turn, the larger the fraction of the W-water in the mixed parcel, the larger is its density. Experimentally derived values of λ (see methods) includes a range of ± 0.2 mg L^{-1} (μS cm^{-1})$^{-1}$ around $\lambda = 0.8$; hence, both conditions are possible.

2.4.2 Experiment I

The experiment was conducted shortly after a major rainfall event. Inflow rates from the W-River were approximately 700 m^3 s^{-1} on day 50, almost seven times larger than the N-inflows (Table 2.2). These differences in flow rates are typically observed in winter, as reported, for example, by *Prats et al.* [2010]. The weather during the field campaign was cold, cloudy at night, and calm most of the time. The internal Froude number Fr_i, estimated using cross-sectional average velocities and temperature differences (Table 2.2 and Figure 2.3a), varied from O (1) to O (10), and was always > 4, which suggests that flows and circulation patterns near the confluence are dominated by inertial forces. Hence, temperature variations were assumed to be unimportant from a dynamic standpoint.

2.4.2.1 *Spatial arrangement of inflows under weakly stratified conditions*

Given the marked contrast in the specific conductivity *SC*25 between the W- and N-water (≈ 80 μS cm^{-1}), *SC*25 was taken as a tracer of the source of water at the

Table 2.2 Average values in the Segre and Ebro inflow sections before entering the reservoir obtained from ADCP and CTD casts.

Day	Transect	Q[(a)] ($m^3 s^{-1}$)	u_{E-W}[(b)] (ms^{-1})	u_{N-S}[(c)] (ms^{-1})	T (°C)	*Turb* (ntu)	$SC25$[(d)] (μScm^{-1})	T_a[(e)] (°C)	U_{10}[(f)] (ms^{-1})
50	N-F1[g]	-96	-0.050	-0.10	8.2	17.4	713.7	10.6	2.9
50	W-F3	730	0.468	-0.084	8.1	9.7	801.2		
51	N-F1	-116	-0.054	-0.11	7.4	13.2	722.5	8.5	1.8
51	W-F3	624	0.371	-0.040	-	-	-		
202	N-J1	- 50	-0.021	-0.051	24.1	61.1	909.3	27.7	8.4
203	W-J3-5	220	0.146	-0.031	20.8	5.2	1061.7	28.7	7.0
329	N-N2	-12	0.007	-0.010	10.9	18.2	838.8	9.0	1.9
329	W-N5	253	0.163	-0.003	14.2	7.4	1758.2		
330	N-N2	-69	-0.006	-0.066	10.3	17.6	833.6	14.4	0.8
330	W-N5	172	0.108	-0.003	14.1	8.8	1743.4		

(a) Q = Inflow rate.
(b) u_{E-W} = average E-W velocity (positive value if westward).
(c) u_{N-S} = average N-S velocity (positive value if southward).
(d) $SC25$ =specific conductivity (T = 25°C).
(e) T_a = average temperature of air at the time when transects where collected.
(f) U_{10} = average wind speed (10 m height) at the time when transects were collected.
(g) F=February, J= July, N=November. Numbers account for transects in Figure 2.1. N=Segre, W= Ebro.

confluence [*Gaudet and Roy*, 1995; *Laraque et al.*, 2009; *Rueda and MacIntyre*, 2010], and the dilution of the W-water at any given site i was calculated as follows:

$$\Gamma = \frac{SC25_i - SC25_N}{SC25_W - SC25_N} \tag{2.4}$$

Here $SC25_i$ is the specific conductivity of the mixture at site i, and $SC25_W$ and $SC25_N$ denote the conductivity of the end members (Figure 2.3a and Table 2.2). The conductivity plots in Figure 2.3a and the spatial distribution of dilution rates (Figure 2.5a) suggest that the N-water flowed attached to the left side of the confluence with a nearly vertical interface. Assuming (1) that vertically well mixed conditions prevail at and downstream of the confluence, (2) that mixing is not affected by the small density differences encountered in the field, and (3) that hydraulic forcing remains steady, the transverse mixing coefficient ε_t between the W- and N-water masses downstream of the confluence can be estimated by fitting the steady-state depth-integrated diffusion equation for $SC25$ [*Bouchez et al.*, 2010]

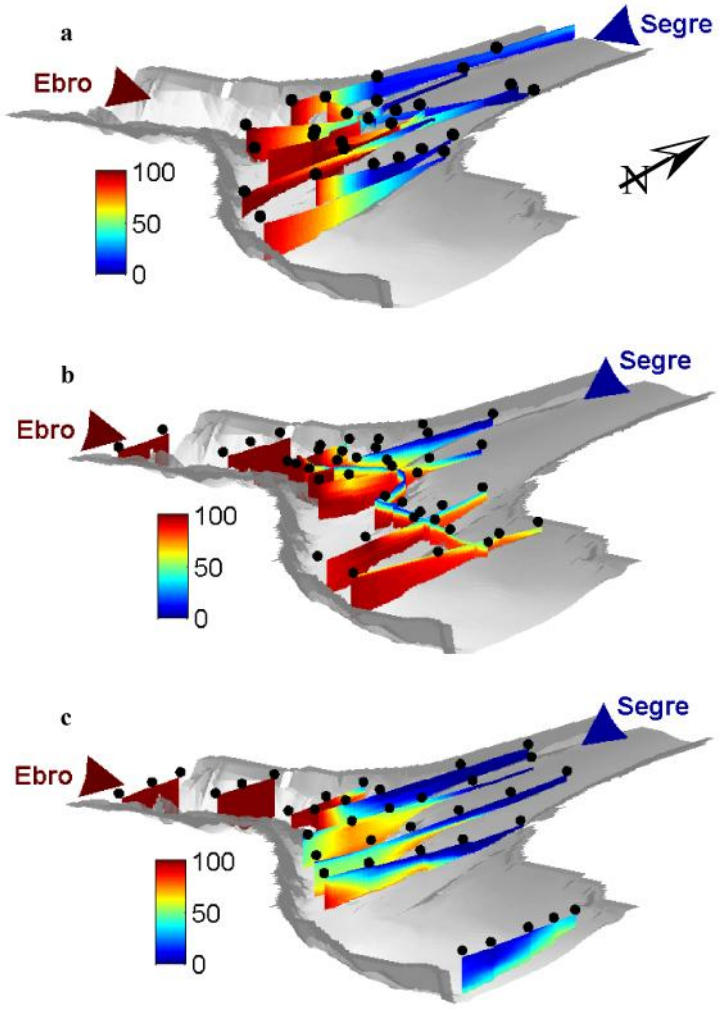

Figure 2.5 Dilution rates (%) from linearly-interpolated specific conductance collected from CTD casts on days (a) 50–51, (b) 329, and (c) 330 at the confluence. Dots account for locations of CTD casts. Red and blue arrows show the direction of the flow. North direction is shown.

$$\frac{\partial \varsigma}{\partial \Lambda} = \frac{\partial^2 \varsigma}{\partial Y^2} \tag{2.5}$$

to the observations. Here, ς (= $[SC25_i]_{int}/SC25_W$) is the ratio between the depth-integrated specific conductance of a given site and the specific conductance of the W-water; Y (= n/b_p) is the transverse distance n divided by the river width b_p, assumed constant over the whole reach (≈ 400 m); and Λ (= $\varepsilon_t\, t/b_p^2$) is the nondimensional elapsed time, where the time $t = s/\langle u_s \rangle$, s being the distance downstream and $\langle u_s \rangle$ the average streamwise velocity (= 0.4 m s^{-1}). To solve equation (2.5), the fluxes through the banks are assumed negligible, i.e., $\partial\varsigma/\partial\Lambda = 0$ at $Y = 0$ and $Y = 1$. The N-water ($\varsigma = 0.89$) was initially assumed to occupy 22.5% of the cross section; the remaining was filled with W-water (ς

= 1). This initial distribution of the N- and W-water arise from the assumption of uniform velocities at cross section A (Figure 2.1), with the observed inflow rates Q_W and Q_N on day 50 (Table 2.2). Equation (2.5) was calibrated against measured *SC*25 profiles collected at (1) sites a and b, 250 m downstream of the confluence; (2) site d, 5.7 km downstream of the confluence; and (3) sites e and f, 13.8 km downstream of the confluence (Figure 2.1). The best agreement between equation (2.5) and observed *SC*25 (

Table **2.3**) was found for ε_t = 1.7 ± 0.1 m^2 s^{-1} (RMSE = 1.5 μS cm^{-1}). This is consistent with values of ε_t reported for large river confluences. For example, *Bouchez et al*. [2010] found ε_t to be 1.8 m^2 s^{-1} at the confluence between the Solimões and the Purús rivers, and *Lane et al.* [2008] found ε_t to vary between 5.6 m^2 s^{-1} and 266.0 m^2 s^{-1} at the confluence between the Paraná and Paraguay rivers. If we assume that complete mixing occurs when cross-stream conductivity gradients become < 1 μS cm^{-1}, and if we ignore the effect of the dam, the mixing length L_M needed for the W- and N-water to become fully mixed is L_M = 16.3 ± 1 km (or 40.75 ± 2.5 channel widths). These estimates of L_M of O (10-10^2) times the channel widths agree with mixing lengths encountered at large river confluences during periods of weak density differences [e.g., *Lane et al.*, 2008, and references therein], and, suggest that the W- and N-masses would mix before reaching the dam (located ≈ 27 km downstream of the confluence).

Table 2.3 Measured — CTD profiles a, b, d, e and f in Figure 2.1— and modeled (Eq. 2.5) depth-integrated specific conductance *SC*25 (μS cm^{-1})[(a)].

CTD Profile	s[(b)] (m)	Y[(c)]	Mesured *SC25* (μScm^{-1})	Modelled *SC25* (μScm^{-1})
a	250	0.067	719.6	720.9
b	250	0.916	801.0	801.0
d	5700	0.513	780.5	782.2
e	13800	0.990	780.3	781.7
f	13800	0.635	779.5	781.6

[(a)] Modeled values correspond to a transverse mixing coefficient ε_t =1.7 m^2 s^{-1}.
[(b)] s = distance downstream of the confluence.
[(c)] Y= n/b_p = non-dimensional transverse distance, where n = transverse distance from the left bank and b_p = channel width.

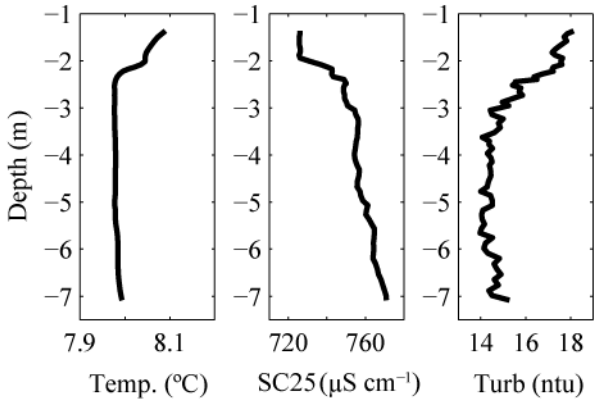

Figure 2.6 Temperature (ºC), specific conductivity (µS cm^{-1}), and turbidity (ntu) profiles collected on day 50. CTD profile c in Figure 2.1.

2.4.2.2 *Transverse circulation*

The CTD profiles collected downstream of the confluence only exhibit some stratification toward the left bank with lower conductivity values and slightly larger temperatures toward the surface (Figure 2.6). This pattern is indicative of N-water overflowing southward, though slowly, on top of the W-water, transversely to the streamwise direction as it is carried downstream. The slow transverse circulation can be the result of (1) momentum of the N-water, flowing southward in a shallow channel and into the reservoir; (2) secondary circulation occurring in the main channel as a result of its meandering planform; and (3) N-water being positively buoyant. All processes should lead to horizontal motions of similar magnitude of order O (10^{-2}) m s^{-1}. For example, the average southward speed of water in the N-River upstream of the confluence, estimated from the ADCP transect, was O (10^{-1}) m s^{-1} (Table 2.2). Once in the reservoir, the N- and W-waters moving in different directions mix and given the different flow rates of both rivers, the transverse velocity of the mixture should be at least seven times smaller and become O (10^{-2}) m s^{-1}. The maximum transverse velocity $u_{n,c}$ that develops in flows in curved or meandering channels, as a result of the centrifugal acceleration, can be estimated following *Johannesson and Parker* [1988] (see also *Geyer* [1993]) as follows

$$u_{n,c} \approx \frac{6\langle u_s \rangle h}{R_s}, \tag{2.6}$$

where R_s is the radius of curvature. For a curved channel, with R_s = 750 m (see Figure 2.1), and the flow conditions prevailing in this scenario (D = 10 m, $\langle u_s \rangle$ = 0.4 m s^{-1}), the

secondary currents should be approximately 3×10^{-2} m s^{-1}. Finally, the velocity magnitude that develops in a channel of depth D in response to a change in temperature ΔT can be estimated as [*Fischer et al.*, 1979]

$$u_{n,b} \approx \sqrt{\alpha \Delta T g D} \tag{2.7}$$

Here α is the thermal expansion coefficient, which depends on temperature. For D = 10 m, ΔT = 1 ºC, and $\alpha = 6 \times 10^{-5}$ $ºC^{-1}$ (value of α for T = 8 ºC) density-driven transverse velocities $u_{n,b}$ should be O (10^{-2}) m s^{-1}. Hence, neglecting frictional effects, one would expect the N-water to move southward with a speed $u_{n,b\,-\mathrm{Segre}} = 10^{-2}$ m s^{-1}. At that speed, the water on one side of a 400 m wide channel can reach the other bank in ≈ 5-10 hr. For $\langle u_s \rangle$ = 0.4 m s^{-1}, as observed in Ribarroja, the water would have travelled 7-14 km downstream before reaching the right margin. Note, however, that 6 hr is also the length of time that the temperature in the N-River takes to increase 1 ºC above the temperature of the W-River (Figure 2.4). Hence, our calculations, being based on steady-state equations, are only approximate. In any case, they suggest that for a significant portion of the length of Ribarroja, the N- and W-waters flow side by side. This is consistent with the results of *Cook et al.* [2006] in the study of the confluence of the Clearwater and Snake rivers, with similar length scales to those of the confluence of the W- and N-rivers (width ≈ 500 m and maximum channel depths of ≈ 16 m). They presented Multispectral Thermal Images (MTIs) of the confluence taken under nonstratified conditions that demonstrate that both rivers meet and flow parallel to each other for several kilometers downstream. The lateral extent occupied by the N-waters in the Ribarroja reservoir will likely depend on the inflow southward momentum of the N-water, the relative flow rates and the buoyancy differences, which in this period of time, should be small but not negligible. All these factors will change, especially the relative flow rates (as seen, for example, in Figure 2.2).

2.4.2.3 *Horizontal circulation*

Horizontal recirculation patterns, or gyres, were only observed in a reach far downstream of the confluence where the channel widens; leaving a shallow region to the left (transects F22‑24 in Figure 2.1). The recirculation cell in this reach is approximately 1 km long, occupying the shallowest regions of the channel and attached to the left bank

(Figure 2.1). Upstream velocities with depth-averaged values of ≈ 10^{-2} m s^{-1} were observed in a fringe of ≈ 300 m from the left bank (Figure 2.7a). This recirculation was also observed in summer (Figure 2.7b). Recirculation and flow separation, however, were not observed immediately downstream of the confluence, on the left margin of the W-River, as expected according to laboratory and numerical experiments of 90º confluences [e.g., *Gurram et al.,* 1997; *Weber et al.,* 2001]. The absence of recirculation downstream of a confluence, though, has also been reported in other studies of natural junctions [*Roy et al.,* 1988; *Roy and Bergeron*, 1990; *Biron et al.,* 1993; *De Serres et al.,* 1999]. The presence of a deposition bar just downstream of the confluence at the bank closer to the tributary and the differences in channel bottom depth between the mainstream and the side channel (bed discordance) have been proposed in the literature as possible causes to explain the absence of flow separation [*De Serres et al.*, 1999]. Both conditions apply in our study site (Figure 2.1, and *Bladé i Castellet et al.* [2010], their Figure 5]). In fact, the N-water flows into the reservoir through two channels (Figure 2.1), with depths of 4 and 2 m depth, respectively, which are shallower than the W-channel (≈ 10 m). The fact that the N-channel is curved and not a straight channel (Figure 2.1) [*Biron et al.*, 1993] as well as the smoothly curving geometry of the downstream junction corner [*Rhoads and Kenworthy,* 1995] could also explain the absence of recirculation and flow detachment.

2.4.3 Experiment II

The weather during the experiment was dry with high temperatures and strong winds (Table 2.2) from the Southeast. Average water temperatures were ≈ 22 ºC, but the N-water was, in general, warmer (ΔT ≈ 4-6 ºC), more turbid, and less salty than the W-water (Figure 2.3b and Table 2.2). Water releases from Mequinenza followed the same schedule in both days of the experiment. Releases started at 0800 hr and completed at 2200 hr. Flow rates increased from ≈ 150 $m^3 s^{-1}$ at 0800 hr to ≈ 250‑280 $m^3 s^{-1}$ from 1300 hr to 1600 hr, to supply electricity at peak demand. This schedule is typical of a summer day. These changes in flow rates are translated downstream at a velocity scale $u_{s,b}$ characterizing the propagation of perturbations in a density-stratified fluid, which can be estimated as in equation (2.7). For α =2.25 × 10^{-4} $ºC^{-1}$, ΔT ≈ 4‑6 ºC and D = 10 m, $u_{s,b}$ is ≈ 0.3 m s^{-1} and the changes in release rates at the dam would propagate to the confluence in 2‑3 hr. Hence, our observations, collected at the confluence from ≈ 16 to 18 hr, largely represent the hydrodynamic conditions for maximum or near-maximum flow rates.

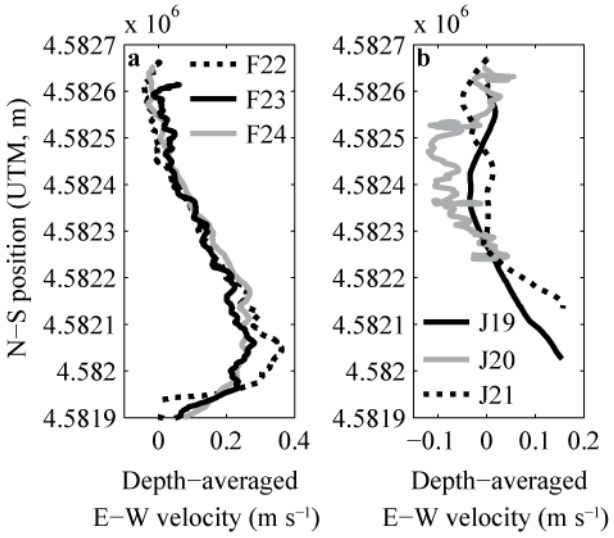

Figure 2.7 Depth-averaged E-W velocities (m s^{-1}) from (a) ADCP transects F22 and F24 on day 50 and F23 on day 51 and (b) ADCP transects J19-J21 on day 203.

2.4.3.1 *Spatial arrangement of inflows under strongly stratified conditions*

Turbidity records from our CTD casts collected at the confluence were used to recreate the spatial distribution of the N- and W-waters at the confluence. This approach was considered valid given that the differences in turbidity between the sources were large (at least 1 order of magnitude, see Table 2.2) and, hence, turbidity can be used to trace the source of water at the confluence. This assumption is reasonable as long as the time needed to settle for a sediment particle is much larger than the travel time needed by a particle to flow through the confluence, so that it behaves as a conservative tracer in the region of interest. The flow time scales T_f can be calculated as the time to transverse the O (10^3) m reach that includes the confluence region at a speed of 0.1 m s^{-1}, as observed in our velocity profiles. That time scale T_f is ≈ 2 hr. The time scales of deposition T_d, in turn, can be estimated by dividing the depth of the confluence D ≈ 10 m by a velocity scale representing the settling velocity w_0 of the particles, which can be estimated from Stokes law [*van Rijn*, 1987]. For particle diameters $d \leq 25$ mm [*Flumen-Group*, 2009] and $SG \approx 2.65$, w_0 is of O (10^{-4}) m s^{-1} and T_d is ≥ 5 hr. Hence, given that $T_f < T_d$, our approach to trace source water from turbidity values appears to be justified. In general, the minimum values of turbidity, indicative of Mequinenza water, appear in the deepest areas of the confluence (Figure 2.8). Two plumes, with large turbidity values, characteristic of the N-water, appear near the surface both at the northeastern and western ends of the confluence as shown by the longitudinal transect in Figure 2.8. These two plumes correspond to the

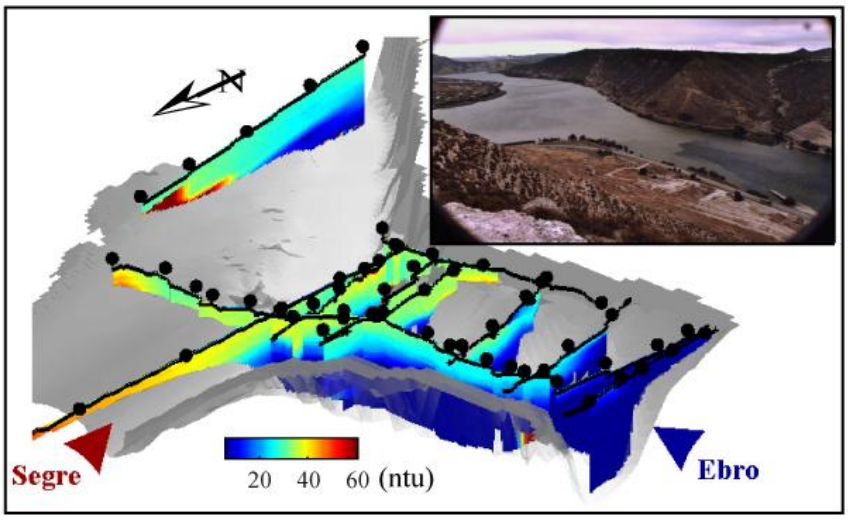

Figure 2.8 Linearly interpolated turbidity values (ntu) from CTD casts collected on day 203 and picture taken on day 202 at 1528 P.M. from location shown in Figure 2.1 (star). July experiment. Dots account for locations of CTD casts. Red and blue arrows show the direction of the flow. North direction is shown.

two inflow channels from the N-River. Minimum turbidity values appear along the center of the W-channel, upstream of the westernmost plume due to the entrance of low turbidity water from the W-River. Turbidity also peaks along the northern and southern shore of the W-River, which is either (1) water that existed there early in the morning before the start of discharge operations in Mequinenza or (2) water from the most upstream plume formed by the N-River flowing upstream along the W-River. Photographs taken on day 202, one day before the CTD profiles were collected, support our interpretation of the distribution of waters at the confluence (Figure 2.8).

2.4.3.2 *Inertial, buoyancy and wind forcings*

Average flow velocities were 0.1-0.2 m s^{-1}, and the internal Froude number Fr_i for these velocities was O (10^{-1}). For the maximum velocities of 0.3 m s^{-1} observed near the center of the W-channel, though, Fr_i was close to O (1), which suggests that even though buoyancy may be the dominant force driving motion, inertial forces cannot be ignored in our analysis. The sheared velocity profiles encountered along the W-River, with the largest downstream velocities occurring near the bottom, in fact, appear to be controlled by an inertial-buoyancy balance (Figure 2.9). The buoyancy forces work to arrest the downstream flow near the surface and make the warmer water flow upstream over the cold Mequinenza water. The latter, in turn, will tend to flow downstream driven both by

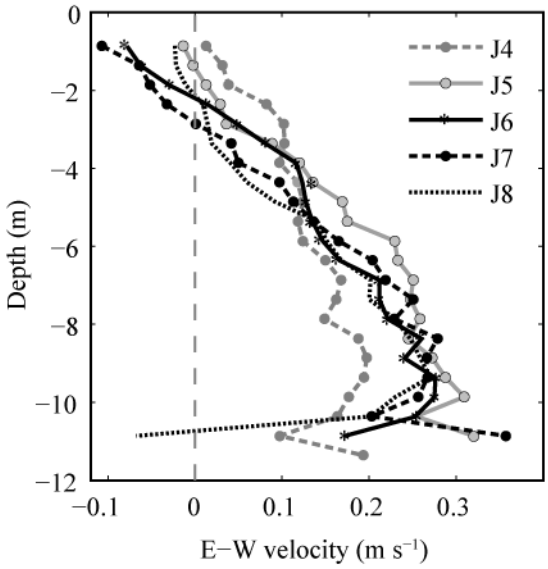

Figure 2.9 Laterally averaged E-W velocities for transects J4-8 (Figure 2.1) across the Ebro channel on day 203.

the inertial and buoyancy forces. Upstream of the confluence, water flowed mostly downstream with the largest velocities (0.2 m s^{-1}) occurring near the bottom and nearly stagnant water near the top (Figure 2.9, J4). Downstream, the inertial forces diminish as a consequence of (1) mixing and (2) friction with the bottom and lateral boundaries, and buoyancy forces drive the top of the water column flow upstream (Figure 2.9). Given that streamwise velocity maxima occur near the channel bed (Figure 2.9), and that $Fr_i \approx 1$, W-flows likely behave as density currents below the N-waters [e.g., *Kneller et al.*, 1999].

Wind forcing could have also contributed to the balance of forces at the confluence and need to be taken into account to interpret the field observations. For example, water in the N-channel appeared to flow upstream along the shallowest sections (Figure 2.10), probably as a result of strong southeasterly winds. The low turbidity values existing between the two inflow channels of the N-River in Figure 2.8 could be the result of the wind-driven upstream flow of the low turbidity W-water. Also as a result of the strong wind forcing, turbidity and temperatures varied laterally in the N-channel. Temperatures, for example, varied from 24 ºC to 25 ºC in most of the profiles, reaching values of up to 28 ºC near the right bank. This distribution could be interpreted as the result of the strong wind forcing accumulation of warm surface water in the westernmost boundaries of the reservoir and tilting of the isotherms.

The CTD casts collected along transect J4 in the W-channel also reveal a stratified water column with tilted isotherms (Figure 2.11). Near the center of the channel, a sharp interface at a depth of 2 m separates the cold water (19 ºC - 20 ºC) at the bottom from warmer (23 ºC) at the surface. At the left bank, in turn, the surface water is warmer (24 ºC) and the temperature gradients are smoother. The tilting of the isotherms, in this case, could be attributed to the strong southeasterly winds acting on the stratified water column. The southeasterly winds will tend to elevate and widen the isotherms near the southern shore. Assuming a two-layer stratification with an upper mixed layer of thickness H, the displacement of the isotherms Δh driven by wind forcing can be estimated in terms of the Wedderburn number, W, as $\Delta h = 0.5H/W$ [*Shintani et al.*, 2010]. The Wedderburn number, W, expressing the balance between wind and baroclinic forcing was calculated in the cross-stream direction as follows:

$$W = \frac{g' H^2}{u_a^{*2} b}, \tag{2.8}$$

where u_a* is the shear velocity of air ($u_a{}^{*2} = \rho_a/\rho_0\, C_{dw} U_{10}{}^2$) calculated from the air density ρ_a, wind drag coefficient C_{dw} ($\approx 10^{-3}$, *Fischer et al.* [1979]), and wind speeds U_{10}

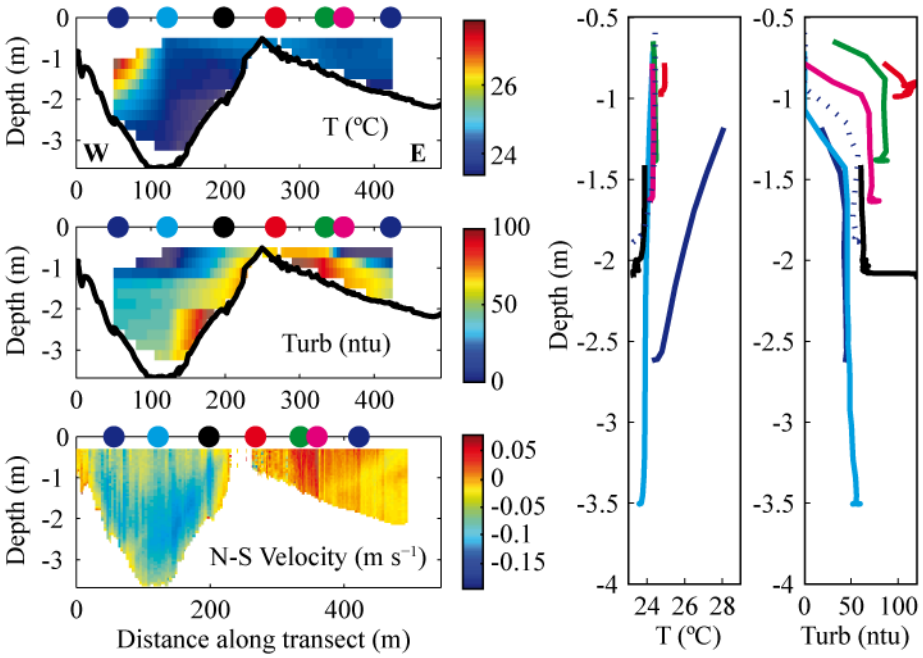

Figure 2.10 Temperature (ºC) and turbidity (ntu) from CTD casts, and N-S velocity (m s^{-1}) from ADCP transect at the Segre River (transect J1 in Figure 2.1) on day 202. Dots account for locations of CTD casts at right. W = western (rigth) bank, E = eastern (left) bank.

measured at 10 m above the free surface. For H = 2 m and average wind speeds of U_{10} of ≈ 7 m s^{-1}, as measured on day 203, u_a* = 8 × 10^{-3} m s^{-1}, W ≈ 2, and the isotherm displacements Δh could be up to 0.5 m, lower than observed in the field (Figure 2.11). The tilting of the isotherms upstream of the confluence can also be interpreted as the result of the secondary circulation that develops due to the curved shape of the W-riverbed upstream of the confluence (Figure 2.1). Similar observations have been reported for density currents flowing in sinuous subaqueous channels [*Cossu and Wells*, 2010], estuarine flows through curved channels [*Seim and Gregg*, 1997; *Lacy and Monismith*, 2001], and turbulent buoyant flows in curved open channels [*Shen et al*., 2003]. The isotherm displacement Δh driven by secondary flows in a curved channel can be estimated if we assume a steady-state balance between centrifugal acceleration and cross-channel baroclinic pressure gradients in the channel. The timescale T_b to reach steady state is determined by the cross-channel baroclinic adjustment time and can be estimated as [*Lacy and Monismith*, 2001] $T_b = b/(g' H)^{0.5}$. For a channel width in the W-inflow channel b_W = 300 m and H = 2 m (mean depth of the N-River at this section and time), T_b ≈ 0.5 hr. This is lower than the advective time for the flow to pass around the bend (2-3 hr for a distance of 3 km), which suggests that the isotherms rapidly adjust to any changes in the flow field driven by perturbations in inflow rates, and, hence, that the steady-state assumption for the cross-channel flow in Ribarroja is reasonable. Under steady-state conditions, in a two-layer flow in a curved channel, in which only the bottom layer flows as a gravity current, the isotherm displacement Δh can be calculated as follows [*Komar*, 1969]

$$\Delta h = \frac{\langle u_s \rangle^2 b}{R_s g'} \tag{2.9}$$

For R_s = 1 km (as is the case of W-channel, upstream of the confluence, Figure 2.1), ‹u_s› = 0.3 m s^{-1}, and $\Delta\rho/\rho_0$ = 10^{-3} as observed in transects J4-5, the expected displacement of the isotherms Δh = 2.5 m, in agreement with the observations (Figure 2.11). The tilting of the isotherms shown in Figure 2.11 suggests the existence of secondary circulation, with water in the upper layers flowing toward the inner bank, which is opposite in sign to the classical circulation in open-channel flow through bends [*Rozovskii*, 1961]. This type of reversed secondary circulation has been observed under nonlogarithmic streamwise

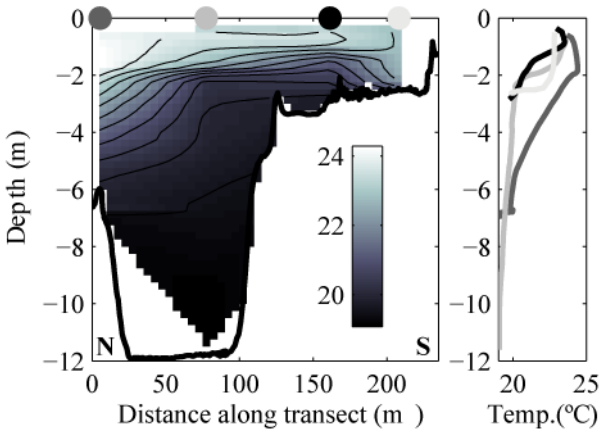

Figure 2.11 Linearly interpolated temperature (ºC) from CTD casts in transect J4 (Figure 2.1) on day 203. Dots show the locations of CTD profiles at right. N = northern (left) bank; S = southern (right) bank.

velocity profiles in curved estuarine channels [*Seim and Gregg*, 1997; *Lacy and Monismith*, 2001], and it is a common feature in density currents flowing in sinuous subaqueous channels [e.g., *Corney et al.*, 2006; *Keevil et al.*, 2006, 2007; *Cossu and Wells*, 2010; *Parsons et al.*, 2010]. *Corney et al.* [2006, 2008] suggested that the sign of the secondary circulation in stratified sinuous channels is largely controlled by the height above the channel bed where the streamwise velocity is maximal. Reversed secondary circulation will develop for streamwise velocity profiles exhibiting peak values below ≈ 40% - 45% of the channel depth, as it is the case in Ribarroja (see Figure 2.9). Driven by either centrifugal and/or wind forcings, isotherm tilting could be important to understand mixing between the two sources at the confluence, given that the area of the mixing interface increases as a result of the tilt, and water parcels are allowed to mix horizontally, at faster rates than vertical mixing under stratified conditions [e.g., *Imboden and Wüest*, 1995].

2.4.3.3 *Mixing at the confluence*

Using laterally averaged velocity profiles and CTD profiles at the deepest points along transects J8 and J9 (near the confluence), gradient Richardson numbers Ri_g were estimated as follows:

$$Ri_g = \frac{-g(d\rho/dz)}{\rho(du/dz)^2} \tag{2.10}$$

These calculations suggest that indeed there is a shear mixing-layer between 4 and 5 m of depth, where $Ri_g < 0.25$ (Figure 2.12), indicative of active mixing [*Rohr et al.*, 1988]. The thickness of the shear layer encountered at the confluence agrees with the scaling proposed by *Sherman et al.* [1978]. A shear layer forming as a result of billowing in stratified flows should have a thickness at equilibrium θ_B of the form

$$\theta_B = 0.3\frac{(\Delta u)^2}{g\alpha\Delta T} \tag{2.11}$$

For $\alpha = 2.25 \times 10^{-4}$ ºC^{-1}, $\Delta T = 4$ ºC – 5 ºC, and a velocity difference $\Delta u = 0.2$ m s^{-1} (the laterally averaged speed in the W-River upstream of the confluence, at the time of maximum discharge), equation (2.11) predicts a shear layer of approximately 1 m. This is indicative of strong mixing at the confluence tending to form a diffused interface between the W- and N-waters. Immediately below the shear layer (deeper than 5 m), there exists an interface (thermocline) where the temperature changes from 25 ºC to 20 ºC and gradient Richardson numbers are well above 0.25. Vertical diffusivities at the thermocline

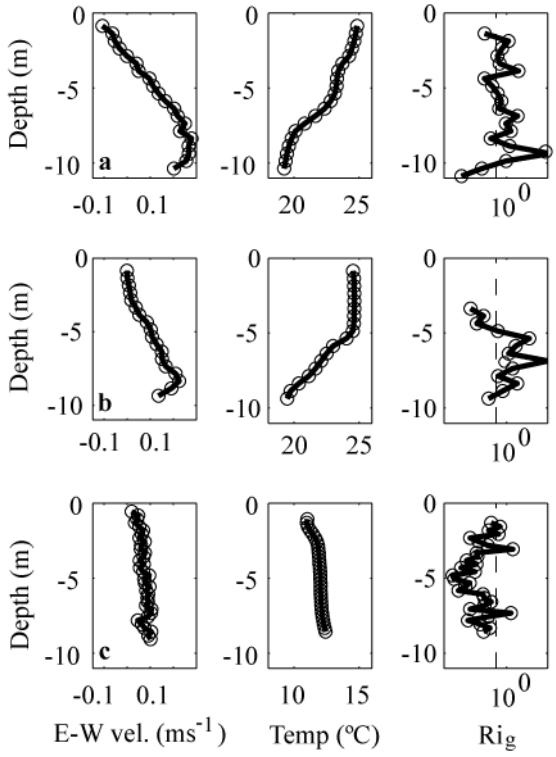

Figure 2.12 Laterally averaged E-W velocities from ADCP transects, temperature profiles from CTD casts, and estimated Ri_g for transects (a) J8, (b) J9 and (c) N10 in Figure 2.1. Dashed lines account for $Ri_g = 0.25$.

were calculated from our estimates of Ri_g as *Latif et al.* [1994]

$$K_z = \frac{D_0}{1+(5Ri_g)^2}; D_0 = 2 \times 10^{-3}\ \mathrm{m^2\ s^{-1}} \quad (2.12)$$

For Ri_g of O (1), equation (2.12) predicts values of O (10^{-5}) $m^2\ s^{-1}$ for the thermocline at the confluence (transect J9). These values are consistent with those calculated using a three-dimensional hydrodynamic model of the confluence for the same period of time, as reported by *Ramón* [2011]. Assuming that the W-water flows as a layer of 2 m (the average thickness of the hypolimnion, based on temperature profiles in Figure 2.12a and Figure 2.12b), below the water from the N-River, in a channel of constant depth *D* equal to the depth of the W-channel at the confluence (10 m), and assuming that mixing rate is constant in time, both layers would need ≈ 37 hr to mix. With average downstream speeds of 0.2 m s^{-1} as measured in the field, these two layers would be mixed ≈ 27 km downstream of the confluence. These calculations suggest stratification near the dam being largely inherited from the difference in properties between the W- and N-waters.

2.4.4 Experiment III

During experiment III, the weather was cold, foggy during the morning, and sunny from noon to sunset. Wind was weak at all times (Table 2.2). Average discharge rates from Mequinenza estimated from ADCP transects varied from 240 to 266 $m^3\ s^{-1}$ on day 329 and from 144 to 200 $m^3\ s^{-1}$ on day 330. Measured discharges at the inflow section of the N-River were 12 and 69 $m^3\ s^{-1}$ on day 329 and 330, respectively. This order of magnitude for the inflows from the W- and N-rivers agrees with inflows at the confluence in 1998 (Figure 2.2) and 2004 and 2005 during this month [*Prats et al*., 2010]. Average water velocities were O (10^{-1}) m s^{-1} in the W-River and O (10^{-2}) m s^{-1} in the N-River upstream of the confluence (Table 2.2). The internal Froude number Fr_i was O (1), which suggest that an equilibrium between inertial and buoyancy forces exists at the confluence. The N-water was, in general, colder and more turbid but had lower specific conductance values than the W-water (Table 2.2).

2.4.4.1 *Spatial arrangement of inflows*

Given the strong differences in the conductivity of the sources (≈ 900 μS cm^{-1}), *SC*25 was used to trace the source of the water at the confluence. The conductivity was

taken here to be 837 and 1755 μS cm^{-1}, for the N- and W-waters, respectively (Table 2.2). Dilution rates were estimated from *SC*25 data as in equation (2.4). All profiles were collected from 1100 hr to 1400 hr in the vicinity of the confluence of the N- and W-rivers. Hence, they represent a synoptic view of the flow field and the distribution of the W- and N-waters as they flow into the reservoir. On day 329, with a discharge ratio $R_q = Q_N/Q_W$ = 0.047, the water column in the reservoir appeared unstratified upstream of the confluence but stratified downstream, with the N-water occupying the shallower layers. At the confluence, the N-plume appeared confined to the left margin, but, further downstream it moved toward the right margin. The lateral extension of the plume was limited and only reached the right margin of the channel very close to the surface (Figure 2.5b). On day 330, with N-inflow rates almost six times those recorded on day 329 (R_q = 0.4), the N-water reached the right bank at the confluence and mixing between the sources appears to be stronger (Figure 2.5c). Immediately downstream of the confluence (transect N12 in Figure 2.1), the W-water accumulated near the right bank (Figure 2.5c). The interpolated conductivity plots show two local maxima, which can also be interpreted as a result of two plumes. One, formed near the upstream end of the confluence where the deepest channel of the N-River discharged into the reservoir, corresponds to the southernmost maximum. The second formed at the downstream end of the confluence as a result of the discharge of the shallowest (easternmost) channel of the N-River. Farther downstream (transect N18 in Figure 2.1), the low conductivity water from the N-River appeared attached to the right margin, while the high conductivity water from Mequinenza accumulated near the left margin (Figure 2.5c). These observations are suggestive of a strong lateral circulation set up as a result of the inertia of the side inflow being of similar magnitude to the longitudinal inertia of the main-stream inflows. This braided circulation is consistent with field data and results of three-dimensional simulations of the confluence between the Snake and Clearwater rivers [*Cook et al.*, 2006] for R_q = 0.87 and $\Delta\rho/\rho_0$ of O (10^{-3}). It seems plausible that the W-water might have been preferably flowing near the right margin, and we could have missed it in our CTD casts.

2.4.4.2 *Mixing at the confluence*

On day 330, the fraction of W-water in the lower layer in transect N18 (Figure 2.1), estimated from conductivity values as in equation (2.4), was only 53%, which is indicative of very strong mixing between the W- and N-waters. Large mixing rates could

have occurred as a consequence of (1) high shear near the bottom in a weakly stratified water column, or alternatively, (2) as a result of the development of weakly unstable density profiles during mixing of the W- and N-waters. Whether shear mixing or density-driven instabilities are responsible for the strong mixing that appears to occur downstream of the confluence is beyond the scope of this manuscript. In any case, shear could be strong enough to reduce the density gradients across a large fraction of the water column. Assuming a stably stratified water column on day 330 with density differences of ≈ 0.05 kg m^{-3} and longitudinal velocity differences of 0.1 m s^{-1} between the W- and N-water in the main channel (Figure 2.12c), one would expect a shear layer of thickness $\theta_B \approx 6$ m, which is similar in magnitude to the depth of the channel D. The gradient Richardson number is < 0.25 at all depths, indicative of active mixing. For Ri_g of O (10^{-1}), as encountered at the thermocline, vertical diffusivities were of O (10^{-4}) m^2 s^{-1}. Assuming a constant mixing rate, and that the W-River flows as a layer of ≈ 7 m thick (thickness of the hypolimnion based on the temperature profiles, Figure 2.12c) below the N-water in a channel of constant depth D = 10 m (depth of the W-channel at the confluence region), both layers would need ≈ 35 hr to mix. With average observed velocities of 0.1 m s^{-1}, both rivers would appear mixed after 13 km downstream of the confluence.

2.4.5 Parameterization of Flows at River Confluences

Our results from Experiments I‑III suggest that the spatial arrangement of two rivers at a large asymmetrical river confluence with a junction angle of nearly 90º is largely controlled not only by the inflow velocities of the tributary U_t and the mainstream U_m but also by the density differences between the two rivers. The velocity ratio R_u (= U_t/U_m) represents the ratio of inertial forces between the side inflow and the mainstream, and for a given geometry is determined by the discharge ratio of tributary to mainstream inflows R_q (= Q_t/Q_m). The ratio of the buoyancy of the side stream, parameterized in terms of the celerity of the internal perturbations $(g' D)^{0.5}$, and the magnitude of the inertial forces, characterized by the streamwise velocities along the main channel, is the inverse of the internal Froude number Fr_i of the confluence. For $Fr_i >> 1$, the effect of density differences can be neglected, and the mixing interface between the confluent rivers remains largely vertical (Figure 2.13a and Figure 2.13b). The location of the mixing layer, in this case, is largely controlled by the magnitude of R_u. For $R_u << 1$, the mixing interface will be close to the tributary bank. This was the case of Experiment I in

Ribarroja conducted under weakly stratified conditions. For $R_u >> 1$, in turn, the interface gets closer to the opposite bank (Figure 2.13b). Earlier work conducted under nearly neutrally buoyant conditions conducted in the laboratory [*Best*, 1987] or in small river confluences [*Biron et al.*, 1993; *Rhoads and Kenworthy*, 1995, 1998; *De Serres et al.*, 1999] are consistent with our results and suggest that the location of the mixing interface largely depends on the momentum flux ratio R_m (= $[U_t Q_t \rho_t]/[U_m Q_m \rho_m]$) and the junction angle. The confluent rivers flow side by side (Figure 2.13a and Figure 2.13b), mixing laterally at a rate controlled by shear-driven horizontal turbulence and the existence of secondary circulation. In general, under weakly buoyant conditions, mixing rates will be small, unless the mixing interface becomes distorted due to channel-scale secondary circulation [*Rhoads and Kenworthy*, 1995, 1998] or under the influence of topographic forcings such as the presence of bed discordance [*Gaudet and Roy*, 1995].

Vertical stratification will develop at the confluence if $Fr_i < 1$, and even upstream of the confluence if $Fr_i << 1$, as a result of the nonneutrally buoyant side-inflow moving upstream along the mainstream (Figure 2.13c). Under those conditions, the mixing interface will tilt and become horizontal at or immediately downstream of the confluence if $R_u < 1$. Mixing rates will decrease as a result of vertical stratification and the two rivers

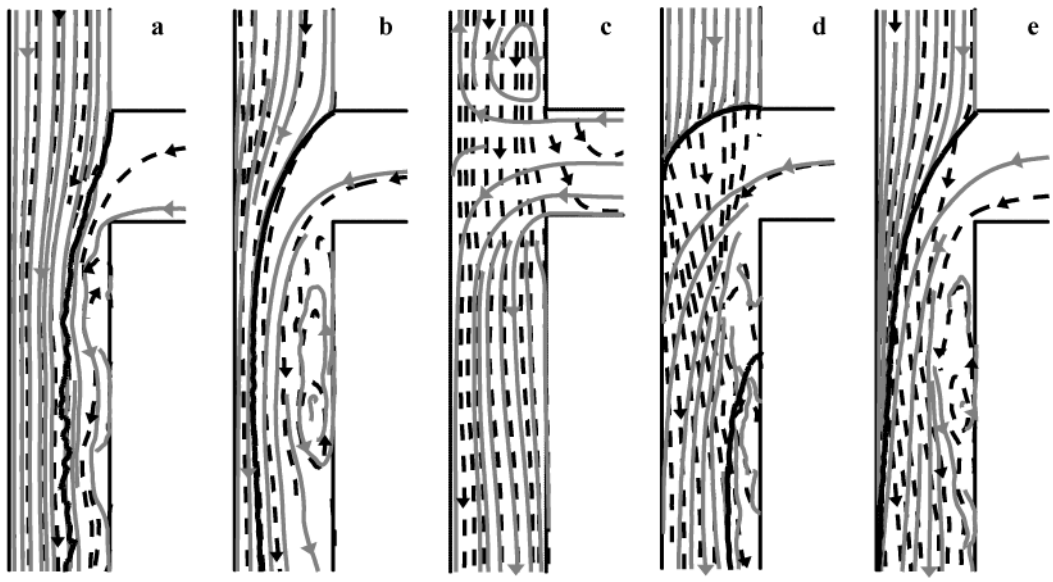

Figure 2.13 Conceptual model for the near surface (gray lines) and near bottom (black dashed lines) velocity streamlines and for the location of the mixing interface at the surface plane (black straight lines) for different velocity ratios ($R_u = U_t/U_m$) between the tributary *t* and the main stream *m* and internal Froude numbers Fr_i ($=U_m/(g'D)^{0.5}$) at an asymmetrical confluence with a 90º junction angle. (a) $R_u = 0.25$ and $Fr_i >> 1$, (b) $R_u = 2$ and $Fr_i >> 1$, (c) $Fr_i << 1$, (d) $R_u = 2$ and $Fr_i \leq 1$, and (e) $R_u = 1$ and $Fr_i > 1$.

may remain unmixed long distances downstream of the confluence. This was the case of Experiment II in Ribarroja, where stratification, as observed near the dam, is largely determined by the differences in buoyancy between the N- and W-waters. If $R_u > 1$, in turn, the mixing interface may become tilted across the mainstream as a result of the large lateral inertia of the side inflow in comparison with the stability of the water column, and the negatively buoyant flow may even upwell downstream of the confluence at the tributary bank (Figure 2.13d; Experiment III). For intermediate values of Fr_i of O (1), the distance downstream needed for the tributary water to reach its opposite bank will depend both on Fr_i and R_u (Figure 2.13e). This distance will decrease in response to increases in Fr_i^{-1} and R_u.

The dependence of large river confluences on Fr_i is consistent with field observations at large river confluences. For example, vertical stratification develops for nonneutrally buoyant side flows ($Fr_i \leq 1$) at the confluence between the Snake and Clearwater rivers [*Cook et al.*, 2006]. Near vertical mixing interfaces were, in turn, reported for weakly buoyant side flows, $Fr_i >> 1$. *Laraque et al.* [2009] also reported observations collected at the confluence between the Negros and Solimões rivers, with widths of O (1) km downstream of the confluence, and suggest that under weakly buoyant side flows, with $Fr_i > 1$, the mixing interface between the confluent rivers was significantly distorted. Note, however, that in our analysis we have ignored other important effects, such as, those of the centrifugal forces, wind forcing or topographic forcing (such as the presence of bed discordance). For example, secondary circulations driven by the curvature of the streamlines at the confluence and/or the planform curvature of the confluence could lead to a higher distortion of the mixing interface than expected from baroclinic effects alone [e.g., *Rhoads and Kenworthy*, 1995; *Rhoads and Sukhodolov*, 2001].

2.5 Conclusions

The spatial arrangement of inflows and their mixing rates in large asymmetrical river confluences are largely controlled by the ratio between forces driving the crossstream motion of the side inflow (inertia, buoyancy, and centrifugal forces associated with the meandering form of the main stream) and the inertial forces in the mainstream. The behavior of the confluent streams can be parameterized in terms of an

internal Froude number and the velocity ratio between the confluent streams. For $Fr_i >> 1$, buoyancy forces are negligible compared with inertia and the mixing interface remains vertical. For $Fr_i < 1$ the confluence becomes vertically stratified. For intermediate values of Fr_i, the distance downstream needed for the tributary water to reach its opposite bank will depend on the velocity ratio. For higher velocity ratios, the mixing interface would locate farther from the tributary bank, and these distances become shorter. The influence in a specific location of other forces such as centrifugal forces, topographic forcing, and/or wind forcing will increase or decrease this length scale. A more quantitative and exact relationship between these controlling factors and the lateral extension of the tributary waters should be further explored with the aid of three-dimensional modeling tools.

Chapter 3

Mixing dynamics at the confluence of two large rivers undergoing weak density variations

Published in *J. Geophys. Res. Oceans*,
doi: 10.1002/2013JC009488.

Abstract

Simulations of tracer experiments conducted with a three-dimensional primitive-equation hydrodynamic and transport model are used to understand the processes controlling the rate of mixing between two rivers (Ebro and Segre), with distinct physical and chemical properties, at their confluence, upstream of a meandering reservoir (Ribarroja reservoir). Mixing rates downstream of the confluence are subject to hourly scale oscillations, driven partly by changes in inflow densities and also as a result of turbulent eddies that develop within the shear layer between the confluent rivers and near a dead zone located downstream of the confluence. Even though density contrasts are low—at most O (10^{-1}) kg m^{-3} difference among sources—and almost negligible from a dynamic point of view—compared with inertial forces—they are important for mixing. Mixing rates between the confluent streams under weakly buoyant conditions can be up to 40% larger than those occurring under neutrally buoyant conditions. The buoyancy effects on mixing rates are interpreted as the result of changes in the contact area available for mixing (distortion of the mixing layer). For strong density contrasts, though, when the contact area between the streams becomes nearly horizontal, larger density differences between streams will lead to weaker mixing rates, as a result of the stabilizing effect of vertical density gradients.

3.1 Introduction

River confluences are critical points in river networks where strong physical and chemical gradients develop [*Kiffney et al.*, 2006; *Bigelow et al.*, 2007; *Gooseff et al.*, 2008], resulting in a wide range of distinctive environmental conditions (habitats) for biological growth. As a consequence, river confluences behave as biological hotspots,

where the number of species appears to increase very significantly in comparison with other river reaches [*Benda et al.*, 2004]. The effects of river confluences persist downstream, hence, affecting biological communities and ecological processes at scales of river reaches and channel networks [*Rice et al.*, 2001]. The spatial extent of the reaches downstream of river junctions where heterogeneous habitat conditions persist largely depends on the rate at which fluid elements are exchanged across the mixing interface separating mainstream and tributary waters. Mixing rates are largely dependent on the development of two-dimensional vortices in the shear layer between the confluent flows, and, particularly, on processes leading to the distortion of the mixing layer and the consequent increase in the area of contact between water masses. The distortion of the mixing layer, in turn, has been shown to occur as a result of differences in depths between the main channel and the tributary (bed discordance) or channel-scale helical motions, which, in general, result in significant reductions in mixing lengths [e.g., *Gaudet and Roy*, 1995; *Rhoads and Kenworthy*, 1995]. *Lane et al.* [2008], for example, found that mixing lengths between the Paraná and Paraguay rivers can vary from ca. 8 to 400 km depending on whether helical motions develop or not. Farther downstream of the confluence, mixing rates largely depend on the local characteristics of the channel [*Boxall and Guymer*, 2001; *Heard et al.*, 2001], such as the presence of channel bends where strong secondary currents develop, or on the existence of dead zones, such as pools, gravel beds, side arms, or, in general, any other irregularity in the river morphology.

Our understanding of flow and mixing dynamics in river confluences, however, is still far from complete. In particular, the effect on mixing of the density contrast between the confluent streams have been traditionally neglected, which has been justified by differences in the inertia of the confluent flows being much higher than density differences [e.g., *Rhoads*, 1996]. *Laraque et al.* [2009], in their field study of the confluence between the Negro and Solimões rivers, however, argued that the small density differences, associated with slight changes in suspended solid concentrations, made the waters from the Negro River to flow over those of the Solimões River, widening and distorting the mixing layer, and, hence, increasing mixing rates. These density differences, in general, are more likely to occur in large-scale confluent channels, with the mainstream and tributary draining different geological terrains [*Parsons et al.*, 2008]. They could also be the result of differences in the thermal inertia between the mainstream and the tributary, and, in this case, one would expect the temperature-driven variations in

density to occur at hourly scales, as a result of diurnal variations in insolation. The contribution of small density differences to mixing dynamics in confluences has not been addressed before, with the exception of the numerical study of *Biron and Lane* [2008] in a simplified 90º junction of two rectangular channels with density differences of O (1) kg m^{-3}. In that study, *Biron and Lane* [2008] demonstrated that mixing rates increased if the mixing layer distorted as a result of density differences. It is not clear, however, whether weaker or stronger density differences, or hourly scale variations in density, will have an effect or not on the mixing rates in river confluences.

Our goal is to understand the effects of density differences on the mixing dynamics in and downstream of large-scale asymmetric confluences. The junction of two medium-size rivers (Ebro and Segre) in northern Spain is used as an example of a large confluence with weak and time-varying density differences, driven by diurnal changes in water temperatures [*Ramón et al.*, 2013; Chapter 2]. The two rivers join at the upstream end of a meandering reservoir (Ribarroja) with a complex geometry characterized by bed discordance and changes in channel geometry and planform occurring sequentially (Figure 3.1). Hence, mixing rates between the confluent rivers are expected to exhibit changes both in time and downstream of the confluence along the river channel. We analyze those changes through simulations conducted with a three-dimensional primitive-equation (3D-PE) model. Our modeling approach is justified given the need to conduct unsteady simulations of density-driven changes [*Ramón et al.*, 2013; Chapter 2] in the mixing layer between two water masses in a large domain with a reasonable computational cost. The 3D-PE models have been successfully applied, during the last few years, to reproduce and analyze space-time changes of density interfaces in large-scale systems, during periods of time of days to years with reasonable computational cost. For example, they have been used to simulate the dynamics of salt wedges in estuaries [*Robson and Hamilton*, 2004] or the internal wave fields and mixing across pycnoclines in lakes and reservoirs [*Hodges et al.*, 2000; *Rueda et al.*, 2003; *Vidal et al.*, 2007]. In the particular case of the confluence between the Ebro (hereon western W-River) and Segre (hereon northern N-River) rivers, the large spatial scales of the domain of interest (see Figure 3.1) and the need to account for the variability of the density changes at hourly scales prevent the use of more sophisticated modeling approaches, such as well-resolved Large Eddy Simulations (LES) [*Rodi*, 2010]. Even the hybrid Reynolds-Averaged Navier Stokes (RANS)-LES approach of *Constantinescu et al.* [2011, 2011] is too

computationally costly and not viable. For their RANS-LES simulation of the small river confluence between the KasKaskia and Copper Slough rivers, for example, *Constantinescu et al.* [2011, 2011] used a total of ≈ 5 ×10^6 cells to discretize the ≈ 52 m length and ≈ 8 m width computational domain and they could only simulate steady state conditions. Our unsteady simulations with a 10-m resolution grid, however, require time scales of O (10^5) time steps. RANS models are alternative to LES models to conduct unsteady simulations, providing reasonable and cost-effective results. *Biron et al.* [2004], for example, used RANS models to simulate the downstream evolution of mixing between the Bayonne and Berthier rivers and were able to reproduce the field observations collected by *Gaudet and Roy* [1995]. Still, full 3-D RANS models based on nonhydrostatic equations are very demanding, and the additional simplifications of the governing equations incorporated in the 3D-PE are needed. The ability of 3D-PE models to simulate relevant physical processes in river mixing and dynamics has been recently analyzed by *Ramón et al.* [2015] (Appendix A). Their results suggest that 3D-PE models,

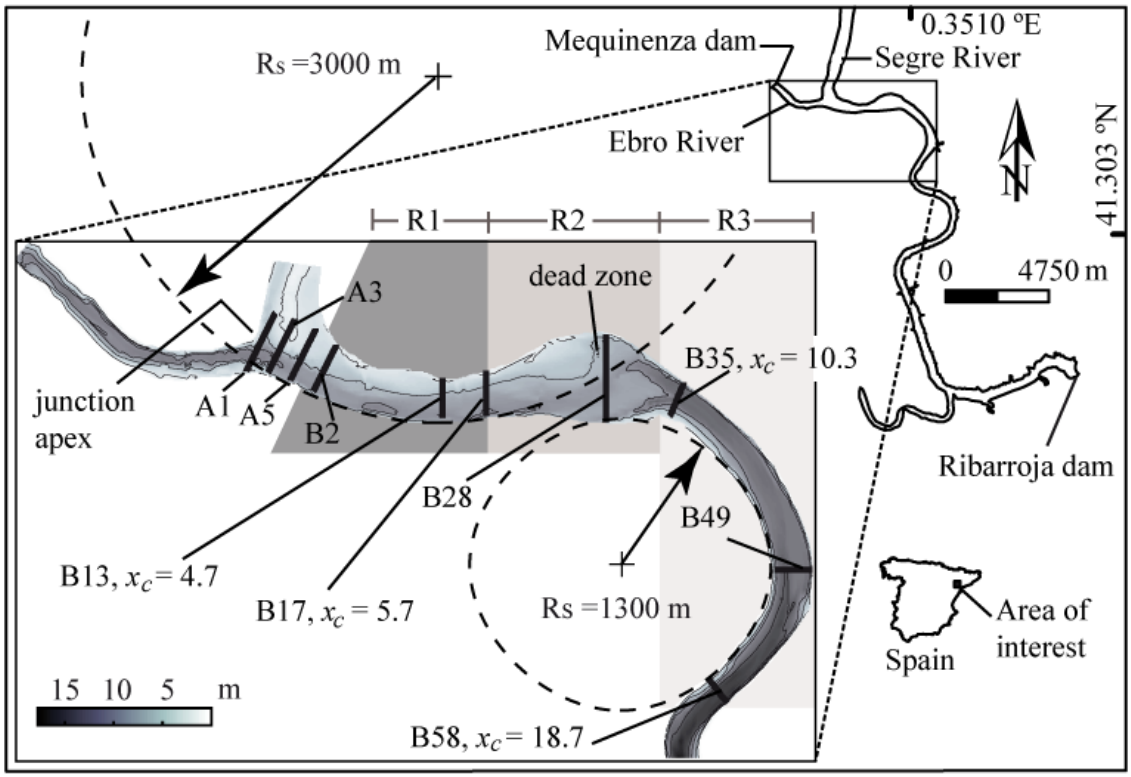

Figure 3.1 The Ribarroja reservoir and bathymetry of the computational domain (rectangle). The location of sections A1, A3 and A5 at the confluence region, the location of some of the B sections downstream of the confluence region and the location of the dead zone are also shown. x_c is the non-dimensional distance downstream of the junction apex. R_s = radius of curvature. Shaded areas show the extension of reaches R1, R2 and R3.

although approximate and hence less expensive than more sophisticated approaches, yield solutions which are consistent with experimental observations.

The present study is distinctive in several important aspects. First and most important, the influence of weak density differences on mixing dynamics is taken into account. Given the paucity of publications on this topic, we believe that this is an important contribution. Second, the computational domain extends ≈ 8 km downstream of the confluence so the streamwise variability of mixing rates can be evaluated. Few studies have extended their analysis farther downstream of the confluence, but those that have, suggest that different phenomena may have different contributions to mixing depending on flow rates. For instance, *Biron et al.* [2004] suggest that for the Bayonne-Berthier confluence, the effect of bed discordance is particularly pronounced during low flow conditions, while the effect of river bending farther downstream of the confluence appears to be stronger during high flow conditions. Hence, mixing rates are expected to vary in space which supports our analysis in the downstream reach of the confluence.

3.2 Study site

The Ribarroja reservoir (41º18'N, 0º21'E) is the second of a chain of three reservoirs (Mequinenza-Ribarroja-Flix) constructed along the lower reaches of the W-River for hydroelectric power generation. The basin is relatively shallow, with an average depth of 9.8 m, reaching values of up to 34 m near the dam. Inflows and outflows are regulated so that the free surface elevation is kept at a nearly constant value of ca. 69 m above sea level throughout the year. During peak through flows in winter, the nominal residence time of the reservoir can be as low as 3 days [*Cruzado et al.*, 2002]. The reservoir has an elongated and meandering shape (Figure 3.1), with the two largest inflows (W-River and N-River) occurring at the NW end. The river confluence is characterized by a large (near 90º) junction angle and a curved planform which bends to the left immediately downstream of the confluence with a radius of curvature R_s of ca. 3 km, almost 7 times the channel width b_p downstream of the confluence, $R_s/b_p \approx 7.5$ (Figure 3.1, reach R1). Depths of the W-River and N-River are discordant: the N-River enters the confluence through two channels of depths D of 4 and 2 m, respectively, while depths encountered at the W-River are of ≈ 10 m. Downstream of reach R1, the channel widens as it veers to the right, leaving a wide shallow embayment on the left margin (reach R2). Finally, in reach R3, the channel bends sharply to the right with a radius of

curvature R_s ca. 1.3 km ($R_s/b_p \approx 3.25$, Figure 3.1). Inflows from the W-River are regulated by the Mequinenza dam, which discharges directly into the Ribarroja reservoir 3 km upstream of the confluence. Only the hydroelectric intake, releasing deep cold hypolimnetic water, and the spillway in the Mequinenza dam are operated on a regular basis [*Prats et al.*, 2010].

3.3 Methods

3.3.1 Approach

The model was first used to simulate the flow fields at the confluence during a period of time in February 2009, when experimental observations are available [*Ramón et al.*, 2013; Chapter 2]. At that time, conductivity differences between rivers were of ≈ 80 μS cm^{-1} and river temperatures varied weakly (at most 1ºC) in time, so that density differences between rivers ranged from O (10^{-2}) to O (10^{-1}) kg m^{-3} with the W-River being denser. Inflow rates were constant, but almost 8 times larger from the W-River (Q_W) than from the side inflows along the N-River (Q_N). This simulation corresponds to the base case (*Base*) in Table 3.1 and was used by *Ramón et al.* [2015] (Appendix A) for validation purposes. Additional simulations were conducted in this work with different inflow densities and discharge ratios R_q ($=Q_N/Q_W$), both constant in time (Table 3.1). Runs T1 through T8 refer to those simulations conducted with different density contrasts between the W-(ρ_W) and N-(ρ_N) rivers, but setting the inflow rates equal to the observations. The density contrast $\Delta\rho/\rho_0$ is defined as $(\rho_W-\rho_N)/\rho_0$, where ρ_0 (=1000 kg m^{-3}) is a reference density. Hence, $\Delta\rho/\rho_0 > 0$ will refer to scenarios with positively buoyant side inflows. Runs M1-M5 and m1-m5 refer to those simulations conducted both with different $\Delta\rho/\rho_0$ and R_q (Table 3.1). M-simulations and m-simulations correspond to R_q = 0.65 (momentum ratio R_m = 0.72) and 1.53 (R_m = 4.58), respectively. In all M-simulations and m-simulations total discharge was equal to that observed in the field, so that the influence of R_q could be compared. The selection of the values of R_q of 0.65 and 1.53 was intended to include situations in which inflows from the W-River are still dominant but R_q is closer to 1, and the reversed situation, in which the N-River dominates the flow. All discharge ratios are within the range of variation of R_q observed in Ribarroja under weakly stratified conditions [e.g., *Ramón et al.*, 2013; Chapter 2]. The simulated velocity fields for the different scenarios were used to drive transport simulations in which the W-

inflows were traced as they entered into the computational domain. The results of the hydrodynamic and transport models were analyzed to understand the processes driving mixing at and downstream of the junction.

3.3.2 Computational model

Simulations were conducted with a parallel version [*Acosta et al.*, 2010] of a 3D-PE model [*Smith*, 2006]. The governing equations are first posed in layer-averaged form by integrating over the height of a series of horizontal layers separated by level planes. The layer-averaged momentum equations are solved using a semi-implicit, three-level, iterative leapfrog-trapezoidal finite difference scheme on a staggered Cartesian grid. Nonactive (i.e., tracers) and active scalar transport equations were solved using a two-level semi-implicit scheme, in which only vertical diffusion is discretized implicitly. The advection terms in the transport equation for scalars are discretized with a second-order accurate flux-limiting scheme [e.g., *Durran*, 1999] with use of the Superbee limiter [*Roe*, 1984]. Turbulent mixing is represented in the 3-D model using diffusion-like terms. A Laplacian operator with constant mixing coefficients (K_h) is used to represent horizontal mixing of momentum and scalars. Vertical eddy coefficients of mixing K_z are calculated using a two-equation model originally proposed by *Mellor and Yamada* [1974]. This turbulent modeling approach is typically used in large-scale models for geophysical flows due to their reduced computational burden. The model has been extensively validated both against analytical solutions and field data sets collected in a variety of lake environments [*Rueda and Cowen*, 2005; *Rueda and MacIntyre*, 2010, and references therein] and estuaries [*Zamani et al.*, 2010]. The model was also validated for relevant physical processes occurring at the confluence between the W-River and N-River [*Ramón et al.*, 2015] (Appendix A). Those processes include (1) the development of a shallow mixing layer between two confluent streams, (2) flow past a cavity, and (3) flow in open channels of mildly curvature with and without stratification. *Ramón et al.* [2015] (Appendix A) also validated the model results against field data (*base* case, Table 3.1).

3.3.3 Transport and mixing model of the Ribarroja reservoir

Our computational domain extends from the Mequinenza dam to a section existing ca. 8 km downstream of the junction (Figure 3.1) along the W-River, and approximately 500

Table 3.1 Model inputs for the simulation runs

Run case	$\Delta\rho/\rho_0$ [(a)]	Q_W [(b)] ($m^3 s^{-1}$)	Q_N [(b)] ($m^3 s^{-1}$)	$R_q(=Q_N/Q_W)$	R_m [(c)]
Base	3.6×10^{-5}-1.2×10^{-4}	730	96	0.13	0.03
T1	2.4×10^{-4}	730	96	0.13	0.03
T2	1.5×10^{-4}	730	96	0.13	0.03
T3	6.8×10^{-5}	730	96	0.13	0.03
T4	3.2×10^{-5}	730	96	0.13	0.03
T5	0	730	96	0.13	0.03
T6	-6.8×10^{-5}	730	96	0.13	0.03
T7	-1.5×10^{-4}	730	96	0.13	0.03
T8	-2.4×10^{-4}	730	96	0.13	0.03
M1	1.5×10^{-4}	500	326	0.65	0.72
M2	6.8×10^{-5}	500	326	0.65	0.72
M3	0	500	326	0.65	0.72
M4	-6.8×10^{-5}	500	326	0.65	0.72
M5	-1.5×10^{-4}	500	326	0.65	0.72
m1	1.5×10^{-4}	326	500	1.53	4.58
m2	6.8×10^{-5}	326	500	1.53	4.58
m3	0	326	500	1.53	4.58
m4	-6.8×10^{-5}	326	500	1.53	4.58
m5	-1.5×10^{-4}	326	500	1.53	4.58

[(a)] Density contrast ($\Delta\rho = \rho_W - \rho_N$) between the Ebro ($\rho_W$) and Segre ($\rho_N$) rivers expressed in terms of a reference density ($\Delta\rho/\rho_0$)

[(b)] Inflow rates Q ($m^3 s^{-1}$) for the Ebro Q_W and the Segre Q_N rivers.

[(c)] Momentum ratio between the Ebro and Segre rivers ($= Q_N \times U_N \times \rho_N / (Q_W \times U_W \times \rho_W)$), U_N and U_W being the inflow velocities of the Segre and Ebro rivers, respectively, immediately upstream of their confluence.

m upstream of the confluence along the N-River. The lake geometry was discretized using grid cells of size (Δx, Δy, Δz) = (10, 10, 0.5) m in the longitudinal, lateral, and vertical direction, respectively. The time step Δt was set to 2 s for stability purposes. The bottom drag coefficient, C_d, was set to 0.003 as proposed by *Smith* [2006]. The horizontal mixing coefficient K_h was set to 5×10^{-2} $m^2 s^{-1}$. This estimate corresponds to the product of the friction velocity u^* ($= C_d^{0.5} \langle u_s \rangle$, $\langle u_s \rangle$ being the cross-sectional averaged streamwise velocity) and the channel depth D, as proposed by *Rastogi and Rodi* [1978] to quantify turbulent transfer of momentum and temperature. The values of u^* and D were, in turn, estimated from field data ($\langle u_s \rangle$ = 0.4 m s^{-1} and D = 10 m; *Ramón et al.* [2013]; Chapter 2). Preliminary simulations showed, however, that the actual value of K_h can be ignored for the advection of scalars, since changes in mixing rates of at most 4% occurred in response to decreases in K_h from 10^{-2} to 0 $m^2 s^{-1}$. The model was set to run using a second-order

space-centered method for momentum advection and two trapezoidal iterations after the initial non-smoothed leapfrog predictive step.

The reservoir was assumed initially at rest with a uniform density, equal to the averaged density of the W-River and N-River. At the downstream end, the free surface elevation was fixed, with densities and tracer concentrations having zero gradients. Inflow rates and densities at the upstream boundaries, in turn, were set to follow the field data of *Ramón et al.* [2013] (Chapter 2). Inflow rates from the W-River were set to a constant value of 730 $m^3 s^{-1}$ and were distributed uniformly in the inflow section. Inflows from the N-River were also constant but assumed to occur through two sections with different velocities, as observed in the field. Almost 2/3 of the total inflow rate (96 $m^3 s^{-1}$) from the N-River was presumed to enter through the main channel (66 $m^3 s^{-1}$) and the remaining through the secondary channel. Inflow temperatures were allowed to vary in time, with the hourly variations within any given day of the simulation following the observations collected on day 50 (2009). Wind forcing was weak at the time of the experiments [*Ramón et al.*, 2013; Chapter 2] and was assumed negligible in the model. The model was run until more than 99% of the tracer mass initially existing in the domain has left (approximately 9 days).

3.3.4 Tracer experiment and mixing rates

W-water was traced using a constant tracer concentration C_W = 100 ppm. The tracer concentrations downstream, varying from 0 to 100, indicated the percentage of W-water in the mixture and, hence, were used to establish the level of mixing between the W-River and N-River. Mixing ratios were evaluated each 0.25 hr at 58 cross sections downstream of the confluence (cross sections B1–B58, Figure 3.1). The distance between consecutive B sections was ≈ 120 m, and the last section was almost 1 km from the downstream boundary to avoid the influence of boundary conditions. Other simulations (not shown) were conducted with the downstream boundary displaced 1.5 km farther downstream, with estimates of mixing rates at section 58 which varied less than 1% with respect to the reference case. We will use the symbol x_c to refer to the distance downstream of the junction apex of each of these cross sections and will be given as a multiple of b_p. Two different approaches proposed by *Biron et al.* [2004] were used to quantify mixing levels. The first is based on an index referred to as deviation from

complete mixing δ [*Gaudet and Roy*, 1995]. For a given cell *i*, in a cross section, the deviation from complete mixing δ was calculated as follows:

$$\delta(i) = \frac{C(i) - C_p}{C_p} \cdot 100\,, \tag{3.1}$$

where *C(i)* is the simulated tracer concentration at cell *i* and C_p is the theoretical concentration after complete mixing [*Gaudet and Roy*, 1995]. If C_N and C_W are the tracer concentrations in the N-River and W-River, respectively, upstream of the confluence, C_p, is calculated as follows:

$$C_p = \frac{C_N Q_N + C_W Q_W}{Q_N + Q_W} \tag{3.2}$$

For Q_W = 730 $m^3\ s^{-1}$, Q_N = 96 $m^3\ s^{-1}$, C_W = 100 ppm, and C_N = 0 ppm, for example, as used in the T runs, C_p is of ≈ 88.4 ppm. For the M-simulations and m-simulations C_p is 60.5 and 39.5 ppm, respectively. The mixing layer was defined as the set of cells where the tracer concentration equals C_p ±10%, i.e., $\delta(i)$ = ±10%. To evaluate the level of mixing at any given cross section, *Gaudet and Roy* [1995] proposed to calculate δ for the cells with maximum and minimum tracer concentrations in that cross section, δ_{max} and δ_{min}. Note that δ_{max} will be positive, but δ_{min} will take negative values. Their absolute values will tend to decrease as tracer concentrations get closer to C_p, as a result of mixing. Complete mixing between the side discharge and main stem inflows would be achieved if δ_{max} and δ_{min} are in the range ±10% [*Gaudet and Roy*, 1995].

The second approach to quantify mixing levels consists of calculating the standard deviation of the concentration field in a given cross section σ. Standard deviations will tend to decrease downstream as a result of mixing, and they will become zero when tracer concentrations are uniform in a given cross section. Longitudinal variations of δ_{min} and σ can be used to asses mixing rates. Note that both approaches to evaluate mixing levels are complementary. Values of δ_{min} or δ_{max} remaining equal to those calculated with the initial concentration of the rivers, in particular, are indicative of part of the river flows remaining unmixed in a given cross section. Standard deviation σ, in turn, allows one to determine the level of mixing, even if part of the source water remains unmixed. Note

also that both the initial values of δ and σ will depend on flow rates and initial tracer concentrations.

3.4 Results and Discussion

3.4.1 Spatial distribution of source water near the confluence

Flow stagnation near the junction apex, flow deflection where each stream enters the confluence, and a shear and mixing layers between the two confluent streams can be identified in the simulations (Figure 3.2 and Figure 3.3). This is consistent with the classical model of flow at river confluences proposed by *Best* [1987], except for the absence of flow separation downstream of the junction corner. The absence of flow separation is, however, consistent with the field observations [*Ramón et al.*, 2013; Chapter 2] and has also been reported in other studies of natural confluences [e.g., *Biron et al.*, 1993; *Rhoads and Kenworthy*, 1995]. Our simulations are also consistent with those of *Bradbrook et al.* [2000] for asymmetrical confluences, in that water superelevations moved gradually, within the confluence region, toward the bank opposite to the side inflow (Figure 3.2a). The mixing layer between the confluent streams remains slightly slanted as widens downstream of the confluence (Figure 3.2). The level of tilting of the mixing interface, though, changes depending on the time of the day (Figure 3.2e and Figure 3.2g). These changes are linked to variations in the magnitude of the cross flows (Figure 3.2f and Figure 3.2h), which, in turn, are driven either by (1) the development of turbulent eddies shed from the stagnation area (which can be observed from tracer concentrations in Figure 3.2b–d and vertical vorticity in Figure 3.3) and (2) the time-varying density contrast $\Delta\rho/\rho_0$ between streams, which creates large-scale lateral circulation. Each of these processes has different characteristic frequencies (Figure 3.4); hence, their effect on the velocity and water properties can be isolated. The spectrum of the inflow densities peaked near a frequency of 1.1×10^{-5} Hz (period $T_p \approx 24$ hr), with additional peaks at $T_p = 12.7$ hr and $T_p = 8.5$ hr corresponding to peaks in the incident radiation signal collected in the meteorological station (Figure 3.4b). The spectra of the velocity fluctuations in the streamwise (u_s') and lateral (u_n') directions within the stagnation area and the mixing interface, however, exhibit peaks at frequencies f_p of 6.2×10^{-4} Hz and 3.2×10^{-4} Hz (Figure 3.4c and Figure 3.4d), the former f_p being indicative of vortex shedding from the stagnation area with a period $T_p = 0.45$ hr.

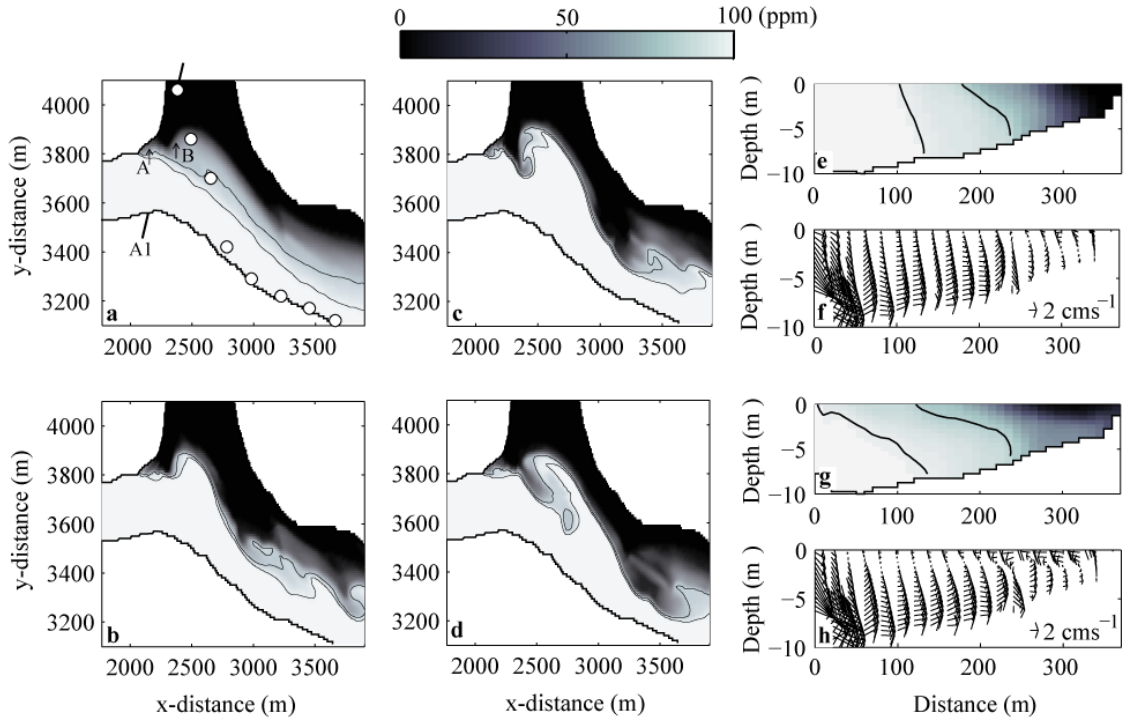

Figure 3.2 (a) Time-averaged and (b, c, d) instant tracer concentrations at the surface plane. (b) 19:00 hr, (c) 19:15 hr, (d) 19:30 hr. And time-averaged (e, g) tracer concentration (ppm) and (f, h) cross-stream velocities at section B13 (x_c = 4.7) between (e, f) 11-12 hr and (g, h) 19-20 hr. Distance = 0 m at the right bank. Black solid lines in (a-e, g) account for the location of the mixing interface (= C_p ±10%) and white dots in (a) show the location of the maximum time-averaged water surface elevation at sections A1 (x_c = 0.17) to B12 (x_c = 4.4). Arrows in (a) show the locations − stagnation zone (A) and mixing layer (B) − where the spectral signal of the velocity fluctuations was calculated in Figure 3.4c-d. Run case *Base* in Table 3.1.

The 6.2 × 10^{-4} Hz frequency in the stagnation area agrees with the theoretical estimates of frequency of Kelvin-Helmholtz instabilities in shallow mixing layers [*Vowinckel et al.*, 2007] f_p (= 4.57 × 10^{-4} Hz), calculated as [*Sukhodolov and Sukhodolova*, 2007]

$$f_p = \frac{\bar{U}_c}{\gamma}\left[\frac{2}{C_d}\frac{U_c}{\Delta U}\right]^{-1/3} \tag{3.3}$$

Here $\bar{U}_c$ (= 0.25 m s^{-1}) is the depth-averaged mixing layer centerline velocity, $\Delta\bar{U}$ (= 0.331 m s^{-1}) is the difference between the depth-averaged downstream velocities in the W-River and the N-River, and γ (≈ 60 m) is the width of the area of flow stagnation (Figure 3.2a). Hence, the vortices simulated in the shear layer between the W-River and N-River are Kelvin-Helmholtz (KH) structures (Figure 3.3), consistently with the

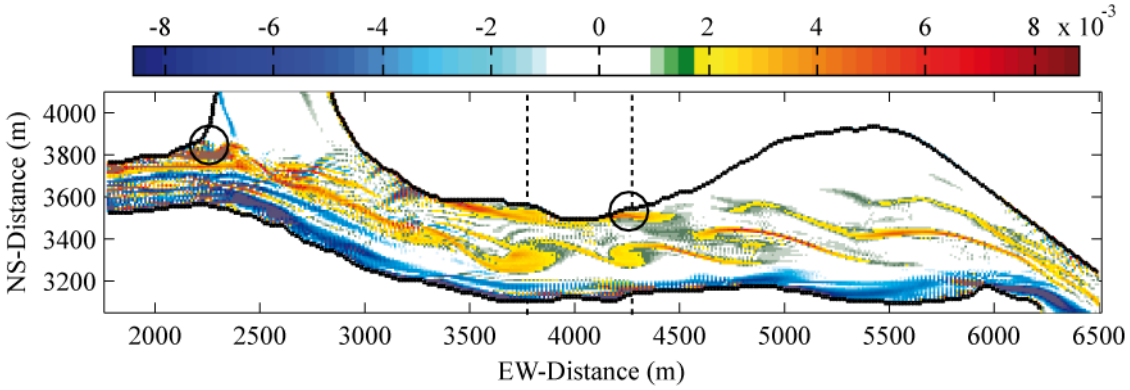

Figure 3.3 Vertical vorticity (s^{-1}) at the surface plane at 11:30 hr. Circles show the locations where eddies are shed (stagnation area and upstream corner of the dead zone). Dashed lines show the location of two eddies shed from the stagnation area, which are ~ 0.5 hr apart. Run case *Base* in Table 3.1.

simulations of the confluence between the Kaskaskia and Copper Slough by *Constantinescu et al.* [2011, 2012], where KH vortices were shown to develop within the shear layer both for $R_m >> 1$ and $R_m << 1$.

3.4.2 Dead zone dynamics

The channel widens in reach R2 (Figure 3.1) between x_c = 5.7 and x_c = 9.7 creating a dead zone on the left bank. Instantaneous and mean (averaged over 24 hr) depth-averaged flow fields at the dead zone are shown in Figure 3.5. Note that a shear layer develops between the mainstream and the dead zone, with vortices that grow in size and entrain water from the main channel as they move downstream from the upstream corner (Figure 3.3, Figure 3.5a and Figure 3.5b). Consistently with the simulations of shallow mixing layers around dead zones [*Constantinescu et al.*, 2009], the vortices shown in Figure 3.5 are KH instabilities. They are shed with a frequency f_p of 3.06×10^{-4} Hz (T_p = 0.91 hr), which agrees with the theoretical KH instability frequency ($f_p = 2.7 \times 10^{-4}$ Hz) calculated with equation (3.3), for $\bar{U}c$ = 0.18 m s^{-1}, differences between the depth-averaged downstream velocities in the mainstream and dead zone $\Delta\bar{U}$ = 0.38 m s^{-1}, and $\gamma \approx 100$ m (Figure 3.5).

The time-averaged velocity fields reveal the existence of a large gyre within the embayment (Figure 3.5c). Previous laboratory experiments, though, suggest that a secondary gyre, with the opposite circulation to the primary gyre, should also develop for

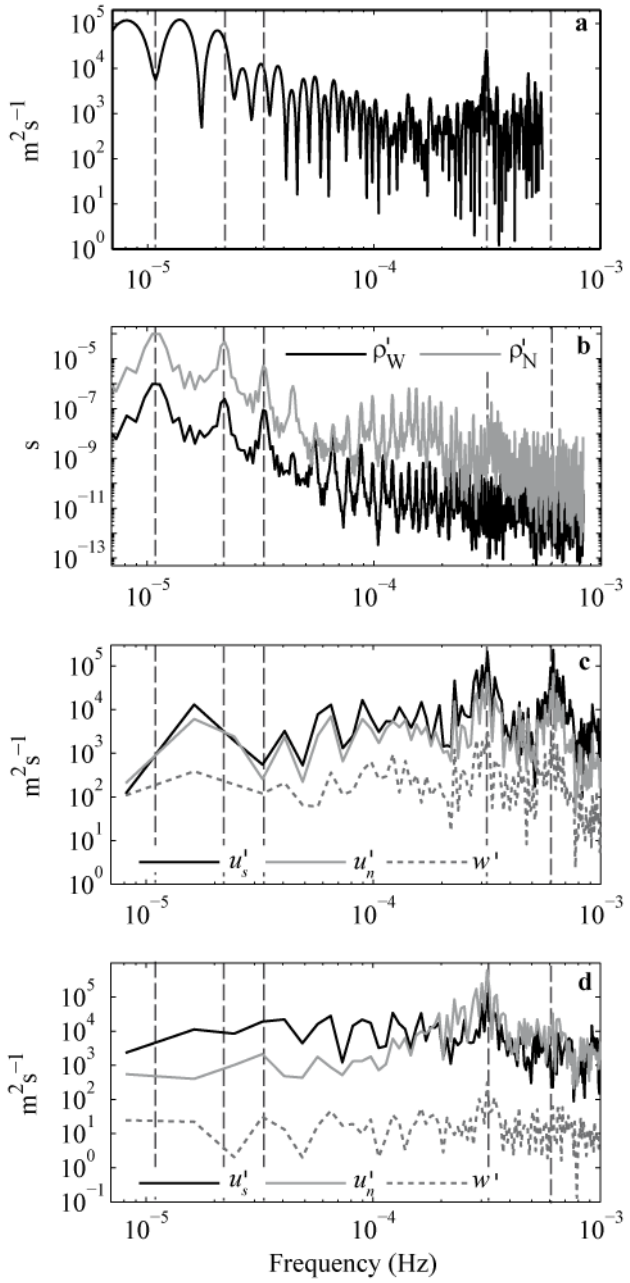

Figure 3.4 Power spectra of (a) the maximum outward velocities at section B13 (x_c = 4.7), (b) the fluctuations of the normalized inflow densities ($(\rho-\rho_0)/\rho_0$) for the Ebro and Segre rivers after a six-day simulation, and (c, d) the fluctuations of the depth-averaged velocity fields u_s', u_n' and w' during the last two days of simulations at locations (c) A (inside the stagnation zone) and (d) B (mixing layer) shown in Figure 3.2a. Vertical dashed gray lines show the location of frequencies $f = 1.1\times10^{-5}$ Hz, $f = 2.2\times10^{-5}$ Hz, $f = 3.3\times10^{-5}$, $f = 3.3\times10^{-4}$ Hz, and $f = 6.2\times10^{-4}$ Hz. Run case *Base* in Table 3.1.

dead zones having width-to-length ratios $b_0/L_0 < 0.5$ [e.g., *Weitbrecht and Jirka*, 2001], as is the case of our study site. The fact that this secondary gyre is not reproduced in our simulations may be the result of the semicircular planform geometry of the embayment (see Figure 3.1) or bathymetric effects. As suggested by *Sukhodolov et al.* [2002], the riverbed geometry of dead zones with complex morphological structures in natural rivers may produce velocity patterns that differ from those observed in laboratory studies. For example, they observed a secondary gyre that rotates in the same direction as the main gyre. *Muto et al.* [2002] also observed a unique small cell in an embayment in a natural river ($b_0/L_0 = 0.25$), which they attributed to bed irregularities, such as bed undulation. Alternatively, the absence of this secondary gyre in our simulations could be due to the inability of the two-equation turbulence model closure. *Gualtieri* [2008], for example, also failed to reproduce the secondary gyre in his 2-D computations of the experiment of *Weitbrecht and Jirka* [2001] with a standard two-equation *k-ε* turbulence model. Later,

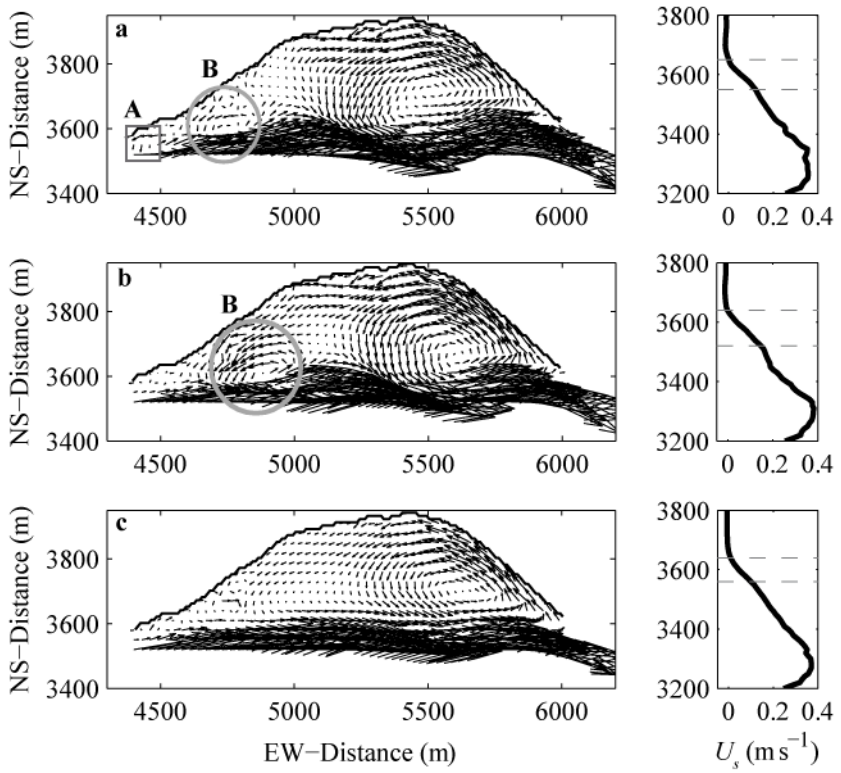

Figure 3.5 Depth-averaged velocity fields at the dead zone region and depth-averaged downstream velocities U_s at section B23 ($x_c = 7.2$) located at EW-Distance 4960 m. (a) Instant velocities at time t = 11:30 hr, (b) instant velocities at t = 12:00 hr, and (c) time-averaged values. Run case *Base* in Table 3.1. The upstream junction corner where eddies are shed (square A), the evolution of eddy B (circle), and the limits of the shear layer between the dead zone and the main stream (gray dashed lines) are also shown.

Gualtieri et al. [2009] were able to reproduce the laboratory experiments of *Muto et al.* [2000] on a flume with a unique dead zone. They compared the standard k-ε model, which assumes isotropic turbulence, and a nonisotropic Reynolds stress model, and found that the estimates of the transverse velocities, though similar, were better predicted when the anisotropy of the Reynolds stresses was explicitly represented.

3.4.3 Physical drivers of cross-stream fluid motion

The contribution of baroclinic forces, associated with the time-varying side-inflow density, to the development of cross-stream circulation and, thus, mixing layer distortion, is examined next. Following assumptions by *Kalkwijk and Booij* [1986], adding the lateral baroclinic forces and neglecting Coriolis, the transverse momentum equation can be written as:

$$\underbrace{\frac{\partial u_n}{\partial t}}_{(1)} + \underbrace{u_s \frac{\partial u_n}{\partial s}}_{(2)} - \underbrace{\frac{u_s^{\,2}}{R_S}}_{(3)} + \left(\underbrace{g \frac{\partial \zeta}{\partial n}}_{(4)} + \underbrace{g \frac{1}{\rho_0} \int_z^{\zeta} \frac{\partial \rho}{\partial n} dz'}_{(5)} \right) - \underbrace{\frac{\partial}{\partial z}\left(A_z \frac{\partial u_n}{\partial z} \right)}_{(6)} = 0 \qquad (3.4)$$

Here u_s and u_n represent the velocity components in the streamwise s and lateral n directions; g is the acceleration of gravity; ζ is the free surface elevation; and A_z is the kinematic eddy viscosity in the vertical z direction. The first and second terms in equation (3.4) are local acceleration and lateral inertia; terms 3 through 5 represent the centrifugal F_c, barotropic F_p, and baroclinic F_b forcings of the cross flow. The sixth term represents momentum transport by turbulent diffusion. Note that R_s in term 3 is negative for channels veering to the left and positive otherwise. Negative values in equation (3.4) indicate acceleration toward the left bank.

The time-averaged magnitude of each term in equation (3.4) was evaluated from simulated variables at x_c = 4.7 and x_c = 15.3, in three different scenarios with $\Delta\rho/\rho_0$ set to 0 and ± 2.4 × 10^{-4} (runs T1, T5, and T8 in Table 3.1). The results are shown in Table 3.2. For neutrally buoyant side inflows (run T5), the cross-stream motion is largely controlled by a balance between F_c and F_p, both of O (10^{-5}) m s^{-2}. For nonneutrally buoyant side inflows (runs T1, T8), in turn, even with weak density differences, the force balance becomes even more complex, and F_b becomes one of the dominant terms, also of O (10^{-5}) m s^{-2}, especially immediately downstream of the confluence where the density contrast is

larger. The magnitude of F_c compared to that of F_b will vary depending on the cross section. The former can be quantified using the maximum transverse velocities in a curved channel $u_{n,c}$ estimated as in *Johannesson and Parker* [1988], $u_{n,c} = 6\langle u_s\rangle D/R_s$. The ideal speed of the gravity current in the absence of shear and mixing, $c = (g\,\Delta\rho/\rho_0\,D)^{0.5}/2$ will be taken as a proxy of the magnitude of F_b. This value increases from 0.03 m s^{-1} for $\Delta\rho/\rho_0 = \pm 3.2 \times 10^{-5}$ to 0.07 m s^{-1} for $\Delta\rho/\rho_0 = \pm 2.4 \times 10^{-4}$. Lateral velocities induced by F_c are weak compared to those induced by F_b especially in the first bend, where, for $\langle u_s\rangle$ = 0.32 m s^{-1} and D = 10 m as observed at x_c = 4.7, $u_{n,c} \approx 6.4 \times 10^{-3}$ m s^{-1}. Modeled maximum outward lateral velocities in this section agree with these estimates. For example, low-pass filtered ($f < 4 \times 10^{-5}$ Hz) cross-flow velocities near surface at x_c = 4.7 ranged from 3.2 to 5.1 cm s^{-1} depending on $\Delta\rho/\rho_0$. This indicates that cross-stream motion is largely set up by the existence of density contrasts. Farther downstream, at x_c = 15.3 ($\langle u_s\rangle$ = 0.2 m s^{-1}, D = 14 m), $u_{n,c}$ increases to ca. 0.013 m s^{-1}, and the centrifugal and baroclinic forcings become comparable.

Baroclinic and centrifugal forcings act in the same or in opposite direction, depending on whether side inflows are positively or negatively buoyant and on whether the flow bends to the left or to the right. For example, in the first bend to the left (reach R1), the cross-stream flow will be stronger in response to increases in density contrasts for $\Delta\rho/\rho_0 > 0$, tilting and distorting the mixing layer toward the right bank (Figure 3.6a and Figure 3.6b). For $\Delta\rho/\rho_0 = 0$, F_c is weak to effectively tilt the mixing layer (Figure 3.6e

Table 3.2 Time- and section- averaged magnitude (m s^{-2}) of terms in Eq. 3.4 (transverse momentum equation) at x_c = 4.7 and x_c = 15.3. Negative values indicate forcing towards the left bank.

	Section					
	B13 (x_c = 4.7)			**B49 (x_c = 15.3)**		
	Run case			**Run case**		
Term in Eq. 4	**T1**	**T5**	**T8**	**T1**	**T5**	**T8**
2 [(a)]	-2.1×10^{-5}	-1.7×10^{-5}	-1.8×10^{-5}	2.9×10^{-6}	4.3×10^{-6}	2.3×10^{-6}
3 [(b)]	3.8×10^{-5}	3.8×10^{-5}	3.7×10^{-5}	-3.4×10^{-5}	-3.4×10^{-5}	-4.3×10^{-5}
4 [(c)]	-1.1×10^{-5}	-1.1×10^{-5}	-3.4×10^{-5}	2.8×10^{-5}	3.5×10^{-5}	4.7×10^{-5}
5 [(d)]	4.9×10^{-6}	-7.8×10^{-9}	-2.1×10^{-5}	-3.5×10^{-6}	8.9×10^{-9}	7.2×10^{-6}
6 [(e)]	3.2×10^{-6}	6.2×10^{-7}	-1.7×10^{-6}	-6.1×10^{-7}	-2.2×10^{-7}	2.0×10^{-6}

[(a)] Advection, [(b)] centrifugal forcing, [(c)] barotropic forcing, [(d)]baroclinic forcing, [(e)] turbulent diffusion

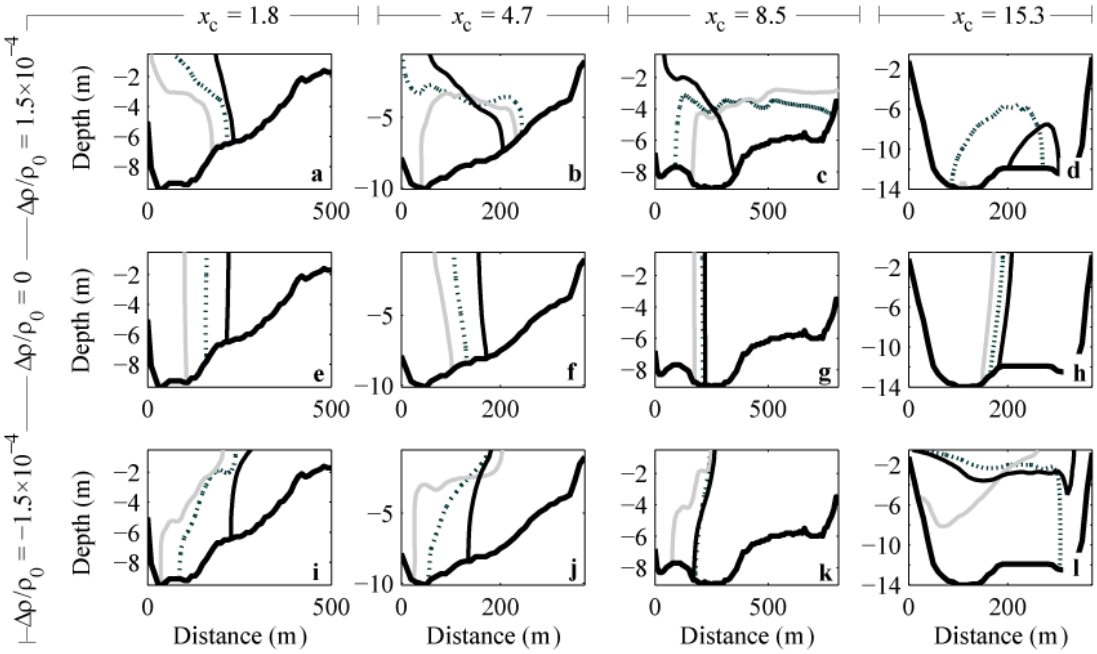

Figure 3.6 Time-averaged location of isolines of tracer concentration $C = C_p$ for different discharge ratios R_q and density constrasts $\Delta\rho/\rho_0$ between the Ebro and Segre rivers and distance downstream. Sections (a, e, i) B2 (x_c = 1.8), (b, f, j) B13 (x_c = 4.7), (e, g, k) B28 (x_c = 8.5) and (d, h, l) B49 (x_c = 15.3). R_q = 0.13 (black solid lines), R_q = 0.65 (black dotted lines), and R_q = 1.53 (gray solid lines).

and Figure 3.6f). For $\Delta\rho/\rho_0 < 0$, the mixing interface remains largely vertical until density contrasts are large enough to overcome F_c ($|\Delta\rho/\rho_0| > O(10^{-6})$) and to tilt the mixing interface toward the left bank (Figure 3.6i and Figure 3.6j). In the second bend to the right ($x_c \geq 10.3$, reach R3), negatively buoyant side inflows increase cross-flow strength, and the mixing interface tilts to the left (Figure 3.6d, Figure 3.6h, and Figure 3.6l).

Lateral inertia (term 2 in Eq. (3.4)) is particularly significant close to the confluence (see section B13 in Table 3.2). Its magnitude is, in turn, linked to the momentum ratio R_m. As a result of changes in R_m., several changes occur in the flow field near the confluence. First, as R_m. increases, the location of the mixing layer moves farther away from the tributary bank (see, for example, Figure 3.6e and Figure 3.6f). This is consistent with earlier work conducted under nearly neutrally buoyant conditions in river confluences [e.g., *Biron et al.*, 1993; *Rhoads and Kenworthy*, 1995, 1998]. Second, under nonneutrally buoyant conditions, the tilting of the mixing layer increases (Figure 3.6a and Figure 3.6i).

3.4.4 Mixing rates between the Ebro and Segre rivers

In the base case simulation, mixing is complete at the most downstream section, almost 7.5 km ($x_c \approx 18.7$) from the junction apex, where average absolute values of δ_{min} and δ_{max} become < 10% (Figure 3.7a). Minimum deviation δ_{min} remained constant and close to −100% (i.e., indicative of weak mixing) but only for $x_c \leq 5.4$ within reach R1. Strong mixing occurs, as revealed by increasing values of δ_{min} (or decreasing σ, Figure 3.7 and Table 3.3) once in reach R2, where the channel widens to form a dead zone ($5.7 \leq x_c \leq 9.7$), and downstream, as the channel narrows again and bends to the right ($x_c > 9.7$, reach R3). Mixing lengths between the W-River and the N-River are of O (10^1) channel widths which are indicative of rapid mixing between the confluent streams, consistently with the field observations of *Ramón et al.* [2013] (Chapter 2) and the prior results on mixing in river confluences [e.g., *Rhoads and Kenworthy*, 1995; *Rhoads and Sukhodolov*, 2001; *Lane et al.*, 2008, and references therein].

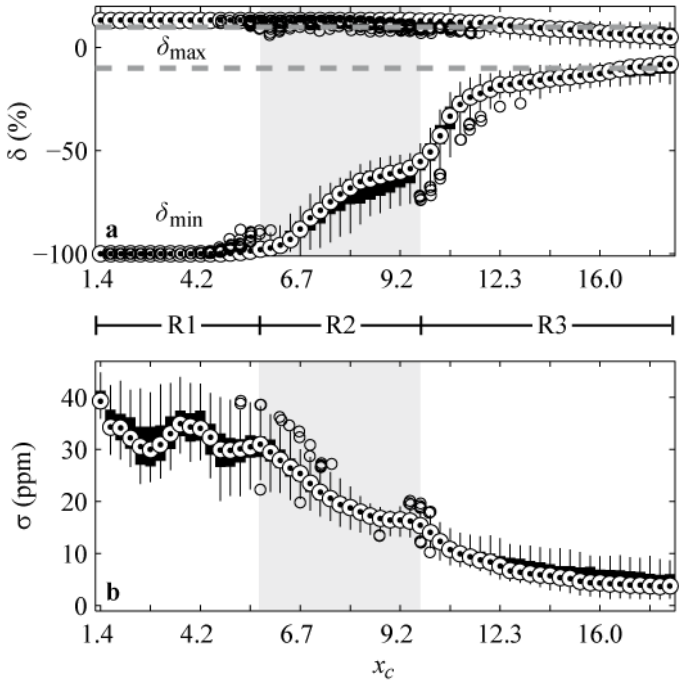

Figure 3.7 Boxplot of (a) maximum δ_{max} and minimum δ_{min} deviations from complete mixing δ (%), and of (b) standard deviations σ (ppm) of tracer concentrations at sections B1-B58 for the *Base* case simulation in Table 3.1. The gray dashed lines in (a) show the upper and lower limits (δ_{max} = 10% and δ_{min} = −10%) within which complete mixing is achieved [*Gaudet and Roy*, 1995]. The shaded area shows sections within reach R2.

Table 3.3 Time-averaged mixing rates (absolute values) — $\Delta\sigma/\Delta s$ (ppm m^{-1}) — evaluated in reaches R1, R2, R3 and along the study reach (Total).

Run case	R1	R2	R3	Total
Base	5.3×10^{-3}	9.8×10^{-3}	2.4×10^{-3}	5.1×10^{-3}
T1	1.1×10^{-2}	6.2×10^{-3}	1.9×10^{-3}	5.3×10^{-3}
T2	9.1×10^{-3}	7.9×10^{-3}	2.5×10^{-3}	5.6×10^{-3}
T3	4.7×10^{-3}	1.0×10^{-2}	2.2×10^{-3}	5.0×10^{-3}
T4	3.7×10^{-3}	9.2×10^{-3}	2.0×10^{-3}	4.4×10^{-3}
T5	3.7×10^{-3}	3.7×10^{-3}	3.8×10^{-3}	4.0×10^{-3}
T6	5.0×10^{-3}	7.4×10^{-3}	4.1×10^{-3}	5.3×10^{-3}
T7	7.1×10^{-3}	7.6×10^{-3}	2.7×10^{-3}	5.2×10^{-3}
T8	8.7×10^{-3}	7.2×10^{-3}	1.9×10^{-3}	5.1×10^{-3}
M1	5.5×10^{-3}	2.3×10^{-3}	5.5×10^{-3}	4.8×10^{-3}
M2	3.7×10^{-3}	1.7×10^{-3}	8.0×10^{-3}	5.4×10^{-3}
M3	2.9×10^{-3}	1.5×10^{-3}	3.6×10^{-3}	2.9×10^{-3}
M4	4.9×10^{-3}	1.2×10^{-2}	4.0×10^{-3}	6.3×10^{-3}
M5	5.7×10^{-3}	8.7×10^{-3}	4.6×10^{-3}	5.8×10^{-3}
m1	1.1×10^{-2}	3.1×10^{-3}	3.8×10^{-3}	5.5×10^{-3}
m2	8.4×10^{-3}	2.0×10^{-3}	5.5×10^{-3}	5.1×10^{-3}
m3	8.0×10^{-3}	1.5×10^{-3}	2.6×10^{-3}	3.4×10^{-3}
m4	1.0×10^{-2}	8.6×10^{-3}	2.5×10^{-3}	6.2×10^{-3}
m5	9.0×10^{-3}	5.7×10^{-3}	4.3×10^{-3}	5.8×10^{-3}

Mixing rates, as revealed by δ_{min} and σ, were also subject to changes in time, as shown by the upper and lower whiskers in Figure 3.7a and Figure 3.7b. These changes can only be attributed in our simulations to either changes in inflow densities (Figure 3.4b) or the existence of large coherent structures developing at the dead zone (Figure 3.5) and at the stagnation area (Figure 3.2, Figure 3.3, and Figure 3.4c). The time series of σ and $\Delta\rho/\rho_0$ at x_c = 4.7, x_c = 8.5, and x_c = 15.3 during the last two days of simulation are shown in Figure 3.8a-c. The spectra of the signals are also shown (Figure 3.8d-f). Note that the variability of σ in reach R1, with peak frequencies near 3.1×10^{-4} Hz (Figure 3.8d), is largely associated with unsteady large coherent structures which exhibit similar frequencies (see Figure 3.4c and Figure 3.4d). The contribution of the coherent structures, however, weakens downstream (for example, at x_c = 15.3) where the variability of σ (from 2 ppm to 9 ppm) becomes dominated by the diurnal changes in inflow densities (Figure 3.8f).

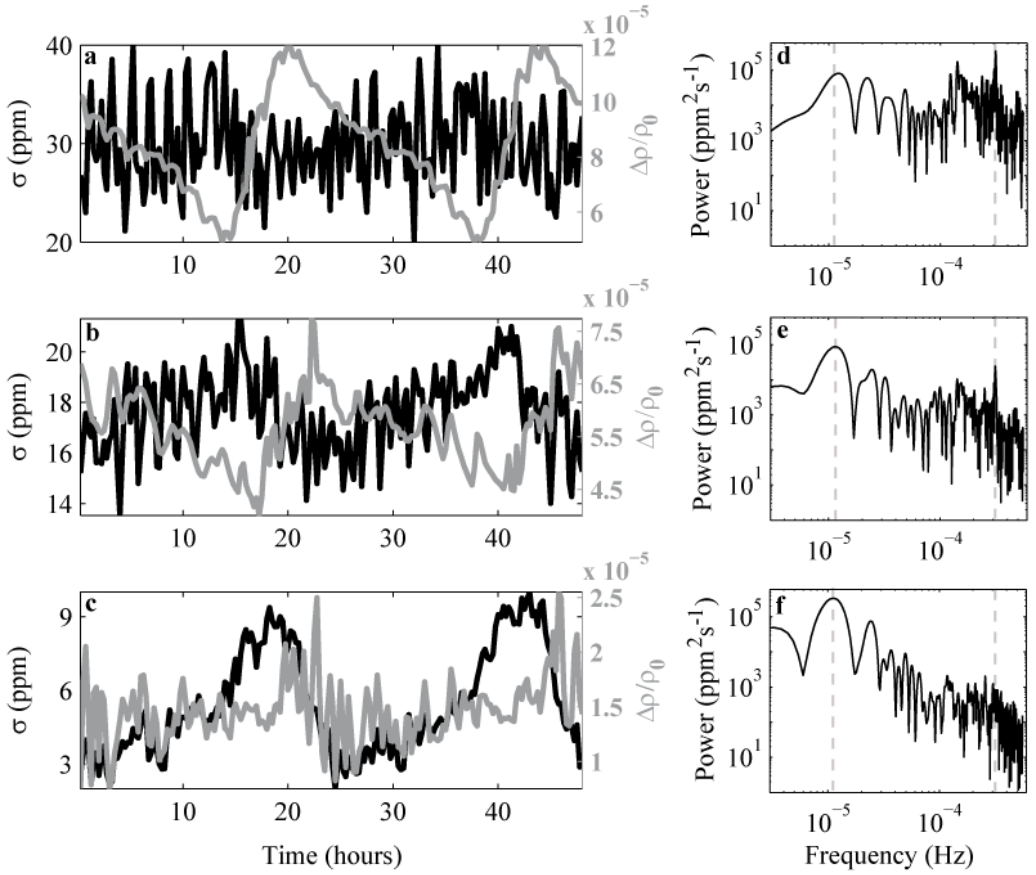

Figure 3.8 (a-c) Time-varying standard deviation σ of tracer concentrations (black lines) and density contrast $\Delta\rho/\rho_0$ between rivers (gray lines) during the last two days of simulations in the *Base* case simulation (Table 3.1), and (d-f) spectral curves for the time-varying σ. (a, d) Section B13 (x_c = 4.7) in reach R1, (b, e) section B28 (x_c = 8.5) in reach R2, and (c, f) section B49 (x_c = 15.3) in reach R3. The frequency peaks $f_p = 1.14\times10^{-5}$ Hz (period $T_p \sim 24$ hr) and $f_p = 3.1\times10^{-4}$ Hz (T_p = 0.9 hr) characteristic of the density signal and of the coherent structures, respectively, are shown (gray dashed lines).

3.4.5 Influence of density differences on mixing rates

Time-averaged values of σ for runs T1‑T8 (Table 3.1) are plotted in Figure 3.9a as function of the distance downstream of the junction apex x_c and the density contrast $\Delta\rho/\rho_0$. For any given run with a fixed value of $\Delta\rho/\rho_0$, the separation between isolines will vary with distance and represents the magnitude of the local mixing rate: the closer the isolines the stronger the mixing. Values of mixing rates $\Delta\sigma/\Delta s$, evaluated in reaches R1‑R3 and along the study reach (x_c = 0-18.7), are also shown in Table 3.3. Mixing rates, for example, tend to be larger in reach R2 compared to reach R1, consistently with Figure 3.7. The weakest mixing ($\Delta\sigma/\Delta s = 4.0\times10^{-3}$ ppm m^{-1}) occurred for $\Delta\rho/\rho_0 = 0$, tending to increase for weakly buoyant side inflows in response to changes of O (10^{-5}) in $\Delta\rho/\rho_0$. For

the largest values of $\Delta\rho/\rho_0$ tested ($> 10^{-4}$), in turn, mixing rates in the study reach tended to decrease in response to increases in side-inflow buoyancy. Note that the differences in mixing rates between weakly and strongly buoyant side inflows occur mainly in reach R3. In this reach, mixing rates appeared to be weaker for strongly buoyant conditions (more spaced isolines in Figure 3.9a and Table 3.3) and stronger for weakly buoyant conditions. For positively buoyant inflows maximal mixing rates occurred at $\Delta\rho/\rho_0 = 1.5 \times 10^{-4}$ ($\Delta\sigma/\Delta s = 5.6 \times 10^{-3}$ ppm m^{-1}). For negatively buoyant inflows, maximal rates occurred at $\Delta\rho/\rho_0 = -6.8 \times 10^{-5}$ ($\Delta\sigma/\Delta s = 5.3 \times 10^{-3}$ ppm m^{-1}). These mixing rates, in general, were up to 40% larger than those simulated with $\Delta\rho/\rho_0 = 0$ (Table 3.3).

Any differences in mixing rates between simulations in Figure 3.9a should be the result of differences in (1) the contact area between the water masses, where the spatial gradients of tracer concentration are significant, and/or (2) the diffusion coefficients near that mixing interface. The contact area at any given cross section was identified as the set of vertical and horizontal interfaces between adjacent cells where the tracer concentration

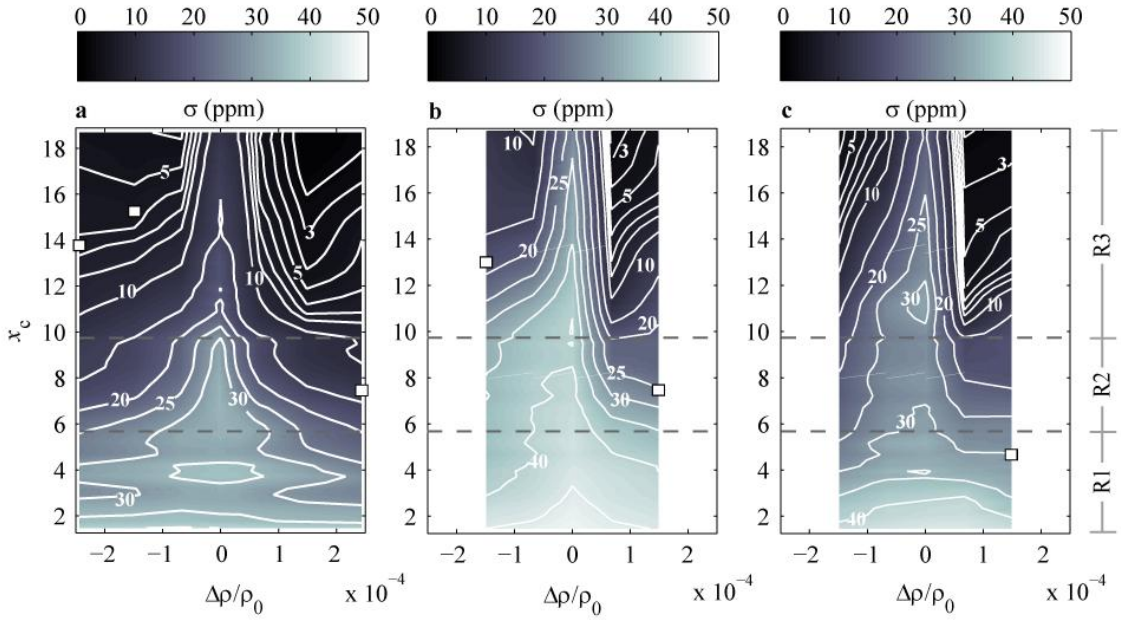

Figure 3.9 Variation with non-dimensional distance downstream of the junction apex (x_c) of the linearly-interpolated time-averaged values of standard deviations σ, for different density contrasts ($\Delta\rho/\rho_0$) between the Ebro and Segre rivers. Run cases (a) T1-T8 (b) M1-M5 and (c) m1-m5 in Table 3.1. The location of $x_c = 5.7$ —start of reach R2— and $x_c = 9.7$ — start of reach R3— is shown (gray dashed lines). Note that the resolution of the σ isolines (white lines) increases downstream from gradients 5 ppm within reaches R1 and R2 to gradients of 1 ppm within reach R3. White squares in (b, c, d) show locations of x_H points.

changes from $C > C_p$ to $C < C_p$. It can be decomposed in the model into a set of interfaces available for vertical mixing, of area S_z, and another set of interfaces available for horizontal mixing, of area S_h. Surface of contact areas (S_z and S_h) and their average vertical diffusion coefficients at several cross sections downstream of the confluence are shown in Table 3.4, for side inflows with different density contrasts.

3.4.5.1 *Mixing layer distortion*

As shown in Figure 3.6, the tilting of the mixing interface, and hence the contact area between the rivers, is tightly linked to the magnitude of $\Delta\rho/\rho_0$. The changes in S_h occurring in response to buoyant side inflows are, in general, weak (at most of ± 10%) within reach R1 compared to the changes in the area available for vertical mixing S_z (Table 3.4). For example, the area S_z was ca. 13 and 5 times larger for $\Delta\rho/\rho_0 = +2.4 \times 10^{-4}$ and $\Delta\rho/\rho_0 = -2.4 \times 10^{-4}$, respectively, than for $\Delta\rho/\rho_0 = 0$, at $x_c = 4.7$ (compare, also, Figure 3.6b, Figure 3.6f, and Figure 3.6j). Farther downstream, at $x_c = 8.5$, S_z for $\Delta\rho/\rho_0 = \pm 2.4 \times 10^{-4}$ is two order of magnitude larger than S_z for $\Delta\rho/\rho_0 = 0$ (Table 3.4 and Figure 3.6c, Figure 3.6g, and Figure 3.6k). Note, also in Table 3.4, that S_z tends to be larger for positively buoyant side inflows, compared to the cases of negatively buoyant side inflows at $x_c = 4.7$. This occurs also at $x_c = 8.5$ and can be first attributed to the effect of bottom friction, which will tend to decelerate the downslope lateral flow of negatively buoyant side inflows, but will not affect the lateral near-surface motion of positively buoyant side inflows. Second, it can also be understood as a result of the interplay between F_c and F_b (Equation (3.4)). Although the cross flows, $u_{n,c}$, induced by F_c are small compared to those induced by F_b in reaches R1 and R2 (see section 3.4.3), they can delay the tilting of the mixing interface for $\Delta\rho/\rho_0 < 0$. For example, for $\langle u_s \rangle = 0.32$ m s^{-1}, $u_{n,c} \approx 6.4 \times 10^{-3}$ m s^{-1}, and $c \approx \pm 0.07$ m s^{-1}, as expected for $\Delta\rho/\rho_0 = \pm 2.4 \times 10^{-4}$ (see section 3.4.3), S_z could increase ca. 500 m^2 more for positively buoyant side inflows in the time the mean flow goes from $x_c = 1.8$ to $x_c = 4.7$.

3.4.5.2 *Eddy diffussivities*

As density contrasts increase and the mixing layer tilts, the vertical density gradients across the mixing interface tend to suppress turbulent motions, causing vertical diffusivities K_z to decrease. These effects of side-inflow buoyancy on K_z, though, are smaller than the effects on the area of contact near the confluence. For example, at $x_c = 1.8$, K_z averages ≈ 0.01 m^{2}s^{-1} at the interface for $\Delta\rho/\rho_0 = 0$ (Table 3.4), but is 1.5 times

lower for $\Delta\rho/\rho_0 = +2.4 \times 10^{-4}$ (Table 3.4). By contrast, the interface area is up to 16 times larger under nonneutrally buoyant conditions, compared to the simulation with $\Delta\rho/\rho_0 = 0$. These results, hence, suggest that the higher mixing rates under nonneutrally buoyant conditions are largely the result of a higher level of distortion of the mixing layer. This conclusion is consistent with simulations [*Bradbrook et al.*, 2001; *Biron and Lane*, 2008] and field observations [*Rhoads and Kenworthy*, 1995; *Rhoads and Sukhodolov*, 2001] of river confluences reported earlier. The mechanisms causing distortion in Ribarroja, though, are not the same as those reported earlier.

Once the side inflows have reached the opposite side of the main channel and the interface becomes nearly horizontal, further changes in the density contrast do not affect the contact area. Note, for example, that S_z is nearly constant for $\Delta\rho/\rho_0 > +1.5 \times 10^{-4}$, at x_c = 8.5 (Table 3.4). The effects of side-inflow buoyancy on K_z, though, become important at that point. At x_c = 8.5, in particular, K_z for $\Delta\rho/\rho_0 = +1.5 \times 10^{-4}$ is 1.3 times higher than K_z for $\Delta\rho/\rho_0 = +2.4 \times 10^{-4}$ (Table 3.4). The distance downstream to this point where the interface becomes horizontal will be referred to as x_H and has been plotted in Figure 3.9a for those simulations where the mixing interface became horizontal within the computational domain. Note that mixing rates decrease (i.e., the spacing between isolines increases) downstream of x_H in Figure 3.9a. Any changes in the contact area occurring downstream of x_H will be the result of the balance between the centrifugal forcing, controlled by channel geometry, and the stability of the water column, resulting from vertical density gradients. Inflows with larger density contrasts will lead to more stable interfaces downstream, which will tend to remain closer to horizontal in channels with a given curvature. At x_c = 15.3, for example, S_z for $\Delta\rho/\rho_0 = +2.4 \times 10^{-4}$ is almost twice the value calculated for $\Delta\rho/\rho_0 = +1.5 \times 10^{-4}$ (Table 3.4). Thus, the negative effect of large density contrasts on mixing rates should be understood as a result of the development of very stable horizontal interfaces where mixing is suppressed by vertical density gradients. Centrifugal forcing, in turn, will tend to generate lateral density gradients, hence, increasing mixing rates.

3.4.5.3 *Influence of momentum ratios*

The lowest mixing rates still occur for $\Delta\rho/\rho_0 = 0$, independently of R_m (or R_q) (Figure 3.9b and Figure 3.9c and Table 3.3). Also independently of R_m, mixing rates

Table 3.4 Time-averaged mean values at the mixing interface between the Ebro and Segre rivers at x_c = 1.8, x_c = 4.7, x_c = 8.5 and x_c = 15.3. Runs T1-T8 in Table 3.1.

	Section B2, x_c = 1.8			**Section B13, x_c = 4.7**			**Section B28, x_c = 8.5**			**Section B49, x_c = 15.3**		
$\Delta\rho/\rho_0$	K_z (m^2s^{-1})	S_h (m^2)	S_z (m^2)	K_z (m^2s^{-1})	S_h (m^2)	S_z (m^2)	K_z (m^2s^{-1})	S_h (m^2)	S_z (m^2)	K_z (m^2s^{-1})	S_h (m^2)	S_z (m^2)
2.4×10^{-4}	6.31×10^{-3}	55.10	833.23	2.78×10^{-3}	64.75	2075.78	1.77×10^{-3}	60.93	3522.83	6.02×10^{-3}	116.07	2352.27
1.5×10^{-4}	8.02×10^{-3}	58.51	492.81	3.87×10^{-3}	68.92	1479.28	2.37×10^{-3}	77.68	3103.30	5.45×10^{-3}	49.38	1029.28
6.8×10^{-5}	9.16×10^{-3}	60.00	86.82	5.05×10^{-3}	73.52	825.40	4.11×10^{-3}	84.99	1355.30	7.73×10^{-3}	132.38	550.67
3.2×10^{-5}	8.52×10^{-3}	60.00	37.12	6.14×10^{-3}	73.13	702.97	5.79×10^{-3}	85.00	630.85	8.08×10^{-3}	123.89	211.08
0	9.00×10^{-3}	60.00	51.19	6.49×10^{-3}	74.81	157.64	8.07×10^{-3}	84.27	18.94	1.04×10^{-2}	114.78	259.45
-6.8×10^{-5}	6.54×10^{-3}	59.00	175.23	6.47×10^{-3}	76.00	239.22	6.94×10^{-3}	85.00	430.22	2.16×10^{-3}	106.17	2278.04
-1.5×10^{-4}	6.79×10^{-3}	59.21	548.33	6.94×10^{-3}	79.00	457.13	5.08×10^{-3}	83.01	926.85	2.32×10^{-3}	44.79	3248.66
-2.4×10^{-4}	4.35×10^{-3}	59.73	1015.82	5.52×10^{-3}	82.21	863.33	3.11×10^{-3}	73.92	1663.57	2.50×10^{-3}	120.01	2929.74

increase or decrease in response to increases in $|\Delta\rho/\rho_0|$, depending on whether the side inflows are weakly or strongly buoyant. The value of $\Delta\rho/\rho_0$ for maximal mixing rates ($\Delta\rho/\rho_0$*), though, changes in response to stronger side-inflow momentum. Note that $\Delta\rho/\rho_0$* decreases in response to increases in R_m for positively buoyant side inflows but increases for $\Delta\rho/\rho_0 < 0$. The site where the mixing interface becomes horizontal also changes in response to changes in R_m. For positively buoyant side flows, x_H moves upstream as a result of stronger side-inflow momentum, but it moves downstream for negatively buoyant side inflows. Note that for R_q = 1.53 the interface did not even become horizontal (Figure 3.6l) for the most negatively buoyant flows tested, and, hence, mixing rates always increased in response to increases in side-inflow density (see Table 3.3 and the upper left side of the plot in Figure 3.9c, where the isolines are monotonically decreasing as a function of $\Delta\rho/\rho_0$).

This different behavior of x_H for positively versus negatively buoyant side inflows can be understood as the result of the interplay between the inertia of the tributary and the mixing induced by its initial acceleration at and near the confluence. The inertia of the tributary favors the distortion of the mixing interface both for positively and negatively buoyant side inflows (Figure 3.6a and Figure 3.6i) and, as a result, mixing rates increase. Compare, for example, the location of the isoline of 40 ppm in Figure 3.9b and Figure 3.9c, for the M-simulations and m-simulations in which the initial σ, upstream the confluence, is similar. For $\Delta\rho/\rho_0 > 0$, a horizontal mixing interface develops within reaches R1 or R2 which counteracts the mixing induced by the lateral inertia of the tributary. For $\Delta\rho/\rho_0 < 0$, a horizontal mixing interface does not develop in R1 or R2 and mixing continues increasing. The effect on mixing of the tributary lateral inertia increases with R_m, and, as a result, the density contrast between the two sources of water $\Delta\rho/\rho_0$, and thus F_b, decreases more rapidly downstream with increasing R_m (Figure 3.10a and Figure 3.10b). Once in reach R3, the interplay between F_b and F_c (Figure 3.10b-d) pushes the mixing interface to tilt toward the left bank for negatively buoyant side inflows. A weaker F_b explains why for R_q = 1.53 the interface did not become horizontal within reach R3.

As R_m increases, the influence on mixing of the dynamics of the dead zone decreases. See, for example, that σ remains equal to ca. 30 ppm within reach R2 for $\Delta\rho/\rho_0$ = 0 and R_m = 4.58 in Figure 3.9c. This is the result of the mixing interface between rivers moving laterally toward the bank opposite to the tributary bank (where the dead zone is

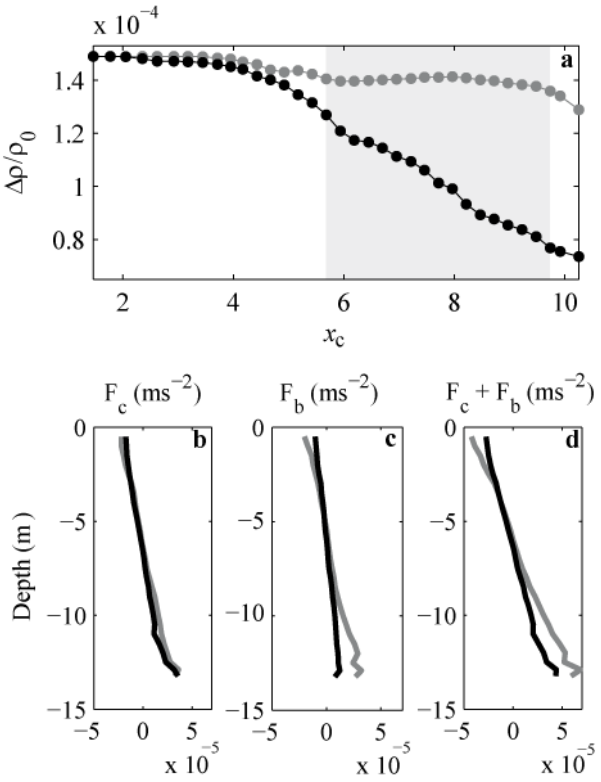

Figure 3.10 (a) Variation with distance downstream of the time-averaged density contrast between the Ebro and Segre rivers, and time- and width-averaged (b) centrifugal forcing F_c, (c) baroclinic forcing F_b, and (d) $F_c + F_b$ at section B35 (x_c = 10.3) for runs M5 (gray line) and m5 (black line). The shaded area in (a) shows sections within reach R2.

located) as R_m increases (Figure 3.6), so that it moves farther away from the shear layer that forms between the mainstream and the dead zone (Figure 3.3 and Figure 3.5). The interaction between the mixing interface and the dead zone will be then dependent on the mechanisms forcing the distortion of the mixing layer (here, the baroclinic forcing) which brings them closer again (Figure 3.6c, Figure 3.6g, and Figure 3.6k).

3.5 Summary and Conclusions

The effect of weak density contrasts on mixing rates between two rivers of asymmetrical confluence and meandering planform were analyzed with a three-dimensional model. Mixing rates under weak density contrast of up to O (10^{-1}) kg m^{-3}, typical of large river confluences, were up to 40% larger than those simulated under neutrally buoyant conditions. This increase in mixing is largely the result of density contrasts leading to changes in the contact area between water masses available for

mixing. Stronger density contrasts, which might lead to nearly horizontal contact areas shortly downstream of the confluence, will lead to weaker mixing rates compared to weakly buoyant conditions, as a result of the stabilizing effect of strong vertical density gradients. As shown through unsteady simulations, even weak time-varying density differences, driven by diurnal changes in inflow temperatures, could lead to significant changes in mixing rates between the confluent rivers depending on the time of the day.

The distortion of the mixing layer is largely controlled by the strength of the cross-stream motions, which, in turn, is driven by a subtle interaction between baroclinic and centrifugal forces. The first is associated with the magnitude and sign of the density contrasts; the second, with the magnitude and sign of the curvature. In our study site, with the channel veering to the left downstream of the confluence, centrifugal forcing increases the distortion of the mixing layer induced by positively buoyant side inflows, but, tends to diminish the tilting of the interface that results from negatively buoyant inflows. Hence, as a result of the channel geometry, mixing rates at river confluences could respond differently depending on whether the side inflows are negatively buoyant or positively buoyant. As the side-inflow inertia increases, the mixing interface moves closer to the bank opposite to the side inflow and mixing increases immediately downstream of the confluence, favoring the development of horizontal mixing layers for weakly density contrasts. These results, in general, strongly suggest that density differences between confluent rivers, even though weak, have a strong impact on mixing rates and patterns at large river confluences.

Mixing ratios also oscillated in time as a result of large-scale coherent vortices developing (a) in the shear layer between the two river sources near the confluence and (b) in a dead zone sited shortly downstream. The dead zone, though, appears ― under the conditions observed in the field―as the site where mixing is more energetic. Changes in standard deviations of 0.01 ppm m^{-1} were found in the dead zone, almost twice the rates observed in other reaches. This suggests that the existence of channel irregularities near confluences leading to the development of dead zones might accelerate the rate at which water masses mix downstream of river junctions. The contribution of side irregularities to mixing, though, will depend on whether the mixing interface between the confluent rivers becomes close or not to the shear layer generated at those sites. This, in turn, will depend on (1) the momentun ratio between the confluent rivers, which determines the position of

the vertical mixing interface to the tributary bank, under neutrally buoyant conditions, and (2) the forces controlling the tilting of the interface.

Chapter 4

The influence of flow inertia, buoyancy, wind, and flow unsteadiness on mixing at the asymmetrical confluence of two large rivers

Under review in *J. Hydrol.*

Abstract

The rates and patterns of mixing of two large rivers with large density differences at a strongly asymmetrical confluence in northern Spain are analyzed. We assess the factors controlling the site where the denser river plunges and the mixing rates between the rivers. In particular, we focus on the interaction between inertial and buoyancy forces, the effect of wind forcing and the unsteady nature of the hydraulic forcing. The steady-state location of the plunge line is shown to be controlled by an inertia-buoyancy balance, which accounts for the relative magnitude of the buoyancy forcing associated to density differences between the confluent rivers, and the magnitudes of both the main-stream and the side-flow (tributary) inertia. The plunge line moves to upstream locations as the inertia of the tributary increases (for low tributary inertia) and/or the density contrast between the rivers increases. This has important consequences for river mixing since mixing rates increase as the plunging occurs at the confluence. The high mixing rates in this case occur as a result of a large mixing interface surface and high diffusivities. As the plunge moves upstream or downstream of the confluence, vertical diffusivities or the area of contact available for mixing decrease and constrain mixing rates. Wind forcing, depending on its velocity and direction, affects mixing rates through (1) altering the buoyancy-inertia equilibrium and so changing the location of the plunge line, (2) altering the pattern of secondary circulation within the confluence and/or (3) increasing shear at the confluence. Flow unsteadiness can lead to changes in the location of the plunge line through time and thus can strongly modify mixing rates at the confluence. The downstream movement of the plunge line is advection dominated, while its upstream movement seems to respond to a baroclinic response of the confluence.

4.1 Introduction

The strongest physical and chemical gradients in river networks occur in river confluences, where two rivers draining different watersheds merge [*Bigelow et al.*, 2007; *Gooseff et al.*, 2008; *Kiffney et al.*, 2006]. A wide range of environmental conditions for growth occur at those sites, leading to species-rich biological communities, with a number of species that tends to be larger than elsewhere in the river network [*Benda et al.*, 2004; *Rice et al.*, 2006]. The persistence downstream of heterogeneous habitat conditions largely depends on the rate of mixing between the confluent flows and on the spatial arrangement of the flows at and downstream of the confluence, that is, whether rivers flow side by side or one on top of the other. Water from the two confluent rivers will flow side by side if their densities are similar and the rate at which they mix will largely depend on the extent to which the nearly-vertical mixing layer that develops between the confluent rivers distorts, increasing the area of contact between water masses. The distortion of the mixing layer, in turn, may occur as a result of differences in depths between the main channel and the tributary (bed discordance) or channel-scale helical motions, which in general result in significant reductions in mixing lengths [e.g., *Gaudet and Roy*, 1995; *Lane et al.*, 2008; *Rhoads and Kenworthy*, 1995]. The development of two dimensional vortices in the shear layer between the confluent rivers have also been shown to increase mixing rates between the water masses but their effect on river mixing could be rather limited [*Konsoer and Rhoads*, 2014; *Lane et al.*, 2008]. Very recently *Ramón et al.* [2014] (Chapter 3) also argued that weak density differences between the confluent rivers may lead to larger distortion rates of the mixing interface, hence larger contact areas between rivers and enhanced mixing rates.

Most studies published in the literature on river confluences have been conducted under homogeneous or weakly stratified conditions. Few studies, however, have focused on confluences of rivers with strong density contrasts. Under those conditions, the denser river will plunge and flow below the less dense river and the interface separating the confluent rivers will tend to become nearly horizontal downstream of the plunge point [*Cook et al.*, 2006; *Ramón et al.*, 2013 (Chapter 2); *Lyubimova et al*., 2014]. *Lyubimova et al.* [2014] further observed that the position on the water surface where the denser flow actually plunges (plunge point) could be upstream of the confluence under strongly buoyant conditions, and low flow rates along the main river. The behavior of plunging

flows has been thoroughly studied in long, narrow, straight and quiescent basins with simple geometries, using laboratory experiments [e.g., *Wells and Wettlaufer*, 2007; *Wells and Nadarajah*, 2009 and references therein; *Sequeiros et al*., 2010; *Cortés et al.*, 2014], numerical simulations [e.g., *Chung and Gu*, 1998; *Bournet et al*., 1999; *Kassem et al.*, 2003] and analysis of field data [e.g., *Hebbert et al.*, 1979; *Fischer and Smith*, 1983; *Dallimore et al*., 2001; *Arneborg et al.*, 2007]. The behavior of the buoyant river inflows can be interpreted as the interplay between the inertia of the river inflow and buoyancy forces, associated with the density differences between the inflow and the stagnant water in the basin. Hence, it can be parameterized in terms of the internal Froude number, $Fr_i = U/(g'D)^{1/2}$ where, U represents the inflow velocity, D the depth of the channel and g' (= $g\,\Delta\rho/\rho_0$), the reduced gravity calculated from the density differences between lake and river water and a reference density ρ_0. Upstream of the plunge/lift point it is assumed that motion is dominated by inertial forces and $Fr_i >> 1$. Downstream, in turn, buoyancy forces dominate the motion and $Fr_i << 1$. At the plunge/lift point Fr_i is O (1), and most expressions proposed to determine the location of the plunge/lift points are based on this condition. Similar arguments can be used to analyze the behavior of confluent rivers with strong buoyancy differences. Side-flow inertia and the basin geometry, however, need to be also taken into account in determining the site of the plunging and the shape of the mixing interface in river confluences. The role of side-flow inertia and, in general, the behavior of river confluences under strong density contrasts have not been studied in detail before in the literature.

Our general goal is to understand the factors that control the spatial arrangement of water masses and mixing rates across the contact interface, in river confluences under strong density contrasts. To that end, we conduct simulations of hydrodynamic and transport processes occurring in a confluence in Northern Spain where the Ebro (hereon, Western W- or main River) and Segre rivers (Northern N-River or tributary) merge with a strong asymmetry, i.e. a nearly 90º junction angle [*Ramón et al.*, 2013] (Chapter 2). The flow rates along the main river are regulated by a dam constructed ≈ 2.5 km upstream of the junction apex (Figure 4.1a), which could result in high fluctuations in the W-inflow rates throughout the day, following hydro-power generation rules (e.g., Figure 4.1b-c). The W-River is denser than the N-River during most times of the year (up to 63% of the time in the stratification period, from June to November, and 79% when considering the whole year, based on the analysis of available historical data). Hence, here we focus on

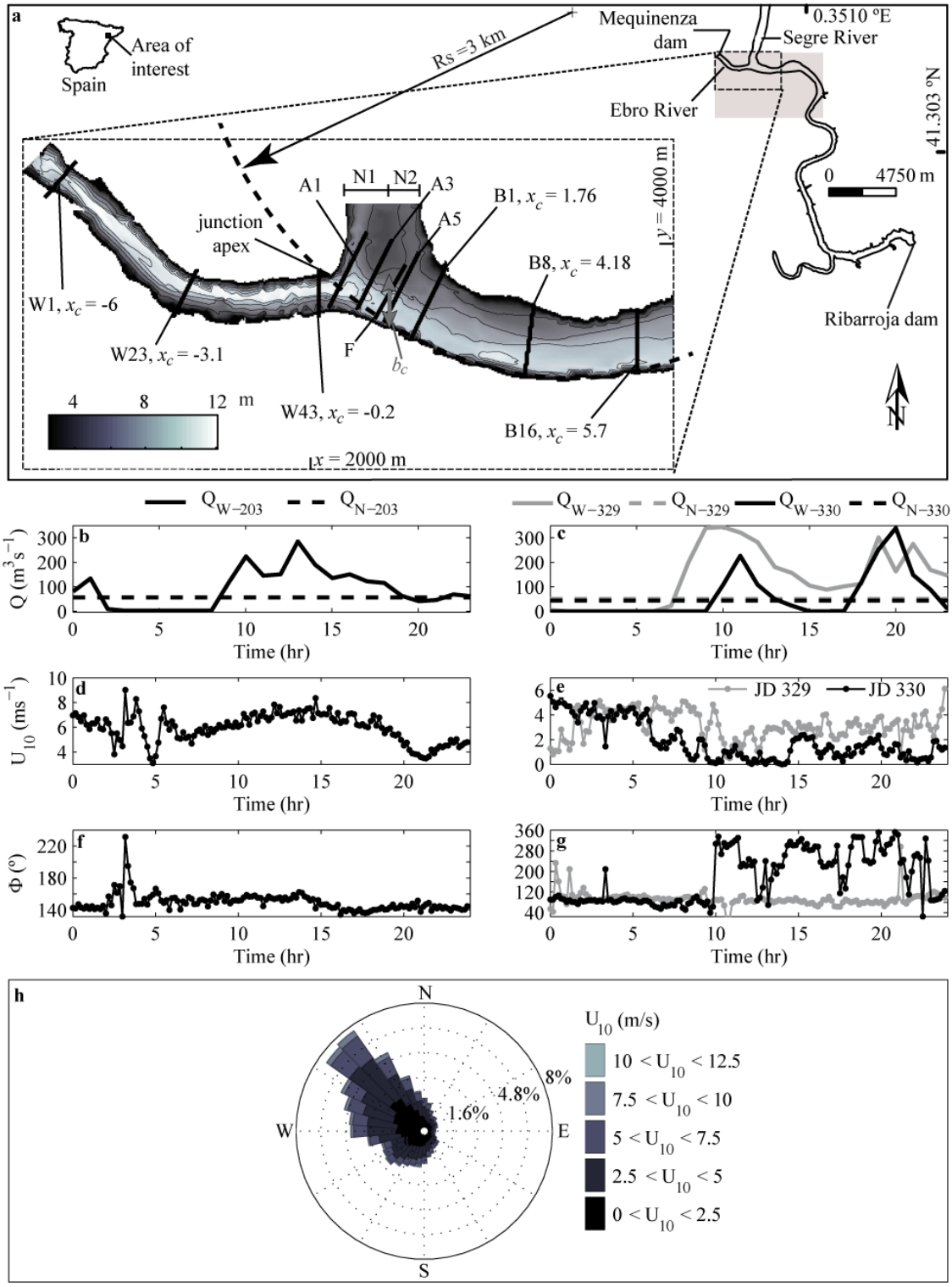

Figure 4.1 (a) The Ribarroja reservoir, model domain (shaded gray area) and bathymetry of the region of interest (rectangle). The location is shown for the N-River inflow sections (N1 and N2), three of the W sections in the W-channel, three of the A-sections, one of the ADCP transect collected in the field on day 329 (transect F) at the confluence region, and three of the B sections downstream of the confluence. (b, c) Inflow rates from the W- and N- rivers, and hourly-averaged (d-e) wind velocities and (f, g) directions on (b, d, f) day 203 and (c, e, g) days 329-330 in 2009. (h) Wind rose for the whole year 2009 at the Ribarroja reservoir. The wind rose in (h) shows directions the wind was blowing towards.

the analysis of the spatial arrangement of the rivers when the main river is denser than the tributary. We hypothesize that the mixing rates and the spatial arrangement of the two rivers at the confluence under steady forcing, whether the confluence appears stratified or not, depends on whether the denser main river plunges upstream or downstream of the confluence. This, in turn, is controlled by (1) the ratio of inertial forces between the confluent rivers, which can be parameterized in terms of the ratio between the tributary to the main velocities R_u (= U_N/U_W), and (2) the ratio of the buoyancy of the tributary and the magnitude of the inertial forces along the main channel, which can be parameterized in terms of a confluence internal Froude number Fr_{ic} (=$U_W/(g'D)^{0.5}$). Here, U_N and U_W are the inflow velocities in the tributary and the main stream, respectively, and the reduced gravity g' (= $g\ (\rho_W - \rho_N)/\rho_0 = g\ \Delta\rho/\rho_0$) is calculated from the density difference between the two rivers and a reference density ρ_0 (= 1000 kg m^{-3}). Although the discharge ratio R_q (= Q_N/Q_W) and the momentum flux ratio R_m (= $[U_N\ Q_N\ \rho_N]\ /\ [U_W\ Q_W\ \rho_W]$) are commonly used as a metric for the bulk inertial forces of confluent flows, in this study R_u corresponds directly (same order of magnitude) to R_q, and it was chosen over R_q to be consistent with the parameterization of inertial forces given by the Froude number. Other factors that may control the spatial arrangement, and, hence, mixing rates observed at a given time at the confluence include: the time-varying nature of the inflow rates along the main river and wind forcing. In their analysis of data from their field experiments, *Ramón et al.* [2013] (Chapter 2) suggested that the strong southeasterly winds that blew during the stratification period were playing an important role in the spatial arrangement of the W- and N-rivers at their confluence. To the extent of our knowledge, these effects have not been analyzed previously in the literature.

4.2 Study site

The Ribarroja reservoir (41º18' N, 0º21' E) is the second of a chain of three reservoirs (Mequinenza-Ribarroja-Flix) constructed along the lower reaches of the W-River for hydroelectric power generation. The reservoir has an elongated and meandering shape (Figure 4.1a), with an average depth of 9.8 m, reaching values of up to 34 m near the dam. The system is strongly regulated (Inflows and outflows) so that the free surface elevation is kept at a nearly constant value of ≈ 69 m above sea level throughout the year. The residence time of the water in the reservoir is low and never exceeds one month even during the lowest through-flows typically observed in summer [*Cruzado et al.*, 2002].

The two largest inflows to the reservoir are the W- and N- rivers, which merge at a near 90º junction angle at the NW end of the reservoir. The confluence is characterized by its curved planform which bends to the left with a radius of curvature R_s of ≈ 3 km, almost 7 times the channel-width b_p (≈ 400 m) downstream of the confluence, $R_s/b_p \approx 7.5$ (Figure 4.1a). Depths of the W- and N- rivers are discordant: the N-River enters the confluence through two channels of depths D of 4 m and 2 m, respectively, while depths encountered at the W-River are of ≈ 10 m.

4.3 Methods

4.3.1 Computational model

Simulations were conducted using a parallel version [*Acosta et al.*, 2010] of a three-dimensional primitive-equation (3D-PE) model, solving the layer-averaged form of the shallow water equations [*Smith*, 2006]. The momentum equations are solved on a staggered Cartesian grid, using an efficient second-order accurate, space-centered, semi-implicit and three-level iterative leapfrog-trapezoidal finite difference scheme. Non-active- (i.e. tracers) and active-scalar transport equations were solved using a two-level semi-implicit scheme, in which only vertical diffusion is discretized implicitly. The advection terms in the transport equation for active and non-active scalars are discretized with a second-order accurate flux-limiting scheme [e.g., *Durran*, 1999]. Turbulent mixing is represented in the 3D-PE model using diffusion-like terms. A Laplacian operator with constant mixing coefficients (K_h) is used to represent the unresolved horizontal turbulent mixing of momentum and scalars. Vertical eddy coefficients of mixing K_z are calculated using a two-equation model originally proposed by *Mellor and Yamada* [1974] and later modified by *Kantha and Clayson* [1994]. This turbulent modeling approach is typically used in large scale models of river and estuarine flows [e.g., *Morillo et al.*, 2008; *Chua and Fringer*, 2011; *Wang et al.*, 2011; *Gleichauf et al.*, 2014] given the large aspect ratios of their grids and its reduced computational burden. The present implementation of the model follows the formulation of *Gross et al.* [1999], which considers vertical diffusion as the only form of transport.

Our modeling approach is further justified given the need to conduct unsteady simulations of time-varying inflow rates during the stratification period [*Ramón et al.*,

2013; Chapter 2] in a large domain with a reasonable computational cost. Our simulations with a 10-m-resolution grid require O (10^5) computational time steps, which limits the use of full 3D RANS models based on non-hydrostatic equations or the use of more sophisticated modeling approaches such as well-resolved Large Eddy Simulations (LES) [*Rodi*, 2010] or even the hybrid Reynolds-Averaged Navier Stokes (RANS)-LES approach of *Constantinescu et al.* [2011, 2012]. The model has been validated both against analytical solutions and field data sets collected in a variety of lake environments [*Rueda and MacIntyre*, 2010 and references therein] and estuaries [*Llebot et al.*, 2014], and for relevant physical processes occurring in river confluences, including: (1) the development of a shallow mixing layer between two confluent streams, (2) flow past a cavity and (3) flow in open channels of mild curvature with and without stratification [*Ramón et al.*, 2015, Appendix A]. Additional tests (not shown) were conducted to check the ability of the model to represent Kelvin Helmholtz instabilities. These additional tests included simulations of the shallow mixing layers reported by *Chu and Babarutsi* [1988] and *Uijttewaal and Booij* [2000] *Ramón et al.* [2015] (Appendix A) also validated the model results (runs U1-3, Table 4.1) against field data collected at the confluence.

4.3.2 Approach

The model was first used to evaluate our hypothesis of an inertia-buoyancy balance at the Ebro-Segre confluence. A first set of simulations (A-series in Table 4.1) were conducted under steady hydraulic and buoyancy forcing. The forcing conditions correspond to a range of values for the river velocity ratio R_u and confluence internal Froude number Fr_{ic} that can potentially occur at the confluence during the stratification period (Figure 4.2). Modeled velocities were then applied to simulate the transport of a tracer injected in the domain through the W-River. The time-averaged spatial arrangement of the confluent rivers, the location of the plunge line (the region at surface where the denser W-River plunges below the N-River) and mixing rates were analyzed. A subset of the simulations included in the A-series corresponds to the daily-averaged forcing conditions observed under stratified conditions in 2009 [*Ramón et al.*, 2013; Chapter 2]. This subset is referred to as S-runs in Table 4.1. These simulations were re-run but subject, this time, to different wind speeds and directions (SW-runs in Table 4.1), to analyze the interaction of wind forcing, R_u and Fr_{ic} in determining the spatial

arrangement of the rivers and their mixing rates at the confluence. A final set of simulations was conducted subject to the time

Table 4.1 Model inputs for the simulation runs

Run case	JD[(a)]	$\Delta\rho/\rho_0$	Q_W (m^3/s)	Q_N (m^3/s)	R_u	R_q	R_m	Fr_{ic}	U_{10} (m/s)	Φ [(b)] (º)
A-series	-	1.01×10^{-4}, 1.4×10^{-3} or 4.7×10^{-3}	34 to 351	6 to 944	0.15 to 18	0.1 to 11.8	0.015 to 213	0.04 to 2	0	-
	Runs with steady flows:									
S1	203	1.4×10^{-3}	86	57	1.02	0.58	0.67	0.13	0	-
S2	329	1.01×10^{-4}	138	51	0.57	0.37	0.21	0.79	0	-
S3	330	7×10^{-5}	61	43.5	1.09	0.71	0.78	0.42	0	-
	Runs with steady flows and constant wind forcing:									
SW1	203	1.4×10^{-3}	86	57	1.02	0.58	0.67	0.13	6	0
SW2	203	1.4×10^{-3}	86	57	1.02	0.58	0.67	0.13	6	90
SW3	203	1.4×10^{-3}	86	57	1.02	0.58	0.67	0.13	6	135
SW4	203	1.4×10^{-3}	86	57	1.02	0.58	0.67	0.13	6	180
SW5	203	1.4×10^{-3}	86	57	1.02	0.58	0.67	0.13	6	270
SW6	203	1.4×10^{-3}	86	57	1.02	0.58	0.67	0.13	12	0
SW7	203	1.4×10^{-3}	86	57	1.02	0.58	0.67	0.13	12	90
SW8	203	1.4×10^{-3}	86	57	1.02	0.58	0.67	0.13	12	135
SW9	203	1.4×10^{-3}	86	57	1.02	0.58	0.67	0.13	12	180
SW10	203	1.4×10^{-3}	86	57	1.02	0.58	0.67	0.13	12	270
SW11	329	1.01×10^{-4}	138	51	0.57	0.37	0.21	0.79	6	0
SW12	329	1.01×10^{-4}	138	51	0.57	0.37	0.21	0.79	6	90
SW13	329	1.01×10^{-4}	138	51	0.57	0.37	0.21	0.79	6	135
SW14	329	1.01×10^{-4}	138	51	0.57	0.37	0.21	0.79	6	180
SW15	329	1.01×10^{-4}	138	51	0.57	0.37	0.21	0.79	6	270
SW16	329	1.01×10^{-4}	138	51	0.57	0.37	0.21	0.79	12	0
SW17	329	1.01×10^{-4}	138	51	0.57	0.37	0.21	0.79	12	90
SW18	329	1.01×10^{-4}	138	51	0.57	0.37	0.21	0.79	12	135
SW19	329	1.01×10^{-4}	138	51	0.57	0.37	0.21	0.79	12	180
SW20	329	1.01×10^{-4}	138	51	0.57	0.37	0.21	0.79	12	270
	Runs with unsteady flows and wind forcing (field conditions):									
U1	203	1.4×10^{-3}	0-288	57	f (t)[(c)]	f (t)	f (t)	f (t)	f (t)	f (t)
U2	329	1.01×10^{-4}	0-344	51	f (t)	f (t)	f (t)	f (t)	f (t)	f (t)
U3	330	7×10^{-5}	0-340	43.5	f (t)	f (t)	f (t)	f (t)	f (t)	f (t)

[(a)] JD = Julian day.

[(b)] 0^o = northerly winds.

[(c)] f (t) = values are variable in time.

varying flow rates and wind forcing (U-runs in Table 4.1) observed in 2009 [*Ramón et al.*, 2013; Chapter 2] (Figure 4.1b-g). The results of these runs focus on the effect of unsteadiness in the hydraulic forcing on the relevant time scales of response (location of the plunge point) of the system.

4.3.3 Transport and mixing model of the the Ribarroja reservoir

Our computational domain extends from the Mequinenza dam to a section ≈ 8 km downstream of the junction apex (shaded gray area in Figure 4.1a) along the W-River, and approximately 500 m upstream of the confluence along the N-River. Our study area, however, is shorter and extends only 2.3 km downstream of the junction apex (Figure 4.1a). The N-boundary was placed 1 km upstream of the confluence. The lake geometry was discretized using grid cells of size (Δx, Δy, Δz) = (10, 10, 0.5) meters in x- y- and z-directions, respectively. For stability purposes, the time step Δt was set to 3 s in all but in the SW- runs, for which Δt = 2 s. The bottom drag coefficient, C_d, was set to 0.003 as proposed by *Smith* [2006]. The reservoir was assumed initially at rest with a uniform density, equal to the averaged density of the W- and N- rivers. At the downstream end, the free surface elevation was fixed, with densities and tracer concentrations having zero gradients. Inflow rates at the upstream boundaries, in turn, were changed depending on the simulation series, and either set to conform to the field data of *Ramón et al*. [2013] (Chapter 2), or to constant values representing a range of density and momentum conditions. N-inflows were assumed to occur through two sections (Figure 4.1) with different velocities, as observed in the field. Almost 2/3 of the total inflow rate from the N-River was presumed to enter through the main channel and the remaining through the secondary channel. Inflow rates in the W-River were distributed uniformly in the inflow section. All inflow densities were set to be constant in time (Table 4.1).

The model was set to run using two trapezoidal iterations after the initial non-smoothed leapfrog predictive step, and the superbee limiter [*Roe*, 1984] in the solution of the scalar transport equation. Other flux-limiters tested [*van Leer*, 1974] yielded similar results. With approximately 40 grid cells across the channel, and almost 20 cells in depth, mixing and dispersive processes scaling with the channel dimensions are well resolved, and the sub-grid scale mixing to parameterize is mainly the turbulent diffusion. Based on a large set of experiments in rivers, *Fischer et al.* [1979] argued that the non-dimensional transverse mixing coefficient ε_t/Du^*(= K_h/ Du^*) should be approximately 0.15 with an

error bound of ± 50%, u^* being the shear velocity (= $u_s C_d^{0.5}$). For average post-confluence streamwise velocities u_s ranging from 0.03 to 0.45 m s^{-1}, as encountered in the simulations and D = 10 m, K_h could range from O (10^{-3}) to O (10^{-2}) m^2 s^{-1}. Even lower values, of O (10^{-4}) m^2 s^{-1} and zero, were used by *Wang et al.* [2011] or *Chua and Fringer* [2011] in their simulations of the Snohomish River estuary, and North San Francisco Bay, respectively, and justified based on the high numerical diffusion of their advective scheme. In our simulations, with a non-diffusive advective algorithm, the horizontal mixing coefficient K_h was still set to 10^{-5} m^2 s^{-1}, but, additional runs were conducted with K_h up to 10^{-1} m^2 s^{-1}, to check the sensitivity of our results to this parameter.

Given that the 3D-PE model is hydrostatic, and, being the grid aspect ratio $\Delta z/\Delta x$ of O (10^{-2}), hence, $\Delta z/\Delta x << 1$, non-hydrostatic flow features will not be resolved. The importance of the non-hydrostatic pressure effects in a given flow can be assessed, as pointed by *Wang et al.* [2009], by considering the ratio β of the scales for the vertical and horizontal variability of the flow. For features with β ≈ O (1), those effects are significant and should not be neglected. For those with $\beta^2 << 1$, non-hydrostatic effects can be safely ignored. The latter is the case of the secondary circulation that develops at the confluence, which has length scales ranging from ≈125 m to the channel width b_p and a vertical scale equal to the depth of the channel D, and for which β^2 is of O (10^{-3}-10^{-4}), i.e. $\beta^2 << 1$. The role of these largely-hydrostatic features in controlling river mixing in confluences is well documented in the literature [see, for example, *Rhoads and Kenworthy*, 1995, 1998; *Rhoads and Sukhodolov*, 2001]. The influence of non-hydrostatic flow phenomena, in turn, remains largely unexplored, and an open question. Hence, the 3D-PE model should provide, at least to first order, a reasonable representation of flow and mixing at the confluence.

A total of 74 simulations were run in the A-series (Table 4.1), with values of R_u and Fr_{ic} encompassing conditions observed at the confluence under the stratified conditions in 2009 [*Ramón et al.*, 2013; Chapter 2] and other years (Figure 4.2). River density contrasts $\Delta\rho/\rho_0$ were set equal to those observed in 2009 [*Ramón et al.*, 2013; Chapter 2] and river inflow rates were varied to achieve different values for R_u and Fr_{ic}. For the Fr_{ic} calculations the average depth of the W-River (D = 10 m) was used. Only for the simulations with the lowest Fr_{ic} (≤ 0.08), a fictitious river density contrast of 4.7 ×

10^{-3} was used. In all A-simulations, the density contrast was assumed driven by temperature differences alone.

The particular forcing conditions observed on days 203, 329 and 330 in 2009 [*Ramón et al.*, 2013; Chapter 2] were used to develop boundary and initial conditions for the S-, SW-, and U-runs (Figure 4.1b-g, Table 4.1). The confluence was then stratified, and density contrasts between the rivers were driven by both differences in temperature and salinity/conductivity. On day 203, the density difference was O (10^{-3}) and on days 329 and 330, in turn, $\Delta\rho/\rho_0$ was O (10^{-4}). Inflow rates from the N-River, Q_N, were constant but those from the W-River, Q_W, were variable (Figure 4.1b-c). The daily-averaged R_q, R_u, R_m and Fr_{ic} values on days 203, 329 and 330 are shown in Table 4.1. Winds were moderate in November, but strong, with average speeds of 7 m s^{-1} (Figure 4.1d), and from the SSE-SE on day 203 (Figure 4.1f). In the S-runs (runs S1-3 in Table 4.1) the model was forced using the observed daily-average inflow rates and the observed density differences, until reaching steady-state. In the SW-runs (runs SW1-SW20 in

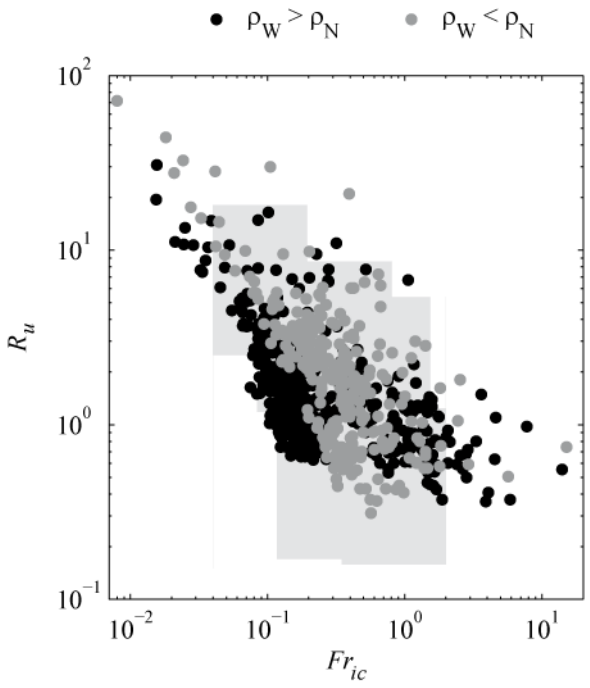

Figure 4.2 Combinations of R_u and Fr_{ic} occurring at the confluence during the stratification period (summer and autumn), calculated from daily-averaged historical discharges, temperatures and conductivities collected at the confluence in 1998, 1999, 2003 and 2004 (for details on the density and flow data from which R_u and Fr_{ic} were calculated, see *Prats et al*. [2010] and *Prats* [2011]). Situations in which the W-River is denser (black dots) than the N-River account for 63% of the time. The shaded area shows the range of R_u and Fr_{ic} values analyzed in the A-series.

Table 4.1), the steady-state simulations on days 203 and 329 were forced with different, but constant, wind speeds U_{10} and directions Φ. A total of 20 simulations were conducted in which we tested the dominant wind direction, as observed in 2009 (southeasterly winds, ≈ 135º, Figure 4.1h); together with 4 ideal winds blowing from each of the four cardinal directions. We also tested two wind speeds: U_{10} = 6 m s^{-1}, which correspond to the 85 percentile of wind velocities in 2009, and U_{10} = 12 m s^{-1}, the largest magnitude observed in 2009 (Figure 4.1h). Finally, in the U-runs (runs U1-U3 in Table 4.1), the model was run subject to unsteady W-inflow rates and wind forcing as observed on days 203, 329 and 330 in 2009.

In any given simulation, the model was run with the same inflow and outflow conditions day after day until at least 99% of the water mass initially existing in the domain had left the computational domain. This length of time was 7 days, on average, and always less than 20 days for the flow rates tested.

4.3.4 Tracer experiments, mixing rates and plunging point

W-water was traced using a constant tracer concentration C_W = 100 ppm. Tracer concentrations downstream, varying from 0 to 100, indicated the percentage of W-water in the mixture, and hence, were used to establish the level of mixing between the W- and N- rivers. Tracer variability was evaluated each 0.25 hours at 16 cross-sections downstream of the confluence (cross-sections B1-B16, Figure 4.1a). The distance between consecutive B-sections was ≈ 120 m. Tracer variability was also evaluated at 43 sections in the W-channel (cross-sections W1-W43, Figure 4.1a), which are ≈ 55 m apart, and at 6 sections within the confluence region (cross-sections A1-A6, Figure 4.1a). We will use the symbol x_c to refer to the distance downstream of the junction apex of each of these cross-sections (W-sections will take negative values), and will be given as a multiple of b_p. We used the standard deviation σ of tracer concentration [*Biron et al.*, 2004; *Ramón et al.*, 2014; Chapter 3] to quantify mixing levels. Standard deviations will tend to decrease downstream of the confluence as a result of mixing (Figure 4.3), and they will become zero when tracer concentrations are uniform in a given cross-section. By contrast, standard deviations > 0 ppm upstream of the confluence in the W-channel, will be indicative of the presence of N-water in the W-channel (Figure 4.3). To compare mixing among simulations and different days, mixing rates, calculated as $\Delta\sigma/s$ =

$(\sigma_i - \sigma_0)/s_i$, and total mixing, calculated as $TM = (1 - \sigma_i/\sigma_0) \times 100$, were evaluated at section i = B16 (Figure 4.1a). Here, s_i and σ_i are the distance downstream of the junction apex and the standard deviation of tracer concentrations at B16, respectively. The expected standard deviation of tracer concentrations if no mixing occurs between the two rivers, is represented by $\sigma_{0,}$ and is calculated from the flow rates and tracer concentrations in each of the rivers similarly to *Lewis and Rhoads* [2015]:

$$\sigma_0 = \left(\frac{Q_W (C_W - C_p)^2 + Q_N (C_N - C_p)^2}{Q_W + Q_N} \right)^{0.5}, \tag{4.1}$$

where C_p is the theoretical concentration after complete mixing [*Gaudet and Roy*, 1995], calculated with the daily-averaged inflow rates as:

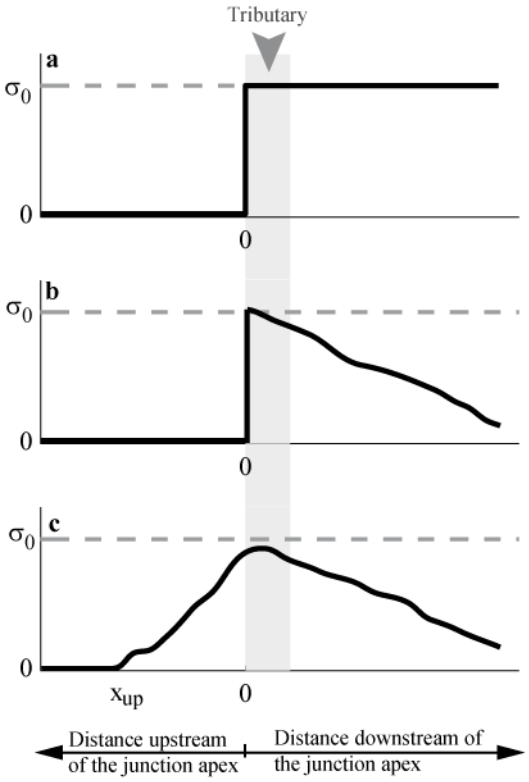

Figure 4.3 Expected shapes of standard deviations of tracer concentration in the streamwise direction if (a) the tributary is not able to flow upstream into the main river channel (σ = 0 ppm at distances < 0) and no mixing occurs between rivers downstream of the junction apex ($\sigma = \sigma_0$ at distances > 0), (b) the tributary is not able to flow upstream into the main river channel but river mixing occurs downstream of the junction apex and (c) some fraction of the tributary is able to flow upstream into the main river channel until distance x_{up} and river mixing occurs downstream of the confluence.

$$C_p = \frac{C_N Q_N + C_W Q_W}{Q_N + Q_W} \tag{4.2}$$

For example, for the values of input tracer concentrations and the daily-averaged inflows used in the model in the S-runs, C_p = 60.13, 73.02 and 58.4 ppm and σ_0 = 48.96, 44.36 and 49.27 ppm on days 203, 329 and 330, respectively. The mixing interface was defined as the set of cells where tracer concentration equals $C_p \pm 10\%$. Cells with C > C_p +10% will be representative of the W-water while cells with $C < C_p - 10\%$ will be representative of the N-water [*Gaudet and Roy*, 1995]. Plunging is assumed complete once the maximum surface concentration at any given point in a cross-section is < C_p + 10%. The distance from the junction apex to this section will be taken as representing the location of the plunge point $x_{c\text{-}PL}$. The plunge line is identified as the group of surface cells where tracer concentrations transition from C ≥ C_p + 10% to C < C_p + 10%.

4.4 Results and Discussion

4.4.1 Plunging and stratification at the confluence

The location of the plunge point is represented in Figure 4.4 (white isolines) for the different values of R_u and Fr_{ic} shown in Table 4.1. For the range of R_u values analyzed, there exists a critical Fr_{ic} value ($Fr_{ic} \approx 0.3$), above which the location of the plunge line is always downstream of the junction apex. For $Fr_{ic} > 0.3$, independently of R_u, buoyancy forces associated with the density differences between the rivers are not strong enough to overcome the inertia of the main stream flow and plunging occurs downstream of the junction apex ($x_{c\text{-}PL} > 0$). For $Fr_{ic} \approx 0.9$ and larger the W-River plunges downstream of the confluence ($x_{c\text{-}PL} > 1.76$). The exact location of the plunge point downstream of the junction apex depends, though, on both R_u and Fr_{ic}. Note, for example, that the plunge point is at the center of the confluence ($x_{c\text{-}PL}$ = 0.93) for $R_u \approx 0.5$ and $Fr_{ic} \approx$ 0.7. As R_u becomes < 0.5 or > 0.5, the plunge point will only remain at the center of the confluence if Fr_{ic} falls below 0.7 (note that the $x_{c\text{-}PL}$ isoline = 0.93 distances from the vertical black line, marking $Fr_{ic} \approx 0.7$, for values of $0.5 < R_u < 0.5$ in Figure 4.4). Thus, for $Fr_{ic} > 0.3$, the plunge point forms at the most upstream location for R_u of 0.5 and it is displaced downstream as R_u increases or decreases from that value (Figure 4.5a-d).

The tendency of the plunge point to move downstream for $R_u << 1$ for a given Fr_{ic} (> 0.3) can be explained in terms of inertial and buoyancy effects at the confluence. As reported earlier in the literature [e.g., *Biron et al*., 1993; *Rhoads and Kenworthy*, 1995, 1998] for neutrally buoyant conditions, the location of the mixing layer moves farther away from the tributary bank as inertial forces in the tributary increase. This is consistent with the location of the mixing layer moving closer to the W-bank as R_u increased from, for example, ≈ 0.15 to ≈ 0.5 for Fr_{ic} ≈ 0.7. By adding a density difference, buoyancy effects sum up to this inertial effect, which allows water from the tributary to reach the opposite bank faster (the plunge point moves upstream) as R_u increases. However, as inertial forces in the tributary keep increasing ($R_u >> 1$ and $R_m >> 1$), inertial effects start controlling the location and orientation of the mixing interface. As tributary inertia

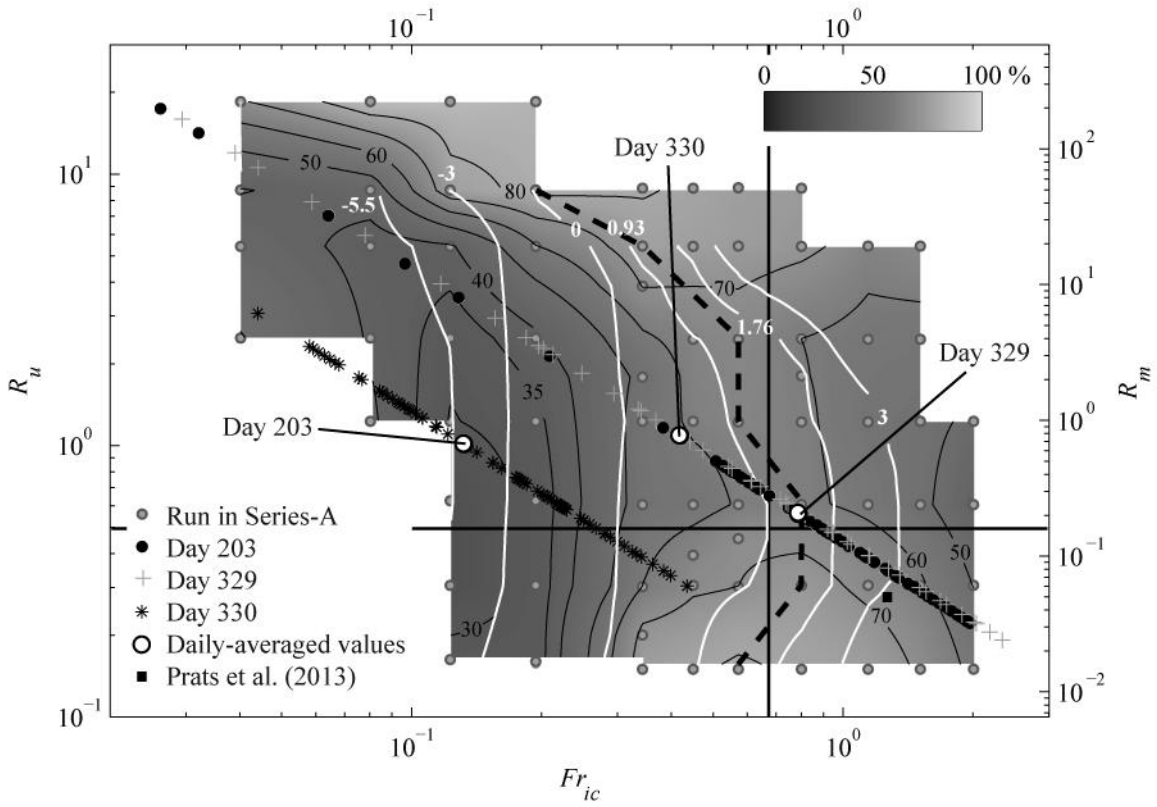

Figure 4.4 Results of the A-series of simulations. Time-averaged linearly-interpolated total mixing *TM* (%) and time-averaged location of the plunge point $x_{c\text{-}PL}$ (white solid isolines) as function of R_u (left *y*-axis) and Fr_{ic}. Gray dots represent the actual values of R_u and Fr_{ic} tested (see Table 4.1). The dashed black line identifies the Fr_{ic} values for which the largest total mixing *TM* occurs for a given R_u. The location is also shown for the daily-averaged (black-encircled white dots) and instant R_u *vs*. Fr_{ic} observed on Julian days 203 (stars), 329 (black dots) and 330 (crosses). Black square shows the daily-averaged conditions observed by *Prats et al.* [2013]. The horizontal and vertical black lines mark R_u values = 0.5 and Fr_{ic} values = 0.67, respectively. For a more complete description, the right *y*-axis show the corresponding values of R_m for a given value of R_u in the left *y*-axis.

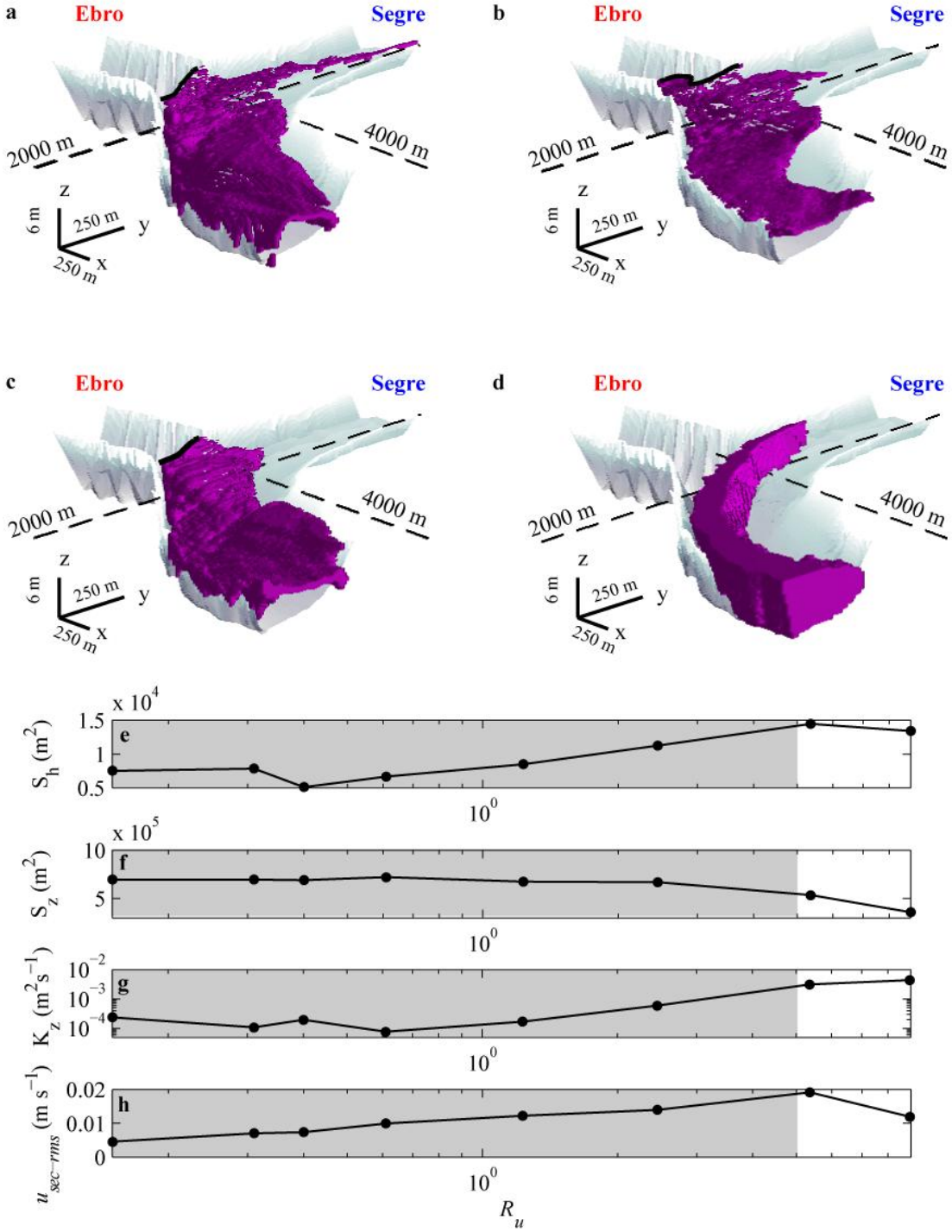

Figure 4.5 (a-d) Time-averaged location of the mixing interface (magenta) between the W-(Ebro) and N-(Segre) rivers, area of the mixing interface available for (e) horizontal S_h and (f) vertical S_z mixing, (g) average value of K_z within the mixing interface, and (h) width-averaged $u_{sec\text{-}rms}$ at section A5. Simulations in the A-series with Fr_{ic} = 0.45 and (a) R_u = 0.15, (b) R_u = 0.4, (c) R_u = 2.5, and (d) R_u = 8.9. Black lines in (a-c) show the location of the plunge line. Gray shaded areas in (e-h) show simulations in which plunging occurs within the confluence. Values of S_h, S_z and Kz are evaluated for the whole extension of the mixing layer within the study reach ($-6 \leq x_c \leq 5.6$). The aspect ratio (x:y:z) in (a-d) is 40:20:1

increases, the increasing rates of turbulent diffusion will tend to keep the tributary flow attached to bed, counteracting buoyancy effects. This tendency results in a shift in the orientation of the mixing interface towards more vertical positions (e.g., Figure 4.5b-d), and thus, in a downstream displacement of the plunge point in Figure 4.4 as R_u increases.

As the mixing layer shifts towards more vertical positions for $R_u >> 1$, lateral shear along this interface increases, and as a result, flow structures similar to Kelvin-Helmholtz (KH) instabilities develop (Figure 4.6), which may contribute to increasing lateral mixing. The occurrence of strong KH structures for both $R_m >> 1$ and $R_m << 1$ is consistent with simulations of other river confluences [*Constantinescu et al.*, 2011, 2012]. It is also consistent with the work of *Prats et al.* [2013], based on the analysis of airborne thermal images, which provided evidence of the occurrence of KH-instabilities at the confluence, under $R_u = 0.28$ ($R_m = 0.05$) and $Fr_{ic} = 1.26$. These conditions are among those simulated to produce Figure 4.4. In those simulations (not shown), the scales and position of the oscillations in the shear layer were similar to those reported by *Prats et al.* [2013].

4.4.2 Mixing rates

River mixing varied with both R_u and Fr_{ic} as shown in Figure 4.4. For any given R_u, Froude numbers for which mixing rates were maximal ($0.6 < Fr_{ic} < 0.8$) tended to coincide with those for which plunging occurred within the downstream half of the confluence ($0.93 < x_{c\text{-}PL} < 1.76$, see the dashed black line in Figure 4.4). Mixing rates decreased away from that range. For $R_u \approx 1$, as Fr_{ic} decreased from O (1) to O (10^{-1}), *TM* dropped from ≈ 60% to 30%. Those changes are largely the result of the increasing density contrasts between the rivers inhibiting vertical mixing across the mixing interface (see Figure 4.7). In the transition of Fr_{ic} from O (1) to O (10^{-1}), the mixing interface between the rivers tended to become horizontal (Figure 4.7d-a). The area available for horizontal mixing S_h decreased from O (10^4) to O (10^3) m^2 (Figure 4.7e). The area of the mixing interface available for vertical mixing S_z, in turn, increased almost one order of magnitude, from O (10^4) to O (10^5) m^2 (Figure 4.7f). But the vertical diffusivities K_z within the mixing layer decreased almost two orders of magnitude from O (10^{-3}) $m^2\,s^{-1}$ to nearly molecular values of O (10^{-5}) $m^2\,s^{-1}$ (Figure 4.7g), as typically reported in stratified flow such as estuarine environments [e.g., *Lung and O'Connor*, 1984]

For $R_u \approx 1$, as Fr_{ic} increased above 0.8, river mixing decreased again (Figure 4.4). The mixing interface in those cases tilts and becomes more vertical and aligned with the axis of the main channel for the largest Fr_{ic} tested (Figure 4.7c and Figure 4.7d). The vertical diffusivities K_z remained constant and of O (10^{-3}) $m^2\ s^{-1}$ (Figure 4.7g). The area for horizontal mixing S_h remained similar as Fr_{ic} increased above 0.8 (Figure 4.7e). The area for vertical mixing S_z and the total area of the mixing interface decreased (Figure 4.7f). Hence, maximal mixing rates occur if plunging occurs at the confluence. If it occurs upstream, river mixing tends to decrease as a result of lower vertical diffusivities. If it occurs downstream, in turn, total mixing decreases as a result of reductions in the areas available for mixing. Mixing rates between rivers, hence, are subject to seasonal changes resulting from changes in the position of the plunge point. On day 203, when the plunge

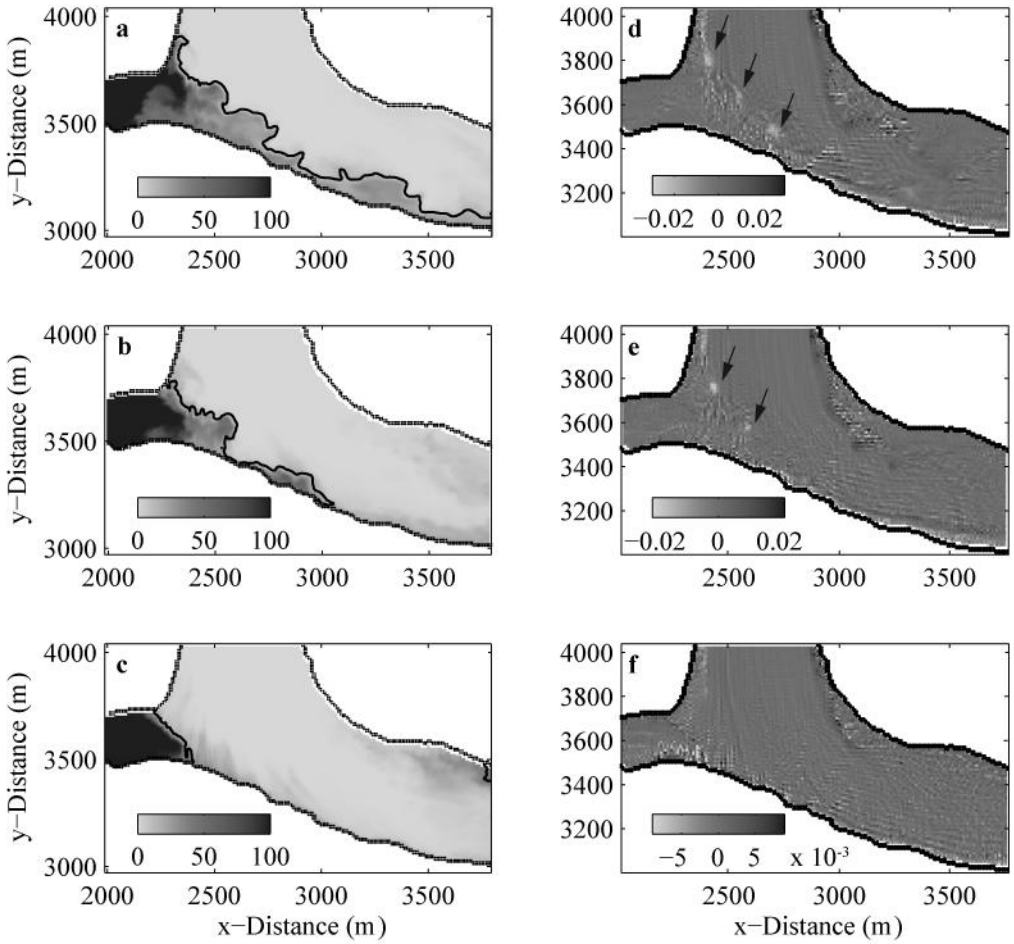

Figure 4.6 Instant values of (a-c) tracer concentrations (ppm) and (d-f) vertical vorticities (s^{-1}) at the surface plane for simulations in the A-series with Fr_{ic} = 0.45 and (a,d) R_u = 8.9, (b,e) R_u = 5.4 and (c,f) R_u = 2.5. Black isolines in (a-c) show tracer concentrations $C = C_p$. Black arrows in (c-d) show the location of eddies within the mixing layer.

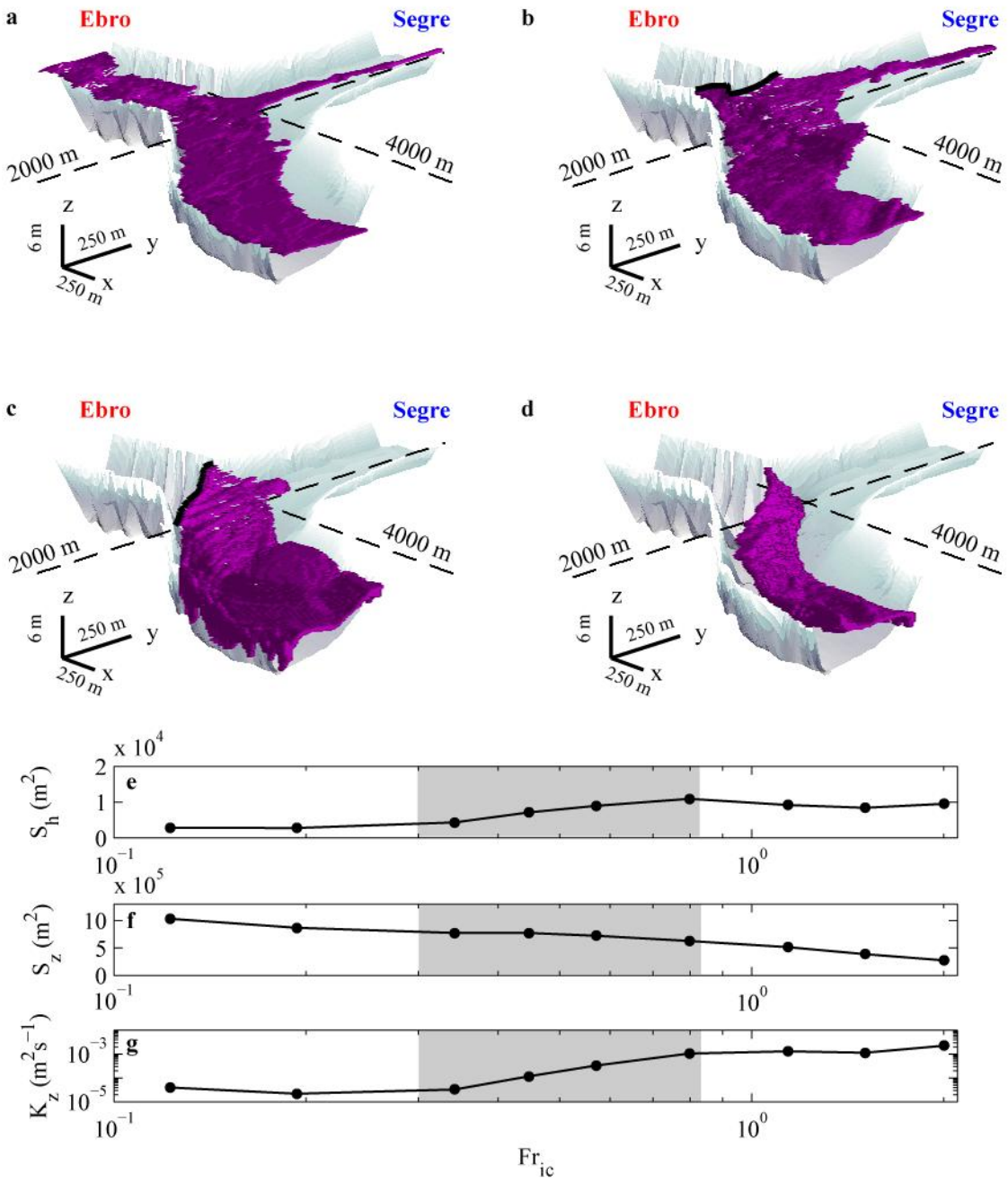

Figure 4.7 (a-d) Time-averaged location of the mixing interface (magenta) between the W-(Ebro) and N-(Segre) rivers, area of the mixing interface available for (e) horizontal S_h and (f) vertical S_z mixing and average value of (g) K_z within the mixing interface for simulations in the A-series with R_u = 1.2 and (a) Fr_{ic} = 0.12, (b) Fr_{ic} = 0.34, (c) Fr_{ic} = 0.80, and (d) Fr_{ic} = 1.5. Black lines in (a-d) show the location of the plunge line. Gray shaded areas in (e-g) show simulations in which plunging occurs within the confluence. Values of S_h, S_z and K_z are evaluated for the whole extension of the mixing layer within the study reach ($-6 \leq x_c \leq 5.6$). The aspect ratio (x:y:z) in (a-d) is 40:20:1

Table 4.2 Absolute values of time-averaged mixing rates and total mixing at x_c = 5.7, location of the plunge point and ratios of time-averaged energy available through stirring and shear within the domain volume between $0 \le x_c \le 5.7$. The presence of hyphens indicates that term has not been evaluated in that simulation.

Run case	Julian day	$\Delta\sigma/s$ (ppm m^{-1})	*TM* (%)	$x_{c\text{-}PL}$	$R_{sk\text{-}s}$ [a,b] (%)	$R_{sk\text{-}sk0}$ [c]	$R_{s\text{-}s0}$ [d]
S1	203	6.2×10^{-3}	29.0	−5.35	1	-	-
S2	329	1.2×10^{-2}	64.0	1.52	28	-	-
S3	330	1.4×10^{-2}	66.4	0.89	11	-	-
SW1	203	1.0×10^{-2}	46.8	−1.23	1	3.4	4.4
SW2	203	1.7×10^{-2}	80.9	−5.40	2	7.8	6.0
SW3	203	1.6×10^{-2}	72.0	−5.29	3	12.6	4.8
SW4	203	8.8×10^{-3}	41.1	−2.10	10	19.9	2.5
SW5	203	1.3×10^{-2}	61.8	1.27	14	71.5	6.3
SW6	203	2.0×10^{-2}	91.9	1.14	3	49.8	17.7
SW7	203	2.1×10^{-2}	99.2	−1.60	5	119.8	27.6
SW8	203	2.1×10^{-2}	95.6	−1.48	1	12.6	27.8
SW9	203	1.6×10^{-2}	71.9	−1.48	13	144.5	13.3
SW10	203	1.8×10^{-2}	82.1	5.64	7	130.6	21.7
SW11	329	1.6×10^{-2}	84.1	3.02	25	5.91	4.6
SW12	329	1.8×10^{-2}	93.1	1.15	15	4.81	6.3
SW13	329	1.9×10^{-2}	95.5	0.89	11	2.90	5.3
SW14	329	7.3×10^{-3}	37.3	>5.7	0	0.02	2.7
SW15	329	9.8×10^{-3}	50.5	>5.7	19	3.8	3.9
SW16	329	1.5×10^{-2}	78.2	5.27	12	12.3	20.0
SW17	329	1.9×10^{-2}	97.8	1.02	2	3.73	46.3
SW18	329	1.9×10^{-2}	95.9	1.40	6	15.2	49.6
SW19	329	1.7×10^{-2}	88.9	>5.7	4	3.6	18.6
SW20	329	7.7×10^{-3}	39.7	>5.7	7	7.0	20.4
U1	203	1.4×10^{-2}	65.5	-	-	-	-
U2	329	1.5×10^{-2}	79.1	-	-	-	-
U3	330	1.6×10^{-2}	72.8	-	-	-	-

[a] V = volume of the domain downstream of $x_c > 0$, ‹› = time-averaged values.

[c] $R_{sk\text{-}s} = \sum_V \langle \rho P_{sk} \rangle \Big/ \sum_V \langle \rho P_s \rangle \times 100$

[d] $R_{sk\text{-}sk0} = \sum_V \langle \rho P_{sk} \rangle \Big/ \sum_V \langle \rho P_{sk} \rangle_{U10=0}$, where the subscript "U_{10}=0" refers to the steady simulation without wind forcing (here S1 or S2)

[e] $R_{s\text{-}s0} = \sum_V \langle \rho P_s \rangle \Big/ \sum_V \langle \rho P_s \rangle_{U10=0}$

line under steady state was located upstream of the confluence (Figure 4.4 and *Ramón et al.* [2013]; Chapter 2), mixing rates were O (10^{-3}) ppm m^{-1} (and $TM \approx 29\%$), one order of magnitude lower than mixing rates on days 329 and 330 ($TM > 50\%$) (runs S1-3 in Table 4.2), when the plunge line was located at the confluence region.

For any given value of the Froude number, Fr_{ic}, total mixing was minimal for R_u of ≈ O (1), increasing both as R_u becomes larger or lower than O (1). Larger mixing rates for larger velocity ratios ($R_u >> 1$) could be the result of high tributary inertia leading to wide and nearly vertical mixing interfaces where strong KH structures develop (e.g., Figure 4.5d and Figure 4.6). Mixing in those cases is energetic, with *TM* being larger than 70% for $R_u >> 1$ and all Fr_{ic} tested (Figure 4.4). Note that, the mixing layer in Figure 4.5d even attached to the W-bank within the study reach. However, *TM* also increased with R_u in our simulations with $K_h = 10^{-1}$ m^2 s, for which KH billows are inhibited, which suggests that another mechanisms could be at play. Past work has shown that the secondary circulation at river confluences typically consists of two counter-rotating cells, which converge near the surface towards the mixing layer and diverge towards the river banks near the bed [e.g., *Ashmore et al.*, 1992; *Rhoads and Kenworthy*, 1995, 1998; *Rhoads*, 1996; *Rhoads and Sukhodolov*, 2001]. Depending on factors such as the momentum ratio, the junction planform or the junction angle [*Rhoads and Kenworthy*, 1998; *Bradbrook et al*., 2000], one of the cells can dominate over the other and even occupy the whole channel. *Lewis and Rhoads* [2015] argued that mixing rates could increase with R_m as the result of the increasing dominance of the tributary cell. In the A-series, for $Fr_{ic} = 0.45$, for example, the high junction angle together with a positively buoyant tributary produces a secondary circulation which is already dominated by the tributary cell at the confluence, even for the lowest R_u (R_m) tested. As R_u (R_m) increases the strength of the secondary circulation also increases, which is parameterized in Figure 4.5h as the Root Mean Square of the width-averaged secondary velocity $u_{sec\text{-}rms}$ at section A5 (Figure 4.1a). The secondary velocity was calculated with the Rozovskii method [*Rozovskii*, 1961; *Parsons et al.*, 2013]. An increase in the strength of the secondary circulation at the confluence could be then also responsible for an increase in river mixing as $R_u >> 1$.

The larger mixing rates observed for lower velocity ratios as $R_u << 1$ (see *TM* values for $R_u < 0.4$ and $0.3 < Fr_{ic} < 1.2$ in Figure 4.4) are likely the results of the limited vertical extent of the upper layer carrying N-water at the confluence under those

conditions. As the velocity ratio decreases, the discharge ratio, and hence, the thickness of the N-layer in the water column also decreases. The distance downstream of the confluence where a layer of limited extent initially occupying the top of the water column becomes fully mixed L_{Mz} can be estimated as $L_{Mz} \approx \langle u_s \rangle H^2/K_z$, in terms of the average streamwise velocity $\langle u_s \rangle$, vertical diffusivity K_z and the layer depth H [e.g., *Rutherford*, 1994]. The streamwise velocity at the confluence for $R_u << 1$ is largely dictated by the inflow velocity of the main river U_W. For $R_u << 1$, K_z also remained almost unchanged (see Figure 4.5 for $R_u < 0.61$). Hence, L_{Mz} decreased as discharge ratios decreased, and hence, as the thickness of the N-layer decreased, leading to higher *TM*s for the lowest R_u analyzed.

4.4.3 Wind driven changes

The mechanical energy introduced in the water column by wind forcing acting on the air-water interface alters the large-scale flow field and the turbulent kinetic energy TKE balance, hence, changing mixing rates and the spatial arrangement of the river masses at the confluence. This effect, in turn, is likely to vary depending on the wind direction. Although the winds in Ribarroja are predominantly from the South-East and against the flow in the W-River (Figure 4.1a), here, and for the sake of completeness, we analyze the effect of wind forcing, in the four cardinal directions. We further consider two different scenarios with the hydraulic conditions prevailing on days 203 and 329, with strong- and moderate- buoyancy differences between the rivers. The changes in the vertical turbulent kinetic energy (TKE) balance introduced by winds are either the result of increasing fluxes of TKE across the air-water interface, redistributed in the water column through turbulent diffusion, or, alternatively, the result of the increasing magnitude of vertical shear leading to the local production of TKE within the water column. These two mechanisms of production of TKE are referred to as stirring (P_{sk}) and shear production (P_s). These two terms are balanced by the sinks of TKE, which include frictional dissipation and, in the case of stratified water columns, buoyant dissipation (see *Gross et al*. [1999], for example). Both the energy available in the system through stirring and shear increased in response to wind forcing (see ratios $R_{sk\text{-}sk0}$ and $R_{s\text{-}s0}$ for the SW-runs in Table 4.2 which represent percentages with respect to the P_{sk} and P_s values in the S-runs). However, P_{sk} represented always less than 30% of P_s (see ratios $R_{sk\text{-}s}$ in Table 4.2), which suggests that wind forcing increased mixing at the confluence mainly through

shear. Hence, the shear production term is taken as a proxy for the effect of wind on the mixing rates.

The easterly winds tended to decelerate the flow along the main river, producing a similar effect as if decreasing Fr_{ic} and increasing R_u relative to the reference values with no winds. As a result of the weaker inertial forces along the channel compared to the buoyancy differences, the plunge point tended to move upstream (see $x_{c\text{-}PL}$ values in Table 4.2 for S1 and SW2). Note that in Figure 4.8a, the plunge point is already upstream of the plotted area, hence, this upstream retreat of the plunging is not evident in Figure 4.8c. River mixing increased (Table 4.2) in response to E-winds. Total mixing was almost three times larger when the river was subject to E-winds of 6 m s^{-1} (run SW2) compared to conditions without any wind. Since the retreat of the plunge point upstream was only ≈ 20 m, the increasing mixing rate was mainly the result of the increasing level of turbulence existing in the water column. Note, for example, in Table 4.2 that shear production of turbulent kinetic energy at the confluence on day 203, under strong density differences, was six times larger when subject to moderate-to-strong E-winds (run SW2) compared with the conditions under no wind forcing.

The westerly winds, in turn, tended to accelerate the inflow along the main river, with an effect similar to increasing the Fr_{ic} and decreasing R_u in relation to the reference conditions, hence, displacing the plunge point downstream. On day 203, for example, with strong density differences, the plunge point moved in response to the W-winds from a position upstream of the junction apex into the confluence (Figure 4.8e). With the plunging interface at the confluence, where horizontal shear at the interface from the side-stream flow increases, mixing rates tended to increase. Total mixing, in this case, was ≈ 30% larger when compared with the reference conditions under no wind (see run SW5 in Table 4.2). The effects of W-winds on river mixing with moderate density contrasts between the rivers, as observed on day 329, appeared contradictory. Total mixing under moderate density contrast decreased 15% (run SW15) in spite of increasing vertical shear (Table 4.2). But note that the tributary was forced to remain attached to its bank and the interface between the two rivers moved towards a more vertical position (Figure 4.8j). The two rivers were forced by the winds to flow side by side within the study reach and the areas available for mixing decreased as the wind speed increased (see Figure 4.8j) and, as a result, mixing decreased (runs SW15 and SW20 in Table 4.2). The confinement of the tributary waters towards its bank under the influence of the strong westerly winds

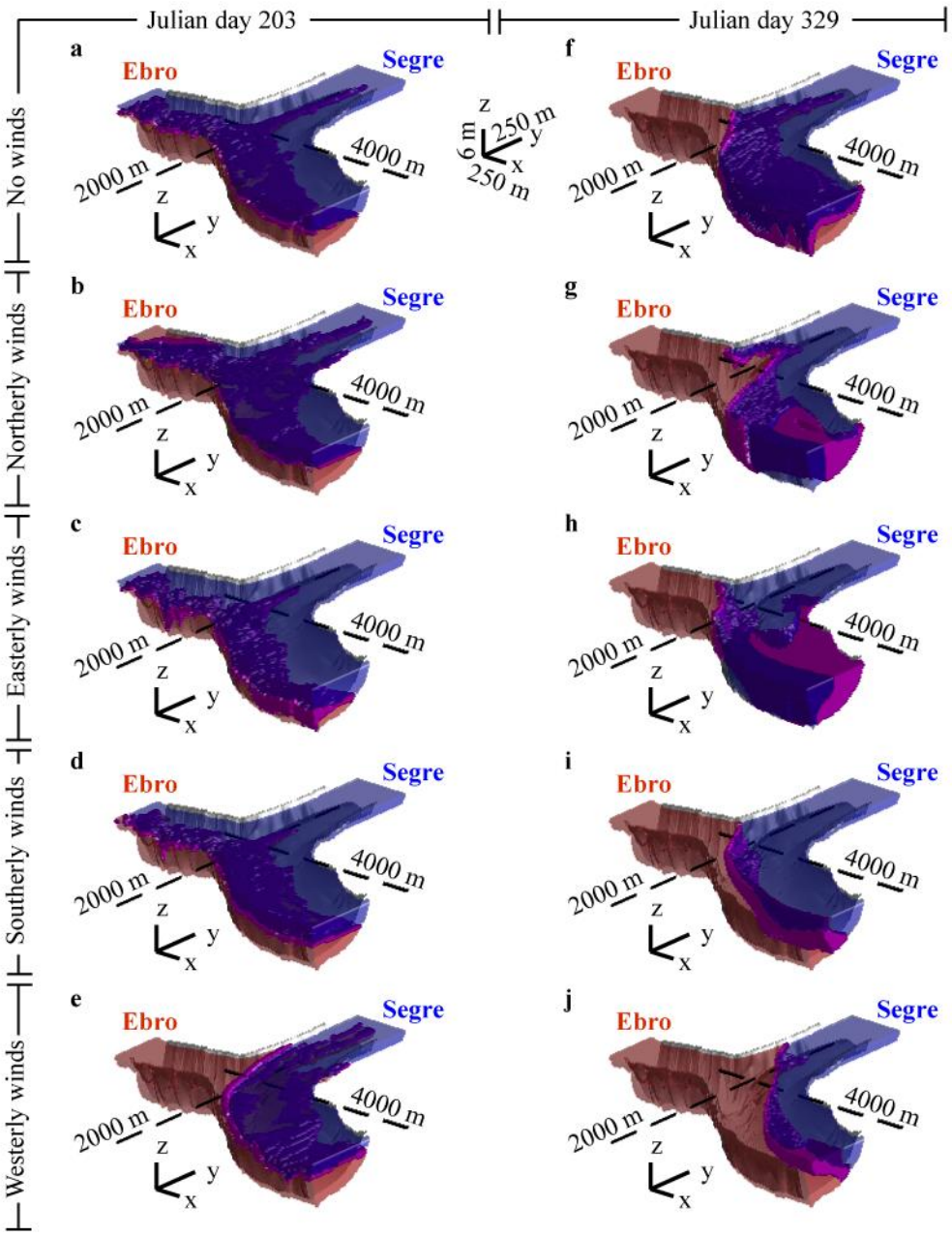

Figure 4.8 Time-averaged spatial arrangement of the Ebro (W-) water (red), the Segre (N-) water (blue), and the mixing interface (magenta) for constant wind velocities of 6 m s^{-1} and different directions. Runs (a) S1, (b) SW1, (c) SW2, (d) SW4, (e) SW5, (f) S2, (g) SW11, (h) SW12, (i) SW14 and (j) SW15 in Table 4.1. The *y*-axis is aligned with the North direction. The Ebro and Segre waters are 60% opaque. Aspect ratio (*x*:*y*:*z*) 40:20:1.

in Figure 4.8j is similar to observations and simulations of river plumes under the influence of strong downwelling winds pushing the plume towards the coast [e.g., *Hickey et al.*, 1998; *García Berdeal et al.*, 2002; *Otero et al.*, 2008]. *Fong and Geyer* [2001] attributed the lower mixing rates observed in river plumes being confined under the

influence of downwelling winds to a decrease in the contact area between the water from the river plume and the surrounding ambient water.

Winds acting along the tributary (S- and N-winds) control the intensity of the secondary circulation and, hence, the spatial distribution of the rivers at the confluence. Southerly winds, in general, weaken the secondary circulation that develops at the confluence because of the tributary inertia and its positive buoyancy, which tends to position the tributary water along the right margin in the main river. Depending on the wind speed, and the density contrast, the tributary may even remain attached to its bank, along the left margin of the main channel. Note, for example, that on day 203, with strong density differences, the interface remained nearly horizontal independently of the wind forcing (Figure 4.8d). On day 329, in turn, with moderate density contrasts, the tilting of the interface changed drastically in response to winds (see Figure 4.8i). Under no wind forcing (Figure 4.9b and Figure 4.9c), and consistent with field observations (Figure 4.9a and Figure 4.9b), the secondary circulation within the confluence on day 329 became rapidly dominated by the tributary cell, which occupied all the channel cross-section and pushed water towards the right bank near the surface and towards the left bank near the bottom. As a result, under no wind forcing, the interface in the main channel was near the surface along the left margin (Figure 4.8f). The S-winds counteract the inertia of the tributary and the baroclinic forces related to the density differences, reinforcing the W-cell (Figure 4.9f). Under steady 6 m s^{-1} southerly winds, the two rivers were forced to flow side by side with a more vertical interface (Figure 4.8i and Figure 4.9f). The contact area available for mixing was in this case smaller than under the reference conditions, and hence, river mixing was weaker (Figure 4.8i and Table 4.2). This is, for example, the case of run SW14 in Table 4.2, for which *TM* is ≈ 27% weaker than *TM* under the reference conditions. In contrast to S-winds, N-winds tend to intensify the tributary cell (Figure 4.9d), favoring the upwelling of the W-river near the left bank (see Figure 4.8b and Figure 4.8g as an example) downstream of the confluence. *TM* increases and the plunge point moves downstream in response to N-winds (see Figure 4.8b, Figure 4.8g, Table 4.2). These effects are consistent with an increase in R_u (Figure 4.4). Easterly and westerly winds also changed the secondary circulation at the confluence on day 329. By decelerating the flow along the main river, easterly winds reinforce the tributary cell, which increases in strength (Figure 4.9e) and mixing increases (runs SW12 and SW17). In contrast, by accelerating the flow along the main river, westerly winds reinforce the W-

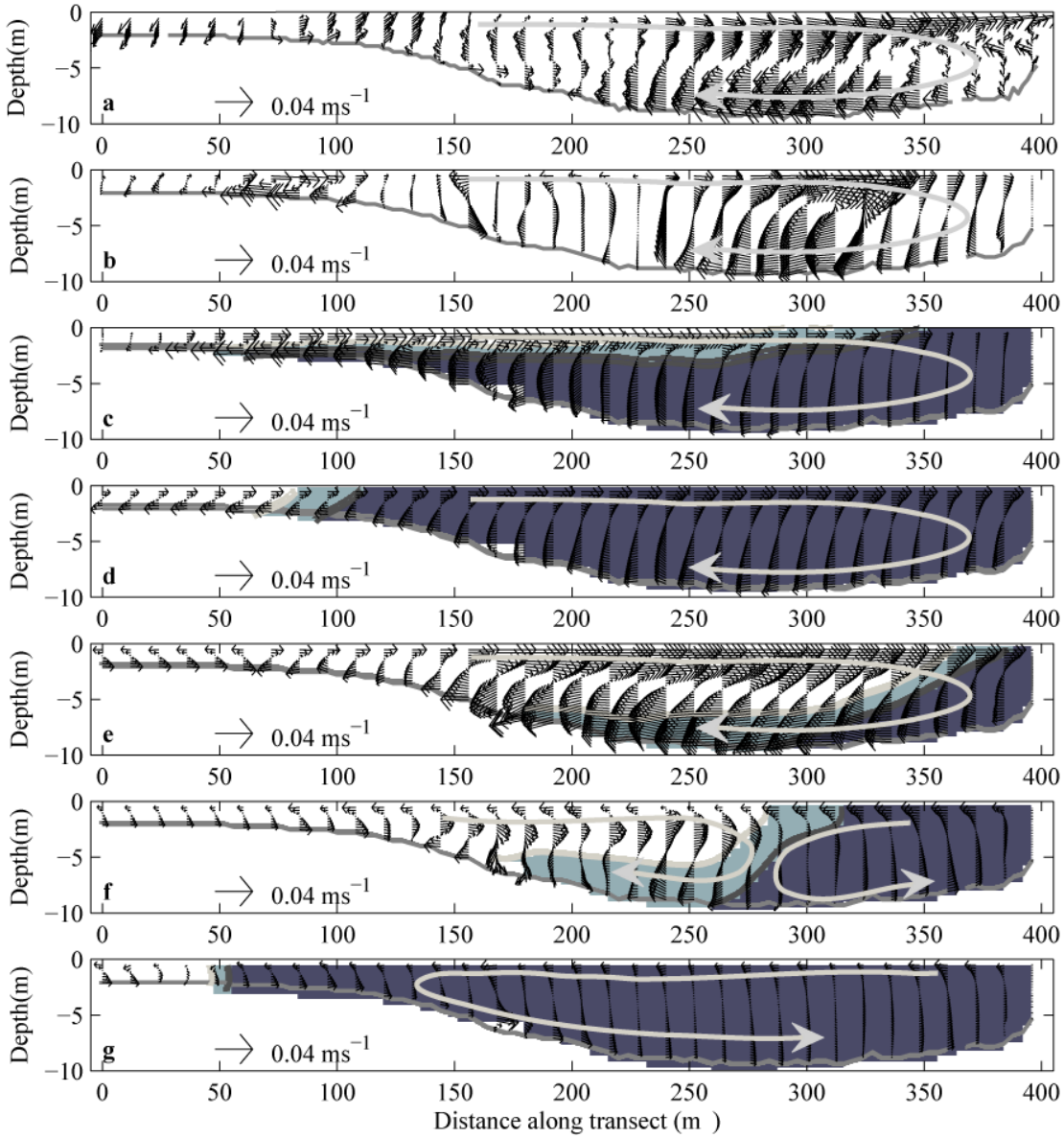

Figure 4.9 Secondary circulation at section F (see its location in Figure 4.1a). (a) Instant secondary circulation measured with an ADCP in the field around 13 hr on day 329, (b) instant secondary circulation predicted by the model in the simulation of field conditions (run U2) at the time the ADCP transect was collected, and (c-g) time-averaged secondary circulation in (c) the simulation under steady-state in the absence of wind (run S2) and (d-g) the simulations under steady-state with a constant wind forcing of 6 m s^{-1} from the (d) North (run SW11), (e) East (run SW12), (f) South (run SW14) and (g) West (run SW15). Dark and light gray colors in c-g show the location of the W-River and the mixing layer, respectively. Secondary circulation was calculated with the Rozovskii method [*Rozovskii*, 1961; *Parsons et al.*, 2013]. Arrows show the main pattern of recirculation.

cell (Figure 4.9g), which promotes the confinement of the N-river towards its bank (e.g., Figure 4.8j) and a decrease in river mixing (runs SW15 and SW20 in Table 4.2).

Overall, it is possible to extract the following conclusion: for combinations of R_u and Fr_{ic} that result in locations of the plunge point upstream of the junction apex, wind forcing generally results in an increase in river mixing mainly due to an increase in velocity shear (Table 4.2). This is the case of the particular confluence analyzed here, where the strongest winds (commonly from the SE, Figure 4.1h) tend to coincide with periods with strong buoyancy differences [*Ramón et al.*, 2013; Chapter 2]. For combinations of R_u and Fr_{ic} that result in locations of plunge points downstream of the junction apex, in turn, winds could force (depending on wind direction) the two rivers to flow side by side for longer distances, decreasing the area available for mixing and ultimately decreasing mixing rates.

4.4.4 Flow unsteadiness and plunging

As instant values in Figure 4.4 show, there is a high variability in time of both R_u and Fr_{ic} on the three simulated days (U-runs), due to the highly variable W-inflows (Figure 4.1b and Figure 4.1c). On day 203 all the combinations of R_u and Fr_{ic} lie above the isoline $x_{c\text{-}PL}$ = 0.93 in Figure 4.4, which suggest that the plunge line was always located upstream of the confluence midpoint. Results of run U1 show, in fact, that the plunge line between the W- and N-rivers was at all times located upstream of the confluence on day 203 (Figure 4.10a), even at times of maximum W-discharges (Figure 4.1b). This is consistent with the field observations on that day [*Ramón et al.*, 2013; Chapter 2]. The magnitude of the inflows from the W-River (inertial forces) controlled how far upstream the plunge line moved within the W-channel, which was, at times, located immediately downstream of the Mequinenza dam ($x_c \approx -6$) (Figure 4.10a). On days 329 and 330, however, values in Figure 4.4 lie upstream of, within and downstream of the confluence. At the time when field data were collected (11-14 hr) and consistent with field observations [*Ramón et al.*, 2013; Chapter 2], the plunge point is located downstream of the confluence on day 329 (Figure 4.10b), but it is located in the upstream mid half of the confluence or upstream of it on day 330 (see the location of the plunge point at time 35-38 hr in Figure 4.10b). The plunge point also moved, however, to locations upstream of the confluence midpoint on day 329 during the time of zero withdrawals from Mequinenza and after the time of peak R_q (R_q = 0.58 at 16 hr, Figure

4.1c) in the afternoon (Figure 4.10b). The opposite occurred on day 330, when the plunge point moved to locations downstream of the confluence (Figure 4.10b) after peak flows from the W-River in the evening (R_q = 0.13 at 20 hr in Figure 4.1c).

In what follows, we will use the confluence midpoint (isoline $x_{c\text{-}PL}$ = 0.93 in Figure 4.4) as a reference to understand the response of the plunge point to changes in R_u and Fr_{ic} through time. As shown by the horizontal dark-gray shaded areas in Figure 4.10b, there are times on days 329 and 330 in which the confluence exhibited the opposite to the expected pattern according to the steady inertia-buoyancy equilibrium (Figure 4.4): that

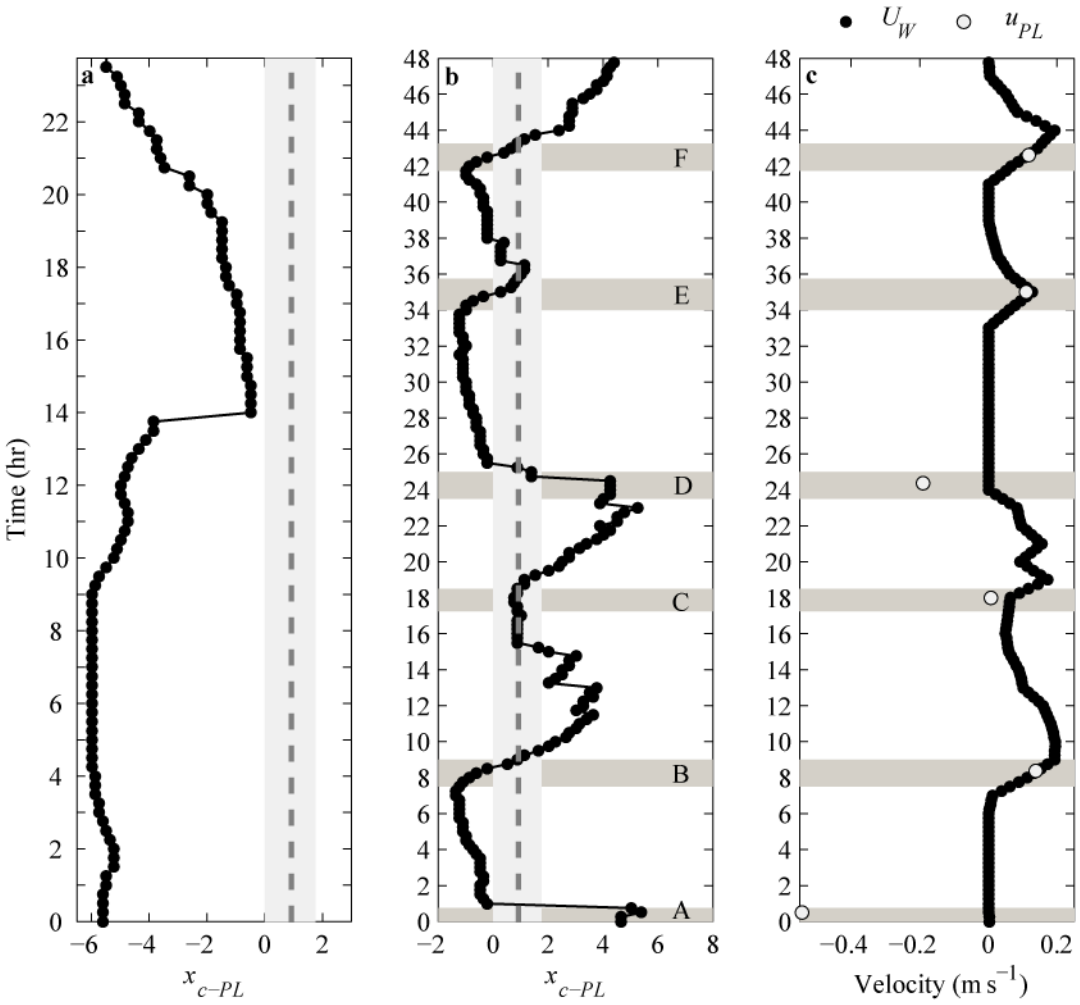

Figure 4.10 (a,b) Variation with time of the streamwise location of the plunge point ($x_{c\text{-}PL}$) between the W- and N- rivers on days (a) 203 (run U1) and (b) 329-330 (runs U2 and U3). And (c) variation with time of the W-inflow velocities (U_W) and average velocities of the streamwise displacement of the plunge line (u_{PL}) at times (A-F horizontal dark-gray shadded areas) when the location of the plunge line is opposite (upstream of or downstream of) to that expected according to the isoline $x_{c\text{-}PL}$ = 0.93 (see Figure 4.4 and section 4.4.1 for further details) on days 339-330. Vertical light-gray shaded areas in (a,b) show the location of the confluence region and gray dotted lines in (a,b) show the location of the confluence midpoint.

is, the plunge point is located downstream of $x_{c\text{-}PL}$ = 0.93 when it was expected to be upstream of it (according to the instant values of R_u and Fr_{ic} at that time) or *vice versa*. For example, between 7.75-8.75 hr on day 329 (time interval B in Figure 4.10b) values of R_u *vs*. Fr_{ic} lie below the isoline $x_{c\text{-}PL}$ = 0.93 in Figure 4.4, which would be indicative of the plunge point being located downstream of the confluence midpoint. During that time, however, the plunge point started moving from upstream locations towards downstream locations (Figure 4.10b). This indicates the system needs time to adjust from one state to another, that is, the system needs time for the plunge point to move in the streamwise direction towards the new equilibrium position. Figure 4.10c shows the time-varying W-inflow velocities on days 329 and 330 and the time-averaged velocity of the plunge-point displacement (u_{PL}) at the times when the location of the plunge point exhibited the reversed pattern. At times when the plunge point is moving from upstream to downstream locations (time intervals B, C, E and F in Figure 4.10b), u_{PL} matches the advective velocity of the main stream U_W (Figure 4.10c). At times when the plunge point is moving from downstream to upstream locations (time intervals A and D in Figure 4.10b) u_{PL} becomes negative and could be as high as ≈ −0.55 m s^{-1} (see time interval A in Figure 4.10c). These high upstream velocities, however, do not reflect a real upstream movement of the plunge point (since flow downstream of the confluence is mostly directed downstream) but are the result of the baroclinic time needed for the new N-water entering the confluence to reach the opposite margin. This time will depend on the lateral location of the mixing interface between rivers at the time the equilibrium R_u-Fr_{ic} changes towards a plunge point that should be located upstream of $x_{c\text{-}PL}$ = 0.93. A and D time intervals in Figure 4.10b cover 1 hr and 1.25 hr, respectively. The ≥ 1 hr time intervals approximate the baroclinic adjustment time T_b (= $b_c/(g'\mathrm{D})^{0.5}$) of the confluence (b_c ≈ 380 m being the average width of the confluence, Figure 4.1a), which for days 329 and 330 are $T_{b\text{-}329}$ = 1.1 hr, $T_{b\text{-}330}$ = 1.3 hr.

4.4.5 Flow unsteadiness and mixing rates

Figure 4.11a-c show the boxplots over time of the standard deviation σ of tracer concentration on days 203, 329 and 330 (U-runs in Table 4.1). On day 203 (Figure 4.11a), σ is highly variable upstream of the confluence (x_c < 0), with σ changing from 0 to 20 ppm even immediately downstream of the Mequinenza dam (x_c ≈ −6). σ values are on average > 0 ppm at x_c ≈ −6 (σ = ≈ 5 ppm, Figure 4.11a), which indicates that on average

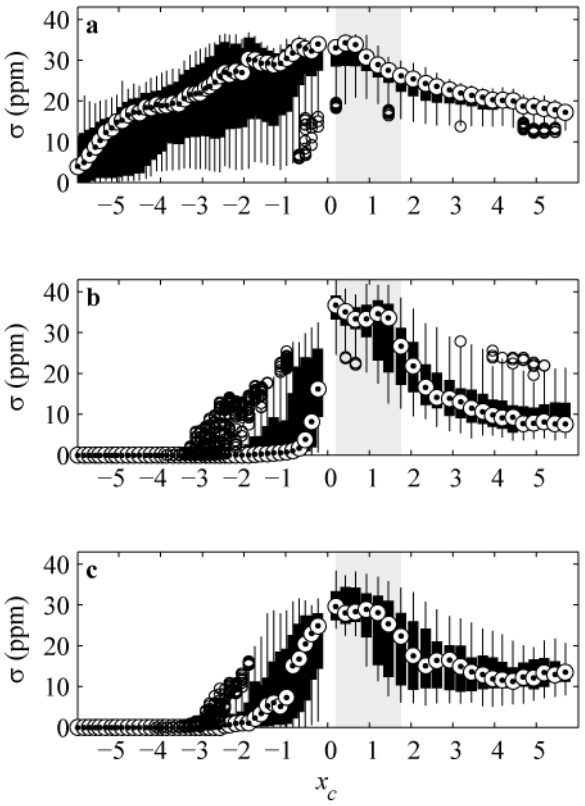

Figure 4.11 Boxplots of standard deviations (σ) of tracer concentrations over a 24 hr period upstream, at and downstream of the confluence on days (a) 203, (b) 329 and (c) 330. The shaded areas show the location of the confluence region ($0 \leq x_c \leq 1.76$). U-runs in Table 4.1

some fraction of the N-water is able to reach locations immediately downstream of the Mequinenza dam. This high variability in σ upstream of the confluence is the result of the unsteadiness in the location of the plunge point between the W- and N- rivers (Figure 4.10a). This variability however, is damped downstream of the confluence ($x_c \geq 1.76$), with σ varying over time in a range of only 5 ppm at $x_c = 5.7$ (Figure 4.11a). This low variability in σ is the result of the plunge point being always located upstream of the confluence (Figure 4.10a), which allows the formation of a stable vertical stratification downstream of the confluence. The 24h-averaged σ results show average mixing rates of O (10^{-2}) ppm m^{-1} ($TM \approx 65\%$) (Table 4.2). This is one order of magnitude higher than mixing rates in the S1 run (steady-state in the absence of wind) and of the same order as mixing rates in the steady-state SW3 run (Table 4.2) in the presence of winds coming from the SE (as on day 203, Figure 4.1d-f) with $U_{10} = 6$ m s^{-1}. This indicates that river mixing was primarily increased by the southeasterly winds blowing on that day and

highlights the importance of the southeasterly winds in increasing river mixing during the stratification period in Ribarroja.

There is also variability in σ upstream of the confluence on days 329 and 330 (Figure 4.11b and Figure 4.11c). Time variability in σ is, however, restricted to a narrower area on those days, indicative of less capability of the N-water to flow upstream on top of the W-water in the W-channel. Note that the plunge point on both days is always located downstream of $x_c = -2$ (Figure 4.10b) and that σ equals 0 ppm at $x_c < -3$ (Figure 4.11b and Figure 4.11), which is indicative of pure (unmixed) W-water. Boxplots in Figure 4.11b and Figure 4.11c show that mixing downstream of the confluence is highly variable on both days 329 and 330, with σ values varying from 4 to 21 ppm and from 8 to 21 ppm at $x_c = 5.7$ on each day, respectively. This high variability in σ both upstream and downstream of the confluence is the result of the plunge point moving both upstream and downstream of the confluence on those days (Figure 4.10b).

4.5 Summary and Conclusions

The confluence between the Ebro and Segre rivers has been presented as an example of a strongly-asymmetrical (junction angle of ≈ 90º) large river confluence subject to strong density contrasts between the confluent rivers. The location of the plunge point between the rivers, at this confluence, is controlled by an inertia-buoyancy equilibrium which can be expressed in terms of the velocity ratio and a confluence Froude number. The plunge point between rivers will move to upstream locations as the confluence Froude number decreases and/or the velocity ratio increases (for low velocity ratios). As the velocity ratio (tributary inertia) keeps increasing, though, the plunge point tends to move to downstream locations due to the increasing rates of turbulent diffusion that tend to keep the tributary flow attached to bed, shifting the orientation of the mixing interface towards more vertical positions.

River mixing downstream of the confluence is strongly dependent on the location of the plunge point between the confluent rivers. The biggest mixing rates occur when the plunge point is located at the confluence itself due to a combination of a big contact area of the interface between rivers and high mixing coefficients, especially in the vertical direction. As the plunge point moves upstream of the junction apex, mixing rates decrease as a result of a decrease in the magnitude of vertical eddy diffusivities within a horizontal

mixing interface. Mixing rates also decrease as the plunge point moves to locations downstream of the confluence as a result of a decrease in the total area of contact between the confluent rivers.

The effect of wind forcing on the spatial arrangement of the confluent rivers depends on both wind velocity and direction, but can completely alter the inertia-buoyancy equilibrium at the confluence and even move the location of the plunge point from locations upstream of the junction apex to locations downstream of the confluence, and hence, modify river mixing rates. Winds opposite to the direction of the main stream are more effective in increasing shear at the confluence, and in turn, in increasing river mixing.

Unsteady river-inflows change the streamwise equilibrium location of the plunge point through time which means that for a given density contrast the plunge point can move from locations upstream of the confluence to locations downstream of the confluence, and *vice versa*, due to changes in river inflows alone. This is important since mixing rates decrease as the plunge point moves to locations upstream of the confluence. There is a delay in time between the shift in the equilibrium conditions and the corresponding streamwise movement of the plunge point.

Although buoyancy and wind effects are shown to be important in this confluence, the characteristics of this confluence are transitional between a lake and a river, which poses limitations to the general applicability of these findings to all river confluences.

Chapter 5

Effect of secondary circulation and fish entrance distribution on entrainment of juvenile salmon into the interior Sacramento-San Joaquin River Delta over a tidal cycle

Abstract

Federally listed Sacramento River Chinook salmon juveniles must survive passage through the Sacramento – San Joaquin River Delta in order to successfully out-migrate to the ocean. Two of the four salmon main migration routes in the Sacramento River direct salmon to the interior of the delta, where salmon survival is known to decrease. Although migration route selection is thought to be advection-dominated, the combination of physical and biological processes that control route selection is still poorly understood. The reach in the Sacramento-River where the entrances (diffluences) of the two lower-survival migration routes are located is strongly influenced by the tides, with flows reversing twice daily, and the two diffluences are located in the outside of the same Sacramento River bend where secondary circulation occurs. Three dimensional simulations are conducted, both in the Eularian and Lagrangian frame, to understand tidal and secondary-circulation effects on the migration route selection of juveniles within this reach of the Sacramento River. Although salmon behavior is reduced to the simplest (passively-driven neutrally-buoyant particles), the preliminary results that are presented in this chapter are consistent with previous studies that show that during the flood tide almost all the flow, and thus, all the salmon, are directed to the interior delta through these two migration routes. This work also suggests that, during ebb tides, fish entrainment rates into the interior of the delta are higher than those expected by flow entrainment alone due to the preference of salmon to migrate near surface, together with

the effect of secondary circulation that pushes the surface-biased salmon towards the outside of the bend where the entrance of these two migration routes are located.

5.1 Introduction

Three of the four Chinook-salmon (*Oncorhynchus tshawytscha*) runs hosted by the Sacramento-San Joaquin River Delta (hereafter, the Delta) are federally listed as endangered, threatened and a "species of concern", respectively [*NMFS*, 1997]. One of their key life stages is the out-migration period (the period of migration from natal tributaries to the ocean), when juveniles must negotiate the Delta, which is a complex network of natural and man-made channels (Figure 5.1a) that has been highly altered to convey water for domestic and agricultural uses via two large pumping stations located in the interior Delta [*Nichols et al*., 1986] (Figure 5.1a). Due to the complexity of the Delta, juveniles may take different migrations routes in their way to the ocean [*Perry et al*., 2010]. In particular, in the Sacramento River (Figure 5.1a) there are four main migration routes [*Perry*, 2010] and those that lead to the interior Delta have the lower survival rates [*Newman and Brandes*, 2010; *Perry*, 2010, *Perry et al*., 2010, 2012, *Singer et al*., 2013], likely due to high predation rates, longer migration times and entrainment into the water pumping stations [*Brandes and Mclain*, 2001; *Newman and Rice*, 2002; *Newman*, 2003; *Kimmerer*, 2008; *Newman and Brandes*, 2010; *Perry et al*., 2010]. Salmon-population survival decreases as the number of fish that select migration routes that lead to the interior Delta increases [e.g., *Perry et al*., 2010, 2012, 2013]. Then, recovering endangered salmon populations in the Delta requires understanding of, among others, migration-route selection.

Two of the four migration routes in the Sacramento River lead to the interior Delta: one crossing the Delta Cross Channel (hereafter, DCC, Figure 5.1) and the other one crossing Georgiana Slough (hereafter, GEO, Figure 5.1), which can entrain up to 50% of juvenile salmon into the interior Delta [*Perry*, 2010]. While GEO is a natural connection between the Upper and interior Delta, DCC is a 1.1 km-long man-made channel used to divert water from the Sacramento River into the interior Delta to reduce salinities at the pumping stations. Both channel-junctions are ≈ 0.9 km apart and are located in the outside of the same Sacramento River bend (hereafter the DCC-GEO bend). The first part of the bend, where the Sacramento-DCC junction (hereon the SD junction)

is located, curves with a radius of curvature R_s of ≈ 0.8 km (R_s/b = 8, where b ≈ 100 m is the average Sacramento-River channel width, Figure 5.1c). The second part of the bend, where the Sacramento-GEO junction (hereafter the SG junction) is located, curves with a sharpest R_s of ≈ 400 m (R_s/b = 4) (Figure 5.1c). The DCC is controlled via moveable

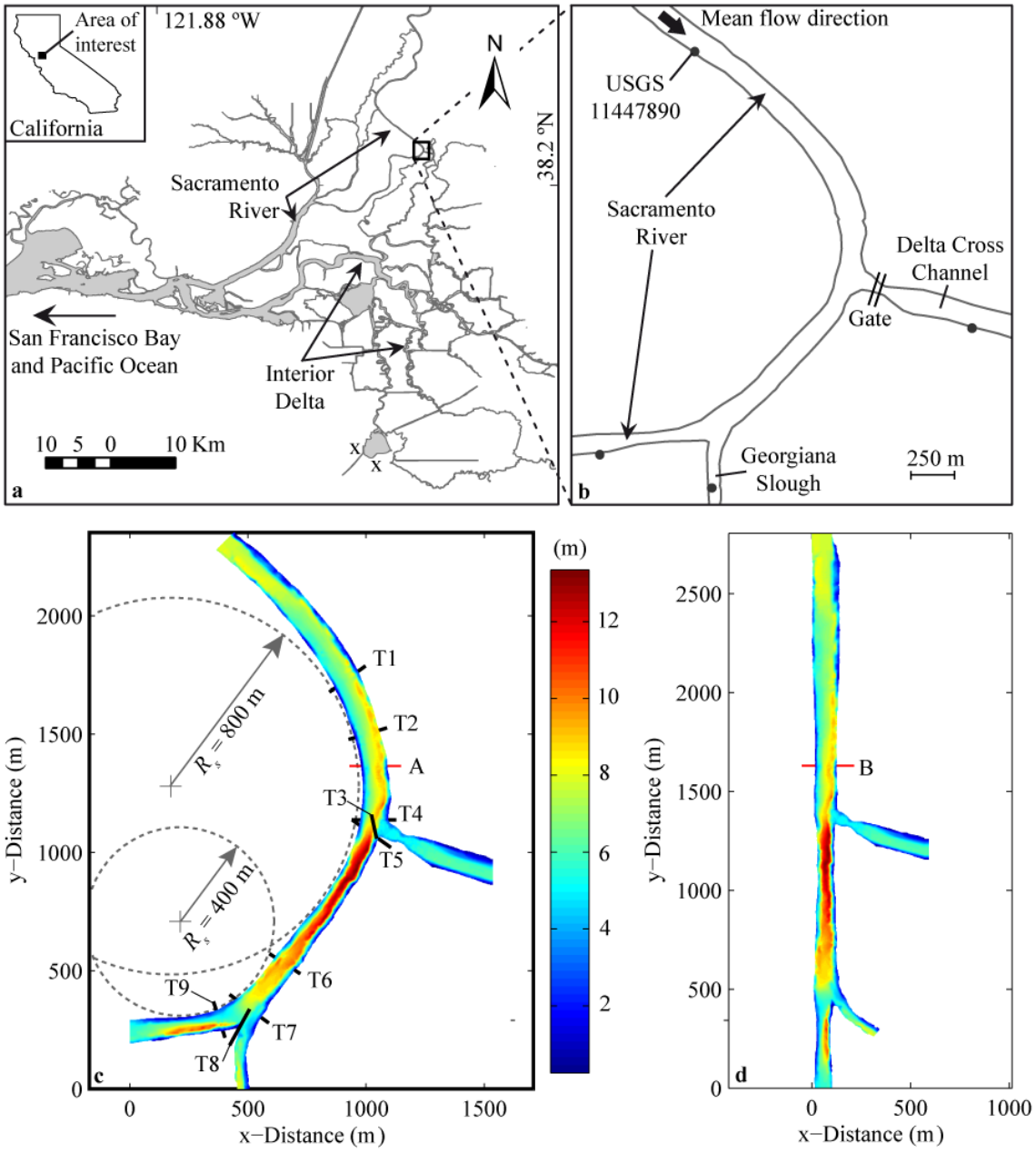

Figure 5.1 (a) The Sacramento-San Joaquin River Delta, (b) close-up view of the area of interest (the DCC-GEO bend) and (c, d) bathymetry of the computational domain for the Dec. 2008 period and for the (c) real and (d) straightened case. The (X) symbols in (a) show the locations of the two pumping stations. The gray dots in (b) show the location of the USGS gaging stations used as model boundary conditions. Black lines in (c) show the location of the ADCP transects. Red lines in (c) and (d) show the particle-release sections A and B, respectively.

control gates located at the SD junction. DCC gates are closed during the emigration period of endangered winter-run juvenile Chinook salmon, assuming that fish entrainment into DCC is directly proportional to the mean fraction of river flow that is diverted to the interior Delta [*SWRCB*, 1995; *Low et al.*, 2006]. However, the validity of this assumption is not clear, since if the DCC gates are closed flow into GEO increases, which could result in an increase in the number of fish entering the interior Delta through GEO. Although migration routes probabilities generally corresponded well with the mean fraction of total Sacramento-River discharge in each route [*Perry*, 2010; *Perry et al.*, 2010; *Steel et al.*, 2013; *Cavallo et al.*, 2015], the proportion of fish entering a route (entrainment rates) can deviate markedly from the mean proportion of flow to that route [*Perry*, 2010; *Perry et al.*, 2010; *Cavallo et al.*, 2015]. For example, *Blake and Horn* [2004] showed that, during the 2001 study, there were times when significant entrainment occurs into DCC (and into GEO) when comparatively little water was moving into these channels. *Perry et al.*, [2010] observed, however, that, during the Dec-2006 and Jan-2007 salmon-release study, the proportion of fish migrating within the Sacramento River was about 10% higher than the fraction of flow remaining in the Sacramento River and the proportion of fish entering GEO could be lower than the fraction of flow into GEO. These examples suggest the mechanisms governing route selection are more complex, and other factors could also influence fish entrainment rates. Examples of other potential factors listed in the literature are [e.g., *Perry et al.*, 2010]: (1) tidal forcing, (2) fish behavior and (3) the presence of secondary circulation in river bends.

Tidal forcing causes the Sacramento River to flow upstream twice daily for flow rates below ≈ 360 m^3 s^{-1} at the USGS (U.S. Geological Survey) station 11447890 (Figure 5.1b). These flow reversals cause the relative distribution of flows among the Sacramento, DCC and GEO channels to vary over hourly time scales (Figure 5.2 and Figure 5.3). For example, nearly all of the river flow is diverted into the DCC and GEO during reversed-flow flood tides (Figure 5.3d and Figure 5.3e), whereas Sacramento-River flow tends to bypass the DCC (almost no flow enters the DCC) during ebb tides [e.g., *Blake and Horn*, 2004; *Dinehart and Burau*, 2005a] (Figure 5.3b). Then, the probability of fish entrainment will depend on the hydraulic conditions that the fish encounter when migrating past each channel entrance [*Blake and Horn*, 2004; *Steel et al.*, 2013]. For example, fish tend to bypass the DCC on an ebb tide and to be advected into the DCC from the Sacramento River (both from locations upstream and downstream of

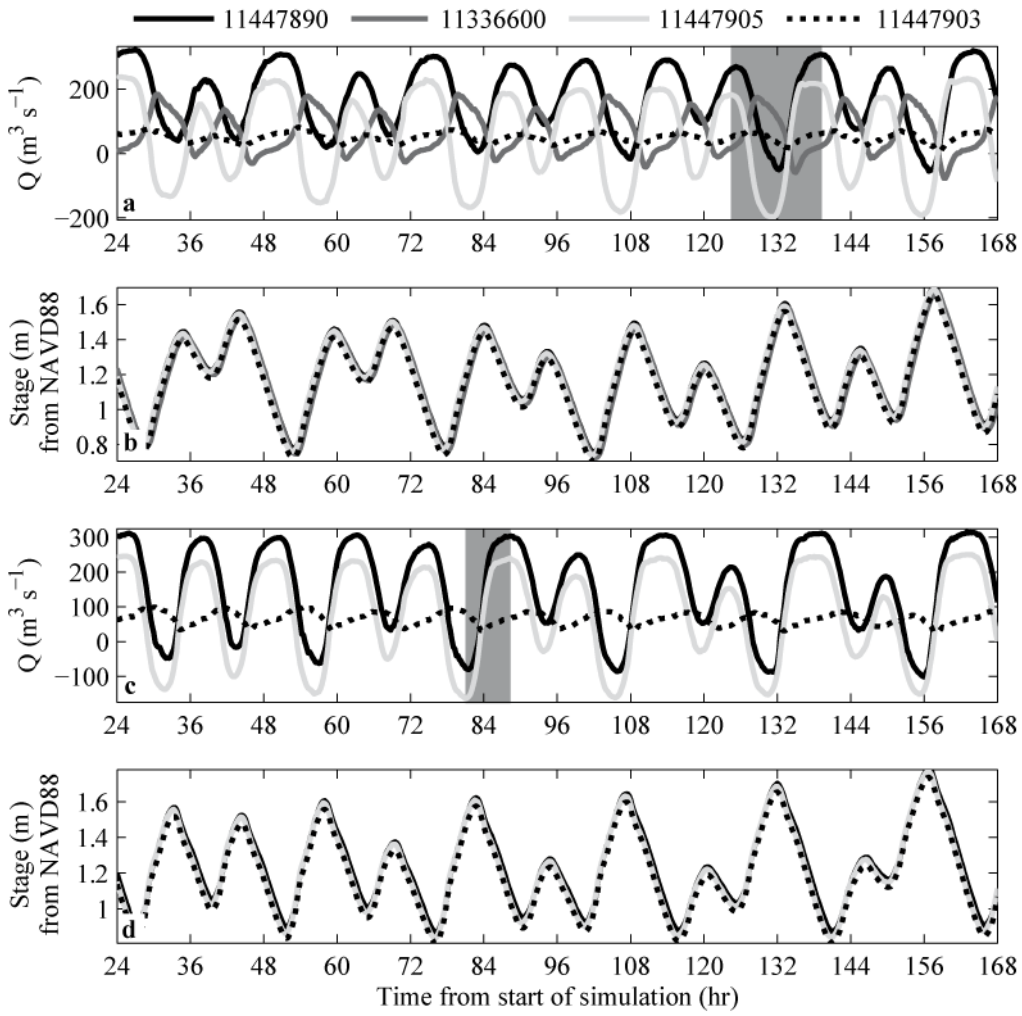

Figure 5.2 Discharge and water stages measured at the USGS gauging stations for the (a, b) Dec. 2008 (DCC gates opened) and (c, d) Jan. 2009 (DCC gates closed) simulation-periods (Warming-up time not shown). Flow is positive if directed downstream. The shaded gray areas in (a, c) show time periods in which ADCP transects were collected.

the DCC entrance) on a flood tide [*Blake and Horn*, 2004] (Figure 5.3). Thus, any fish in the Sacramento River during an ebb tide has to bypass first the DCC entrance and second the GEO entrance and then escape entrainment on the subsequent flood tide [*Blake and Horn*, 2004].

Although migration route selection is thought to be advection-dominated [*Blake and Horn*, 2004; *Perry et al.*, 2015], salmon behavior can still influence entrainment rates. For salmon to be entrained in direct proportion to the flow, fish density distributions should be uniform both in time and space. However, late-fall Chinook salmon juveniles have been shown to exhibit nocturnal migration behavior [*Blake and Horn*, 2004; *Perry*, 2010; *Chapman et al.*, 2013; *Zajanc et al.*, 2013; *Perry et al.*, 2015]. This nighttime

arrival varied from 55% to 86% of the population among releases [*Perry et al.*, 2015], ranging from diel arrival that was proportional to the availability of daylight hours to substantial nocturnal migration [*Blake and Horn*, 2004; *Chapman et al.*, 2013; *Plumb et al.*, 2015; *Perry et al.*, 2015]. Salmon distributions are also not uniform in space. Salmon have preference for locations near surface and fish density tends to be higher near the surface, with most of the salmon located within the first four meters of the water column in the Sacramento River [*Blake and Horn*, 2004]. Salmon are not uniformly distributed in the horizontal direction either [e.g., *Blake and Horn*, 2004; *Perry et al.*, 2014]. *Blake and Horn* [2004] observed that upstream of the DCC entrance, fish density was slightly biased towards the western shore, inside the bend, but closer to the bend the maxima of fish density was displaced to the outside margin of the bend, where the DCC and GEO entrances are located. This horizontal displacement of fish is apparently not related to fish behavior but, instead, it is strongly linked to the horizontal location of maximum velocities within each junction [*Blake and Horn*, 2004]. Hence, it should vary on tidal time scales, predisposing salmon to be entrained into the DCC or GEO on certain tidal phases. In particular, the likelihood of salmon being diverted into DCC should increase towards the end of an ebb tide (Figure 5.2 and Figure 5.3b). In GEO, in turn, this likelihood should be maximal on a full or slackening ebb tide [*Blake and Horn*, 2004; *Dinehart and Burau*, 2005a] (Figure 5.2 and Figure 5.3). However, during peak ebb tides, when the Sacramento-River flows bypass the DCC (Figure 5.2 and Figure 5.3b), the streamlines of maximum velocities are located in the center of the river cross-section, but, yet, fish distributions downstream of the DCC entrance have been shown to be skewed to the eastern bank [*Blake and Horn*, 2004], which proved that juveniles are not simply following a path of maximum velocity through that junction. What is the additional process? *Blake and Horn* [2004] and *Blake et al.* [2012] suggested that strong secondary circulation developing at river bends as it occurs near DCC and GEO [e.g., *Dinehart and Burau*, 2005a; *Bever and MacWilliams*, 2015], could influence the location of salmon in the river cross-section. In particular, fish bypassing the DCC on a peak ebb tide could be predisposed to enter GEO due to secondary-circulation moving the surface-oriented salmon to the outside of the bend. Thus, understanding the interaction of the tidal cycle with the development of secondary circulation in the DCC-GEO bend and fish distributions at the entrance of these junctions is of key importance in order to understand and quantify entrainment rates into these two migration routes. To our knowledge, the

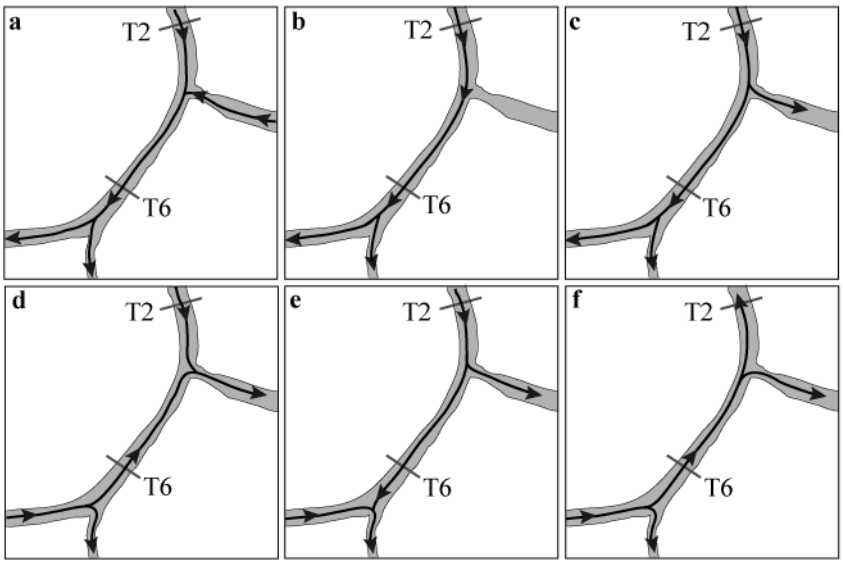

Figure 5.3 Sketches of possible combinations of flow direction within the domain when DCC gates are open. (a) Beginning of the ebb tide, (b) Peak ebb tide, (c) end of the ebb tide, (d) flood tide with flow convergence at the SD junction, (e) flood tide with flow convergence at the SG junction, and (f) flood tide with negative flows in the North boundary.

effects on fish entrainment rates of secondary-circulation developing in river diffluences in channel bends, such as the DCC-GEO bend, remains unexplored.

Our general goal in this work is to understand the factors controlling migration route selection in river junctions existing in curved and tidal rivers. In particular, this study aims to answer two key questions: (1) is fish entrainment higher than flow entrainment due to the presence of secondary circulation at the DCC-GEO bend?, and (2) is fish entrainment different to flow entrainment due to the non-uniform spatial distribution (surface-biased) of salmon at the entrance of both junctions? We hypothesize that fish entrainment increases, especially at GEO, due to secondary-circulation effects during peak ebb tides and that secondary circulation becomes stronger (entrainment rates into GEO increase) when DCC gates are closed. We also hypothesize that the preference for juveniles to out-migrate near the surface makes them more susceptible to be entrained into both DCC and GEO due to a positively interaction with secondary-circulation effects and due to differences in channel depths between the main stem (Sacramento River) and the distributaries. For example, the depth of the distributary at the SD junction is located at ≈ 5 m, while the Sacramento River at that point is ≈ 9 m deep (Figure 5.1c). The likelihood of fish being entrained into DCC should increase if they accumulate near the

surface, and would decrease if the distribution were biased towards the bottom. To that end, we conducted simulations of hydrodynamic and transport processes occurring in the DCC-GEO bend, both under an Eulerian and Lagrangian frame, under the conditions experienced by juvenile salmon during the December-2008 and January-2009 releases (Figure 5.2), when DCC gates were opened and closed, respectively, and when tidal forcing strongly affected flows within the study region.

5.2 Study site

The Delta is one of the most managed river systems in the world [*Cohen and Carlton*, 1998]. In very general terms the Delta can be divided into three physical regions: The Upper Delta, which contains the Sacramento River system, the Central/Interior Delta, containing the Mokelumne and San Joaquin River systems, and the Southern Delta, where the pumping stations are located (Figure 5.1a). The interior Delta supplies water for more than 25 million residents and supports a billion-dollar agricultural industry. The Sacramento River (Upper Delta) accounts for the majority of the fresh and high-quality water entering the Delta (≈ 75%). Thus, in order to improve water quality near the pumping stations, water from the Sacramento River is diverted into the interior Delta through the DCC. Our region of interest comprised the DCC-GEO bend in the Sacramento River, a ≈ 3km-long reach between latitudes 38º14′14″N and 38º15′28″N, and between longitudes 121º31′18″W and 121º30′19″W, where the diversions to DCC and GEO are located (Figure 5.1). Channel walls are generally steep and depths in this reach of the Sacramento River average ≈ 7 m with maximum depths of ≈ 13 m downstream of the DCC entrance and in the outside of the bend downstream of the GEO entrance (Figure 5.1c). The DCC bottom is located at a depth of about 5 m, while the Sacramento River within the SD junction is 9 m deep. The GEO bottom is located at a similar depth (≈ 5.1 m) as the average Sacramento River depth within the SG junction. Junction angles of the SD and SG junctions are ≈ 105º and ≈ 135 º respectively.

The Sacramento River flows are largely dictated by the release of water from upstream storage reservoir, but also by natural processes such as winter precipitation and springtime snowmelt. The distribution of water is determined by the pumping stations that can export up to 50% of the total flow [*Nichols et al.*, 1986]. Flows within our study region are also influenced by the tidal cycles that vary on diel, biweekly and annual

timescales. On a typical tidal cycle, peak flows in the DCC occur approximately 3.5 hr after those in the Sacramento River and peak flows in GEO are ≈ 90º out of phase from those in the Sacramento River (see Figure 5.2a as an example). Flow into DCC is controlled by the timing of the phase lag of water-surface slope between the Sacramento River and the Mokelumne River, which most of the time forces the flow to move towards the Mokelumne River. However, during some time before the peak ebb tide the flow at DCC is directed towards the main Sacramento River (Figure 5.3a and note that flows in the USGS station 11336600 take negative values during some periods in Figure 5.2a). In GEO, the frictional decay of the tidal wave causes the flood tide to be shorter than the ebb tide (e.g., Figure 5.2a and Figure 5.2d)

As flow in the Sacramento River increases, the net flow into DCC and GEO also increases, but the overall percentage of the Sacramento flow entering those channels decreases. In addition, increases in the Sacramento-River flow decreases the relative strength of tidal fluctuations in the junction area, changing the tidal flow pattern in the DCC and in the Sacramento River. When DCC is closed flow into GEO increases. This can be seen in Table 5.1 where the tidally-averaged (Godin filter, *Godin* [1972]) values in the station USGS 11447903 (located in GEO) averaged 49.05 $m^3 s^{-1}$ and 66.16 $m^3 s^{-1}$ in the December-2008 and January-2009 release periods, respectively, despite slightly higher flow rates in the Sacramento River occurring in the first period.

5.3 Methods

5.3.1 Approach

An Eularian model (see details in Section 5.3.2) was first used to simulate the three-dimensional flow field of the study reach during two periods of time, when salmon-release experiments were carried out by the Unites States Geological Survey USGS and when flows within the study reach where strongly affected by the tides (Figure 5.2). The first period extended from December 3 to December 9 in 2008, and is referred to as Dec. period. The second period, referred to as Jan. period, was from January 15 to January 21 in 2009. The simulations of the study reach of these two periods are referred to as Cases E1A and E2A, respectively, in Table 5.2. While tidally-averaged Sacramento-River flows were similar in both periods (Table 5.1), in the Jan. period, DCC gates were closed, which allows us to also analyze the influence of opening/closing the gates on fish entrainment

Table 5.1 Time-average of the tidally-averaged observed discharges (m^3 s^{-1}) at the USGS stations.

	Time period	
USGS station	**From 3 to 9 Dec. 2008**	**From 15 to 21 Jan. 2009**
USGS 11447890	171.67	152.50
USGS 11336600	64.48	0
USGS 11447903	49.05	66.16
USGS 11447905	51.92	78.92
Mass balance error	6.22	7.42

rates. Both time periods were re-run, but in this case the model domain was artificially rotated to transform the DCC-GEO bend into a straight river reach (Figure 5.1d) to evaluate secondary-circulation effects on salmon entrainment rates. These are the run cases E1B and E2B in Table 5.2. The three-dimensional hydrodynamic fields generated by the Eularian model were then used in the Lagrangian model (see details in Section 5.3.5) to predict the local dispersal of particles (salmon) within the model domain. Our approach to the lagrangian frame was based in two main assumptions: (1) The movement of particles is advection-dominated, the salmon behavior being secondary, and (2) Salmon behave as passively and neutrally-buoyant particles. Although *Goodwin et al.* [2001, 2006] suggested that juvenile salmon respond to hydrodynamic features such as localized lateral and vertical shears and local increases in turbulence intensity, in the prismatic channels typical of the Delta there are few physical or bathymetric features that would generate localized lateral and vertical shears or localized increases that would initiate a behavioral response, in particular a response that would change a fish's fate. The first assumption is consistent with the literature since physical variables have been shown to highly explain fish entrainment [*Blake and Horn*, 2004; *Perry et al.*, 2010]. The secondary importance of fish behavior can be broadly explained in terms of current speeds relative to the swimming capabilities. Typically, juvenile Chinook salmon can sustain ≈ 2 body lengths per second [*Nelson et al.*, 1994]. Considering an average fish length of 10 cm [*Brandes and Mclain*, 2001], this transforms to swimming capabilities of 0.2 m s^{-1}. During the time periods under study (Table 5.1 and Table 5.2), average water velocities approach ≈ 0.45 m s^{-1} and ≈ 0.3 m s^{-1} during peaks in the ebb and flood tidal currents, respectively, suggesting that hydrodynamics is dominating over fish behavior. It is only at times when the velocities are weak and lower than O (10^{-1}) m s^{-1}, mainly near

Table 5.2 Simulation runs in the Eularian and Lagrangian frame.

Eulerian runs	Period	Bathymetry	Lagrangian Runs	Release Section	Depth limit in releases
E1A	From 3 to 9 Dec. 2008	Real	L1	A	Non
			L2	A	4 m
E1B	From 3 to 9 Dec. 2008	Straightened	L1	B	Non
			L2	B	4 m
E2A	From 15 to 21 Jan. 2009	Real	L1	A	Non
			L2	A	4 m
E2B	From 15 to 21 Jan. 2009	Straightened	L1	B	Non
			L2	B	4 m

the slack tide, that we expect the fish behavior to be in control of its motion. However, these times of "slack-water" only account for 19% and 26% of the time in the 2008 and 2009 time periods, respectively. The dominance of advective processes is, however, not true in the vertical direction, where water velocities are O (10^{-1}) m s^{-1} and even lower, and salmon should be able to move freely. The exact behavior of salmon in the vertical is largely unkown, hence, salmon free-movement in the vertical direction will be ignored in this first approximation to the problem. Despite the secondary importance of salmon-behavior in the horizontal direction, juvenile salmon could still swim, commonly to maintain position (positive retro-axis) [e.g., *Nelson et al.*, 1994]. In this first approximation we will assume, however, that salmon are passively driven by the currents.

5.3.2 Hydrodynamic model: Eularian frame

Simulations were conducted with a parallel version [*Acosta et al.*, 2010] of a three-dimensional primitive equation 3D-PE model [*Smith*, 2006]. The governing equations are first posed in layer-averaged form by integrating over the height of a series of horizontal layers separated by level planes. The layer-averaged momentum equations are solved using a semi-implicit, three-level, iterative leapfrog-trapezoidal finite difference scheme on a staggered Cartesian grid. Turbulent mixing is represented in the 3-D model using diffusion-like terms. Unresolved horizontal turbulent mixing of momentum and scalars is represented with a constant eddy-viscosity A_h and eddy diffusivity K_h, respectively (see details in Appendix A). The vertical viscosity A_z and diffusivity K_z are calculated using a two-equation model originally proposed by *Mellor and Yamada* [1974] and later modified by *Kantha and Clayson* [1994]. This turbulent

modeling approach is typically used in large scale models for geophysical flows due to their reduced computational burden. The model has been validated against analytical solutions, field and laboratory data sets collected in river confluences [*Ramón et al.*, 2015, Appendix A], and in particular, in the San Francisco Bay and the Delta region [*Smith et al.*, 2005; *Zamani et al.*, 2010]. Being the model hydrostatic, the importance of non-hydrostatic pressure effects need to be assessed. This can be done, as pointed by *Wang et al.* [2009], by considering the ratio β of the scales for the vertical and horizontal variability of the flow. For features with $\beta \approx O(1)$, those effects are significant and should not be neglected. For those with $\beta^2 << 1$, non-hydrostatic effects can be safely ignored. The latter is the case of the secondary circulation that develops within the model domain, which has a length scale in the order of the channel width *b* and a vertical scale equal to the depth of the channel *D*, and for which β^2 is of O (10^{-2}-10^{-3}), i.e. $\beta^2 << 1$. This suggests that these features are largely hydrostatic. The large with-to-depth ratio in the Sacramento River was pointed out by *Bever and MacWilliams* [2015], together with the size of the grid cells in their simulations (10 m, 5m and 0.5 m in the along, across and vertical direction, respectively), to be responsible for their simulations accounting for non-hydrostatic effects not significantly improving their predictions of secondary circulation in our study site.

5.3.3 Transport model of the Sacramento River

The limits of our model domain were chosen to match the location of existing USGS gaging stations. The N-, E-, S- and W- boundaries were placed at the location of USGS gaging stations USGS 11447890 (upstream boundary of the Sacramento River), USGS 11336600 (DCC boundary), USGS 11447903 (GEO boundary), USGS 11447905 (downstream boundary of the Sacramento River), respectively (Figure 5.1). Bathymetric information was provided by the USGS. The river geometry was discretized using grid cells of size (Δx, Δy, Δz) = (2, 2, 0.5) meters. The time step Δt was set to 1 s for stability purposes. The bottom drag coefficient, C_d, was set to 0.004 as proposed by *Smith* [2006] and slip conditions were assumed at the lateral walls. A_h was set to 0.1 $m^2 s^{-1}$. following equation $A_h = 0.3 \times D \times u^*$ [*Rastogi and Rodi*, 1978], where D (= 7 m) is the average depth in the Sacramento River and u^* is the friction velocity, calculated as $u^* = (g \times D \times I_c)^{0.5}$, where g is the acceleration due to gravity and I_c (= 7.4×10^{-4}) is the Sacramenteo-River channel slope within the study reach. This value is comparable to the value (A_h = 0.05 m^2

s^{-1}) used by *Wolfram* [2013] in a tidal river junction located ≈ 20 km downstream of our study site. Baroclinic effects were ignored in the model due to the homogenous density field within the study reach: flows in this portion of the Sacramento River are composed of freshwater inputs from the Sacramento River and the salinity front is located far away downstream of the study reach. The model was set to run using a second order space-centered method for momentum advection and two trapezoidal iterations after the initial non-smoothed leapfrog predictive step.

A spatial and temporal average water surface elevation (ζ) was obtained by averaging ζ values at the four USGS stations over the duration of each modelling period. This elevation was subtracted from water stage information (referred to NAVD88) on the bathymetry data to generate the final bathymetry of the model for each time period. Cells which were not inundated at this depth (those having negative depths relative to the average ζ) were not included in the domain. No allowance was made for lateral increases in the number of computational cells with tidal fluctuations (i.e., no wetting and drying of grid cells) since hydrodynamic effects, related to the expansion and contraction of flow area with tidal fluctuations, were assumed to be small owing to the generally steep channel walls. The river reach was assumed initially at rest. Discharge Q and ζ data recorded at the four USGS gaging stations (Figure 5.2) at 15 minute intervals were used as model boundary conditions. At the Sacramento-River downstream end (West boundary), the model was forced with information on ζ. The other three boundaries (upstream end of the Sacramento River, DCC and GEO) were forced with inflow rates (Figure 5.2). During the second simulated time period, DCC gates were closed, so only the remaining other three UGSG gaging stations were used as boundaries to the model (Figure 5.2c and Figure 5.2d). Simulations were started using boundary condition data one day prior to the modeling period of interest (warm-up period). The 3D velocity field was recorded each 150 s for its posterior use as input to the particle tracking model (see section 5.3.5)

To evaluate secondary-circulation effects on salmon entrainment rates, simulations were also carried out on a straight bathymetry (Run cases E1B and E2B in Table 5.2). The planform geometry for Cases E1B and E2B was obtained by rotating the Sacramento River channel until its axis became aligned with the y-axis (Figure 5.1d). DCC and GEO reaches were also rotated as independent blocks (with respect to the Sacramento River) in order to maintain the same junction angles as in the original

bathymetry. Run cases E1B and E2B were forced with the same boundary conditions as run cases E1A and E2A, respectively.

5.3.4 Model evaluation of river hydrodynamics

To evaluate the accuracy of the computed discharge in the system, modeled water stages in runs E1A and E2A were compared against recorded water stages at the North, East (for run E1A) and South boundaries where flow rates were prescribed, and modeled flow rates were compared against recorded flow rates at the West boundary where water surface elevations were prescribed. The model was also compared against nine ADCP transects collected in the field by the USGS during the simulated periods (Figure 5.1c, Figure 5.2). Transects T1-5 were only measured during the Dec. period, while transect T7 was only measured during the Jan. period. Transects were collected using ADCPs mounted on robotic boats, with bin sizes of 0.25 m in the vertical, and an ensemble spacing ranging between 0.5 to 1 m, depending on the speed of the robotic boat. Robotic boats were programmed to travel six times (three roundtrip passes) along each ADCP transect, so that each ADCP measurement is composed of six ADCP transects. The purpose of collecting six ADCP transects per time and location was to determine the time-averaged flow structures [*Dinehart and Burau*, 2005b; *Parsons et al.*, 2013]. The velocity mapping tool, VMT tool [*Parsons et al.*, 2013], was used in the averaging process. First the data on the six transect was projected onto a single cross-section that is roughly the centerline of the individual transects. Secondly, the projected data was interpolated to the cross-section grid, which was set to have a horizontal and vertical resolution of 1 m and 0.5 m, respectively. Finally, the projected and interpolated data on the six transect was averaged. Primary and secondary flow velocities were calculated using the Rozovskii method [*Rozovskii*, 1961; *Parsons et al.*, 2013], which is commonly used in the identification of helical motion at river confluences [e.g., *Rhoads and Kenworthy*, 1995, 1998] and is less sensitive than the zero-net-discharge method [*Markham and Thorne*, 1992] to deviations from perpendicularity in the angle formed between the cross-section and the depth-averaged flow direction [*Bever and MacWilliams*, 2015]. The Rozovskii's method rotates each vertical ensemble of velocity measurements such that primary and secondary velocity components are aligned parallel and perpendicular, respectively, to the orientation of the depth-averaged velocity vector. The E-W ($u_{E\text{-}W}$), N-S ($u_{N\text{-}S}$), primary (u_p) and secondary (u_{sec}) velocities were smoothed

with a moving average window of 4 and 10 cells in the vertical and horizontal directions. Modeled results were interpolated to each of the output cross-section grids from the VMT tool, and repeated transects were extracted each 150 s during the time that took the group of six transects to be collected in the field (≈ 15 min on average). The modeled transects were also processed using the VMT tool to calculate the time-averaged EW, NS, primary and secondary velocities. No smoothing was applied to the modeled transects.

Differences between observed and modeled quantities were evaluated with the *Murphy and Epstein* [1989] skill score, which is the ratio of the root-mean-square RMS error normalized by the standard deviation of the observation,

$$ME_{ss} = 1 - \frac{\sum (X_m - X_o)^2}{\sum (X_o - \langle X_o \rangle)^2} \tag{5.1}$$

where X_m and X_o are the modeled and the observed quantity at a given location, and $\langle X_0 \rangle$ is the temporal mean (for comparisons with USGS stations) or spatial mean (for comparisons with ADCP transects) of the observed quantity at a given location. A value of $ME_{SS} > 0.65$ is considered as *excellent*, $0.5 \leq ME_{SS} \leq 0.65$ *very good*, $0.2 \leq ME_{SS} \leq 0.5$ *good* and $ME_{SS} < 0.2$ *poor* [*Allen et al.*, 2007; *Wang et al.*, 2011, *Wolfram*, 2013].

5.3.5 Particle tracking model: Lagrangian frame

The positions of salmon within the river reach were simulated using the three-dimensional 3D time varying particle tracking model proposed by *Rueda et al.* [2008] and later modified to include the third dimension by *Hoyer et al.* [2014]. The trajectories of the neutrally-buoyant particles (salmon) were calculated as the summation over time of successive infinitesimal particle displacements dx_i (i = 1, 3):

$$dx_i = u_i(x,t) \cdot dt_T \tag{5.2}$$

Here, x and u are the particle position and velocity, respectively. The velocity at the present position of a given particle is interpolated, as proposed by *Pollock* [1988], from the velocity predicted at the grid points by the 3D hydrodynamic Eularian model. The discretization of Eq. (5.2) that represents the transition from the state (or particle position) at $n_T \Delta t$ to the state $(n_T+1)\Delta t$ is given as:

$$x_i(t+\Delta t_T) = x_i(t) + u_i(x(t),t)\cdot\Delta t_T \quad (5.3)$$

5.3.6 Particle releases and entrainment rates

In order to calculate fish entrainment rates over both simulated time periods, a dense cloud of particles was released every 15 minutes at sections A (real bathymetry) and B (straightened bathymetry) (Figure 5.1c and Figure 5.1d), ≈ 300 m upstream of the DCC entrance. A total of 96 particle-release experiments were run, starting at hour 56.8 and finishing at hour 80.6 from the start of each Eularian simulation. Particles were seeded uniformly: each particle was separated 20 cm from its nearest one, both in the horizontal and vertical direction. The distance of 20 cm was selected to ensure an elevated number of particles in each release. In a first series (runs L1, Table 5.2), particles were uniformly seeded over the whole water column, with an average total number of ≈ 19000 particles per release. In a second series (runs L2, Table 5.2), particles were also uniformly seeded but only in the shallowest 4 meters, where salmon are observed in the Sacramento River, with an average total number of ≈ 9000 particles per release. Any given particle in each release was simulated until it reached one of the model boundaries or until the end of the Lagrangian simulation (10 hr). After 10 hr, less than 2% of the released particles remained in the domain in all releases, except during the strong flood between hours 78-83 in runs E2A and E2B when up to 6% of the particles remained within the model domain after 10 hr. Although the model was able to reproduce the returning of some particles to a given junction in the next tidal cycle, the model tended to underestimate the number of particle returns due to the closeness of the North and West boundaries, falsely counting them as a particle-entrainment in those boundaries.

For each release, we defined a characteristic arrival time, or entrainment times T_e, to the SD and SG junctions, as the time when the maximum number of particles arrived to each of the junctions. This time should be, however interpreted with caution if there are long tales in the distribution of individual arrival times to a given junction, so that the conditions at the junction experienced by the different particles may be different. Also, there are particles that visit a given junction several times during the simulation, for example, if the particle bypass a given junction in an ebb tide, but it is advected back upstream in the following flood tide. Particle entrainment rates E_P into GEO and DCC

were calculated as the fraction of particles, that having left the domain, they did it through the South and East boundary, respectively.

The fraction of total outflow from the main Sacramento River entering the DCC and GEO channels (flow entrainment rates $E_{Q\text{-}DCC}$ and $E_{Q\text{-}GEO}$) was calculated with Eqs. (5.4) and (5.5), assuming that flow travel times are ignorable and assuming conservation of water volume. We further took into account in the calculation of E_Q the direction of the main channel flow (if it comes from upstream or downstream, Figure 5.3) that enters the side channel, as:

$E_{Q-DCC} = Q_{11336600}/Q_{T2}$	for $Q_{T2} > 0$ & $Q_{11336600} \geq 0$ & $Q_{T6} \geq 0$	Ebb tide	(5.4a)
$E_{Q-DCC} = Q_{11336600}/Q_{11447905}$	for $Q_{T2} < 0$ & $Q_{11336600} \geq 0$ & $Q_{T6} < 0$	Flood tide	(5.4b)
$E_{Q-DCC} = 1$	for $Q_{T2} > 0$ & $Q_{11336600} \geq 0$ & $Q_{T6} < 0$	Flow convergence into DCC	(5.4c)
$E_{Q-DCC} = 0$	for $Q_{11336600} < 0$	Flows in DCC entering the model domain	(5.4d)
$E_{Q-GEO} = Q_{11447903}/Q_{T2}$	for $Q_{T2} > 0$ & $Q_{11447905} \geq 0$ & $Q_{11336600} \geq 0$	Ebb tide	(5.5a)
$E_{Q-GEO} = Q_{11447903}/(Q_{T2} + Q_{11336600})$	for $Q_{T2} > 0$ & $Q_{11447905} \geq 0$ & $Q_{11336600} < 0$	Ebb tide with flows in DCC entering the model domain	(5.5b)
$E_{Q-GEO} = Q_{11447903}/Q_{11447905}$	for $Q_{11447905} < 0$ & $Q_{T6} \leq 0$	Flood tide	(5.5c)
$E_{Q-GEO} = 1$	for $Q_{11447905} < 0$ & $Q_{T6} > 0$	Flow convergence into GEO	(5.5d)

Where the different subscripts in the discharge Q refer to a USGS station number or to the T2 or T6 transects. Note that for the Jan. 2009 period when DCC gates were closed, $E_{Q\text{-}DCC} = 0$ during the entire tidal cycle and Eq. (5.5) reduced to conditions (5.5a), (5.5c) and (5.5d).

5.4 Results and Discussion

5.4.1 Hydrodynamic validation

Model skills, evaluated by comparing modeled and observed flows and water stages at the USGS gaging stations were satisfactory in all cases, with $ME_{SS} \geq 0.98$, as reported in Table 5.3. Small errors were expected to occur due to the fact that the observed data used as boundary conditions for the model does not conserve mass, as reported in Table 5.1. Model skills for the $u_{E\text{-}W}$, $u_{N\text{-}S}$, u_p and u_{sec} in transects T1-9 are reported in Table 5.4. Since the direction of the flow is correctly reproduced by the model (see quiver plots of the depth-averaged velocities in Figure 5.4), the behavior of the model in transects T1-T9 is better interpreted in terms of the primary and secondary velocities. Values of $ME_{SS} < 0.2$ for the primary velocities in Table 5.4 are related to model overestimations in the magnitude of the streamwise velocities at the locations of transects T2 and T9 during peak ebb tides (see Figure 5.4b, Figure 5.4h and Figure 5.4l) and to model underestimation of the streamwise velocities at the location of transect T8 during the flood tide (Figure 5.4g and Figure 5.4k). Values of $ME_{SS} < 0.2$ for the secondary velocities in Table 5.4 tend to occur at times when there is not a clear pattern of secondary circulation (helical motions) in the measurements. However, the model compare well ($ME_{SS} \geq 0.5$) with the measurements at times when the helical patterns are strong and evident in the observations. Observed and modeled secondary circulation in transects T1, T2, T4 and T9 during a peak ebb tide in the Dec. 2008 period are shown in Figure 5.5. Secondary flow consisted mainly in the classical secondary circulation in channel bends [*Rozovskii*, 1961] where flow is directed outwards near surface and inwards near the bed. The secondary circulation in T8 during the peak flood tide (Figure

Table 5.3 ME_{SS} of water stage and discharges at model boundaries.

			Run E1A	**Run E2A**
Boundary	**USGS gauging station**	**Variable**	ME_{SS}	ME_{SS}
North	USGS 11447890	Stage	1	1
East	USGS 11336600	Stage	0.99	-
South	USGS 11447903	Stage	0.98	0.99
West	USGS 11447905	Discharge	0.98	0.99

Table 5.4 ME_{SS} of the velocity fields between modeled and measured (ADCP) transects.

				ME_{SS} [a]			
T	**Run**	**Time (hr)**[b]	**Tidal phase**	$u_{E\text{-}W}$	$u_{N\text{-}S}$	u_p	u_{sec}
T1	E1A	125.72	Peak Ebb	−1.3	0.63	0.33	0.59
T2	E1A	127.33	Peak Ebb	-0.4	−1.3	−1.3	0.52
T3	E1A	130.68	Peak flood	0.96	0.86	0.95	−1.5
T4	E1A	139.10	Peak Ebb	0.76	0.22	0.32	0.42
T5	E1A	130.04	Peak flood	0.92	0.75	0.87	−0.5
T6	E1A	137.92	Peak Ebb	0.37	0.12	0.25	−0.5
T8	E1A	129.82	Peak flood	0.04	0.86	−0.7	0.73
T9	E1A	138.46	Peak Ebb	−0.5	0.49	−0.2	0.80
T6	E2A	86.53	Peak Ebb	0.34	0.07	0.21	−0.7
T7	E2A	87.70	Peak Ebb	0.63	0.43	0.50	−0.5
T8	E2A	81.82	Peak flood	0.80	0.94	0.56	0.73
T9	E2A	88.06	Peak Ebb	−0.4	0.68	0	0.86

[a] red = poor, blue = good, green = very good and excellent

[b] Time from start of simulation

5.5d and Figure 5.5i) is not driven by the presence of planform curvature. Instead, the curvature of the streamlines is due to Sacramento-River flows needing to curve, when coming from downstream, to enter GEO (Figure 5.3d-f).

5.4.2 Evolution of the strength of secondary circulation with the tidal flow

Time series of section-averaged primary velocity $\langle u_p \rangle$ and the root mean squared RMS of the secondary velocity $u_{sec\text{-}rms}$ calculated in transects T2, T4, T5, T7 and T9 for the second and third days of simulations in runs E1A and E2A are shown in Figure 5.6. The RMS of the secondary velocity $u_{sec\text{-}rms}$ is used as a proxy for the strength of the secondary circulation in a given cross-section as proposed by *Chant* [2002] and *Bever and MacWilliams* [2015]. When the DCC gates are closed (Figure 5.6a-c), the strength of the secondary circulation follows the average primary velocities (and discharges), with $u_{sec\text{-}rms}$ increasing as the magnitude (absolute values) of the average primary velocities (and discharges) increases, in all transects. $u_{sec\text{-}rms}$ values peak at the end of both the peak ebb and flood tides (see vertical lines in Figure 5.6a-c). Except for transect T9, which is located farther downstream and, thus, it is more influenced by the tides (especially evident during the flood tides, Figure 5.6b), the magnitude of the average primary velocities among transects remains similar for a given time. Yet, the strength of the secondary velocity in transects T5 and T9 (located immediately downstream of the SD

and SG junctions, respectively) at least double the strength of the secondary velocity in the other transects. This is especially evident during the ebb tides (Figure 5.6c). The presence of a strong secondary circulation in T5 and T9 is consistent with experiments with passive surface drifters carried out in the field (UGSG, unpublished results) and it would be consistent with the skewness of the salmon density maxima towards the outside margin of the bend as observed in the field near both transects [Blake and Horn, 2004; USGS, unpublished results]. When DCC is closed (Figure 5.6d-f), the strength of the secondary velocities exhibit similar patterns as if DCC gates were closed, except for transects T4 and T5 during flood tides. At those times, the strength of the secondary circulation in T4 and T5 is influenced by the dynamics of the SD junction, when part of the flow is diverted to the DCC channel (Figure 5.6d). Although the pattern is more erratic during these periods, it is clear from Figure 5.6f that the strength of the secondary circulation in transects T4 and T5 during floods tides almost doubles the strength of the secondary circulation during the flood tides in the E2A run, when the DCC gates were closed (Figure 5.6c).

The strength of the secondary circulation in a given transect, in general, grows almost linearly with the magnitude of the primary velocities during the ebb tides (Figure 5.7), independently of whether DCC gates are closed or open. The slopes of the best-fitting lines tend to be slightly higher when the DCC gates are closed (Table 5.5), but these differences are not significantly different in a statistical sense ($p > 0.01$ in the paired t-test analysis). This suggests that closing the DCC gates *per se* does not significantly increase the strength of the secondary circulation in the downstream sections. Opening the DCC gates seems to affect the strength of the secondary circulation at downstream locations through changes in the discharges (and so in the magnitude of the primary velocities) at those locations. The relationship between the $u_{sec\text{-}rms}$ and $\langle u_p \rangle$ does not change as a result of flow reversals in transects T1, T4 and T5. This is not the case, though, of transects T7 and T9, for which the relation between the $u_{sec\text{-}rms}$ and $\langle u_p \rangle$ changes depending on the phase of the tidal cycle and, hence, on the flow direction (Figure 5.7d and Figure 5.7e). The slopes of the regression lines during the flood tides doubles the slopes during the ebb tides in transect T7 (Table 5.5), while, in transect T9, the slopes during the flood tides, only, represent ≈ 13% of those during the ebb tides (Table 5.5). The opposite behavior of $u_{sec\text{-}rms}$ in transects T7 and T9 is consistent with results by

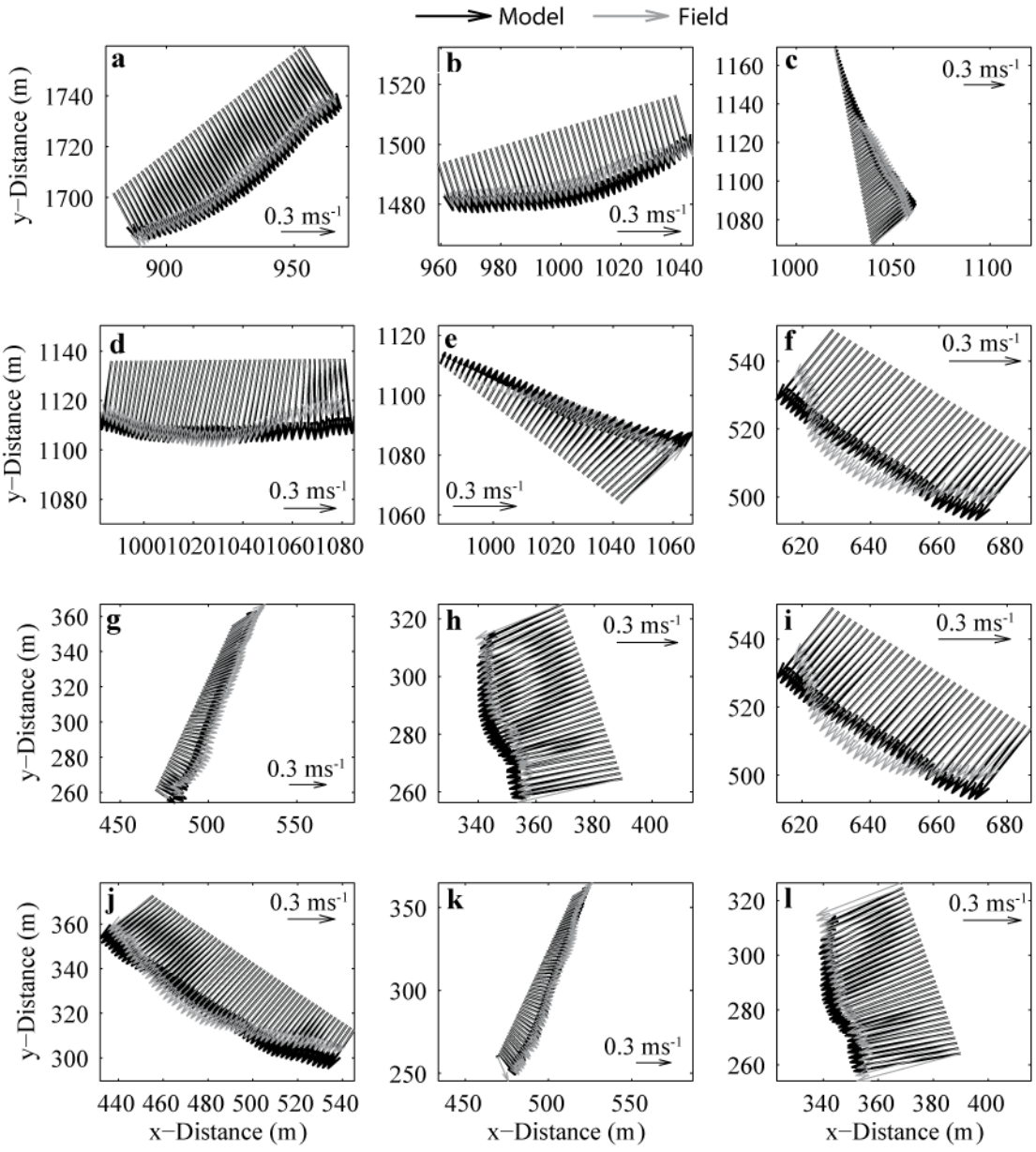

Figure 5.4 Quiver plots of the modeled and observed depth-averaged E-W and N-S velocities in transects (a) T1, (b) T2, (c) T3, (d) T4, (e) T5, (f,i) T6, (g,k) T8, (h,l) T9 and (j) T7 collected during the (a-h) Dec. 2008 and the (i-l) Jan. 2009 periods.

Bever and MacWilliams [2015] at the SG junction. They suggest that transects on the upstream side of a tidal bend experienced the strongest secondary circulation on flood-directed flow because the flow travelled through a longer distance of curved channel than on ebb flow, while the opposite occurs in transects on the downstream side of bends. For that purpose they calculated the relaxation lengths for the generation or decay of the

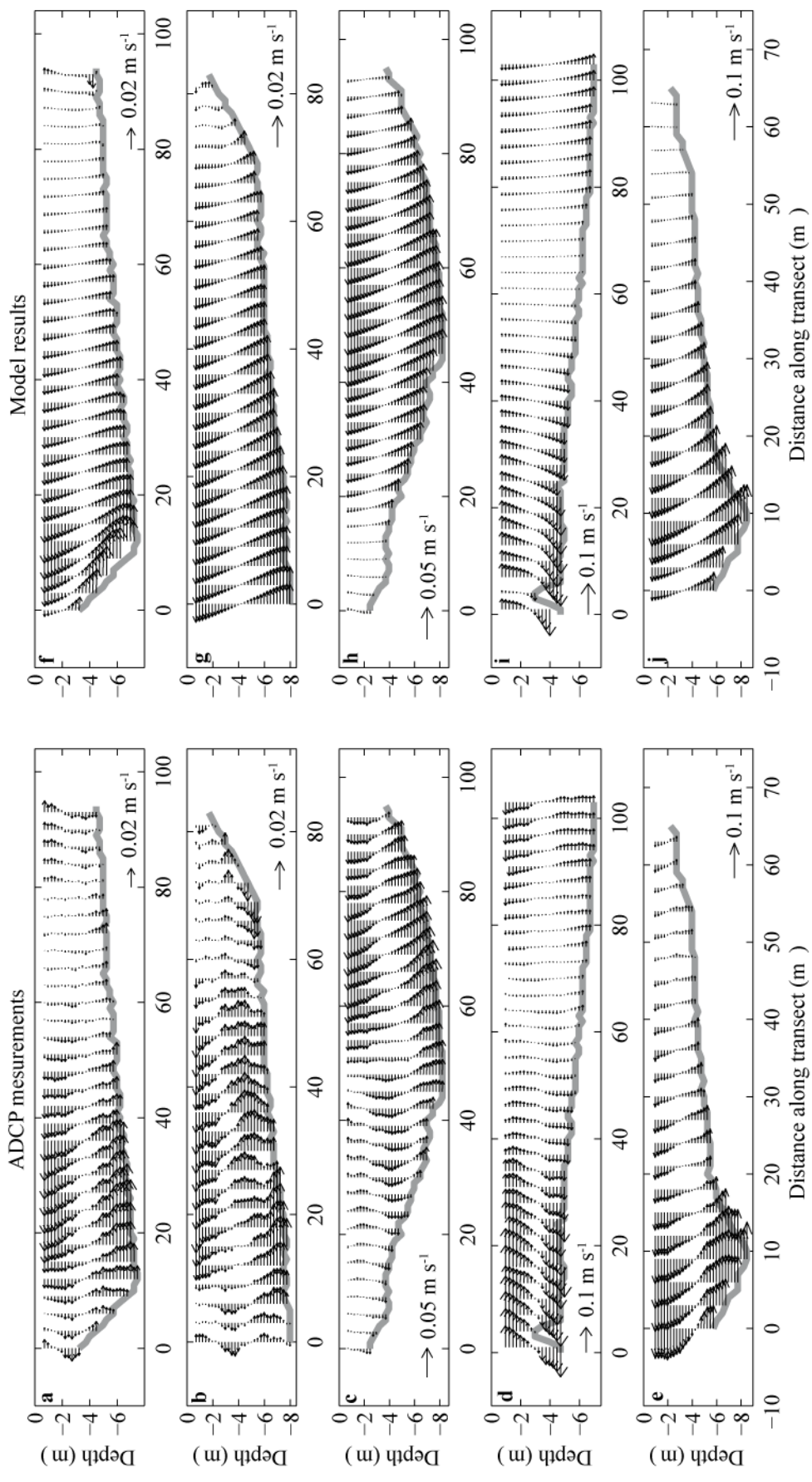

Figure 5.5 Measured (a-e) and modeled (f-j) secondary circulation in transects (a, f) T1, (b, g) T2, (c, h) T4, (d, i) T8, and (e, j) T9 during the Dec. 2008 period (Table 5.4). Every third velocity ensemble is shown for clarity. Secondary velocity is exaggerated by a factor of 100 with respect to the vertical velocity. Views are downstream.

secondary circulation, which represents the distance through the bend necessary for the secondary circulation to reach 63% of the maximum value. For the river bend near the SG junction (Figure 5.1c) they calculated a relaxation length of only 95 m, which would explain the different behavior of T7 and T9 (which are ≈ 125 m apart) in such a short distance. Note that during the ebb tides, transect T9 is in the downstream end of this river bend, and the opposite, during the flood tides, transect T7 is downstream of this river bend.

5.4.3 Fish entrainment: influence of the planform shape of the domain and particle-seeding depths

Flow and particle entrainment rates, E_Q and E_P, during three tidal periods are shown in Figure 5.8 and Figure 5.9 for the experiments conducted in Jan. 2009 and Dec. 2008 period, respectively. Under closed-gate conditions (Jan. 2009), particle entrainment rates in GEO increase during the ebb tide, following the changes in $E_{Q\text{-}GEO}$. In the experiments conducted with the realistic bathymetry, particle entrainment rates tend to be

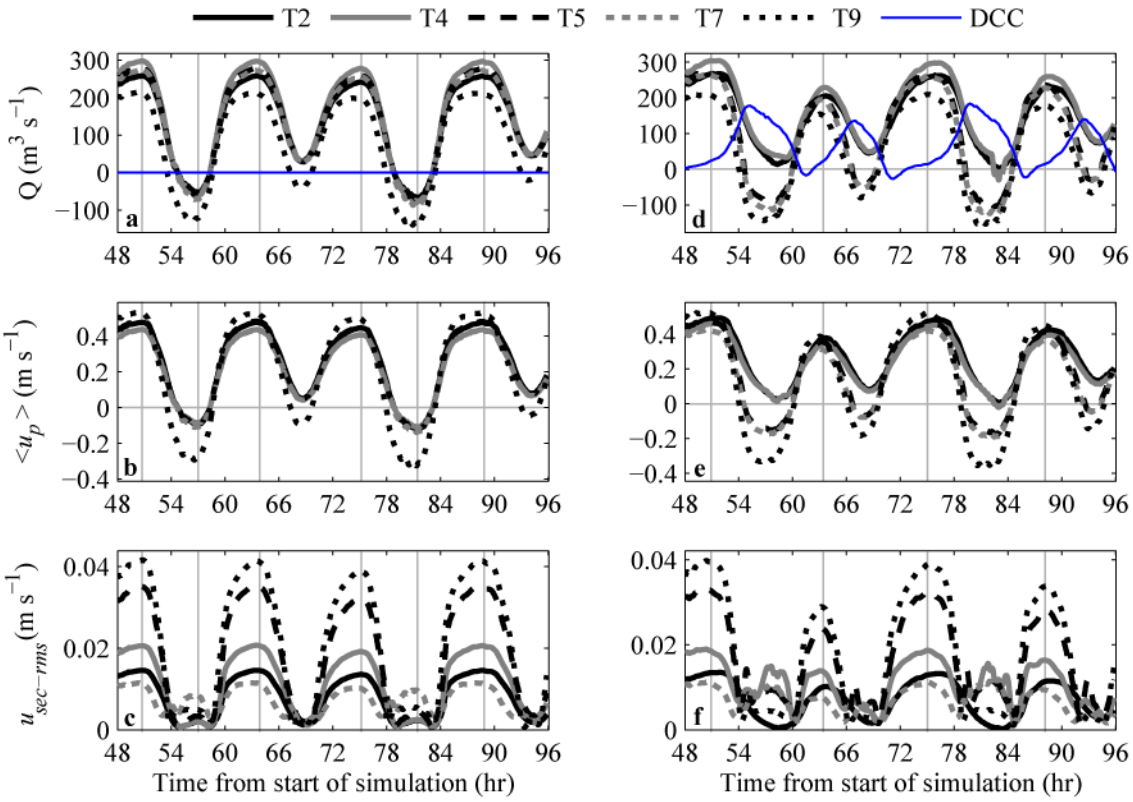

Figure 5.6 (a, d) Discharges, (b, e) section-averaged primary velocities and (c, f) strength of the secondary circulation in transects T2, T4, T5, T7 and T9 for the third and fourth days of simulation in runs (a-c) E2A and (d-f) E1A. Vertical light gray lines show the time of peaks in the strength of the secondary circulation.

lower than $E_{Q\text{-}GEO}$ in the first hours of the ebb tide if the particles are released at all depths, with values of $E_{P\text{-}GEO}$ slight higher than $E_{Q\text{-}GEO}$ at the end of the ebb tide (Figure 5.8c, light blue dots). The magnitude of the particle entrainment rates $E_{P\text{-}GEO}$ for the shallow releases (green dots in Figure 5.8c), in turn, are higher than the $E_{Q\text{-}GEO}$ during practically the entire ebb tide. The strong sensitivity of $E_{P\text{-}GEO}$ exhibited in the simulations conducted with realistic geometry to the depth of the release, was not evident in the simulations with the straightened bathymetry (dark blue and red colors in Figure 5.8c), for which $E_{p\text{-}GEO} \approx E_{Q\text{-}GEO}$. The sensitivity of entrainment rates to the initial distribution of particles is interpreted as the result of the secondary circulation developing in curved channels. These effects, favoring the entrainment rates of shallow populations of particles are only observed during the ebb tides, when the secondary circulation is the strongest (Figure 5.8b and Figure 5.6). Root mean square differences between E_Q and E_p average

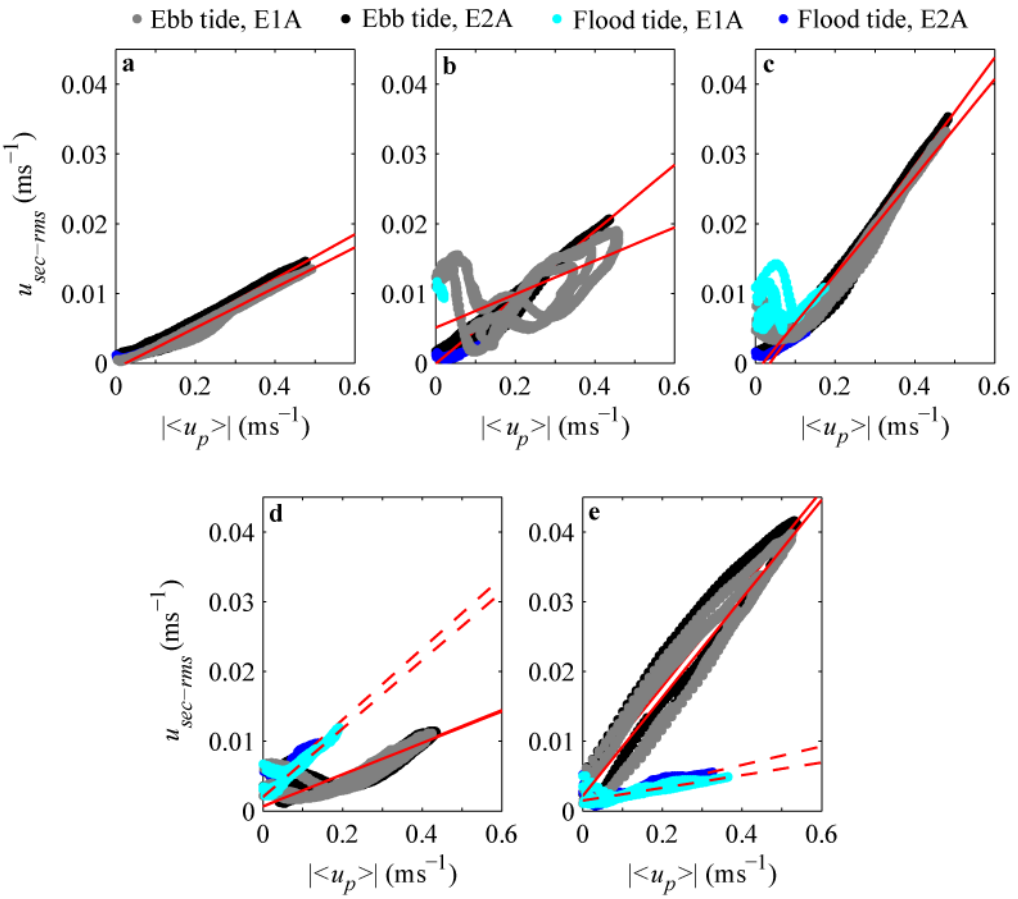

Figure 5.7 Strength of the secondary circulation *vs*. section-averaged primary velocities (|absolute values |) for the third and fourth days of simulations in runs E1A and E2A in transects (a) T2, (b) T4, (c) T5, (d) T7 and (e) T9. Red solid lines in (a-e) and red dashed lines in (d-e) show the fitted lines (least squares fit) for the ebb and flood tides, respectively.

Table 5.5 Slopes *I* and correlation r^2 of the least-squares fit lines in Figure 5.7.

	E1A Ebb		E2A Ebb		E1A Flood		E2A Flood	
Transect	***I***	**r^2**	***I***	**r^2**	***I***	**r^2**	***I***	**r^2**
T2	0.0288	0.990	0.0318	0.985	-	-	-	-
T4	0.0240	0.438	0.0475	0.988	-	-	-	-
T5	0.0701	0.963	0.0776	0.991	-	-	-	-
T7	0.0227	0.822	0.0231	0.826	0.0490	0.956	0.0509	0.867
T9	0.0707	0.951	0.0702	0.947	0.0091	0.826	0.0133	0.884

0.14 and 0.12 during the ebb tides for runs E2AL1 and E2AL2, respectively, indicating and average 13 % deviation with respect to the 1:1 line. While in the simulations with the straight bathymetry these difference average 6 %. The 13% variability would be consistent with the variability observed in the field in previous salmon-release experiments [e.g., *Perry et al.*, 2010; *Cavallo et al.*, 2015; *Perry et al.*, 2015], where salmon entrainment rates into GEO, averaged over a 24-hr release experiment, deviated up to 20% with respect to the 1:1 line with the average flow entrainment on that time period.

When the DCC gates are open, the effect of the secondary-circulation on the particle entrainment rates during the ebb tide are still evident at GEO, especially after the first 2 hr from the beginning of each ebb tide when the signal is not longer influenced by the arrival of particles from the previous flood (Figure 5.9d), and when the RMS difference between particle entrainment and flow entrainment averaged ≈ 10 % in runs E1AL1 and E1AL2, and 5% and 7% in runs E1BL1 and E1BL2, respectively. Those effects are less evident in DCC, with RMS differences of 20% occurring during the ebb tide in all runs (Figure 5.9b), which indicates that the deviation from the 1:1 line is not driven by the secondary-circulation effects. The lower sensitivity of particle entrainment rates to the vertical distribution of particles is consistent with a weaker secondary-circulation in the transects located upstream of DCC (Figure 5.6). Alternatively, a weaker secondary-circulation effect at the SD junction could be due to the proximity of the particle-release section (only 300 m upstream). Within this short distance, secondary circulation effects could have not had time enough to significantly distort the homogeneous shape of the initial particle-release cloud.

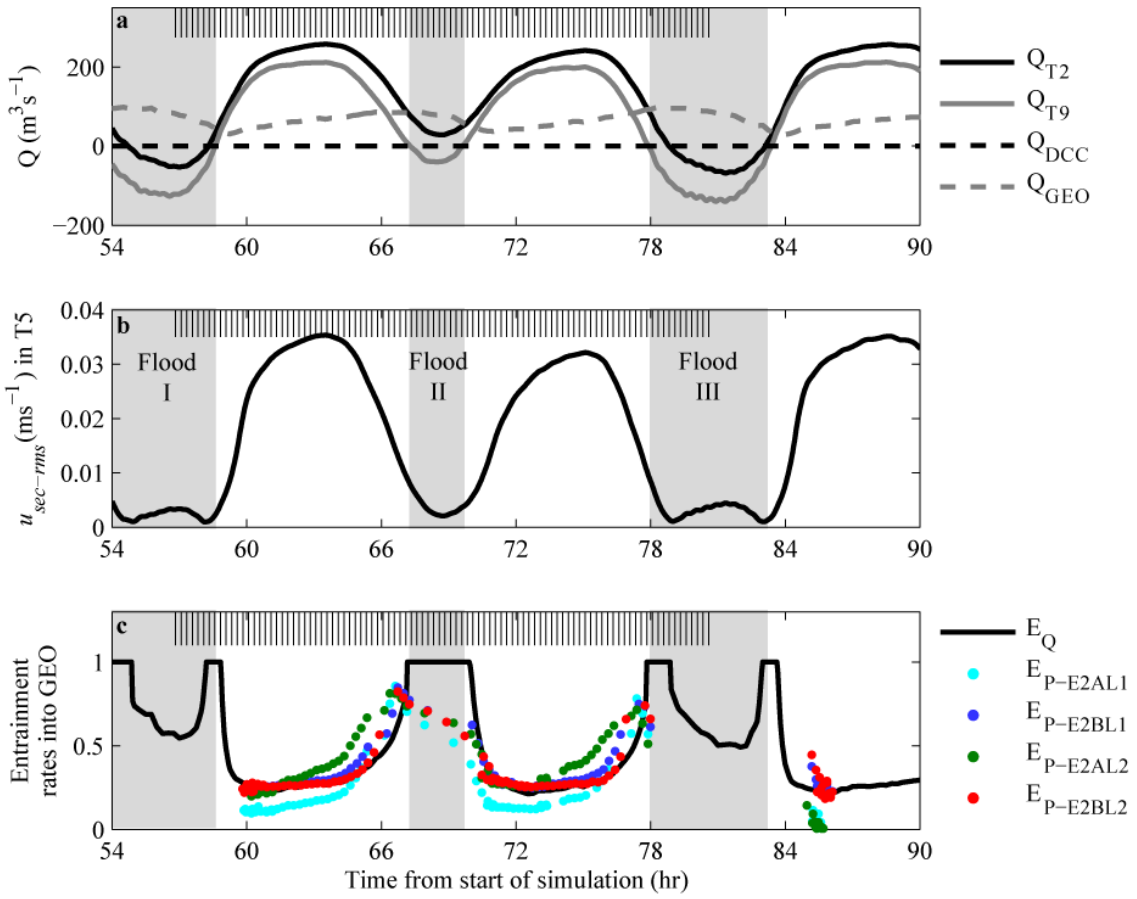

Figure 5.8 (a) Discharges, (b) Strength of the secondary circulation in transect T5 and (c) flow and particle entrainment rates into GEO for the particle release experiments when the DCC gates were closed (Jan. 2009 period). Gray shaded areas mark the flood tides. Vertical lines at the top of each plot show particle-release times.

During flood II in run E2A (Figure 5.8c), $E_{P\text{-}GEO}$ is below $E_{Q\text{-}GEO}$. This is the result of long tales forming in the time of arrival of particles when discharges are so low (see Figure 5.10 as an example). Thus, although a great number of particles arrived at SG during the flood tide, when entrainment rates are supposed to be ≈ 1, a significant amount of particles arrived at the beginning of the next ebb tide, decreasing the overall $E_{P\text{-}GEO}$ of the release. Flood III in Figure 5.8c represents a particular case in which both the flows in T2 and T9 reversed during the flood tide (flow is directed upstream, Figure 5.3f and Figure 5.8a). Thus, during that time none of the particles arrived to the SG junction. Particles that did not leave the domain through the North boundary were advected back downstream in the next ebb tide, with the particle-entrainment times of those releases coinciding within hours 84.5-86 within the following ebb tide, and with $E_{P\text{-}GEO}$ ranging from 0 to 0.23. Overall, our particle-release experiments seem to be more effective in

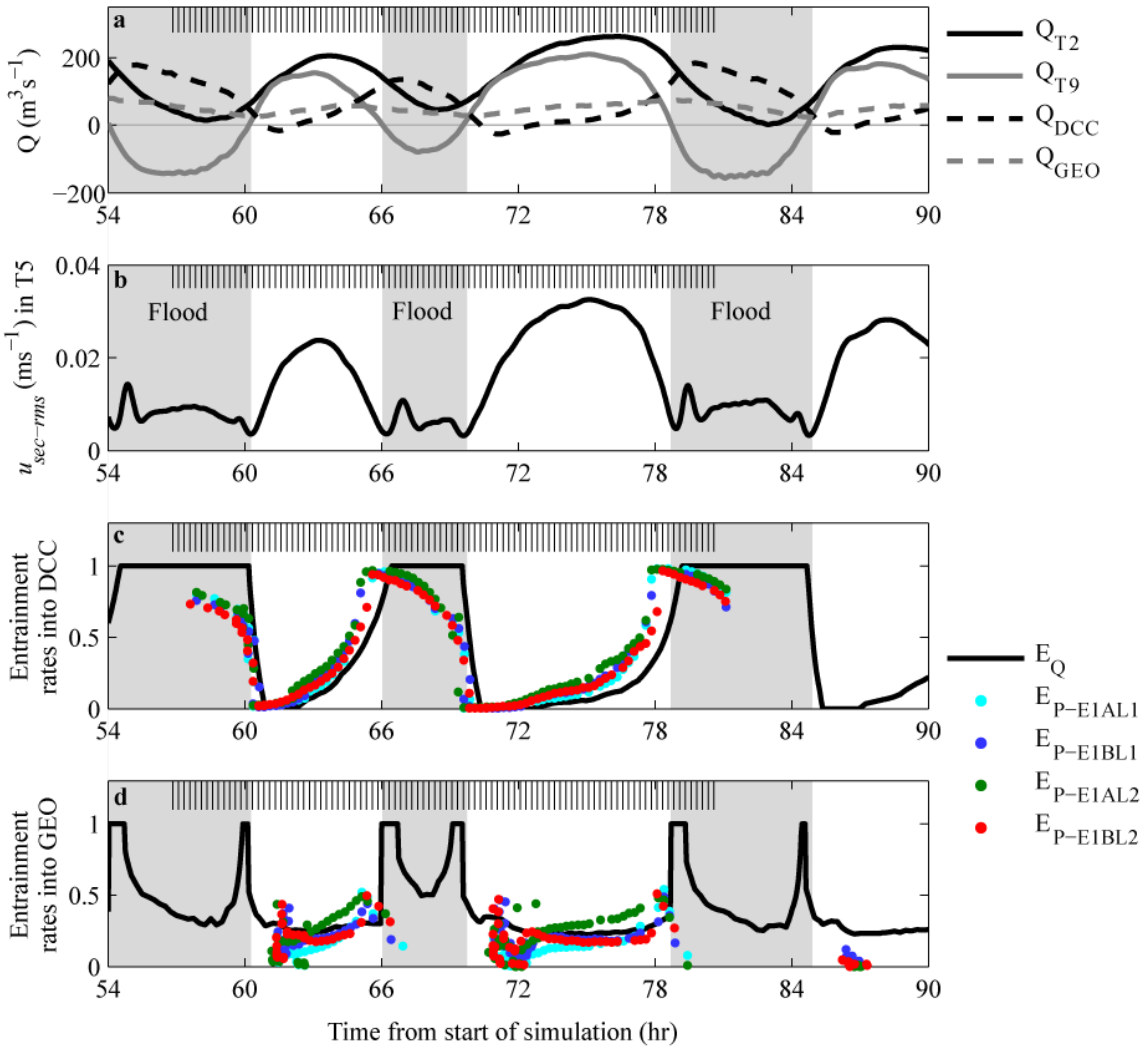

Figure 5.9 (a) Discharges, (b) Strength of the secondary circulation in transect T5, and (c-d) flow and particle entrainment rates into (c) DCC and (d) GEO for the particle release experiments when the DCC gates were open (Dec. 2008 period). Gray shaded areas mark the flood tides. Vertical lines at the top of each plot show particle-release times.

tracking the entrainment rates of particles during the ebb tides, when the tails in the particle arrival times are shorter.

5.5 Preliminary conclusions and future work

Three dimensional simulations, both in the Eularian and Lagrangian frame, have been conducted in a reach in the Sacramento River, which is important in the out-migration of the juvenile Chinook salmon, and where river hydrodynamics is strongly affected by the tides and where strong secondary circulation develops. These preliminary results suggest that the secondary circulation is stronger during the ebb tides, and they also suggest, by

comparing simulations in the real and an straightened bathymetry, that it is during the ebb tides when secondary-circulation effects influence the final fate (migration route selection) of salmon, by pushing water towards the outer side of the bend near surface, where the entrance of the two lower-survival migration routes are located. Secondary-circulation effects are further reinforced by the preference of salmon for migrating within locations near surface. Although promising, further research needs to be done before attempting to publish these results. First, although model results generally compare well with the velocity fields in the ADCP transects collected in the field; there are still some inconsistencies between modeled and measured results. For example, in transect T9 the model tends to overestimate the streamwise velocities (Figure 5.4). This error is, in part, associated with the tendency of the model to overestimate discharges (≈ 10 m^3 s^{-1}) at the West boundary during the peak ebb and flood tides, but also with local underestimations of the bottom drag, and hence, longitudinal water surface slopes. Note that the bottom drag coefficient is assumed constant in the computational domain. Lateral friction effects could be also important in some locations within the river reach (as could be seen for example in transect T7 in Figure 5.4) which are not accounted for in the model, which assumes slip conditions in the lateral walls. Future simulations should include these effects. The importance of non-hydrostatic effects (which are not accounted for in the Eularian model) in this river reach are also unknown. However, *Wolfram* [2013] suggested, in their study of a river reach further downstream in the Delta, that non-hydrostacity could have some important local effects. The way particle entrainment rates

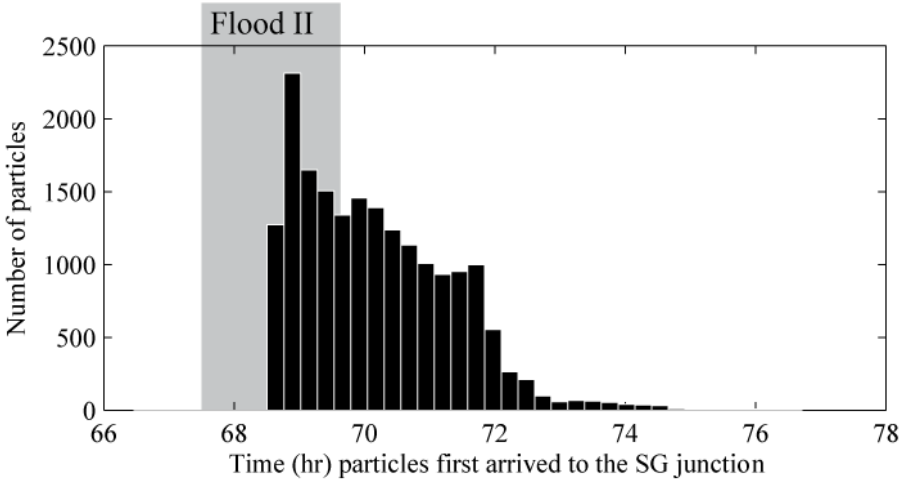

Figure 5.10 Example of histogram showing the distribution of particles first arrival-times to the SG junction during flood II in Figure 5.8.

and times are calculated should be also rethought. Both quantities are strongly influenced by the length of the time interval within which particles arrive to a given junction. It would be then more appropriate to group together particles of all releases based on their time of arrival to a given junction and calculate an entrainment rate for each of these groups. These would be especially important in order to properly quantify entrainment rates during the flood tides. It would be also necessary to increase the model domain, specifically by moving the North and West boundaries farther upstream and downstream, respectively, to correctly account for particles that having bypassed the SD and the SG junctions would have been advected back into the model domain in the following tidal cycle. Very recently, *Hoyer et al.* [2015] developed a novel technique of tracking particle trajectories backwards, from a drinking water intake toward their source areas. This approach would be especially interesting in this river reach where by releasing particles in both GEO and DCC we would be able to define the time-variability of the "entrainment zones" (areas of flow entrainment in the Sacramento River) to these two migration routes, based on the backwards analysis of the trajectories of particles. Given that the behavior of salmon within this river reach is yet poorly understood, there was no attempt to include any sort of behavioral rules; however, future model efforts should try to include the salmon preference for locations near surface, and maybe also their preference for actively migrating at night. These should be the result of a close collaboration with researchers studying the behavior of juveniles in the Delta

General conclusions

By means of field and numerical experiments, we have studied the spatial arrangement of the Ebro and Segre rivers at their confluence and river mixing rates downstream of it in the presence of density contrasts between the two rivers. These are some of the specific conclusions

1. The spatial arrangement of inflows and their mixing rates at the large asymmetrical river confluence under study are largely controlled by the ratio between forces driving the cross-stream motion of the side inflow (inertia, buoyancy, and centrifugal forces associated with the meandering form of the main stream) and the inertial forces in the mainstream. The behavior of the confluent streams can be parameterized in terms of an internal Froude number and the velocity ratio between the confluent streams.

2. Mixing rates under weak density contrast of up to O (10^{-1}) kg m^{-1}, typical of large river confluences, were up to 40% larger than those simulated under neutrally buoyant conditions. This increase in mixing is largely the result of density contrasts leading to changes in the contact area between water masses available for mixing.

3. Stronger density contrasts, which might lead to nearly horizontal contact areas shortly downstream of the confluence, will lead to weaker mixing rates compared to weakly buoyant conditions, as a result of the stabilizing effect of strong vertical density gradients.

4. In the Ebro-Segre confluence the distortion of the mixing layer is largely controlled by the strength of the cross-stream motions, which, in turn, are driven by a subtle interaction between baroclinic, inertial and centrifugal forces.

5. The existence of channel irregularities near confluences leading to the development of dead zones might accelerate the rate at which water masses mix downstream of river junctions.

6. At time of strong density contrasts, the plunge point between rivers will move to upstream locations as the confluence Froude number decreases and/or the velocity ratio increases (for low velocity ratios). As the velocity ratio (tributary inertia) keeps

increasing, though, the plunge point tends to move to downstream locations due to the increasing rates of turbulent diffusion that tend to keep the tributary flow attached to bed, shifting the orientation of the mixing interface towards more vertical positions.

7. River mixing downstream of the confluence is strongly dependent on the location of the plunge point between the confluent rivers. The biggest mixing rates occur when the plunge point is located at the confluence itself due to a combination of a big contact area of the interface between rivers and high mixing coefficients, especially in the vertical direction.

8. The effect of wind forcing on the spatial arrangement of the confluent rivers depends on both wind velocity and direction, but can completely alter the inertia-buoyancy equilibrium at the confluence and even move the location of the plunge point from locations upstream of the junction apex to locations downstream of the confluence, and hence, modify river mixing rates. Winds opposite to the direction of the main stream are more effective in increasing shear at the confluence, and in turn, in increasing river mixing.

9. Unsteady river-inflows change the streamwise equilibrium location of the plunge point through time. This is important since mixing rates decrease as the plunge point moves to locations upstream of the confluence. There is a delay in time between the shift in the equilibrium conditions and the corresponding streamwise movement of the plunge point.

From the numerical experiments performed at the reach of the Sacramento River we have obtained the following conclusion:

10. The secondary circulation in the DCC-GEO bend is generally stronger during the ebb tides and it is during the ebb tides when secondary-circulation effects influence the final fate (migration route selection) of salmon, by pushing water towards the outer side of the bend near surface, where the entrance of the two lower-survival migration routes are located. Secondary-circulation effects are further reinforced by the preference of salmon to migrate within locations near the surface.

Conclusiones generales

A través de experimentos de campo y numéricos, se ha estudiado la distribución espacial de los ríos Ebro y Segre una vez confluyen en el embalse de Ribarroja y sus tasas de mezcla aguas abajo de su confluencia bajo la presencia de contrastes de densidad entre los ríos. Estas son alguna de las conclusiones específicas:

1. La distribución especial de los ríos y la tasa a la que estos se mezclan están controladas, en la confluencia asimétrica de estudio, por la razón entre las fuerzas responsables del movimiento transversal del tributario (inercia, flotabilidad y fuerzas centrífugas asociadas a la forma meandriforme de la corriente principal) y las fuerzas inerciales en la corriente principal. El comportamiento de las masas de agua en la confluencia puede ser parametrizado en términos del número interno de Froude y la razón de velocidades entre los ríos confluyentes.

2. Las tasas de mezcla bajo la presencia de pequeños contrastes de densidad de hasta O (10^{-1}) kg m^{-1}, comúnmente presentes en confluencias de gran tamaño, pueden ser hasta 40% mayores que las tasas de mezcla simuladas en condiciones de cero flotabilidad. Este aumento en la mezcla se debe en gran medida a que los contrastes de densidad llevan a cambios en el área de contacto disponible para la mezcla entre las dos masas de agua.

3. Mayores contrastes de densidad, que podrían resultar en interfases de contacto cercanas a la horizontalidad justo aguas abajo de la confluencia, darían como resultado menores tasas de mezcla comparado con la presencia de débiles contrastes de densidad. Esto se debe al efecto estabilizador de los fuertes gradientes verticales de densidad.

4. En la confluencia de los ríos Ebro y Segre, la deformación de la interfaz de mezcla está controlada principalmente por la intensidad de los movimientos transversales, los cuales a su vez vienen determinados por la interacción entre las fuerzas baroclínicas, inerciales y centrífugas.

5. La existencia de zonas muertas puede acelerar la tasa a la que se mezclan los ríos aguas abajo de su confluencia.

6. Cuando existen fuertes contrastes de densidad, el punto de hundimiento del río más denso se moverá aguas arriba a media que el número de Froude disminuya y/o a medida que la razón de velocidades entre el tributario y la corriente principal aumente (para pequeñas razones de velocidad). Sin embargo, a medida que la razón de velocidades (la inercia del tributario) siga aumentando, el punto de hundimiento tenderá a desplazarse nuevamente hacia localizaciones aguas abajo debido al aumento de la difusión turbulenta que impide que el agua del tributario se separe del lecho, y que hace que la orientación de la interfase de mezcla cambie hacia una disposición vertical.

7. Las tasas de mezcla aguas abajo de la confluencia dependen en gran medida de la localización del punto de hundimiento. Los valores más altos de mezcla se producen cuando el punto de hundimiento se localiza en la región de la confluencia debido a una combinación de grandes superficies de contacto entre las dos masas de agua y a valores altos de difusividad, especialmente importantes en la dirección vertical.

8. El efecto del forzamiento del viento en la distribución espacial de las masas de agua, aunque depende tanto de la magnitud como de la dirección del viento, puede alterar completamente el equilibrio inercia-flotabilidad de la confluencia e incluso desplazar el punto de hundimiento desde localizaciones aguas arriba de la confluencia a localizaciones aguas abajo de la misma, con el consecuente efecto sobre las tasas de mezcla. Los vientos cuyo forzamiento es opuesto a la dirección de flujo de la corriente principal son los más efectivos en el aumento de la cizalla y, por tanto, en el aumento de las tasas de mezcla.

9. La presencia de caudales no estacionarios en los ríos conlleva cambios temporales en la localización de equilibrio del punto de hundimiento, lo que tiene importantes consecuencias en términos de mezcla ya que las tasas de mezcla disminuyen a medida que el punto de hundimiento se aleja (tanto aguas arriba como aguas abajo) de la confluencia. Hay un desfase temporal entre un cambio en las condiciones de equilibrio y el movimiento del punto de hundimiento como respuesta del sistema a dicho cambio.

De los experimentos numéricos realizados en el tramo del río Sacramento se ha obtenido la siguiente conclusión preliminar:

10. La fuerza de la recirculación lateral en el meandro DCC-GEO es generalmente mayor durante la marea vaciante y es en la marea vaciante cuando esta recirculación puede influir en el destino final (elección de una ruta migratoria) de los salmones, mediante el desplazamiento del agua en superficie hacia el exterior del meandro, que es donde se sitúan las entradas a las dos rutas migratorias con las menores tasas de supervivencia de los salmones. La preferencia de los salmones por migrar cerca de superficie refuerza los efectos de la recirculación lateral.

Appendix A

Simulation of turbulent flows in river confluences and meandering channels with a Cartesian 3D free surface hydrodynamic model

Published in *Int .J. Comput. Methods,*
doi: 10.1142/S0219876215500358

Abstract

Three-dimensional primitive equations (3D-PE) become a reasonable approach in hydrodynamics in terms of computational costs when the length of the computational domain and/or computational time scales increases. However, given the simplified set of equations used in the analysis, results with 3D-PE-based models are expected to be approximate and before attempting to reproduce complex natural flows they first need to be validated against more simple flows observed in laboratory settings. Here, the validity of Cartesian free-surface hydrodynamic models to reproduce three turbulent flows characteristic of river environments is tested: (1) the development of shallow mixing layers, (2) flow pass a lateral cavity and (3) flow in open channel with mild curvature. Errors between measured and modeled values were generally less than 10%, proving their validity to reproduce such turbulent flows and their potential for simulations in more complex natural environments, such it is the case of the confluence between the Ebro and Segre rivers into the Ribarroja reservoir.

A.1 Introduction

River confluences are critical points in river networks where strong physical and chemical gradients develop, resulting in a wide range of distinctive environmental conditions (habitats) for biological growth. Large variations in water chemistry [*Kiffney et al.*, 2006; *Gooseff et al.*, 2008] have been reported to occur at these sites. As a consequence of their high spatial and temporal heterogeneity of habitats and resources, river confluences behave as biological hotspots, where the number of species appears to increase very significantly in comparison with other river reaches [*Benda et al.*, 2004].

This is partly due to confluences being sites of complex three-dimensional hydraulics which may include [*Best*, 1987] (1) a zone of flow stagnation at the junction apex, (2) flow deflection where each tributary enters the confluence, (3) a zone of flow separation below the downstream junction corner, (4) an area of maximum velocity, (5) a gradual flow recovery downstream of the flow-separation zone, and (6) several distinct shear layers associated with vortex generation. Another hydrodynamic feature typically present is the development of two counter-rotating cells [e.g., *Rhoads and Kenworthy*, 1995] at both sides of the shear layer which develop due to the presence of transverse pressure gradients as a result of local scale variations in the free surface elevation. The characteristics of all these features are, in turn, influenced by many controlling factors such as the junction planform, junction angle, momentum flux ratio, topographic steering and bed discordance (differences between the depths of the confluent streams) [e.g. *Biron et al*., 1993; *Bradbrook et al*., 2000].

Due to this complexity, developing a general theoretical model for river confluences is a challenge, especially because most of the knowledge of river confluence dynamics comes from laboratory and field studies, which both suffer from limitations, such as being site-specific or having limited spatial and/or temporal data resolution (especially in large river confluences). Numerical models, then, represent the most sophisticated tools for trying to characterize the complexity of river currents at confluences. However, due to complex bed geometry, high three-dimensionality in the flow field and the need for accurate turbulence representation of the mixing-layer zone, river confluences represent also a challenge for hydrodynamic modelling [*Biron and Lane*, 2008]. This is especially the case as the length scales of river confluences and/or the time scales of the phenomena aimed to study increase, where a compromise exists between the accuracy of the turbulent phenomena we need to solve and the practical computational costs of such simulations. The confluence between the Ebro and Segre rivers at the tail of the Ribarroja reservoir in Northern Spain (Figure A.1) is an example of this challenge. The confluence of these rivers is characterized by a large (near 90^o) junction angle and a curved planform which bends to the left immediately downstream of the confluence with a radius of curvature R_s ca. 3 km and a post-confluence width b_p of ≈ 400 m, $R_s/b_p \approx 7.5$ (Figure A.1, reach R1). Depths of the Ebro and Segre rivers are discordant with the Segre River entering the confluence through two channels of depths *D*

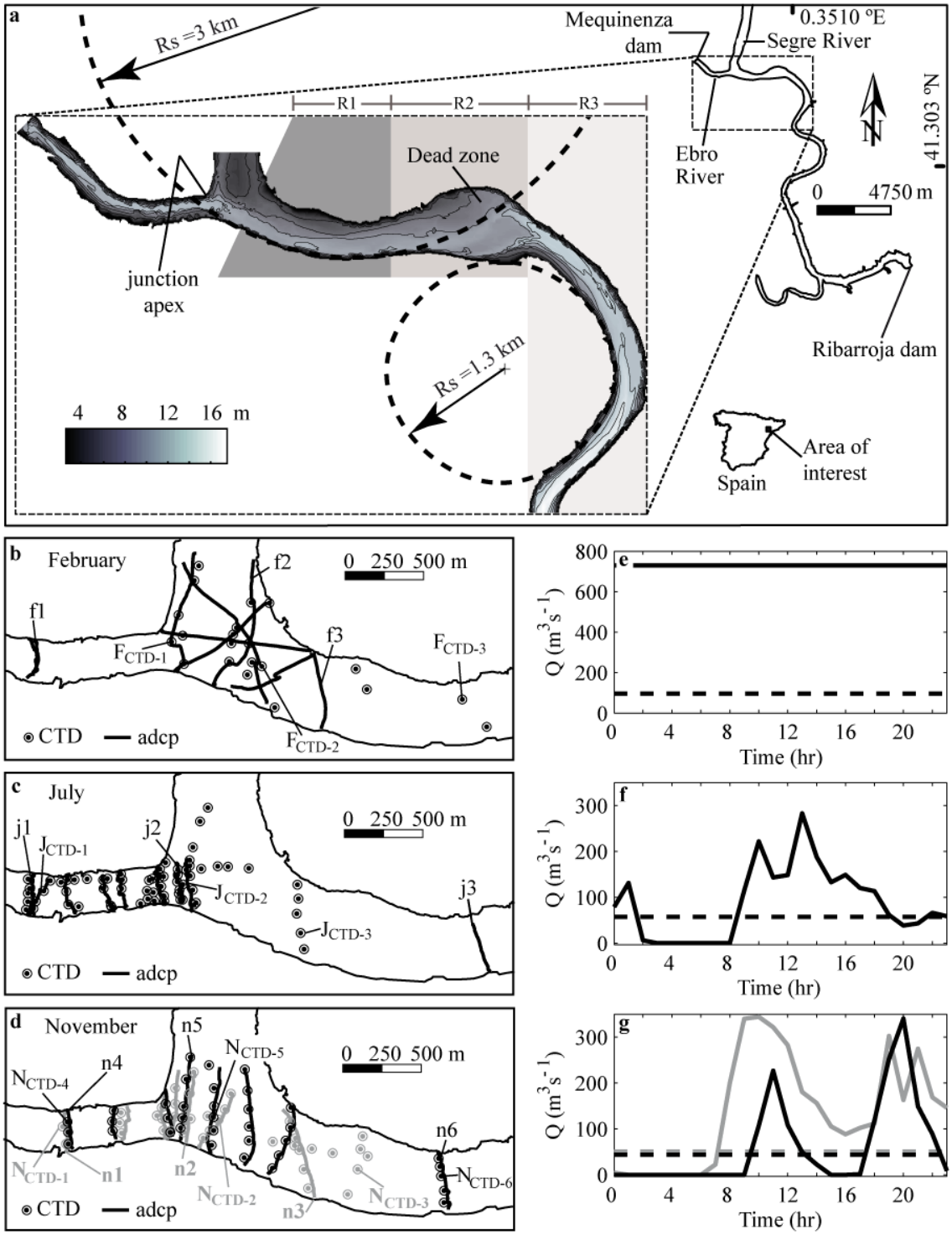

Figure A.1 (a) Location and bathymetry of the confluence between the Ebro and Segre rivers at the tail of the Ribarroja Reservoir, (b-d) ADCP transects and CTD casts collected at the confluence, and (e-g) discharges from the W- (solid lines) and N- (dashed lines) Rivers on days (b,e) 50, (c,f) 203 and (d,g) 329-330. Gray and black colors in (d,g) account for days 329 and 330, respectively. Names are shown in (b-d) for ADCP transects and CTD casts used in Figure A.16 and Figure A.17.

of 4 and 2 m, respectively, while depths encountered at the Ebro River are of ≈ 10 m ($b_p/D \approx 40$). Downstream of reach R1, the channel widens as it veers to the right, leaving a wide shallow dead zone on the left bank (reach R2) where the flow is known to recirculate [*Ramón et al.*, 2013; Chapter 2]. Finally, in reach R3, the channel bends to the right with a radius of curvature R_s ca. 1.3 km ($R_s/b_p \approx 3.25$, Figure A.1a). Inflows from the Ebro River are regulated by the Mequinenza dam, which discharges directly into the Ribarroja reservoir 3 km upstream of the confluence of the Segre into the Ebro River, whereas inflows from the Segre River behave in a more natural manner. A field campaign in 2009 [*Ramón et al.*, 2013; Chapter 2] showed that the flow was highly unsteady during the stratification period in summer, with withdrawals from Mequinenza varying hourly within a day following the electricity demand (Figure A.1e-g), and density contrasts between both river were unsteady in winter, varying also on an hourly basis.

The length of the computational domain (≈ 9 km) together with the time scales of the phenomena aimed to study — as, for example, the influence on mixing of the observed density contrasts between rivers (≥ 1 day), or the streamwise displacement of the plunge point of the denser Ebro River during the time varying discharges observed in the stratification period — make computationally way too expensive any attempt to simulate the hydrodynamics of the confluence between the Ebro and Segre rivers with well-resolved Large Eddy Simulations (LES) [e.g., *Rodi*, 2010] or hybrid LES techniques [e.g., *Constantinescu et al.*, 2012]. Even full 3D RANS models based on non-hydrostatic equations are very demanding, and further simplifications of the governing equations are needed. Thus, models based on the three-dimensional primitive equations (3D-PE) become a reasonable approach in terms of computational costs. Given the high width-to-depth ratios observed in large rivers [*Parsons et al*., 2008], non-hydrostatic effects are expected to be weak and O (D^2/b_p^2) [e.g., *Wang et al.*, 2009], which for the case of the confluence between the Ebro and Segre rivers would be of O (10^{-4}). Thus, the hydrostatic-pressure assumption included in the 3D-PE should not compromise the results. The model adopted for the numerical simulation of flows in Ribarroja is a Cartesian free-surface hydrodynamic model [*Smith*, 2006] which has been validated both against analytical solutions and field data collected in geophysical systems, particularly in lakes and estuaries [*Rueda and Cowen*, 2005; *Rueda and MacIntyre*, 2010 and references therein]. It has not been tested, however, for key hydraulic features of river environments, such as (1) the development of shallow mixing layers between two confluent streams, (2)

the flow pattern at river dead zones (such as pools, gravel beds, side arms), and (3) the three dimensional flow which is known to occur at river bends and which its main characteristics are [*Leschziner and Rodi*, 1979]: (3a) the formation, decay and reversal of the transverse surface slope, (3b) the development of secondary circulation patterns, and (3c) the characteristic radial shift of the tangential velocity maximum either towards the inner or towards the outer bank. All of them are relevant physical processes at the confluence between the Ebro and Segre rivers (Figure A.1a).

Hence, our goal is to study to what extent these relevant physical processes are reproduced with a 3D-PE-based model. For this purpose, we first reproduce laboratory tests present in the literature for each of these processes to test the validity of the model. The physical dimensions and flow conditions in all experiments used for model validation are shown in Table A.1. Given the simplified set of equations used in the analysis, our results are expected to be approximate. Non-hydrostatic effects for the mixing layer experiment [*Chu and Babarutsi*, 1988] are expected to be O (10^{-3}), which are negligible, and they are still weak, O (10^{-2}), for the dead zone experiment of *Kimura and Hosoda* [1997] and the bend experiment of *deVriend* [1979] [e.g., *Wolfram and Fringer*, 2013]. Given that the confluence between the Ebro and the Segre rivers becomes stratified in summer [*Ramón et al.*, 2013; Chapter 2], we also tested the model for the three-

Table A.1 Conditions of the laboratory experiments selected for validation.

Test case		***Q*** **(cm^3/s)**	***D*** **(m)**	***b*** **(m)**	***L*** **(m)**	R_i [(a)] **(m)**	R_o [(a)] **(m)**	**Model run**
Chu and Babarutsi [1988]		Q_1=549 [(b)] Q_2=146	0.05	0.61	7	-	-	A
Kimura and Hosoda [1997]		747	0.0202	b = 0.1 b_0 = 0.15	L = ? [(d)] L_0 = 0.225	-	-	B
deVriend [1979]		1.8×10^5	0.189	1.7	25.35	3.4	5.1	C1-C4
He et al. [1992]	Test 1	Q_u = 750[(c)] Q_l = 4890	0.29	0.4	11.5	1.1	1.5	D1
	Test 2	Q_u = 800.6 Q_l = 4142	0.29	0.4	11.5	1.1	1.5	D2

[(a)] R_i = inner radius of curvature, R_o = outer radius of curvature.

[(b)] Subscripts 1 and 2 refer to each of the confluent streams.

[(c)] Q_u = inflow rate of the upper layer, Q_l = inflow rate of the lower layer.

[(d)] ?= Not specified in the published paper

dimensional flow that occurs in a river bend in the presence of stratification [*He et al.*, 1992]. Due to the higher depth-to-width ratio of the latter experiments, however, non-hydrostatic effects are expected to be O (10^{-1}), and, thus, the hydrostatic assumption starts being compromised. We evaluated the sensitivity of the grid for solutions in all four test cases, through a grid convergence study, but for the sake of conciseness these results are only presented here for the unstratified bend case. Secondly, we will present the model validation with field data collected at the confluence between the Ebro and Segre Rivers in 2009 [*Ramón et al.*, 2013; Chapter 2].

A.2 Methods

A.2.1 Governing equations

Assuming that (1) variations in density are negligible everywhere except in the buoyancy term (the Boussinesq approximation), (2) the weight of the fluid balances the pressure in the equation for vertical momentum (the hydrostatic approximation), and (3) a diffusion-like term can be used to represent turbulent fluxes of scalars and momentum (the eddy diffusivity concept), the governing equations can be written as:

$$\frac{\partial u}{\partial x}+\frac{\partial v}{\partial y}+\frac{\partial w}{\partial z}=0 \tag{A.1}$$

$$\frac{\partial \zeta}{\partial t}+\frac{\partial}{\partial x}\left[\int_{-D}^{\zeta} u dz\right]+\frac{\partial}{\partial y}\left[\int_{-D}^{\zeta} v dz\right]=0 \tag{A.2}$$

$$\begin{aligned}&\frac{\partial u}{\partial t}+u\frac{\partial u}{\partial x}+v\frac{\partial u}{\partial y}+w\frac{\partial u}{\partial z}-fv=-\left(g\frac{\partial \zeta}{\partial x}+g\frac{1}{\rho_0}\int_z^{\zeta}\frac{\partial \rho}{\partial x}dz'\right)+\\&\frac{\partial}{\partial x}\left(A_h\frac{\partial u}{\partial x}\right)+\frac{\partial}{\partial y}\left(A_h\frac{\partial u}{\partial y}\right)+\frac{\partial}{\partial z}\left(A_z\frac{\partial u}{\partial z}\right)\end{aligned} \tag{A.3}$$

$$\begin{aligned}&\frac{\partial v}{\partial t}+u\frac{\partial v}{\partial x}+v\frac{\partial v}{\partial y}+w\frac{\partial v}{\partial z}+fu=-\left(g\frac{\partial \zeta}{\partial y}+g\frac{1}{\rho_0}\int_z^{\zeta}\frac{\partial \rho}{\partial y}dz'\right)+\\&\frac{\partial}{\partial x}\left(A_h\frac{\partial v}{\partial x}\right)+\frac{\partial}{\partial y}\left(A_h\frac{\partial v}{\partial y}\right)+\frac{\partial}{\partial z}\left(A_z\frac{\partial v}{\partial z}\right)\end{aligned} \tag{A.4}$$

$$\frac{\partial \theta}{\partial t} + u\frac{\partial \theta}{\partial x} + v\frac{\partial \theta}{\partial y} + w\frac{\partial \theta}{\partial z} = K_h\frac{\partial^2 \theta}{\partial x^2} + K_h\frac{\partial^2 \theta}{\partial y^2} + \frac{\partial}{\partial z}\left(K_z\frac{\partial \theta}{\partial z}\right) + \frac{H}{\rho c_p}_0 \tag{A.5}$$

These equations comprise the 3D-PE. They express the physical principles of conservation of mass for an incompressible fluid (Eqs. A.1-A.2), conservation of momentum (Eqs. A.3-A.4) and conservation of energy (Eq. A.5). Here *u*, *v*, and *w* represent the velocity components in the *x*-, *y*-, and *z*- directions; *f* is the Coriolis parameter; *g* is the acceleration of gravity; θ represents an active scalar (temperature, conductivity); ζ is the free surface elevation; $z = -D(x, y)$ is the depth of the bottom boundary measured from the undisturbed free surface $z = 0$; *H* is a source of heat associated with heat and energy fluxes due to atmospheric heating or cooling; *A* is the kinematic eddy viscosity and *K* is the turbulent transfer coefficient (eddy diffusivity) for scalars. The density ρ is calculated from temperature (and also from conductivity in the case of the Ebro and Segre rivers) using an equation of state; the subscripts *h* and *z* refer to horizontal and vertical directions, respectively.

A.2.2 Numerical model

Simulations were conducted with a parallel version [*Acosta et al.*, 2010] of the 3D free surface hydrodynamic model [*Smith*, 2006]. The governing equations (Eqs. A.1-A.5) are first posed in layer-averaged form by integrating over the height of a series of horizontal layers separated by level planes. The layer-averaged momentum equations are solved using a semi-implicit, three-level, iterative leapfrog-trapezoidal finite difference scheme on a staggered Cartesian grid. The method gives second order accuracy both in time and space. The semi-implicit approach is based on treating the gravity wave and vertical diffusion terms implicitly to avoid time-step limitations due to gravity-wave Courant-Friedrich-Levy (CFL) conditions, and to guarantee stability of the method [*Casulli and Cheng*, 1992; *Durran*, 1999]. The finite-difference form of the governing equations for the leapfrog semi-implicit scheme can be written as:

$$\zeta_{i,j}^{n+1} = \zeta_{i,j}^{n-1} - \frac{\Delta t}{\Delta x}\left[\sum_{k=k_1}^{km}\left(U_{i+1/2,j,k}^{n+1} - U_{i-1/2,j,k}^{n+1} + U_{i+1/2,j,k}^{n-1} - U_{i-1/2,j,k}^{n-1}\right)\right] - \frac{\Delta t}{\Delta y}\left[\sum_{k=k_1}^{km}\left(V_{i,j+1/2,k}^{n+1} - V_{i,j-1/2,k}^{n+1} + V_{i,j+1/2,k}^{n-1} - V_{i,j-1/2,k}^{n-1}\right)\right] \tag{A.6}$$

$$U_{i+1/2,j,k}^{n+1} = \hat{U}_{i+1/2,j,k} - g\frac{\Delta t}{\Delta x}\bar{h}_{i+1/2,j,k}^{n}\left(\frac{\bar{\rho}_{i+1/2,j,1}^{n}}{\bar{\rho}_{i+1/2,j,k}^{n+1}}\right)\left(\zeta_{i+1,j}^{n+1} - \zeta_{i,j}^{n+1} + \zeta_{i+1,j}^{n-1} - \zeta_{i,j}^{n-1}\right) + \Delta t\left(A_{z\,i+1/2,j,k-1/2}^{n}\left(\frac{(U/\bar{h})_{i+1/2,j,k-1}^{n+1} - (U/\bar{h})_{i+1/2,j,k}^{n+1}}{\bar{h}_{i+1/2,j,k-1/2}^{n+1}} + \frac{(u)_{i+1/2,j,k-1}^{n-1} - (u)_{i+1/2,j,k}^{n-1}}{\bar{h}_{i+1/2,j,k-1/2}^{n-1}}\right)\right) - \Delta t\left(A_{z\,i+1/2,j,k+1/2}^{n}\left(\frac{(U/\bar{h})_{i+1/2,j,k}^{n+1} - (U/\bar{h})_{i+1/2,j,k+1}^{n+1}}{\bar{h}_{i+1/2,j,k+1/2}^{n+1}} + \frac{(u)_{i+1/2,j,k}^{n-1} - (u)_{i+1/2,j,k+1}^{n-1}}{\bar{h}_{i+1/2,j,k+1/2}^{n-1}}\right)\right) \tag{A.7}$$

$$V_{i,j+1/2,k}^{n+1} = \hat{V}_{i,j+1/2,k} - g\frac{\Delta t}{\Delta y}\bar{h}_{i,j+1/2,k}^{n}\left(\frac{\bar{\rho}_{i,j+1/2,1}^{n}}{\bar{\rho}_{i,j+1/2,k}^{n+1}}\right)\left(\zeta_{i,j+1}^{n+1} - \zeta_{i,j}^{n+1} + \zeta_{i,j+1}^{n-1} - \zeta_{i,j}^{n-1}\right) + \Delta t\left(A_{z\,i,j+1/2,k-1/2}^{n}\left(\frac{(V/\bar{h})_{i,j+1/2,k-1}^{n+1} - (V/\bar{h})_{i,j+1/2,k}^{n+1}}{\bar{h}_{i,j+1/2,k-1/2}^{n+1}} + \frac{(v)_{i,j+1/2,k-1}^{n-1} - (v)_{i,j+1/2,k}^{n-1}}{\bar{h}_{i,j+1/2,k-1/2}^{n-1}}\right)\right) - \Delta t\left(A_{z\,i+1/2,j,k+1/2}^{n}\left(\frac{(V/\bar{h})_{i,j+1/2,k}^{n+1} - (V/\bar{h})_{i,j+1/2,k+1}^{n+1}}{\bar{h}_{i,j+1/2,k+1/2}^{n+1}} + \frac{(v)_{i,j+1/2,k}^{n-1} - (v)_{i,j+1/2,k+1}^{n-1}}{\bar{h}_{i,j+1/2,k+1/2}^{n-1}}\right)\right) \tag{A.8}$$

Here, U and V are the volumetric transport in the x- and y- directions, respectively; Δt is the time step, Δx and Δy are the horizontal size of a cell in x- and y-, respectively; subscripts (i, j, k) denote the spatial location in the computational grid, and the superscripts (n), the time t level at which the variable is evaluated. The symbols k_1 and k_m denote the first (shallowest) and last (deepest) layer in a water column, respectively. The overbar on a layer height h or density ρ variable is used to represent a spatial average in the x- or y- direction between adjacent values. The double overbar denotes average of layer heights and (^) denotes a solution for the layer volumetric transport that includes only the contribution from the advection, Coriolis, baroclinic pressure and horizontal diffusion terms, treated explicitly in the semi-implicit scheme. In the course of the computations for a given time step, the volumetric transports at time n+1 in the momentum equations are expressed as a function of the free surface at that time (Eqs. A.7 and A.8) and substituted in Eq. (A.6) to yield a sparse symmetric positive-definite system of equations for ζ^{n+1}. The matrix problem is then solved using a conjugate gradient

iterative method (see *Smith* [2006] for details). The vertical velocity is updated using the continuity equation (Eq. A.1).

The scalar transport equations were solved using a two-level semi-implicit scheme, in which only vertical diffusion is discretized implicitly. The advection terms in the transport equation for scalars are discretized with flux-limiter methods [e.g., *Durran*, 1999]. The correct fluxes are constructed with the monotone upstream differencing scheme, the Lax-Wendroff second-order method and the Superbee limiter [*Roe*, 1984]. Turbulent mixing is represented in the 3-D model using diffusion-like terms. A Laplacian operator with constant mixing coefficients (horizontal eddy viscosity A_h or diffusivity K_h) is used in the model to represent horizontal mixing of momentum and scalars. Vertical eddy coefficients of mixing K_z are calculated using a two-equation model originally proposed by *Mellor and Yamada* [1974], and later modified by *Kantha and Clayson*, [1994]. This turbulent modeling approach is typically used in large scale models for geophysical flows due to their reduced computational burden.

A.2.3 Application to lab-scale river flows

A.2.3.1 *Shallow mixing layers*

Shear layers are ubiquitous in river confluences as a result of the confluent rivers having different mean velocities. Since confluence widths are much larger than confluence depths, shallow mixing layers develop at these environments, where the development of vortices within the shear layers is restricted in the vertical, by the water surface and the riverbed, leading to vortex structures with nearly vertical rotation axis [*Biron et al.*, 1993; *Sukhodolov and Rhoads*, 2001; *Rhoads and Sukhodolov*, 2004]. Beside this, the lateral growth of shallow mixing layers is also restricted by the stabilizing effect of bed friction, so that they stop growing laterally downstream, when the bed-friction number exceeds a certain critical value [e.g., *Chu and Babarutsi*, 1988].

A.2.3.1.1 Experimental data for model validation

We chose the experimental data set collected by *Chu and Babarutsi* [1988] in a laboratory flume to test the validity of the model of *Smith* [2006] to reproduce shallow mixing layers. The flume was a 0.61-m wide and 7-m long open channel with a splitter plate located at the midplane which divided the flow into two streams of different

velocities (Table A.1, Figure A.2a). Velocity measurements were made at 5×10^{-3} m below the water surface at several sections downstream (Figure A.2a), with increasing resolution within the mixing layer. Measured sections (A1 to A5 in Figure A.2a) were located 0.01, 0.5, 1, 1.5 and 2 m downstream of the end of the splitter plate, respectively. They tested several flow conditions. We chose one of their tests for model validation (Table A.1). Measured velocity values in each of these sections were digitized from their published article.

A.2.3.1.2 Model setup

The channel was discretized using cells of size (Δx, Δy, Δz) = (0.01, 0.01, 0.01) m, in the *x*-, *y*- and *z*- directions, respectively, and the time step Δt was fixed to 0.001 seconds for stability purposes (Table A.2). C_d was chosen to be equal to the friction coefficient c_f measured by *Chu and Babarutsi* [1988] in the slowest stream ($C_d = c_f =$ 0.0048). Horizontal eddy viscosity, in turn, was used as a calibrating parameter, and values ranging from 1×10^{-5} to 5×10^{-4} m^2 s^{-1} were tested. Flow rates were fixed to 5.49×10^{-4} and 1.49×10^{-4} m^3 s^{-1} at the two upstream boundary conditions, respectively, assuming that initially all computational cells in each of the streams had a uniform velocity directed downstream and equal to the mean velocity measured in the experiments, u_{s1} = 0.36 m s^{-1} and u_{s2} = 0.096 m s^{-1}, respectively. Thus, the transverse u_l and vertical *w* velocities equaled 0 m s^{-1} at the upstream boundaries. At the downstream

Table A.2 Grid cells and time properties of the simulations

Run	$N_{cell\text{-}xy}$ [(a)]	$N_{cell\text{-}z}$ [(b)]	t_{steady} [(c)] (s)	$N_{times\ steps}$ [(d)]
A	36560	5	90	90000
B	57100	10	90	90000
C1	94759	10	200	40000
C2	36941	10	180	36000
C3	23617	10	180	36000
C4	5869	10	180	36000
D1	11860	29	400	80000
D2	11860	29	400	80000

[(a)] Number of active cells in 2D (x,y) plane
[(b)] Number of cells in the vertical
[(c)] Physical time to reach steady state
[(d)] Number of time steps to reach steady state

end, the free surface elevation was assumed to be constant. The water was initially quiescent and the model was run until steady state (Table A.2). The model was set to run using a second-order space-centered method for momentum advection and 2 trapezoidal iterations, without smoothing of the leapfrog solution. This configuration was kept the same for all three validation tests.

A.2.3.2 *Flow past a lateral cavity*

Dead zones can form in river confluences as a result of irregularities in the river morphology which separates a certain part of the water body from the main stream. In these regions the flow recirculates and, as a result, a shear layer develops between the main channel and the dead zone. The dominant dynamic effect of dead zones in rivers is, then, to increase the transverse velocity shear. Laboratory experiments have shown that

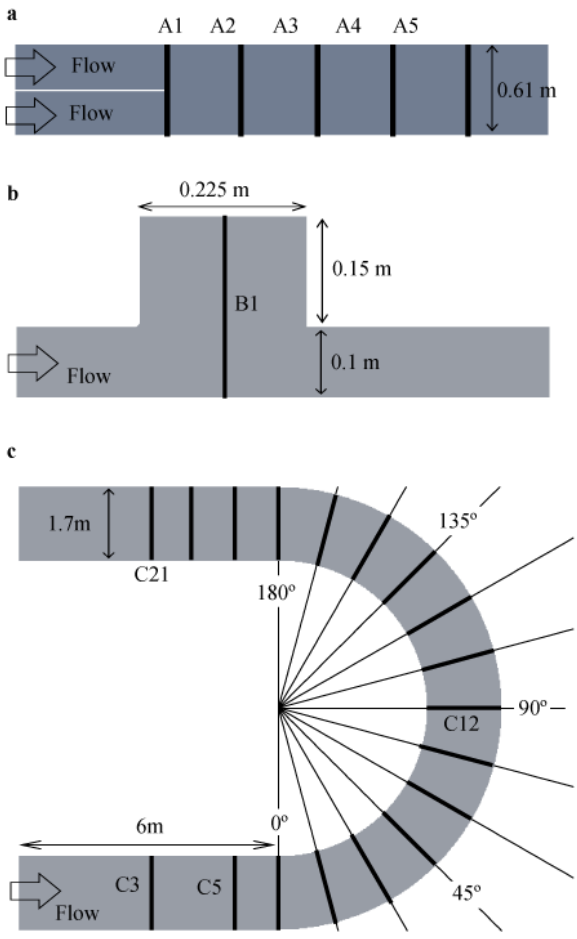

Figure A.2 Configuration sketch of the three physical experiments for model validation (a) *Chu and Babarutsi* [1988], (b) *Kimura and Hosoda* [1997], (c) *deVriend* [1979]. Black lines show sections for model validation in each of the experiments.

different patterns of recirculation are observed as function of the geometry of the dead zone, i.e. as function of its width-to-length ratio b_0/L_0 [e.g., *Weitbrecht et al*., 2008]. When $b_0/L_0 < 0.7$, the mean flow within the dead zone shows two counter-rotating cells: (1) a primary gyre, which is bigger and in direct contact with the main stream and (2) a secondary gyre, which is located near the upstream junction corner of the dead zone and which is only in contact with the primary gyre. Between $0.7 < b_0/L_0 < 1.5$, a unique gyre (the primary gyre) is observed. Finally when $b_0/L_0 > 1.5$, a two-gyre system also develops but this time, the secondary gyre is centered, located further inside the dead zone and behind the primary gyre [e.g., *Weitbrecht et al.*, 2008].

A.2.3.2.1 Experimental data for model validation

The physical model of Kimura and Hosoda's [*Kimura and Hosoda*, 1997] was used for the model validation of flow dynamics past a lateral cavity. The channel consisted of a 0.1-m-wide open channel and an attached dead zone with a b_0 and L_0 of 0.15 and 0.225 m ($b_0/L_0 = 0.67$), respectively (Figure A.2b, see details in Table A.1for the physical dimensions and flow conditions). They measured the streamwise velocities at half the depth at a cross section located in the middle of the dead zone (Section B1 in Figure A.2b). The time-averaged values of these measurements were used for model validation. These values were digitized from their published article.

A.2.3.2.2 Model setup

The channel was discretized using cells of size (Δx, Δy, Δz) = (0.0025, 0.0025, 0.002) m, and the time step was fixed to 0.001 seconds to avoid stability problems. The bottom drag coefficient, C_d, was set to 0.003 as proposed by *Smith* [2006], and the horizontal eddy viscosity was used as a calibrating parameter, and values ranging from 1×10^{-5} to 5×10^{-4} m^2 s^{-1} were tested. Flow boundary conditions were set at the inflow section. Flow rates were fixed to 7.47×10^{-4} m^3 s^{-1} (Table A.1). At the downstream end, the free surface elevation was assumed to be constant. The water was initially quiescent and the model was run until steady state (Table A.2).

A.2.3.3 *Flow in open channel with mild curvature*

When unstratified flows enter a bend, the balance between the pressure forces and the vorticity induced by the centripetal forces at the bend is responsible of the development of a transverse inclination of the free surface and the main transverse

circulation, also referred to as Prandtl's first kind of recirculation [e.g., *van Balen*, 2010]. Near the upper surface, centrifugal forces are higher than the pressure forces. Hence, particles near the surface will be displaced towards the outer bank. Near the bottom, in turn, the pressure forces are greater than centrifugal forces due to frictional effects, and the flow moves towards the inner bank. Finally, a vertical velocity component appears due to the continuity of the flow, yielding to the final helical motion [e.g., *Rozovskii*, 1961]. The transversal tilt of the free surface and the helical motion that develops in curved bends lead to significant changes in the velocity structure as one moves along the bend. The streamwise velocity tends to decrease where the water surface elevation rises and, conversely, it tends to increase where the water surface elevation drops. Hence, the streamwise velocity is higher near the inner bank at the beginning of the bend. As the fluid flows through the bend, the exchange of momentum between horizontal currents owing to the lateral circulation leads to the gradual transition of the maximum velocity towards the outer bank [e.g., *Rozovskii*, 1961]. *Mockmore* [1944] showed that, in addition to the main lateral circulation, a second cell developed near the outer bank. This outer-bank cell is referred to as Prandtl's second kind of recirculation [e.g., *van Balen*, 2010]. In this cell, water rotates in the opposite direction to the main recirculation cell. Although it is smaller and weaker that the main recirculation cell it is of particular importance, when considering erosion problems in meandering channels, as it tends to protect steep outer-banks from erosion [*Christensen et al.*, 1999]. The occurrence of the outer-bank cell is associated with flow instabilities and to the flux of kinetic energy from turbulent scales back in to the larger scales of motion [*Blanckaert and deVriend*, 2004]. *Van Balen* [2010] indicates that the outer-bank cell is the net result of a complex interaction between centripetal effects and anisotropy of the Reynolds stresses.

Under stratification, however, the three-dimensional flows within the bend differ, owing to the added effects due to buoyancy and the presence of non-logarithmic streamwise velocity profiles [e.g., *Corney et al.*, 2006], and secondary flows may be reversed (directed inwards near the surface) [e.g., *Corney et al.*, 2006; *Parsons et al.*, 2010].

A.2.3.3.1 Experimental data for model validation

Following *Jia et al.* [2001], and also *Duan* [2004], we have used the experimental data set collected by *deVriend* [1979] in a laboratory U-shaped channel ($R_s/b \approx 2.5$) as a

reference to test the validity of the model of *Smith* [2006] to simulate non-stratified flows in domains with curved boundaries. The flume was a 180º bend of rectangular cross section, incorporating straight inlet and outlet reaches (Figure A.2c) and a smooth flat bottom. The experiments of *He et al.* [1992] (as reported in *Shen et al.* [2003] and *Chao et al.* [2009]) were, in turn, used as a reference in the validation exercise of the model to represent stratified flows in curved channels. He's flume was also a U-shaped channel ($R_s/b \approx 3.25$). In that experiment a thermally stratified flow is created by joining two streams of water, which are initially separated by a splitter plate, and have different velocities and temperatures before mixing. The streams are discharged from the upper and lower inlets into the channel. At the entrance the total water depth is 0.29 m, in which the upper depth is 0.02 m and the lower depth is 0.27 m. The warmer layer was 10°C warmer than the bottom flowing layer. In all cases [*deVriend*, 1979; *Shen et al.*, 2003], the channel slope was zero (Table A.1).

A.2.3.3.2 Model setup for unstratified conditions

The channel was discretized using computational cells of size (Δx, Δy, Δz) = (0.02125, 0.02125, 0.0189) m (run C1 in Table A.1-Table A.2). The horizontal size of these cells was chosen to match with measured points by *deVriend* [1979]. The code was run until steady state conditions were reached (Table A.2). Δt was set to a constant value in all experiments, and equal to 0.005 s for stability purposes (Table A.2). The cross-sections where model results were checked are the same sections identified by *deVriend* [1979] to observe the flow field in his experiments (Figure A.2c). At each of these sections, streamwise and transverse velocities were measured along 11 vertical profiles. Profiles 1 and 11 were 0.1 m from the inner (left) and outer (right) banks, respectively. Profiles 2 and 10 were located 0.07 m from profiles 1 and 11, respectively. The separation between profiles 2-10 was 0.17 m. Water surface elevations were also measured at profiles 1, 6 and 11 in each of the sections. Flow rate (= 0.18 $m^3 s^{-1}$) was prescribed at the upstream end. The horizontal velocity was assumed to be uniform in each horizontal plane of the upstream section (u_s = 0.56 m s^{-1}) and $u_l = w$ = 0 m s^{-1}. At the downstream end, the water surface elevation was set to a constant value (equal to zero).

The mean roughness height, k_s, was found to be 7.5×10^{-4} m [*Jia and Wang*, 2009]. The bottom drag coefficient was obtained using the Colebrook-White relationship for rough turbulent flows [*Bettess*, 1999], that is:

$$\frac{1}{\sqrt{f_{DW}}} = 2\log\left(12.17\frac{R_h}{k_s}\right), \quad \text{(A.9)}$$

where R_h is the hydraulic radius of the underflow and f_{DW} is the dimensionless Darcy-Weisbach friction factor applied to open channels. The bottom drag coefficient, C_d, was, in turn, estimated through the relation $C_d = f_{DW}/8$ [*Fernandez and Imberger*, 2006]. For $k_s = 7.5\times10^{-4}$ m, C_d is O (10^{-3}) for a depth-integrated circulation model (based on the assumption of a logarithmic velocity profile through the depth). We tried different values of drag coefficient, and analyzed the effects of this choice in the model results. The effects of different values of A_h (and K_h), ranging from 10^{-4} to 10^{-2} m^2 s^{-1}, equal both in the E-W and N-S directions, were also evaluated.

A.2.3.3.3 Model setup for stratified conditions

The channel was discretized using cells of size (Δx, Δy, Δz) = (0.02, 0.02, 0.01) m, and Δt was fixed to 0.005 seconds to avoid stability problems. A_h was set to a small value (10^{-4} m^2 s^{-1}), in both x- and y-directions to allow the advective terms to dominate. This value corresponds to the theoretical value $A_h = 0.1D$u* for prismatic laboratory channels [*Rastogi and Rodi*, 1978], u^* being the friction velocity ($u^* = C_d^{0.5}U_{prom}$, being U_{prom} the cross-sectional averaged downstream velocity). Simulated and observed velocities and temperatures were compared, after reaching steady state at the 90^o section (Table A.2). We did not have access to the velocity data; hence, the velocity comparison was done on a qualitative basis using, as a reference, the streamwise velocity distribution and the lateral circulation in He's experiment 1 [*He et al.*, 1992], and shown as contour plots in Figures 3 and 4 in *Chao et al.* [2009]. The temperature results of He's experiment 2 are also shown in *Chao et al.* [2009], their Figure 5. The temperature data was digitized and used as a basis for model validation. Six vertical temperature profiles were measured. Profile 1 was located 1 cm from the inner bank, and Profile 6 was located 0.01 m from the outer bank. The distance between the other neighboring profiles was 0.076 m.

Dimensionless water depths, channel widths, velocities and temperatures were used to represent simulations and observations, and are defined as:

$$\begin{aligned} z^* &= z / D \\ d^* &= d / b \\ U^* &= u_S / U_0 \\ DT^* &= (T - T_2)/(T_1 - T_2) \end{aligned} \tag{A.10}$$

Here z^* = dimensionless water depth; d^* = dimensionless channel width; d = distance to the inner bank along the channel cross section; U_0 = bulk velocity at inlet section; U^* = dimensionless velocity; DT^* = dimensionless temperature difference; T_1 = Temperature of upper warmer water at inlet; T_2 = Temperature of lower cooler water at inlet; and $T_1 - T_2$ = maximum temperature difference.

A.2.3.3.4 Convergence study

To test the influence of the resolution of the grid in model solutions, *deVriend* [1979]'s channel was discretized using grid cells of different size in the horizontal (C-runs in Table A.1-Table A.2). Grid cells of size Δx (= Δy) 0.034 m, 0.0425 m and 0.085 m were tested in the C2, C3 and C4 runs, respectively. The influence of the resolution of the grid was evaluated through a convergence study. Convergence was evaluated at common nodes (total of N = 7830 nodes) to avoid interpolation errors and E-W u and N-S v velocities, water surface elevations ζ and vertical diffusivities K_z were used to analyze the convergence of the solutions. The error E is expressed as the L_2 norm of the difference between solutions with the different C-grids and a reference solution, obtained with the higher resolution grid (Δx = 0.02125 m) [*Fringer et al.*, 2006]:

$$E = \frac{\sum_{p=1}^{N} \left(f_p - f_p^{ref} \right)^2}{\sum_{p=1}^{N} \left(f_p^{ref} \right)^2} \tag{A.11}$$

where f_p is either u, v, ζ or K_z in each common node p, and f_p^{ref} is the reference solution. A reduced major axis (RMA) regression was also performed between solutions of the different variables with the different grid resolutions. This method is preferable than the simple linear regression since both the dependent and independent variables are sensitive to potential errors [*Ferguson et al.*, 2003; *Hardy et al.*, 2003].

A.2.4 The Ribarroja reservoir: Model validation with field data

A.2.4.1 *Approach*

In order to validate the model with real field-scale data, we simulated the flow and density fields that developed at the confluence between the Ebro (hereon Western W-River) and Segre (hereon Northern N-River) rivers under the non-stratified conditions observed in February 2009 (Julian day 50) and under the stratified conditions observed in July (Julian day 203) and November 2009 (Julian days 329-330) [*Ramón et al.*, 2013; Chapter 2]. On day 50, inflow rates were constant, but almost 8 times larger from the W-River (Q_W) than from the N-River (Q_N) (Figure A.1e). On days 203, 329 and 330 N-inflows remained constant in time but W-inflows varied in time due to the activity of the hydropower company operating in the upstream reservoir (Figure A.1f and Figure A.1g). Time-averaged discharge ratios R_q (=Q_N/Q_W) were 0.13, 0.58, 0.37 and 0.71 on days 50, 203, 329 and 330, respectively. On day 203, the density contrast between rivers, (ρ_W-ρ_N)/ρ_0 = $\Delta\rho/\rho_0$, with ρ_0 (= 1000 kg m^{-3}) being a reference density, was O (10^{-3}) (Table A.3) and was driven mainly by temperature differences of up to 6ºC between the W- (T_W ≈19ºC) and N- (T_N ≈ 25ºC) rivers. On days 329 and 330, however, $\Delta\rho/\rho_0$ = O (10^{-4}) (Table A.3) and it was controlled both by differences in conductivity (≈ 900 μScm^{-1} higher in the W-River) and temperature (4ºC higher in the W-River). On day 50 density differences of O (10^{-4}-10^{-5}) (Table A.3) were driven also by conductivity (≈ 80 μScm^{-1} higher in the W-River) and temperature (at most 1ºC higher in the Segre River) [*Ramón et al.*, 2013; Chapter 2]. On day 203, there were also strong winds (average wind speeds of 7 m s^{-1}) blowing from the SSE-SE (Figure A.3i).

A.2.4.2 *Field data*

The bathymetry information used to construct the model of the confluence was generated using an existing bathymetry map of the upper mid-half of the reservoir (Figure A.1a), and additional bathymetry data collected during the February, July and November 2009 experiments [*Ramón et al.*, 2013; Chapter 2]. The newly acquired data on each day was used instead of the existing information where they disagreed. Field data consisted of water velocity, temperature, conductivity, and turbidity records collected along several sections at the confluence (Figure A.1b-d). Meteorological data was available through a meteorological station located at the reservoir (Figure A.3). On day 50 two thermistor

Table A.3 Model inputs for the simulations in the Ribarroja reservoir

Run	Julian day	$\Delta\rho/\rho_0$	Qw (m^3s^{-1})	Q_N (m^3s^{-1})	R_q [(a)]
R1	50	3.6×10^{-3} to 1.2×10^{-4}	730	96	0.13
R2	203	1.4×10^{-3}	0-284	57	0.58
R3	329	1.01×10^{-4}	0-344	51	0.37
R4	330	7×10^{-5}	0-340	43.5	0.71

[(a)] Daily-averaged discharge ratio

chains were also deployed in the W- and N- rivers ca. 500 m upstream of the confluence. Further information on the field data is given by *Ramón et al.* [2013] (Chapter 2).

The model was forced with data collected on days 50, 203, 329 and 330 in 2009 (Figure A.1e, Figure A.1f and Table A.3). CTD casts and velocity transects collected in the field on each day of experiment (Figure A.1b-d) were used to validate the model with the field data. Root mean square errors (RMSE) were used to quantify the differences between modeled and measured densities and velocity fields in the E-W and N-S directions. The RMSEs of the density field are expressed as percentages (normalized root-mean-squared error, NRMSE) of the difference of maximum and minimum densities encountered at the confluence. NRMSEs of the width-averaged E-W and N-S velocity fields are expressed as percentages of maximum width-averaged E-W and N-S velocities at each of the velocity transects in Figure A.1b-d, respectively.

A.2.4.3 *Model setup*

The computational domain extends from the Mequinenza dam to a section existing ca. 8 km downstream of the junction of the N- and W- rivers (Figure A.1a) along the W-River, and approximately 500 m upstream of the confluence along the N-River. The bathymetry in the N-river was interpolated 500 m farther upstream (so that the N-boundary is 1km upstream of the confluence) to avoid the influence of the closeness of the N-boundary in our results. The lake geometry was discretized using grid cells of size (Δx, Δy, Δz) = (10, 10, 0.5) m in the longitudinal, lateral and vertical direction, respectively. The time step Δt was set to 2 s on day 50 and to 3 s on days 203, 329 and 330, for stability purposes. The bottom drag coefficient, C_d, was set to 0.003 as proposed by *Smith* [2006]. The horizontal eddy viscosity A_h and diffusivity K_h in the model were both set to O (10^{-3}-10^{-2}) $m^2\ s^{-1}$. This value corresponds on each simulation to the product

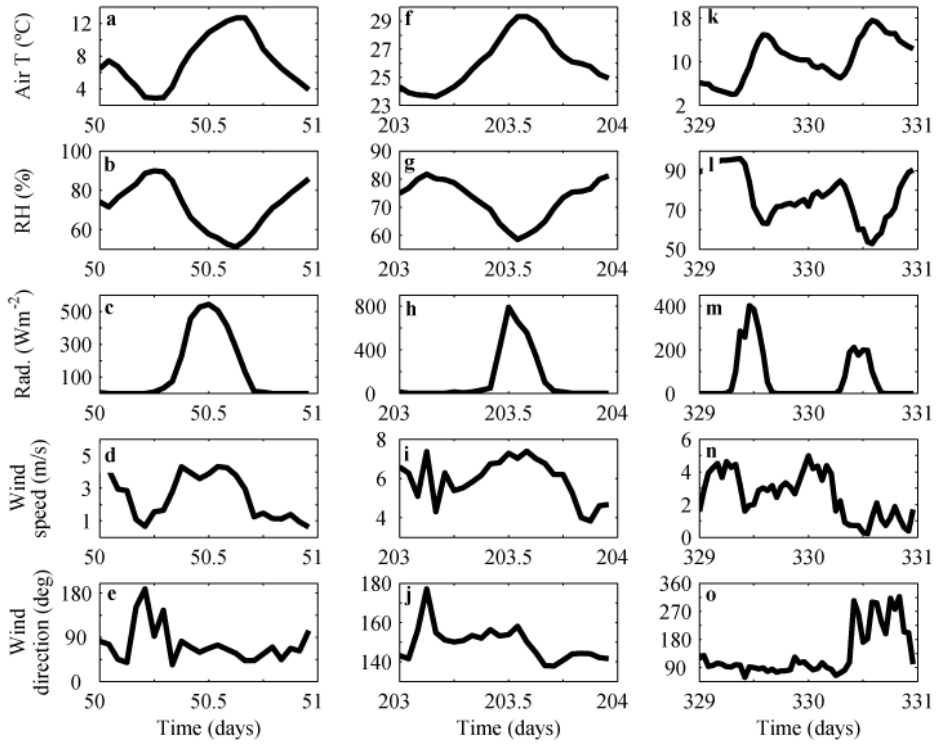

Figure A.3 Hourly-averaged meteorological variables collected at the meteorological station located at the Ribarroja reservoir on days (a –e) 50, (f-j) 203 and (k-o) 329-330.

of the friction velocity u^* and the channel depth D, as proposed by *Rastogi and Rodi* [1978] to quantify turbulent transfer of momentum and temperature. The values of u^* and D were, in turn, estimated from field observations [*Ramón et al.*, 2013; Chapter 2]. The model was set to run using a second order space-centered method for momentum advection and two trapezoidal iterations after the initial non-smoothed leapfrog predictive step.

Inflow rates at the upstream boundaries were set according to the observations collected during the field experiment reported by *Ramón et al.* [2013] (Chapter 2). On day 50 W-inflows were set to a constant value of 730 $m^3 s^{-1}$, while on days 203, 329 and 330 they were allowed to vary in time according to the hourly information given by the hydropower company (Figure A.1d-g). W-inflows were distributed uniformly in the inflow section. N-inflows, in turn, were assumed to occur through two sections with different velocities, as observed in the field. Almost 2/3 of the total inflow rate from the N-River was presumed to enter through the main channel and the remaining through the secondary channel. N-Inflows were all assumed to be constant in time, following the information given by the hydropower company ($Q_{N\text{-}50}$ = 96 $m^3 s^{-1}$, $Q_{N\text{-}203}$ = 57 $m^3 s^{-1}$, $Q_{N\text{-}}$

$_{329}$ = 51 $m^3 s^{-1}$ and $Q_{N\text{-}330}$ = 43.5 $m^3 s^{-1}$). On day 50, density differences were allowed to vary in time on an hourly basis, following the observations collected on Julian day 50 in 2009 [*Ramón et al.*, 2013; Chapter 2]. Inflow densities on days 203, 329 and 330 were set constant in time. River temperatures were directly measured in the field [*Ramón et al.*, 2013; Chapter 2]. Salinities in turn, were estimated from conductivity profiles collected at the inflow sections of the W- and N- rivers, through a scaling factor λ [*Pawlowicz*, 2008], which was estimated to be $\lambda = 0.8 \pm 0.2$ mg L^{-1}(μS cm^{-1}) [*Ramón et al.*, 2013; Chapter 2]. Due to the uncertainty in λ, this parameter was used as a calibrating parameter in the model. Several tests (not shown) were run with λ varying from 0.65 to 0.9 mg L^{-1}(μS cm^{-1}). The lowest NRMSEs between measured and modeled density profiles were achieved with λ = 0.75 mg L^{-1}(μS cm^{-1}) so this is the final value for λ used in the simulations presented in this paper.

The reservoir was assumed initially at rest with a uniform density, equal to the averaged density of the W- and N- rivers. At the downstream end, the free surface elevation was assumed to be constant. The model was run with the meteorological forcings observerd in the field (Figure A.3). The model was run until less than 1% of the mass initially existing in reach R1 (Figure A.1a) remained in the computational domain.

A.3 Results and Discussion

A.3.1 Shallow mixing layers

The best fit of the time-averaged downstream velocities with the experimental data of *Chu and Babarutsi* [1988] − based on the lowest overall root mean square error (RMSE) – was achieved with $A_h = 5\times10^{-5}$ $m^2 s^{-1}$ (Figure A.4). This value of A_h (≈ 0.05Du^*) is half the theoretical value for prismatic laboratory channels [*Rastogi and Rodi*, 1978]. RMSE represented on average less than 6% of the maximum streamwise velocity in the channel. RMSEs represented 4.09, 5.86, 6.85, 6.18 and 4.85% of the maximum streamwise velocity at sections A1 to A5, respectively. Following *Chu and Babarutsi* [1988], the width of the mixing layer β in each section can be defined as $\beta = (u_{s1}\text{-}u_{s2})/(\partial u_s/\partial y)_{max}$, $(\partial u_s/\partial y)_{max}$ being the maximum mean velocity gradient, and u_{s1} and u_{s2}, the mean streamwise velocities in the fast and slow ambient, respectively. Except for section A4, the model correctly predicted the transverse spreading rate of the shallow mixing layer

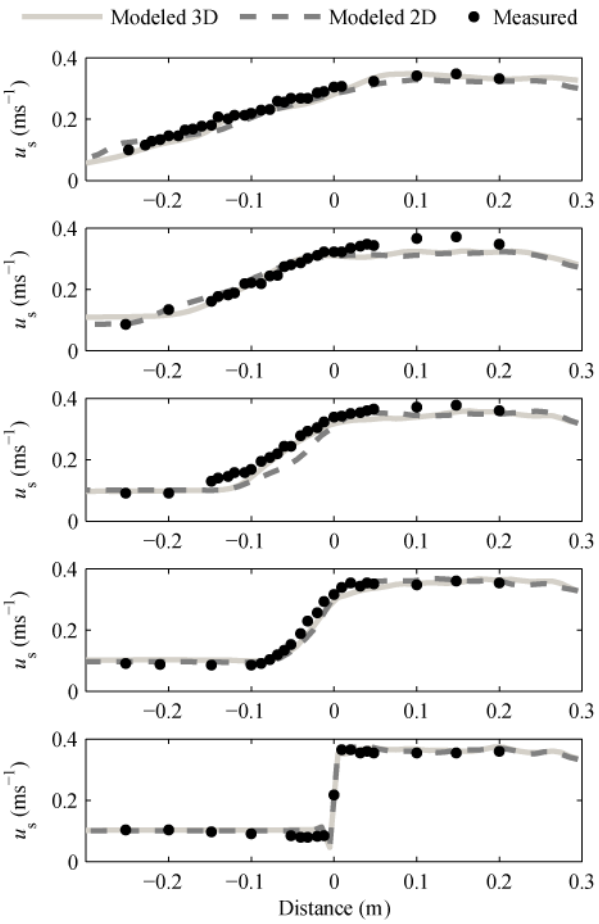

Figure A.4 Modeled and measured [Chu and Babarutsi, 1988] time-averaged streamwise velocities at section (a) A5, (b) A4, (c) A3, (d) A2 and (e) A1 in Figure A.2a

(Table A.4). Experimental data showed that the mixing layer in this test increased almost linearly with distance. The ratio of the slopes ($I_R = I_{exp}/I_m$) of the regression lines between measured I_{exp} and modeled I_m mixing-layer widths in Table A.4 is close to 1 ($I_R = 0.92$).

Table A.4 Modeled and measured non-dimensional mixing-layer widths β/b.

Section	Measured [(a)]	Modeled
A1	-	0.018
A2	0.121	0.135
A3	0.270	0.248
A4	0.411	0.293
A5	-	0.603

[(a)] *Chu and Babarutsi* [1988]

Model results after running the model with only one cell in the vertical (2D-simulation) are similar to those obtained with 3D simulations (Figure A.4), which probed that, for this experiment, 3D effects are of secondary importance.

A.3.2 Flow past a lateral cavity

The best fit based on the lowest RMSE with the experimental data of *Kimura and Hosoda* [1997] was achieved with $A_h = 10^{-4}$ m^2 s^{-1} (two times the theoretical value, $\approx 0.2Du^*$). The model correctly reproduced the time-averaged streamwise velocities at half the depth at section B1 (Figure A.5) and RMSEs represented less than 6% of the mean streamwise velocity in the main channel ($U_m \approx 37$ cm s^{-1}). Most of this error is accounted by the model underprediction of the streamwise velocity in the main channel. Although no measurements of water surface elevations were taken in the main channel, the velocity underprediction is most likely the result of some overestimation of the longitudinal slope of the water surface elevation due to an overestimation of the streamwise drag.

The model reproduced a 1-gyre system inside the dead zone (Figure A.6a-c) which is consistent with the geometry of the dead zone ($b_0/L_0 \approx 0.7$). The streamlines in

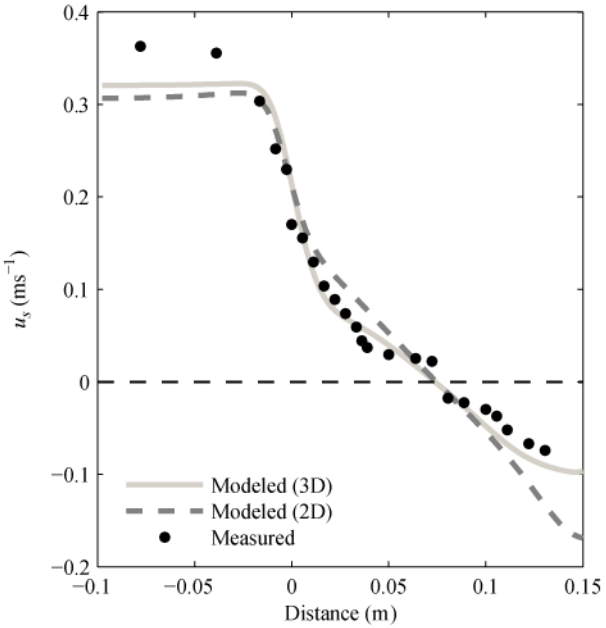

Figure A.5 3D-Modeled and measured [*Kimura and Hosoda*, 1997] time-averaged streamwise velocities at half the depth and 2D-Modeled time-averaged streamwise velocities at section B1 in Figure A.2b, across the dead zone. Distance = 0 at the interface between the dead zone and the main stream.

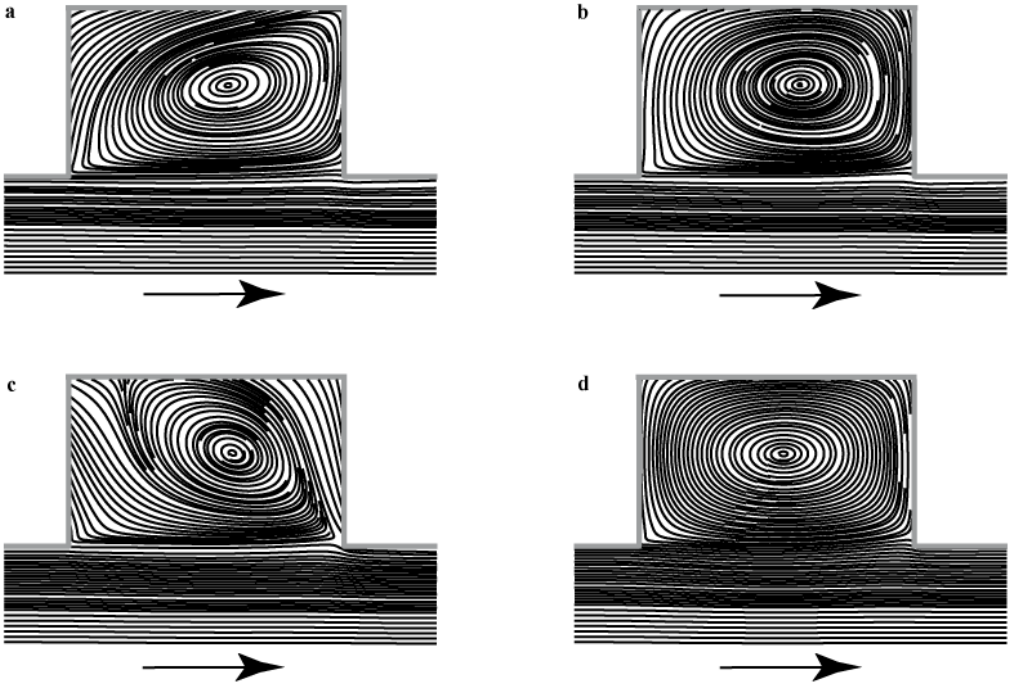

Figure A.6 Modeled time-averaged streamlines in the dead zone (a) at the surface plane, (b) at mid-depth (0.01 m from the surface) and (c) near the channel bed (0.018 m from the surface) for the simulation in 3D and time-averaged streamlines (d) for the simulation in 2D. The arrow shows the direction of the flow in the main stream.

Figure A.6a-c show the importance of three-dimensional effects on the velocity field inside the dead zone. Near the surface (Figure A.6a) the flow is, on average, towards the main channel, while near bed this trend is reversed (Figure A.6c), and the flow is, on average, directed towards the dead zone. Two-dimensional simulations are not able to capture this non-uniformity of the flow over depth (Figure A.6d) and thus, they do not correctly reproduce the horizontal velocity field inside the dead zone (Figure A.5).

A.3.3 Flow in open channels with mild curvature

A.3.3.1 *Unstratified curved channel*

A.3.3.1.1 Water surface elevation

The best fit based on the overall lowest RMSE with measured velocities and water surface elevations was achieved with $A_h = 10^{-3}$ m^2 s^{-1} (two times the theoretical value, $\approx 0.2Du^*$) and $C_d = 0.003$. Although the cross-stream slope is well captured, the longitudinal slope of the free surface increases abruptly for angles < 90º (Sections C6-

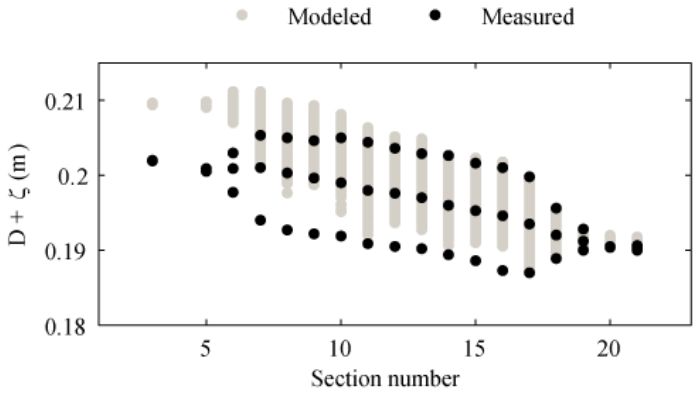

Figure A.7 Modeled water surface elevations (expressed as total elevation from bed) along each C-section in Figure A.2c and measured [*deVriend*, 1979] water surface elevations at the sides and the center line.

C11, Figure A.7). The simulated longitudinal slope along the first 90^{o} of the bend is ca. 3 times larger than measured. The error in the free surface solution is likely associated with the imperfect representation of a curved domain using a rectangular Cartesian grid, which may introduce artificial frictional effects.

A.3.3.1.2 Streamwise velocities

All vertical profiles were cubic interpolated to match the experimental data and root mean square errors (RMSEs) were calculated for each vertical profile at each section. Figure A.8 shows the streamwise velocity profiles at section C12 ($\Phi = 90º$). Experimental data always peak at a point located below surface; however, modeled results peak at the surface from profiles 6 to 11. This discrepancy is due to the inability of the model to reproduce the transport, by the lateral circulation, of low longitudinal momentum fluid from the bottom and sidewalls towards the center of the channel and near the free surface. This has been observed in other model validations [e.g., *Leschziner and Rodi*, 1979]. RMSE for profile number 6, located in the middle of the cross sections, ranged from 9 $\times 10^{-4}$ to 0.096 m s^{-1}, with a mean value of 0.0437 m s^{-1} (c.a. 6.8% of the maximum velocity experimentally achieved at this profile in all computed sections), whilst profiles 1 (inner side) and 11 (outer side) ranged from 2 $\times 10^{-4}$ to 0.304 m s^{-1} and from 0.006 to 0.269 m s^{-1}, respectively, with mean values of 0.145 m s^{-1} (c.a. 22.5% of the maximum velocity achieved at profile 1) and 0.144 m s^{-1} (c.a. 22.3% of the maximum velocity achieved at profile 11), respectively (Table A.5). These errors are of the same order as

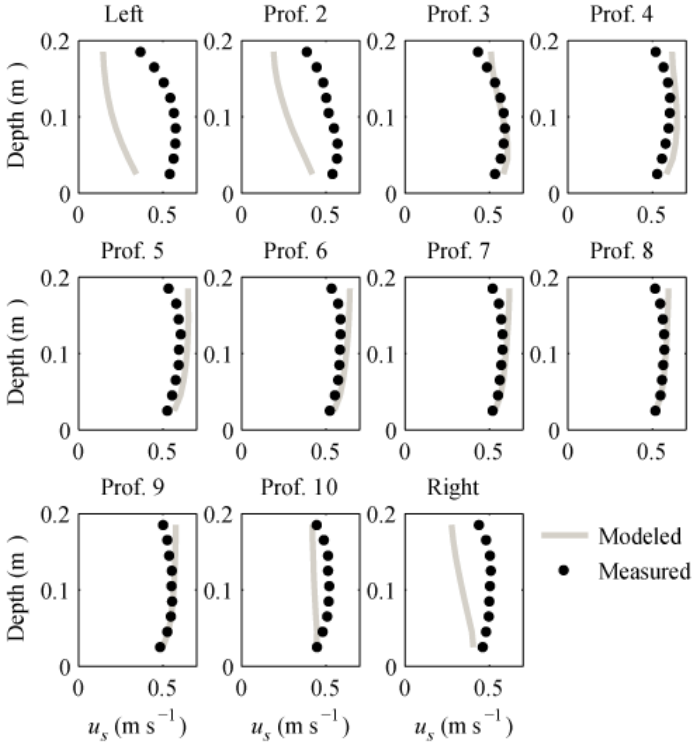

Figure A.8 Modeled and measured [deVriend, 1979] streamwise velocities (profiles 1-11) at section C12 (90º) in Figure A.2c. The left side is the inner bank and the right side the outer bank.

Table A.5 RMSE (ms^{-1}) of the streamwise and lateral velocities in each profile averaged over sections C3 to C21

Profile	**RMSE u_s (ms^{-1})**	**RMSE u_l (ms^{-1})**
Left	0.145	0.0147
1	0.092	0.0165
2	0.032	0.0153
3	0.039	0.0152
5	0.044	0.0129
6	0.039	0.0116
7	0.031	0.011
8	0.033	0.0129
9	0.096	0.0153
10	0.143	0.0146
Right	0.145	0.0147

those of *Leschziner and Rodi* [1979] – averaged RMSE (graphically calculated) of 0.012 m s^{-1} at the section located at 102º at the bend.

The model was capable of reproducing the gradual shift of the maximum value of the streamwise velocity from the inner to the outer bank of the bend (Figure A.9), although depth-averaged streamwise velocities were generally overestimated with a mean RMSE of 0.0879 m s^{-1} (c.a. 13.6% of the maximum depth-averaged streamwise velocity in all sections). The biggest errors occurred near the walls due to the representation of the curved domain with a Cartesian grid.

A.3.3.1.3 Lateral velocities

Model results show Prandtl's first kind cell with the flow at the upper mid-half of the section moving towards the outer bank and in the opposite direction at the lower mid-half (e.g., Figure A.10-A12). RMSEs at profile number 6 ranged from 2.7×10^{-4} to 0.058 m

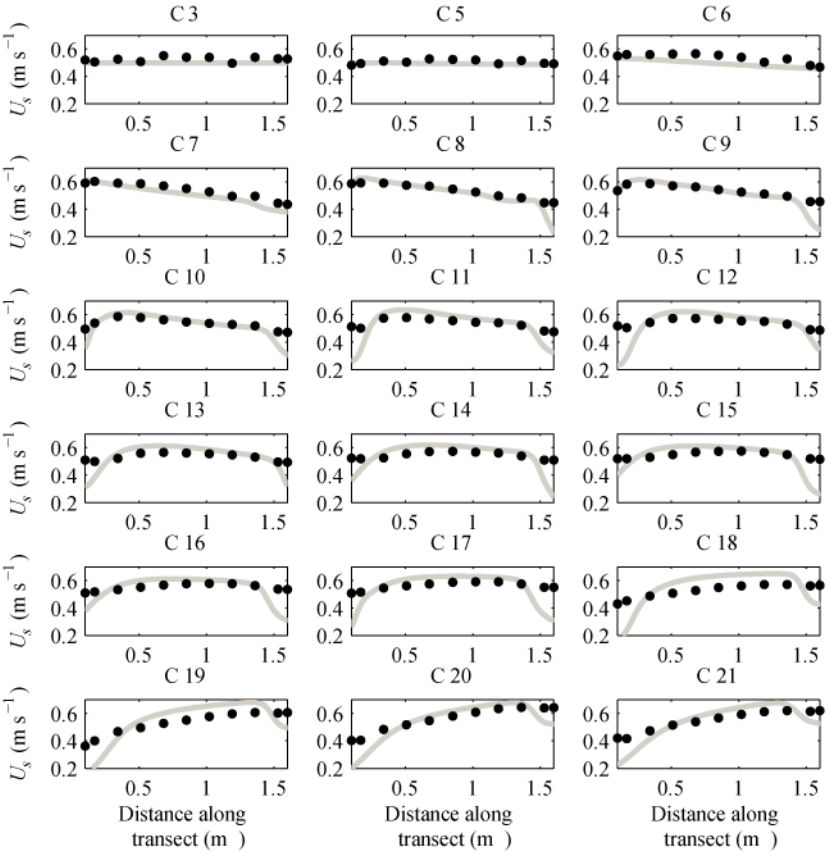

Figure A.9 Modeled and measured [deVriend, 1979] depth-averaged streamwise velocities.

s^{-1}, with a mean value of 0.013 m s^{-1} (c.a. 14.1% of the maximum velocity measured at profile 6), whilst profiles 1 and 11 ranged from 0.001 to 0.032 m s^{-1} and from 5.1×10^{-4} to 0.059 m s^{-1}, respectively, with mean values of 0.015 (c.a. 16 % of the maximum velocity measured at profile 1) and 0.015 m s^{-1} (c.a. 15.9% of the maximum velocity measured at profile 11) respectively (Table A.5). These errors are one order higher than those of *Leschziner and Rodi* [1979] − averaged RMSE (graphically calculated) of 0.003 m s^{-1} for the section located at 102º at the bend −. However, *Leschziner and Rodi* [1979] did not include the profile closest to the inner bank nor the closest to the outer bank, where the highest errors are expected. The model failed to simulate the outer-bank secondary recirculation cell (e.g., Figure A.11 and Figure A.12). This is also the case of other models, as reported in the literature [e.g., *Leschziner and Rodi*, 1979; *Shao et al.*, 2003; *Leupi and Altinakar*, 2005].

Leupi and Altinakar [2005], for example, worked with non-hydrostatic pressure codes and found that the non-hydrostatic corrections to the hydrostatic balance improved the water surface elevation for the sections located at an angle higher than 120º. Through the non-hydrostatic calculations, they decreased the model error in reproducing the Prandtl's first kind secondary circulation. However, they were not able to reproduce the outer-bank cell because of their linear *k-ε* model. *Kawahara and Tamai* [1988] (as reported in *Blanckaert and deVriend* [2004]) demonstrated theoretically that linear eddy viscosity models (typically used in large scale models for geophysical flows, due to their reduced computational burden) cannot represent turbulence-induced vorticity, unless negative mixing coefficients are allowed. Nonlinear turbulence models ―based on a nonlinear relationship between the turbulent stresses and the strain rates―, however, correctly predict the outer-bank cell [*Jia et al.*, 2001; *Blanckaert and deVriend*, 2004]

Van Balen [2010] proved that the anisotropy of the turbulence stresses and the centrifugal effects are the dominant terms in the vorticity budget, and they need to be explicitly represented to simulate correctly the formation of the outer-bank cell. *Christensen et al.* [1999] also simulated the outer-bank cell, accounting for cross-stream turbulence anisotropy in their Reynolds Stress Model (RSM). In any case, the width of the outer-bank cell is approximately equal to the water depth [*van Balen*, 2010], thus, for b= 400 m, and D = 10 m, as observed at the tail of the Ribarroja reservoir, the outer-bank cell would occupy only a 2.5% of the channel width.

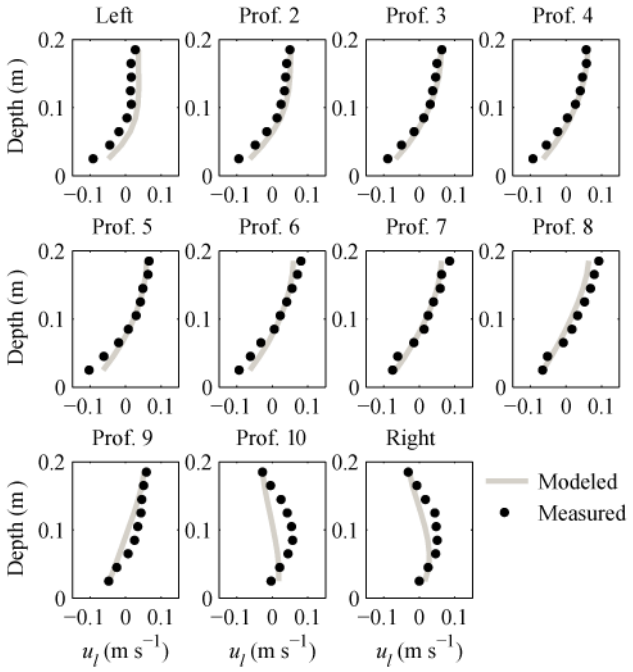

Figure A.10 Modeled and measured [deVriend, 1979] lateral velocities (profiles 1-11) at section C12 (45º) in Figure A.2c. The left side is the inner bank and the right side the outer bank.

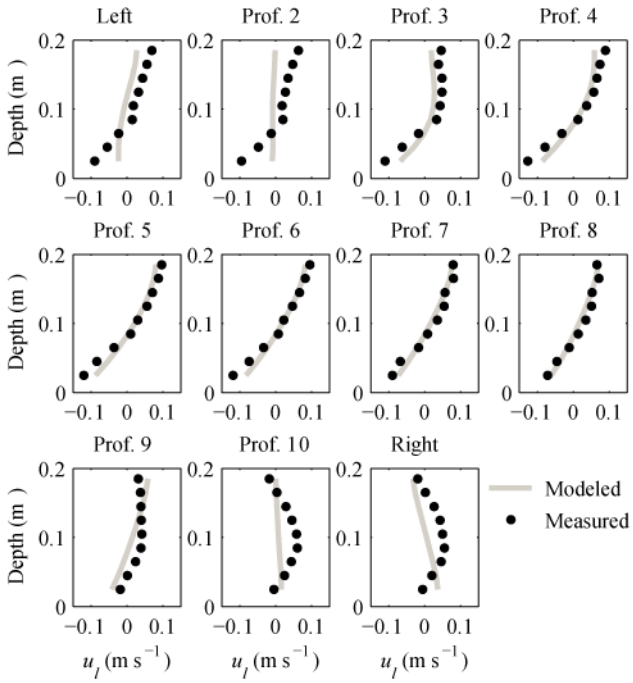

Figure A.11 Modeled and measured [deVriend, 1979] lateral velocities (profiles 1-11) at section C15 (90º) in Figure A.2c. The left side is the inner bank and the right side the outer bank.

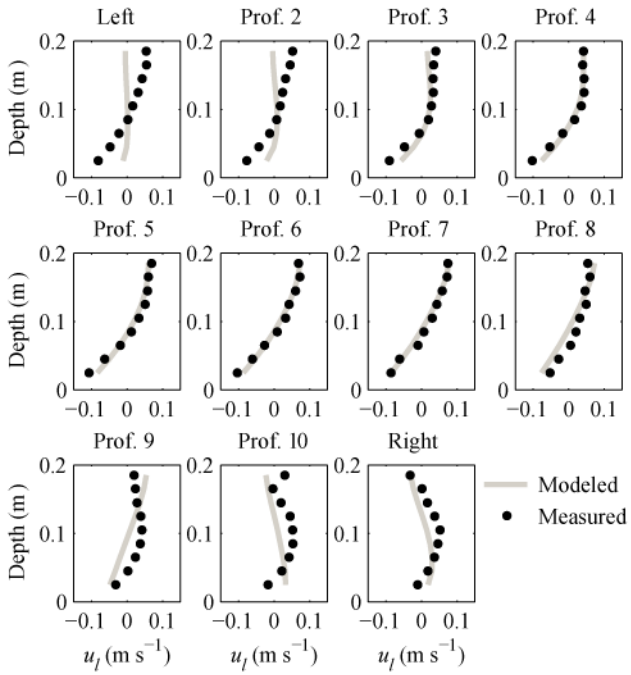

Figure A.12 Modeled and measured [deVriend, 1979] lateral velocities (profiles 1-11) at section C9 (135º) in Figure A.2c. The left side is the inner bank and the right side the outer bank.

A.3.3.1.4 Grid convergence study

Figure A.13 shows the error E (Eq. A.11) and I_{RMA} slopes of each of the variables selected for the convergence study in all common nodes with the three grid resolutions. As the grid resolution increases, errors tend to converge with O (Δx^2) accuracy, except for ζ, which remains O (Δx). The error for the 0.034 m resolution grid is less than 1% for all

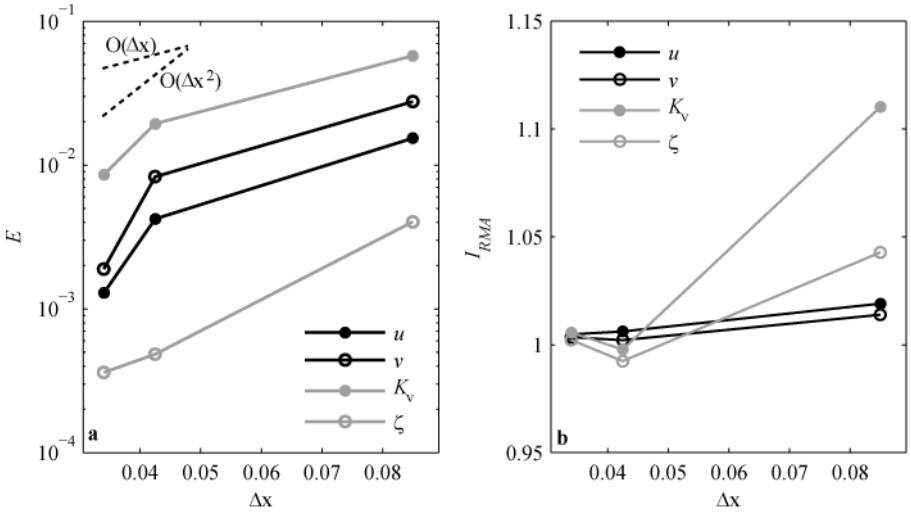

Figure A.13 Errors E (a) and RMA slopes (b) for the three tested grid sizes in the unstratified bend case.

four variables (Figure A.13a), which suggests grid independency. RMA slopes I_{RMA} also decrease as the grid resolution increases and approximate ≈ 1 for the 0.034 m resolution grid, suggesting also grid convergence (Figure A.13b).

A.3.3.2 *Stratified curved channel*

Figure A.14 shows modeled and measured vertical profiles of dimensionless temperature differences at section C12 in Test case 2. The observations reveal that warmer water tends to accumulate near the outer bank, while the colder water tends to upwell near the inner bank. The maximum *DT** near the surface from inner to outer bank varies from 0.45 to 0.6, which is consistent with the experimental data. The model, though, under-predicts the temperatures at intermediate depths (≈ 0.6-0.8 *z*/*D*) near the outer bank.

The results of Test case 1 (with smaller shear, Table A.1) at the apex cross section are shown in Figure A.15. The highest streamwise velocities occur near the surface and towards the outer bank (Figure A.15a). The weakest speeds occur, though, towards the inner bank and towards the bottom. The primary streamwise flow is accompanied by strong secondary motions. There are three secondary cells (Figure A.15b) which rotate in opposite directions: two below the thermocline, and one above it. This is in sharp contrast to isothermal flow in which the secondary motions consist of only one major eddy and a minor eddy, rotating in opposite directions. These results are consistent with the

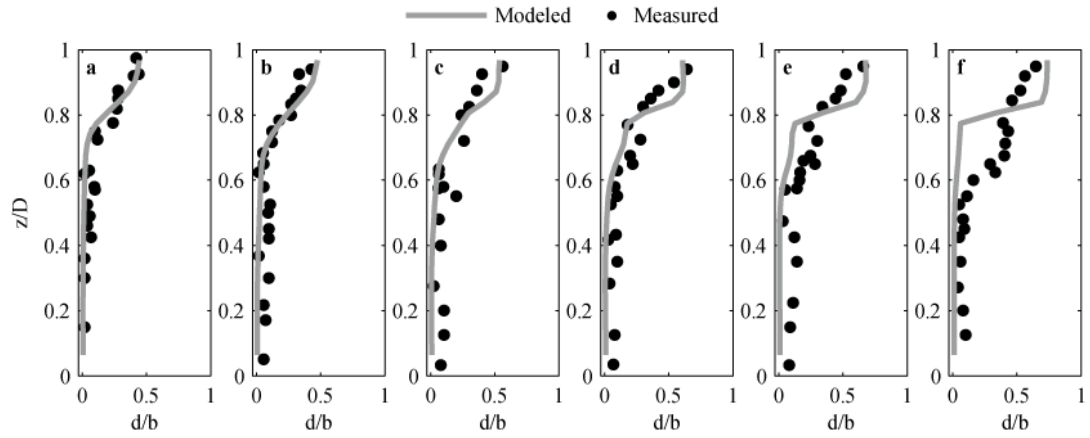

Figure A.14 Vertical profiles of dimensionless temperature differences at (a) the inner bank, (b) 8.6 cm, (c) 16.2 cm, (d) 23.8 cm, (e) 31.4 cm from the inner bank, and (f) at the outer bank. Dots account for experimental data of *He et al.* [1992] (in *Chao et al.* [2009]). Section located at 90º inside the bend (section C12). Test case 2 (run D2) in Table A.1.

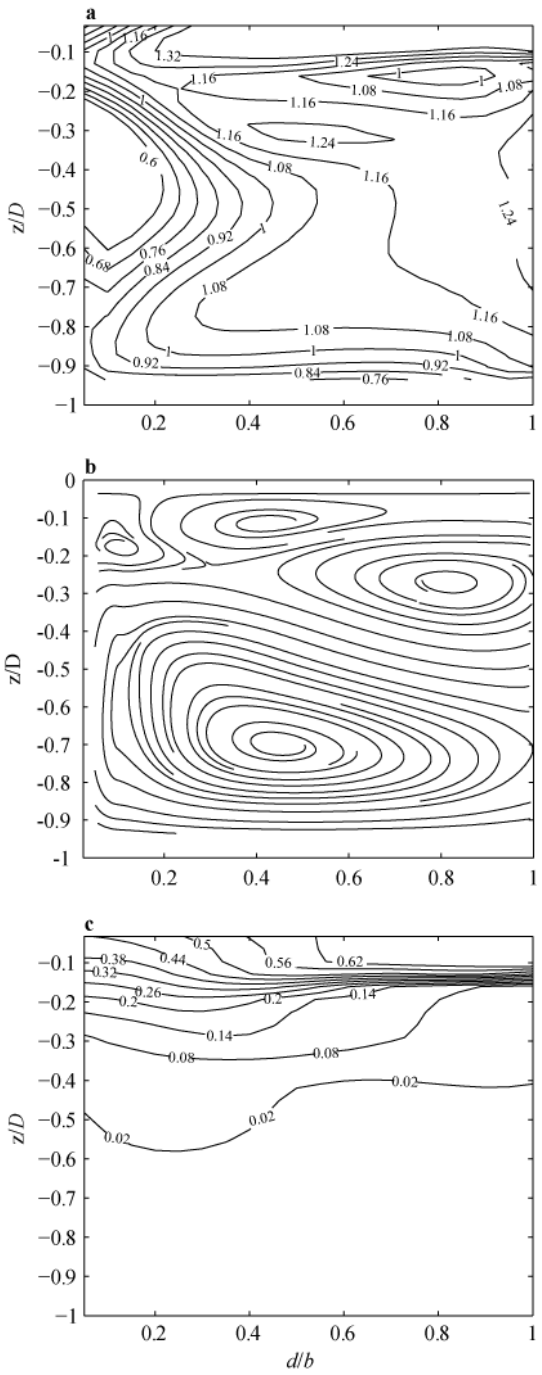

Figure A.15 Modeled (a) dimensionless streamwise velocities, (b) secondary flow streamlines and (c) dimensionless temperature profiles in the 90º cross section inside the bend. Test case 1 (run D1) in Table A.1.

experimental results of *He et al.* [1992] (see Figures 6-7 in *Shen et al.* [2003]), and also with the numerical simulations of *Shen et al.* [2003] and *Chao et al.* [2009]. The differences among models and observations lie on the extent of the different recirculation cells. Although we were not able to find quantitative values of velocities upon which we could conduct a more quantitative comparison, from Figure A.15b it is observable that the model failed to locate the core of the minor eddy, which in Figure A.15b is at $d/b \approx 0.4$. The isotherms for Test Case 1 are shown in Figure A.15c. Note that the isotherms tend to compress near the outer bank, while they tend to expand near the inner bank. Also warmer temperatures tend to accumulate near the outer bank and the mixed layer tends to upwell near the inner bank, as it was the case with Test 2. These results are consistent with those of *Shen et al.* [2003] (see their Figure 5). Due to a more centered location of the core of the minor eddy in the simulations, there is less transport of warm water to the outer bank. This explains the temperature underestimation near the outer bank in Figure A.14.

The large-scale model used here is not expected to provide accurate results in the experimental setup of *He et al.* [1992] for different reasons: (1) the ratio of horizontal and vertical length scales is small and, hence, it is possible that non-hydrostatic effects be at play near the bend; these effects are ignored in the model, which is based on the hydrostatic assumption; (2) the model ignores lateral friction, while other modelling works have used lateral friction on the walls, which might accelerate the rate of mixing when acting on isotherms which are not horizontal. In any case, the relevant features of the flow and temperature fields observed in a curved stratified flow are captured by the large-scale free-surface hydrostatic model.

A.3.4 Model validation with field data

The density field at the confluence between the W- and N- rivers is correctly represented with NRMSEs representing on average less than 5 % of the maximum variability encountered in the field (Figure A.16 and Table A.6). The biggest NRMSEs on day 203 of ca. 14% (Table A.6) occurred at the shallows near the south bank of the W-channel. There are also NRMSEs > 10% at locations at the confluence region close to the entrance of the W-channel on day 203.

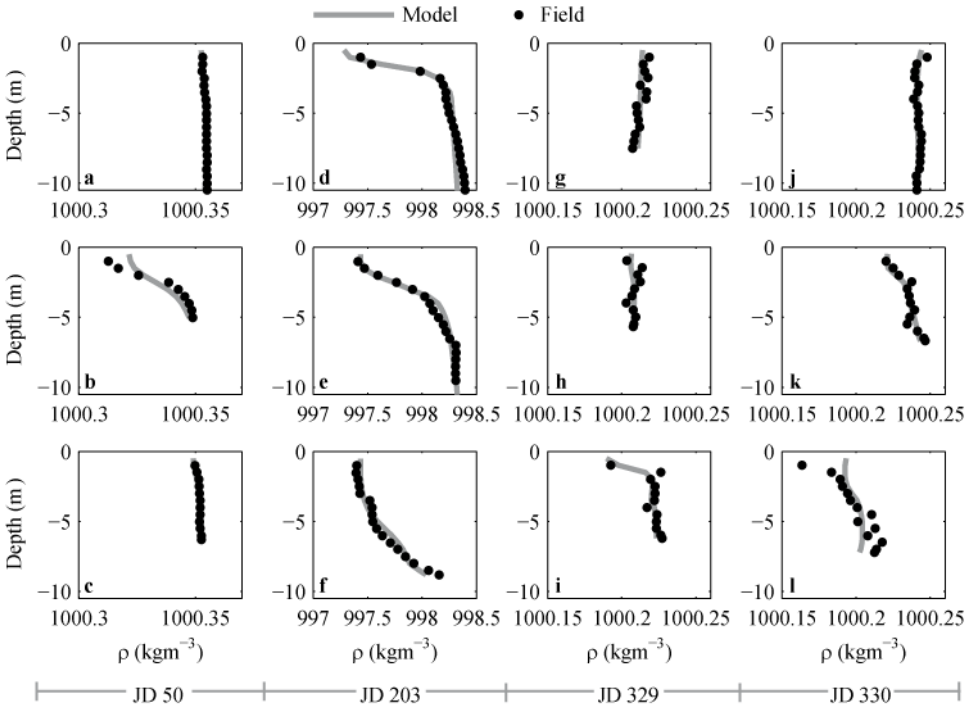

Figure A.16 Modeled (solid lines) and measured (dots) density profiles at locations (a) F_{CTD-1}, (b) F_{CTD-2}, (c) F_{CTD-3}, (d) J_{CTD-1}, (e) J_{CTD-2}, (f) J_{CTD-3}, (g) N_{CTD-1}, (h) N_{CTD-2}, (i) N_{CTD-3}, (j) N_{CTD-4}, (k) N_{CTD-5} and (l) N_{CTD-6} in Figure A.1b and Figure A.1d.

The location of the cores of maximum E-W velocities is generally well represented (not shown) on all days of simulation. NRMSEs of the width-averaged E-W and N-S velocities (Figure A.17) are on average less than 14% and 30%, respectively (Table A.6). Higher errors in the N-S velocities are due to the main flow (except at the confluence itself) being directed towards the East and, thus, N-S velocities being close to zero (see Figure A.17m and Figure A.17u as an example). When small magnitudes of one velocity component occur, percentage differences lead to large percentage differences even when modeled values differ only slightly from measured values [*Abad et al.*, 2008]. Moreover, ADCP transects were collected only once per each location in the field, when a minimum of six crossings are needed to approximate time-averaged velocity fields and eliminate turbulence effects [*Dinehart and Burau*, 2005b; *Parsons et al.*, 2013]. The presence of just one crossing per location complicates the overall capacity of the model to fit the field data. Despite this, RMSEs are comparable with previous numerical studies in rivers [e.g., *Biron et al.*, 2004].

Table A.6 NRMSE (%) between modeled and field data.

	Density			Width-averaged E-W velocity			Width-averaged N-S velocity		
Julian day	**Min.**	**Max.**	**Mean**	**Min.**	**Max.**	**Mean**	**Min.**	**Max.**	**Mean.**
50	0.14	7.8	2.7	4.75	33.36	13.05	5.43	20.30	10.34
203	0.02	14	4.8	2.98	13.27	9.68	10.91	42.63	29.20
329-330	0.04	9.1	2.8	3.2	20.1	9.17	8.8	35.7	17.39

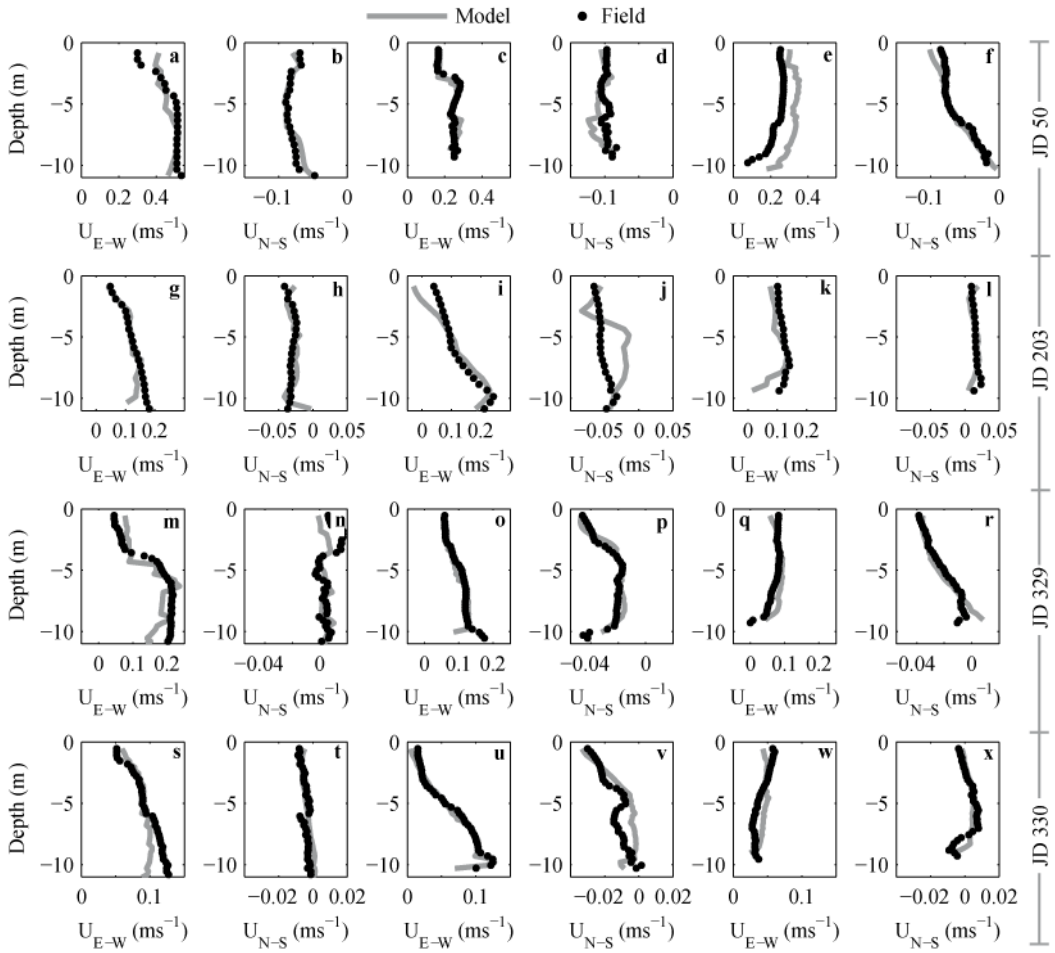

Figure A.17 Modeled (gray lines) and measured (black dots) width-averaged E-W and N-S velocities at transects (a-b) f1, (c-d) f2, (e-f) f3 in Figure A.1b, transects (g-h) j1, (i-j) j2, (k-l) j3 in Figure A.1c and transects (m-n) n1, (o-p) n2, (q-r) n3, (s-t) n4, (u-v) n5 and (w-x) n6 in Figure A.1d.

A.4 Conclusions

A Cartesian free-surface hydrodynamic model has been validated for flows past a lateral cavity, flows in open channel with mild curvature and the development of shallow mixing layer between parallel confluent streams. Despite obtaining results which are approximate as a result of the simplified set of equations in the analysis, the primitive-equation based model shows satisfactory results in all these tests. This study also proves the ability of the model to simulate the more complex flows that develop in natural systems —such as the confluence between the Ebro and Segre rivers into the Ribarroja reservoir— with a reasonable computational cost.

Appendix B

Inflow-outflow boundary conditions along arbitrary directions in Cartesian lake models

Published in *Computers & Geosciences*,
doi: 10.1016/j.cageo.2014.10.002

Abstract

Specifying point sources and sinks of water near boundaries is presented as a flexible approach to prescribe inflows and outflows along arbitrary directions in Cartesian grid lake models. Implementing the approach involves a straightforward modification of the governing equations, to include a first order source term in the continuity and momentum equations. The approach is implemented in a Cartesian grid model and applied to several test cases. First, the flow along a straight flat bottom channel with its axis forming different angles with the grid directions is simulated and the results are compared against well-known analytical solutions. Point-sources are then used to simulate unconfined inflows into a reservoir (a small river entering a reservoir in a jet-like manner), which occur at an angle with the grid directions. The model results are assessed in terms of a mixing ratio between lake and river water, evaluated at a cross-section downstream of the inflow boundary. Those results are particularly sensitive to changes in the inflow angle. It is argued that differences in mixing rates near the inflow sections could affect the fate of river-borne substances in model simulations.

B.1 Introduction

The space-time distribution of particulate and dissolved substances in lakes and reservoirs, the light and nutrient availability for algal growth and, in general, the environment in which biogeochemical reactions occur are largely controlled by transport and mixing processes in the water column. Describing and understanding the physical processes leading to mixing and transport in the water column, hence, is the first step that needs to be taken to understand the chemical and biological properties of aquatic ecosystems, and its spatial and temporal variability. To this end, considerable efforts have

been devoted during the last few years to develop and apply numerical models, capable of solving the governing equations of fluid motion and, hence, describing the flow environment in three-dimensions with a high temporal and spatial resolution and low computational cost. Most of these large-scale flow models are based on the solution of the three-dimensional form of the shallow-water equations 3D-SWE, subject to the appropriate boundary conditions. The correct representation of the specific flow patterns that develop in any given water body depends mainly on the ability of the model to represent accurately the mass and energy fluxes (their frequency, intensity, duration and timing) that occur through the free surface — and which are the drivers of motion in the water column — and the morphometry of the system [*Imboden and Wüest*, 1995]. This, in turn, largely depends on how the physical space is discretized on the model grid (grid system). The most widely used grid system in 3D lake modeling is the Cartesian-grid [e.g., *Hodges et al.*, 2000; *Rueda et al.*, 2000; *Appt et al.*, 2004; *Laval et al.*, 2005; *Okely and Imberger*, 2007; *Hoyer et al.*, 2014]. Model coding and grid definition in this grid-system is much simpler than in others. Grid generation, for example, in unstructured-grid models is not a completely automatic process, requiring separate grid creation software, and user intervention is often need to produce a grid of satisfactory quality [*Liang et al.*, 2007], especially if complex topographic features are present. It is also computationally expensive.

In spite of their simplicity, Cartesian grid lake models tend to produce locally inaccurate solutions where the shoreline is not aligned with the Cartesian grid directions and is represented as a staircase. A variety of approaches have been proposed to resolve correctly the near shore circulation. The grid resolution can be increased near the shoreline, for example, using ‘plaid’ structured meshes (i.e. non-uniform Cartesian grid spacing), adaptive mesh refinements or nested grids [e.g., *Berger and Oliger*, 1984; *Ham et al.*, 2002; *Gibou et al.*, 2007; *Peng et al.*, 2010, and references therein]. Cut cells can also be used for the solution of the shallow water equations [*Causon et al.*, 2000; *Liang et al.*, 2007], and in this case, boundary contours are cut out of a background Cartesian mesh and cells that are partially or completely cut are singled out for special treatment. Other approaches such as the immerse boundary method of *Peskin* [1972, 2002], the virtual boundary method [*Saiki and Biringen*, 1996] or the Brinkman penalization method [e.g., *Reckinger et al.*, 2012] introduce a source (force) term in the momentum equations, to represent the force exerted by solid boundaries on the fluid.

An additional problem arising from the Cartesian representation of lake boundaries is related to the simulation of river inflows and outflows, which may not be aligned with the grid directions (Figure B.1). Flow boundary conditions (clamped boundary conditions) are typically prescribed in lake models [e.g., *Smith*, 2006; *Hodges et al.*, 2000] by setting the values of the velocity components normal to the grid directions at the faces of the boundary cells (Figure B.1). Flow directionality with this approach, which will be referred to as NF-method (for normal velocity component along faces), could be wrong. The effects of inflows on circulation and mixing — whether these effects are localized [*Rueda and Vidal*, 2009] or if they impact the basin-scale motions [*Hollan*, 1998] — or the fate of river-borne substances, may not be correctly simulated with the NF-method. Our goal is to present an alternative approach to specifying inflow and outflow boundary conditions in Cartesian lake models, in which flow direction is independent of grid alignment. It consists of using point sources and sinks of mass and momentum in grid cells which are next to solid boundaries, where water is added or detracted from the computational domain (Figure B.1). This approach, here referred to as SC (for sources and sinks), implies a simple-to-implement modification of the governing equations. The grid, in turn, does not need to be modified. The use of sources and sinks of mass and momentum has been successfully applied in the lake modeling literature

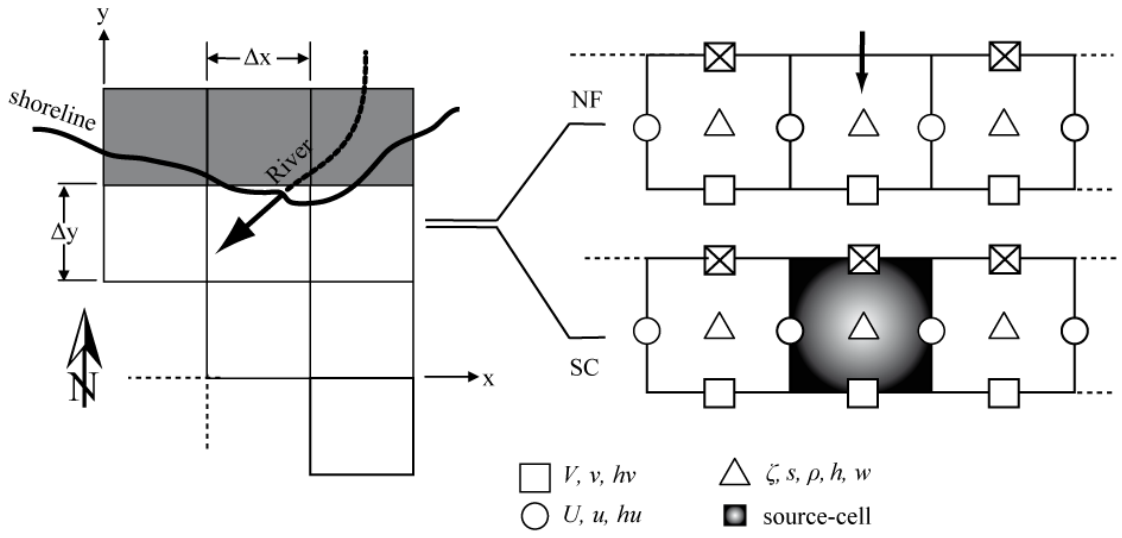

Figure B.1 (Left) Schematic plot illustrating the entrance of river inflows at an angle with the Cartesian grid and (right) how these river inflows would be specified with the (top right) NF-method and the (bottom right) SC-method. Black arrows show the direction of the real inflows (left) and those prescribed with the NF-method (top right). Squares, circles and triangles show where variables are defined within a given cell. Crossed symbols show the defined variable is set to zero.

[*Singleton et al.*, 2010] to simulate the effect of bubble-plumes on lake circulation, and, hence, on hypolimnetic oxygen and density fields. Here, the method is adapted to represent the effect of localized flows into and out of the domain, with length scales which are well below the grid resolution of the model. It is examined whether ignoring the directionality of inflows may affect or not the results of local and larger basin-scale simulations of mixing and transport in lakes and reservoirs.

B.2 Methods

B.2.1 Approach

The SC and the NF approaches to specifying flow boundaries in a 3D-SWE model will be first described. These two approaches were compared in a test case in which the flow boundaries are aligned with the grid directions. The test consists on the simulations of the flow field along a straight rectangular channel with flat bottom laid out along the *x*-axis. The SC-method will be then applied to the same straight channel, but in this case, the channel will be assumed to form an angle with the Cartesian grid directions. The SC-method will be then applied to simulate environmental flows in a lake in which the use of boundaries not aligned to the Cartesian grids are needed.

B.2.2 Governing equations with point sources and sinks of fluid.

Assuming that (1) variations in density are negligible everywhere except in the buoyancy term (the Boussinesq approximation), (2) the weight of the fluid balances the pressure in the equation for vertical momentum (the hydrostatic approximation), and (3) a diffusion-like term can be used to represent turbulent fluxes of scalars and momentum (the eddy diffusivity concept), the Navier-Stokes equations, incorporating point sources and sinks of fluids, can be written as (adapted from the work of *Lynch* [1986]):

$$\frac{\partial u}{\partial x}+\frac{\partial v}{\partial y}+\frac{\partial w}{\partial z}=\frac{\delta}{\rho_0} \tag{B.1}$$

$$\frac{\partial \zeta}{\partial t}+\frac{\partial}{\partial x}\left[\int_{-D}^{\zeta} u dz\right]+\frac{\partial}{\partial y}\left[\int_{-D}^{\zeta} v dz\right]=\int_{-D}^{\zeta}\frac{\delta}{\rho_0}dz \tag{B.2}$$

$$\frac{\partial u}{\partial t}+u\frac{\partial u}{\partial x}+v\frac{\partial u}{\partial y}+w\frac{\partial u}{\partial z}-fv=-\left(g\frac{\partial \zeta}{\partial x}+g\frac{1}{\rho_0}\int_z^{\zeta}\frac{\partial \rho}{\partial x}dz'\right)+\frac{\partial}{\partial x}\left(A_h\frac{\partial u}{\partial x}\right)+\frac{\partial}{\partial y}\left(A_h\frac{\partial u}{\partial y}\right)+\frac{\partial}{\partial z}\left(A_v\frac{\partial u}{\partial z}\right)+\frac{\delta}{\rho_0}(u-u_0) \quad \text{(B.3)}$$

$$\frac{\partial v}{\partial t}+u\frac{\partial v}{\partial x}+v\frac{\partial v}{\partial y}+w\frac{\partial v}{\partial z}+fu=-\left(g\frac{\partial \zeta}{\partial y}+g\frac{1}{\rho_0}\int_z^{\zeta}\frac{\partial \rho}{\partial y}dz'\right)+\frac{\partial}{\partial x}\left(A_h\frac{\partial v}{\partial x}\right)+\frac{\partial}{\partial y}\left(A_h\frac{\partial v}{\partial y}\right)+\frac{\partial}{\partial z}\left(A_v\frac{\partial v}{\partial z}\right)+\frac{\delta}{\rho_0}(v-v_0) \quad \text{(B.4)}$$

$$\frac{\partial \theta}{\partial t}+u\frac{\partial \theta}{\partial x}+v\frac{\partial \theta}{\partial y}+w\frac{\partial \theta}{\partial z}=K_h\frac{\partial^2\theta}{\partial x^2}+K_h\frac{\partial^2\theta}{\partial y^2}+\frac{\partial}{\partial z}\left(K_v\frac{\partial \theta}{\partial z}\right)+\frac{H}{\rho c_p}+\frac{\delta}{\rho_0}\theta_0 \quad \text{(B.5)}$$

$$\frac{\partial O}{\partial t}+u\frac{\partial O}{\partial x}+v\frac{\partial O}{\partial y}+w\frac{\partial O}{\partial z}=K_h\frac{\partial^2 O}{\partial x^2}+K_h\frac{\partial^2 O}{\partial y^2}+\frac{\partial}{\partial z}\left(K_v\frac{\partial O}{\partial z}\right)+\frac{\delta}{\rho_0}O_0 \quad \text{(B.6)}$$

These equations comprise the 3D-SWE. They express the physical principles of conservation of mass for an incompressible fluid (Eqs. B.1-B.2), conservation of momentum (Eqs. B.3-B.4) and conservation of energy (Eq. B.5). Finally, Eq. B.6 is the transport equation for passive tracers, not affecting the fluid density. Here *u*, *v*, and *w* represent the velocity components in the *x*-, *y*-, and *z*- directions; *f* is the Coriolis parameter; *g* is the acceleration of gravity; θ represents temperature; *O* represents the concentration of a passive tracer in the domain; ζ is the free surface elevation; $z = -D(x, y)$ is the depth of the bottom boundary measured from the undisturbed free surface $z = 0$; *H* is a source of heat associated with heat and energy fluxes due to atmospheric heating or cooling; *A* is the kinematic eddy viscosity and *K* is the turbulent transfer coefficient (eddy diffusivity) for temperature. The density ρ is calculated from temperature using an equation of state; the subscript *h* and *v* refer to horizontal and vertical directions, respectively; δ denotes the fluid source strength, and the ratio δ / ρ_0, for a given computational source cell of nominal volume ($= \Delta x \times \Delta y \times \Delta z$), represents the volume of water added/detracted per unit time, divided by the nominal volume of the cell. Note that this term will only be non zero next to the boundaries where inflows and outflows are specified. The subscript 0 in Eqs. B.1-B.6 is intended to define the characteristics of the water being added or removed from the computational domain at a source or sink cell.

The SC-method consists of setting source-sink computational cells adjacent to the flow boundaries in which water is added or detracted from the domain. Note first that, as a result of the source-sink term in the continuity equations — representing the addition and detraction of water from the domain—, the free surface elevation rises and descends and, hence, pressure gradients are generated near the boundaries. The velocity direction of the inflowing or out-flowing water (for example, inflows entering at an angle into a lake) can be prescribed by conveniently specifying u_0 and v_0. The larger is the source strength, the closer the velocity solution will be to u_0 and v_0.

B.2.3 Hydrodynamic model

The SC-method was implemented and tested in a 3D-SWE model [*Smith*, 2006], which has been previously used and validated against analytical solutions and field data sets collected in a variety of environments [*Rueda and Cowen*, 2005; *Rueda and MacIntyre*, 2010, and references therein]. The governing equations (B.1-B.6) are first posed in layer-averaged form by integrating over the height of a series of horizontal layers separated by level planes. The layer-averaged momentum equations are solved using a semi-implicit, three-level, iterative leapfrog-trapezoidal finite difference scheme on a staggered Cartesian grid. The semi-implicit approach is based on treating the gravity wave and vertical diffusion terms in the momentum equations implicitly to avoid time-step limitations due to gravity-wave CFL conditions, and to guarantee stability of the method. All other terms, including advection, are treated explicitly. The leapfrog-trapezoidal algorithm used for time stepping gives second order accuracy both in time and space. The variables are arranged in space on a C-Arakawa staggered Cartesian grid, with the flow variables defined at the interfaces, and the scalars and the pressure at the cell centers (Figure B.1). Non-active (i.e. tracers) and active (i.e. temperature) scalar transport equations were solved using a two-level semi-implicit scheme, in which only vertical diffusion is discretized implicitly. The advection terms in the transport equation for scalars are discretized with flux-limiter methods [e.g., *Durran*, 1999]. Turbulent mixing is represented in the 3-D model using diffusion-like terms. A Laplacian operator with constant mixing coefficients (horizontal eddy viscosity A_h or diffusivity K_h) is used in the model to represent horizontal mixing of momentum and scalars. Vertical eddy coefficients of mixing K_z are calculated using a two-equation model originally proposed by *Mellor and Yamada* [1974], and later modified by *Kantha and Clayson* [1994]. This

turbulent modeling approach is typically used in large scale models for geophysical flows due to their reduced computational burden. The discretized form of the depth-averaged continuity equation, governing the changes in the free-surface elevation (Eq. B.2) is given by

$$\zeta_{i,j}^{n+1} = \zeta_{i,j}^{n-1} - \frac{\Delta t}{\Delta x}\left[\sum_{k=k_1}^{km}\left(U_{i+1/2,j,k}^{n+1} - U_{i-1/2,j,k}^{n+1} + U_{i+1/2,j,k}^{n-1} - U_{i-1/2,j,k}^{n-1}\right)\right] - \frac{\Delta t}{\Delta y}\left[\sum_{k=k_1}^{km}\left(V_{i,j+1/2,k}^{n+1} - V_{i,j-1/2,k}^{n+1} + V_{i,j+1/2,k}^{n-1} - V_{i,j-1/2,k}^{n-1}\right)\right] \tag{B.7}$$

Here, U and V are the volumetric transport in x- and y- directions, respectively; Δt is the time step, Δx and Δy are the horizontal size of a cell in x- and y-, respectively; subscripts (i, j, k) denote the spatial location in the computational grid, and the superscripts (n), the time t level at which the variable is evaluated. The symbols k_1 and k_m denote the first (shallowest) and last (deepest) layer in a water column respectively. In the course of the computations for a given time step, the volumetric transports at time n+1 in the momentum equations are expressed as a function of the free surface at that time, i.e. U^{n+1} = f(ζ^{n+1}) and V^{n+1} = g(ζ^{n+1}) (see Table B.1), and substituted in Eq. B.7 to yield a sparse symmetric positive-definite system of equations for ζ^{n+1}. The matrix problem is then solved using a conjugate gradient iterative method (see *Smith* [2006] for details). Flow boundaries in the NF-approach are prescribed by setting the values of volumetric transports in Eq. B.7 to their known values. These, in turn, are estimated from observed flow rates Q_{FB}, assuming a uniform distribution of velocities along the flow boundaries. In the SC-approach, instead, a source-sink term (Table B.1) is added to f (ζ^{n+1}) or g (ζ^{n+1}) in the momentum equations during the solution process. Distinguishing between boundaries acting as sources (inflows) or sinks (outflows) is done by prescribing positive or negative flows Q_{FB} at the boundary cells, respectively. Flows are prescribed on the E face of a computational cell by adding the source term (E) given in Table B.1, to f(ζ^{n+1}) in the momentum equations for the volumetric transport U at (i+1/2, j). Flows across the N face (i, j+1/2) are prescribed by adding the source term (N) to g (ζ^{n+1}) in the momentum equations for the volumetric transport V at (i+1/2, j). Note that those source-sink terms can only be added to faces within the computational domain, for which momentum equations are being solved. Note also, that the source terms include fractions

Table B.1 Functions f (ζ^{n+1}) and g (ζ^{n+1}) for the expression of the volumetric transports U and V at time n+1 in the momentum equations, and source-sink terms E and N, added to f (ζ^{n+1}) and g (ζ^{n+1}) respectively, to prescribe flow in the SC approach.

Term	Discretized form[1,2,3,4]
f(ζ^{n+1})	$$U_{i+1/2,j,k}^{n+1} = \hat{U}_{i+1/2,j,k} - g\frac{\Delta t}{\Delta x}\bar{h}_{i+1/2,j,k}^{n}\left(\frac{\bar{\rho}_{i+1/2,j,1}^{n}}{\bar{\rho}_{i+1/2,j,k}^{n+1}}\right)\left(\zeta_{i+1,j}^{n+1} - \zeta_{i,j}^{n+1} + \zeta_{i+1,j}^{n-1} - \zeta_{i,j}^{n-1}\right)$$ $$+\Delta t\left(A_{V}{}^{n}_{i+1/2,j,k-1/2}\left(\frac{(U/\bar{h})_{i+1/2,j,k-1}^{n+1} - (U/\bar{h})_{i+1/2,j,k}^{n+1}}{\bar{h}_{i+1/2,j,k-1/2}^{n+1}} + \frac{(u)_{i+1/2,j,k-1}^{n-1} - (u)_{i+1/2,j,k}^{n-1}}{\bar{h}_{i+1/2,j,k-1/2}^{n-1}}\right)\right)$$ $$-\Delta t\left(A_{V}{}^{n}_{i+1/2,j,k+1/2}\left(\frac{(U/\bar{h})_{i+1/2,j,k}^{n+1} - (U/\bar{h})_{i+1/2,j,k+1}^{n+1}}{\bar{h}_{i+1/2,j,k+1/2}^{n+1}} + \frac{(u)_{i+1/2,j,k}^{n-1} - (u)_{i+1/2,j,k+1}^{n-1}}{\bar{h}_{i+1/2,j,k+1/2}^{n-1}}\right)\right)$$
g(ζ^{n+1})	$$V_{i,j+1/2,k}^{n+1} = \hat{V}_{i,j+1/2,k} - g\frac{\Delta t}{\Delta y}\bar{h}_{i,j+1/2,k}^{n}\left(\frac{\bar{\rho}_{i,j+1/2,1}^{n}}{\bar{\rho}_{i,j+1/2,k}^{n+1}}\right)\left(\zeta_{i,j+1}^{n+1} - \zeta_{i,j}^{n+1} + \zeta_{i,j+1}^{n-1} - \zeta_{i,j}^{n-1}\right)$$ $$+\Delta t\left(A_{V}{}^{n}_{i,j+1/2,k-1/2}\left(\frac{(V/\bar{h})_{i,j+1/2,k-1}^{n+1} - (V/\bar{h})_{i,j+1/2,k}^{n+1}}{\bar{h}_{i,j+1/2,k-1/2}^{n+1}} + \frac{(v)_{i,j+1/2,k-1}^{n-1} - (v)_{i,j+1/2,k}^{n-1}}{\bar{h}_{i,j+1/2,k-1/2}^{n-1}}\right)\right)$$ $$-\Delta t\left(A_{V}{}^{n}_{i+1/2,j,k+1/2}\left(\frac{(V/\bar{h})_{i,j+1/2,k}^{n+1} - (V/\bar{h})_{i,j+1/2,k+1}^{n+1}}{\bar{h}_{i,j+1/2,k+1/2}^{n+1}} + \frac{(v)_{i,j+1/2,k}^{n-1} - (v)_{i,j+1/2,k+1}^{n-1}}{\bar{h}_{i,j+1/2,k+1/2}^{n-1}}\right)\right)$$
Source term E	$$\Delta t\frac{Q_{FB}^{n+1}}{\Delta y\cdot\sum_{i=i_{BC1}}^{i_{BCend}}\sum_{j=j_{BC1}}^{j_{BCend}}\sum_{k=1}^{km}\left(\bar{h}_{i,j,k}^{n}\right)}\bar{h}_{i,j,k}^{n}\cdot\alpha_{E}\frac{\delta}{\rho_{i+1/2,j,k}^{n}}$$
Source term N	$$\Delta t\frac{Q_{FB}^{n+1}}{\Delta x\cdot\sum_{i=i_{BC1}}^{i_{BCend}}\sum_{j=j_{BC1}}^{j_{BCend}}\sum_{k=1}^{km}\left(\bar{h}_{i,j,k}^{n}\right)}\bar{h}_{i,j,k}^{n}\cdot\alpha_{N}\frac{\delta}{\rho_{i,j+1/2,k}^{n}}$$

(1) The overbar on a layer height h or density ρ variable is used to represent a spatial average in the x- or y- direction between adjacent values

(2) The double overbar denotes average of layer heights.

(3) ^ denotes a solution for the layer volumetric transport that includes only the contribution from the advection, Coriolis, baroclinic pressure and horizontal diffusion terms, treated explicitly in the semi-implicit scheme.

(4) α_E and α_N = fractions of total flow across the East and North faces of a water column respectively ($\alpha_E + \alpha_N = 1$).

of the total flow entering in a given water column, that flow across the E and N faces (α_E and α_N in Table B.1, respectively).

B.2.4 Simulations in a straight channel aligned with the Cartesian grid

The steady-state flow through an 8-m long straight channel of rectangular cross section and flat bottom was simulated in this first test (Figure B.2). The channel was 1m wide, and the water column was initially 0.6 m deep. The computational cells were (Δx, Δy, Δz) = (0.1, 0.1, 0.12) m in the x-, y- and z- directions, respectively, with a total number of wet grid cells of 10, 80 and 5 in each direction. The time step Δt was set to 0.2 s to meet the advection Courant number criterion ($C_a \leq 1$). For these runs C_a (= u$\Delta t/\Delta x$) was O (10^{-1}). Flow boundary conditions were set both at the inflow and outflow sections. Flow rates in and out of the domain were both equal and fixed to 0.18 $m^3 s^{-1}$ in all cases. The water was initially quiescent and the model was run until steady state. In this first series of simulations (A-simulations) the channel was aligned with the x-grid direction (Figure B.2) and, thus, the flow boundaries were specified normal to the E- and W-boundaries. Both the NF- and the SC- approaches were used to represent flow boundaries.

The slope of the free surface I along the channel in this problem should follow the expression (see *Chaudhry* [1993], for example):

$$I = \frac{\zeta_1 - \zeta_2}{L} = \frac{S_0 - S_f}{1 - Fr^2} \tag{B.8}$$

Here ζ_1 and ζ_2 represent the water free surface elevation at the entrance and at the end of the channel, respectively, L is the channel length, S_0 is the bottom slope, and S_f is the longitudinal slope due to friction. The Froude number Fr is defined in terms of the mean streamwise velocity u_s, the acceleration of gravity g, and the depth D of the channel, $Fr = u_s/(gD)^{1/2}$. The frictional slope, in turn, was estimated as $S_f = C_d\, Fr^2$. If the bottom is level, $S_0 = 0$. Under subcritical conditions ($Fr < 1$), such in this case, the water surface elevation decreases in the flow direction ($I < 0$). The free surface solutions of the model were compared against the theoretical result given by Eq. B.8. The error in the free surface solution was quantified using the bias ε, which is defined in terms of the theoretical I_t and the modeled I_i slopes as

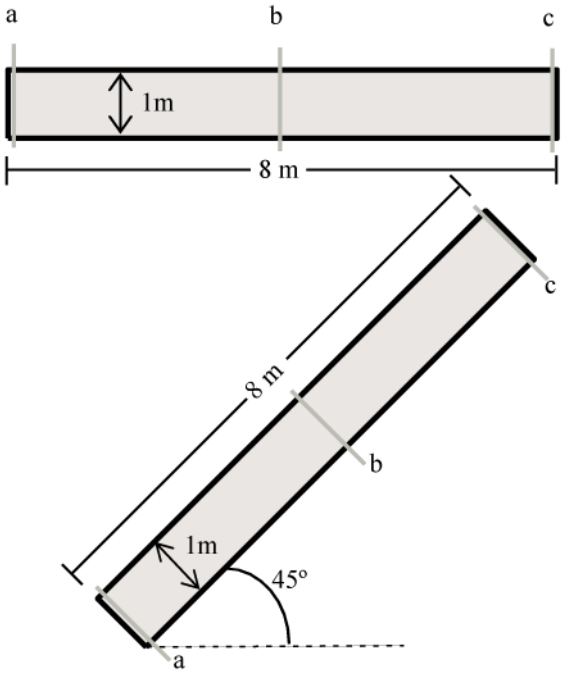

Figure B.2 Configuration sketch of the two sets of experiments: set A (top) and set B (bottom), and location of sections a, b and c for the evaluation of velocity profiles.

$$\varepsilon_I = \frac{(I_i - I_t)}{I_t} \cdot 100 \tag{B.9}$$

The simulated slopes were estimated from the free surface solution at all computational cells existing 1 m away from the boundaries. Velocity and vertical eddy viscosity profiles calculated with the NF- and SC- approaches were compared at several points located at the center of the domain (Section b in Figure B.2) or close to the boundaries (Sections a and c in Figure B.2). The differences between approaches were quantified as

$$\varepsilon_p = \frac{\sqrt{\dfrac{\sum_{i=2}^{km}\left(\psi_i - \psi_{i,0}\right)^2}{km-1}}}{\overline{\psi_0}} \cdot 100 \tag{B.10}$$

Here Ψ represents laterally-averaged values (either velocities or K_z), and the subscript 0 refers to values of the reference simulation, here taken as that conducted with the NF-method. The overbar represents depth-averaged values. Note that the error is

given in non-dimensional form, as a percentage of the mean laterally-averaged value of a given variable in a given section.

The simulations were run with different values of C_d ranging from O (10^{-3}) to O (10^{-1}) and constant horizontal eddy diffusivities (K_h) of 10^{-2} m^2 s^{-1} (Table B.2). The model was set to run (also valid for sections Simulations in a straight channel at an angle with the grid-Simulations of laterally-unconfined inflows to a lake) using a second-order space-centered method for momentum advection and 2 trapezoidal iterations, without smoothing of the leapfrog solution.

B.2.5 Simulations in a straight channel at an angle with the grid

On a second series of simulations, the channel was rotated 45º anticlockwise relative to the *x*-axis (Figure B.2). This channel is referred to as the B-channel, and the simulations conducted are referred to as the B-simulations (Table B.2). Note that, in this case, the lateral boundaries are not straight lines, but are represented as a staircase, which might affect the solution. The flow boundary conditions were prescribed using the SC-method, with velocities aligned with the main axis of the channel. In these B-simulations, though, the total flow was split in equal parts across the N and E faces of the boundary cells (α_N = 0.5 and α_E = 0.5). The same values for C_d and constant K_h as in the A-

Table B.2 Bias (%) of free surface elevation slopes *I*. A- (channel aligned with the grid) and B- (rotated channel) simulations. The presence of hyphens in the last column indicates that no simulation was performed for the corresponding value of C_d and grid resolution.

Simulations	A		B		
$\Delta x = \Delta y$ (m)	0.1	0.1	0.1	0.05	0.01
BC[(1)] \ C_d	NF	SC	SC	SC	SC
0.002	0.37	1.54	3.6	1.2	1.62
0.004	1.07	0.84	4.1	1.6	-
0.006	1.13	1.15	3.4	2.2	-
0.008	1.33	1.22	3.3	2.2	-
0.02	1.34	1.22	3.3	2.4	0.48
0.04	1.28	1.20	3.3	2.5	-
0.06	1.31	1.23	3.4	2.6	-
0.08	1.33	1.24	3.4	2.7	-
0.1	1.33	1.24	3.5	2.7	-
0.2	1.33	1.25	3.5	2.8	0.91

[(1)] BC = type of flow boundary approach.

simulations were used here. Three more grids were tested with higher ($\Delta x = \Delta y = 0.05$ m, with 16430 wet grid cells, and $\Delta x = \Delta y = 0.01$ m, with 399035 wet grid cells) and lower ($\Delta x = \Delta y = 0.2$ m, with 995 wet grid cells) resolution in the horizontal to assess the effects of the staircase representation of the channel banks − as a result of the use of a Cartesian grid − on the modeled free surface slope. The time step Δt was set to 0.5 s, 0.01s and 0.002 s at simulations with the 0.2 × 0.2 m, the 0.05 × 0.05 m and the 0.01 × 0.01m resolution grids, respectively, to meet the criterion $C_a \leq 1$. To compare these results with those with A-simulations, the simulated results within the first and last meters of the channel length were ignored, to avoid the influence of the boundary conditions. Velocity profiles calculated in the B-simulations were also compared at the center of the domain (Section b in Figure B.2) with those calculated in the A-simulations using the NF-method for boundary conditions. The solutions near the boundaries (Sections a and c in Figure B.2) were also compared.

B.2.6 Simulations of laterally-unconfined inflows to a lake

The model was used to simulate near-field (initial) mixing and transport processes associated with a negatively buoyant inflow, the Izbor River, into a small reservoir, Lake Béznar (36º55'N, 3º31'W, Figure B.3a), in southern Spain. The reservoir has a maximum depth of 83.7 m at the dam, and a maximum length of ≈ 4 km. The bottom slope along the thalweg is rather steep (2-3%), similar to many other reservoirs in southern Spain. In September 2009, the Izbor River formed a narrow (≈ 2 m) and shallow channel, discharging ≈ 1 $m^3 s^{-1}$ into a small 'inflow basin' of 30-40 m wide and 200-250 m long (Figure B.3b). The shoreline at that time, widened suddenly downstream of the inflow basin, to reach nearly 400 m at 600 m distance from the inflow section. The inflowing plume did not enter perpendicular to the shoreline, but forming an angle φ ($\neq 90^o$) which changed from day to day, and even hourly (Figure B.3c and Figure B.3d). Our goal is then to evaluate whether inflow angles could affect or not the initial mixing rates between the river plume and the ambient water, and hence, could determine the fate of inflow water in the simulations.

The model grid was constructed with a bathymetry provided by the local government, using $\Delta x = \Delta y = 2$ m, and $\Delta z = 0.1$ m, with a total number of 86585 wet grid cells. Δt was set to 0.3 seconds, C_d was set to 0.003 [*Smith*, 2006], and $A_h = K_h \approx 5 \times 10^{-2}$

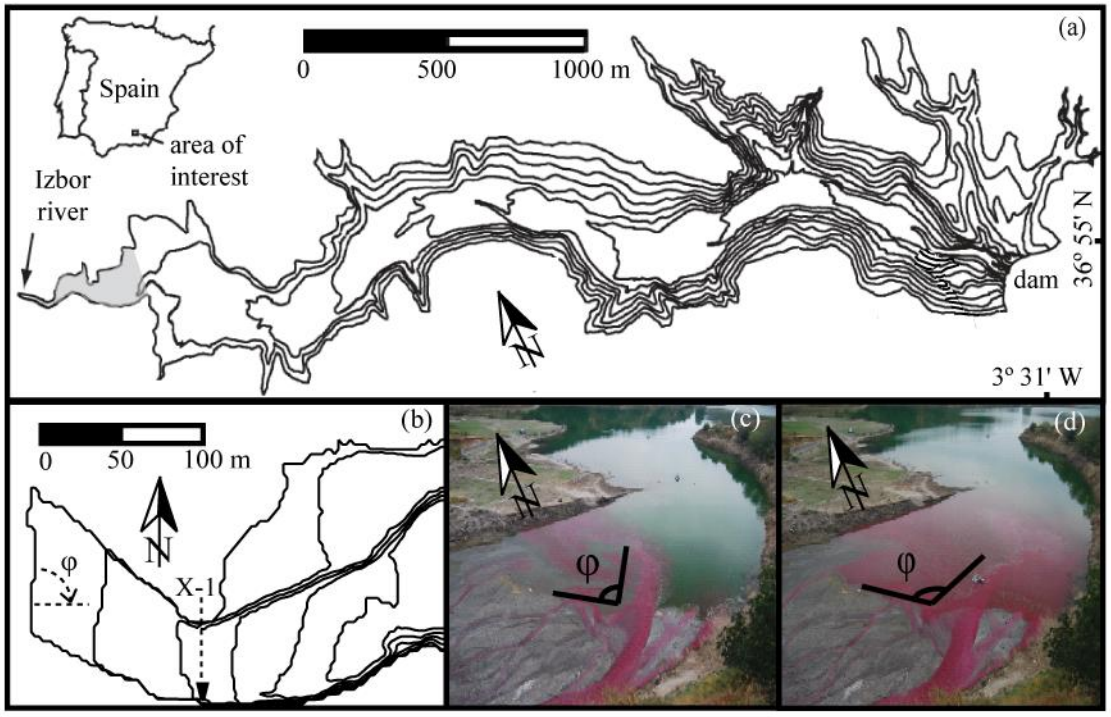

Figure B.3 (a) The Lake Béznar bathymetry with isobaths every 10 m (modified from *Vidal et al.* [2007]). The shadow area marks the inflow basin. (b) Inflow basin with isobaths every meter (computational domain). We define the cross section X-1 and an inflow angle of the plume φ = 90º. (c,d) Photographs of the inflow basin at Lake Béznar during an artificial tracer release experiment undertaken on day 253 in 2009. The inflow angle of the plume φ is marked. These pictures show that the inflow angle φ varied during the dye injection (3 hours).

$m^2\ s^{-1}$ [*Madsen et al.*, 1988]. The reservoir was initially at rest with horizontal isotherms. A stratified temperature profile collected in-situ on day 253 in 2009 at 20.00 hr (not shown) was used to initialize the temperature field in the model. The free surface elevation and temperature gradients were set to zero on the eastern boundary of our computational domain (Figure B.3b). Inflows into the lake were simulated as occurring through a three-layer water column on the western boundary, injecting 19ºC water with a constant flow rate Q_0 = 0.77 $m^3\ s^{-1}$. Inflow temperature corresponds to the daily average temperature measured in the field on day 253. Once the hydrodynamic steady state was reached (after ≈ 10 hr), a conservative tracer — with a concentration C_0 = 100 ppb — was injected with the inflow for 3 hours. A set of 17 simulations were conducted with different inflow angles φ ranging from 0º — when the river entered the basin towards the North (Figure B.3b) — to 180º. The different inflow angles were simulated with the SC-method by prescribing the fractions of the total inflow rate, flowing across the S, E and N faces of the inflow cells. Tracer concentration and velocity fields at a cross-section

located 100 m downstream of the inlet (X-1, Figure B.3b) were averaged in time during the last hour of release, and the time-averaged values were used to characterize the level of mixing between the inflowing plume and the ambient water in the inflow basin. Mixing rates between the river and lake water were calculated from average tracer concentrations C in the density current at section X-1, in terms of the mixing ratio $\Gamma = C_0/C$ [*Fleenor*, 2001]. The density current at section X-1 was assumed to represent the layer exhibiting eastward motion.

B.3 Results and Discussion

B.3.1 Simulations in a straight channel aligned and at an angle with the Cartesian grid

Biases in the free-surface slope were of the same order of magnitude ($\varepsilon_I < 2\%$, Table B.2), independently of whether the NF- or the SC-method was used to prescribe boundary conditions. Biases in the simulations conducted in the B-channel were also of the same order of magnitude as in the A-simulations (Table B.2). Biases in this case decreased with increasing grid resolution, and they were always $\varepsilon < 5\%$ (Table B.2). These sets of simulations suggests that the staircase representation of the lateral boundaries channel affects the solution, but weakly. The SC-method, in general, over-predicted the water surface elevations near the boundaries (Figure B.4a and Figure B.4b). For example, for $C_d = 0.2$, the predicted values of ζ in the reference simulation were 0.25 cm, 0.22 cm and 0.20 cm at a distance of $1\Delta x$, $2\Delta x$ and $3\Delta x$ from the inflow boundary, respectively. The values of ζ at those same distances from the inflow boundary, calculated with the SC-method in the A-channel were 0.93 cm, 0.23 cm and 0.20 (Figure B.4a). Overall, the free surface solution calculated with the SC- and NF- boundary approaches converged within the length of three grid cells both at the inflow and outflow boundaries. The overestimation of ζ at and immediately near to flow boundaries with the SC-method is the result of the source term in the continuity equations (Eqs. B.1-B.2), which generates pressure gradients associated with the slope of the free surface elevation. Outside this boundary region, differences in the free surface solution were ≈ 0.1 %.

The streamwise velocity profiles at the center of the channel were logarithmic and differences between surface and bottom velocities increased as C_d increased (Figure B.5).

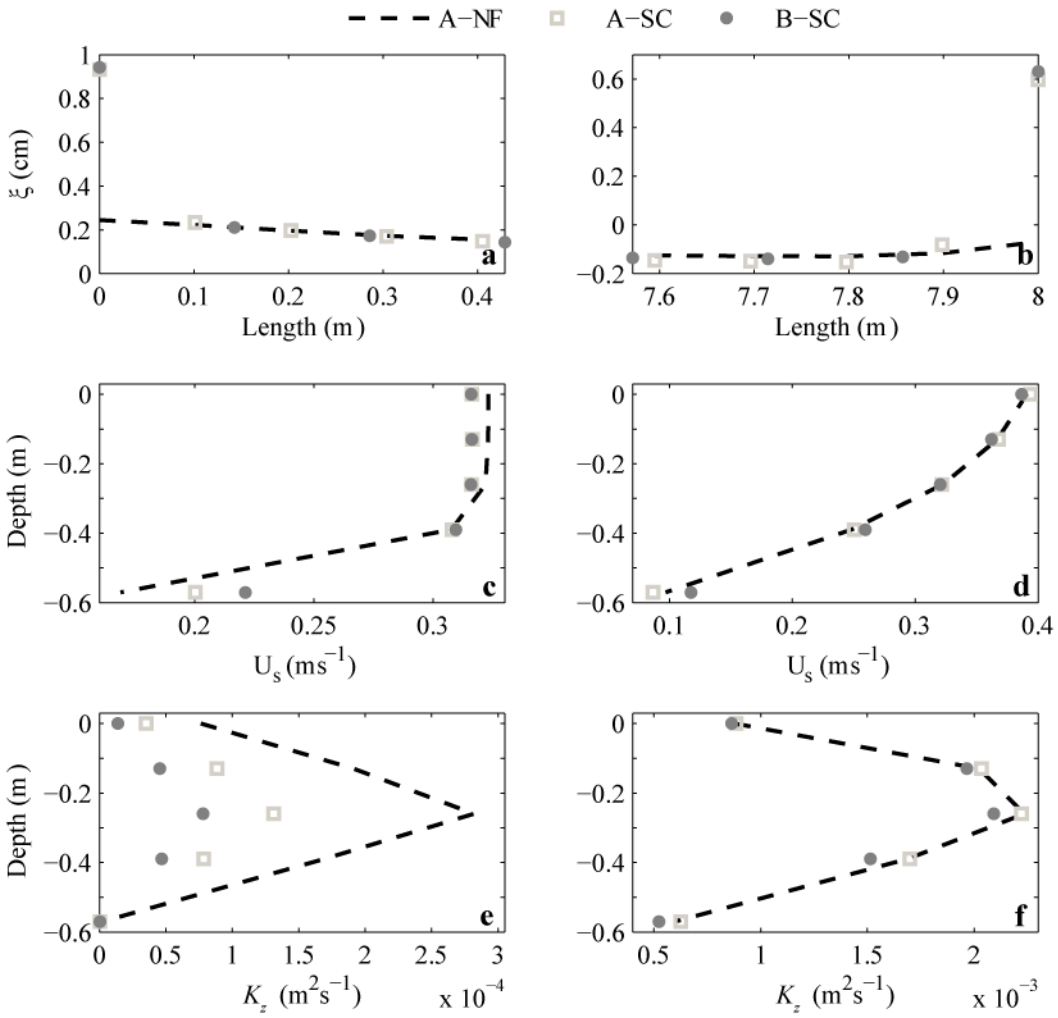

Figure B.4 (a, b) Free surface elevations (ζ), (c, d) laterally-averaged streamwise velocities (U_S) and (e, f) laterally-averaged vertical diffusivities (K_z) near the inflow (a, c, e) and outflow (b, d, f) boundaries (sections a and c in Fig. 2) for A- and B- simulations and the NF and SC methods to prescribe flow at boundaries. $\Delta x = \Delta y = 0.1$ m, $\Delta z = 0.12$ m and $C_d = 0.2$.

Differences between boundary methods were $\varepsilon_p < 0.4$ % in the A-simulations and $\varepsilon_p \approx 1$% in the B-simulations (Table B.3). Errors increased near the inflow and outflow boundaries both in the A- and B-simulations. At sections a and c (Figure B.2), for example, the errors in the A-simulations were up to 5 % and 2% respectively. The errors in the B-simulations were similar (8% and 4% at sections a, c) (Table B.3, Figure B.4c and Figure B.4d). Vertical diffusivities K_z and water surface elevations also differed near boundaries. For example, for $C_d = 0.2$, at section a, the differences in K_z, ε_p, were up to 65% and 90% in the A- and B-simulations, respectively (Figure B.4e). At section c, though, these differences were only 1% and 7%, for A- and B-simulations, respectively (Figure B.4f).

B.3.2 Simulations of laterally-unconfined inflows to a lake

In the simulations of laterally-unconfined inflows in Lake Béznar, initial mixing rates downstream of the inflow section Γ varied from 2.9 to 3.4 depending on the inflow angle φ of the river plume (Figure B.6). These estimates of initial mixing rates are in the upper range of possible values reported in the literature. Ryan and Harleman [1971], for example, is one of the earliest references on initial mixing in the plunge region, and report values of Γ ranging from 1.5 to 3.0 in their laboratory experiments. *Johnson and Stefan* [1988] even report values of Γ as high as 4.5 in their series of inflow laboratory experiments in flat diverging channels, for the largest diverging angles. Despite being higher than previously reported in other lakes — which are, in all cases, below 1.7 [*Elder and Wunderlich*, 1978; *Hebbert et al.*, 1979; *Ford and Johnson*, 1983] —, modeled values of Γ agree with field observations in Lake Béznar [*Cortés et al.*, 2014].

In our simulations, initial mixing rates tended to be bigger ($\Gamma > 3.1$) for the largest inflow angles ($\varphi > 120^{\circ}$), but smaller ($\Gamma < 3.1$) for northward inflows ($\varphi < 120^{\circ}$). The largest dilutions Γ were predicted for $\varphi = 166^{\circ}$, with the river jet pointing south. Dilutions of ≈ 2.9 were estimated when the river inflows pointed north ($\varphi < 90^{\circ}$). Those differences of up to 20% in initial mixing ratios can be the result of differences in the extent of the momentum dominated region x_m, near the inflow section, before the river plunges. In this region, river inertia exceeds buoyancy forces and, as a result, large horizontal velocity gradients develop leading to large mixing rates. The distance x_m from the inflow section to the plunge point for a free buoyant jet entering perpendicular to the lake boundaries

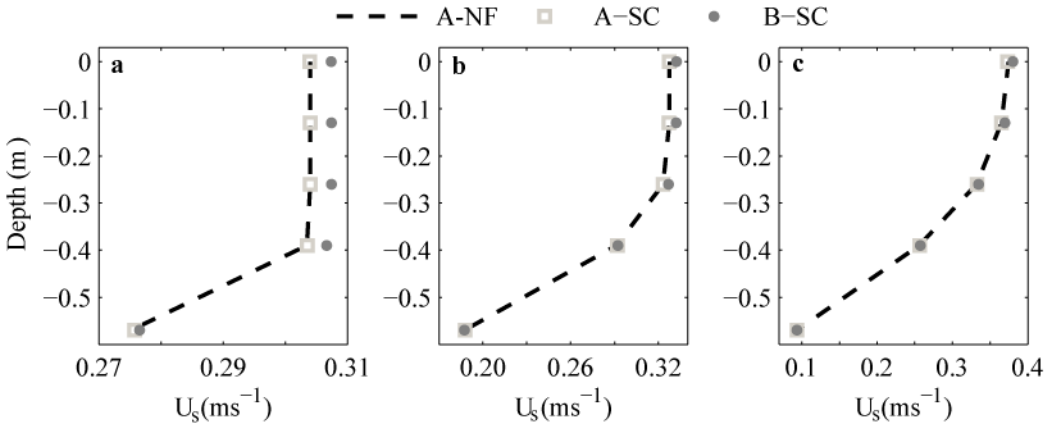

Figure B.5 Laterally-averaged streamwise velocities (U_S) at the centre of the A- and B-channels ($\Delta x = \Delta y = 0.1$ m and $\Delta z = 0.12$ m) with the NF- and SC- flow boundary approaches; (a) $C_d = 0.002$, (b) $C_d = 0.02$ and (c) $C_d = 0.2$.

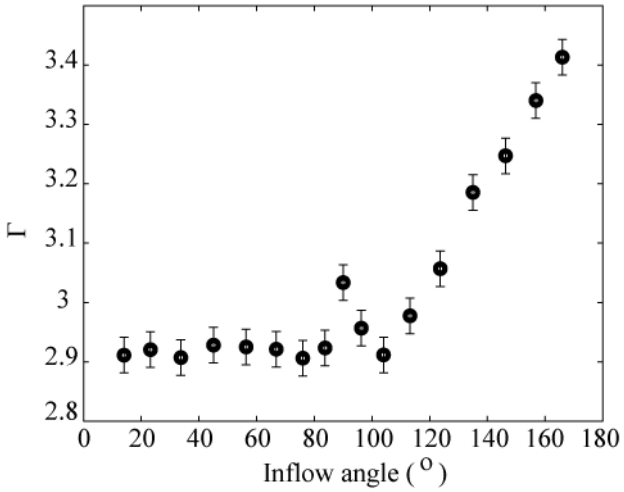

Figure B.6 Simulated values of initial mixing rates Γ at X-1 in the inflow basin of Lake Béznar as a function of the inflow angle φ

(i.e. $\varphi \approx 90^o$) can be estimated from the hydraulic and buoyant characteristics of the inflow, the slope angle of the basin and a lateral entrainment constant, using the semi-analytical model of *Hauenstein and Dracos* [1984]. For Lake Béznar x_m is approximately 100 m, which agrees with the results of our simulations with $\varphi \approx 90^o$ (Figure B.7b). The river forms a free jet for inflows entering nearly perpendicular to the shoreline ($\varphi \approx 90^o$, Figure B.7b). Moreover, in that case, the buoyant jet does not intersect the physical boundary and the momentum dominated region develops freely in the inflow basin. For inflow angles $\varphi \approx 0$ or $\varphi \approx 180^o$ (Figure B.7a and Figure B.7c, respectively), in turn, the extent of the momentum dominated region becomes limited by the geometry: the buoyant impinges on the shoreline, as shown by the tracer concentration field at the bottom layer on the inflow basin. Moreover, the jet tends to become attached to the boundaries. Hence, one might expect lower dilution rates for angles $\varphi \approx 0$ or $\varphi \approx 180^o$. Note, though, that the interface at the study section X-1 between the density current and the ambient water tilts at different angles, depending on the inflow angle, as shown by the white line in Figure B.7d, Figure B**.7**e and Figure B**.7**f, based on the longitudinal velocity direction. As a result of differences in the tilt in the interface, one expects differences in the area of contact S_c between the river and lake water and in the shear in the flow field. In general, a larger area of contact between the river and lake water is observed when inflow angles are $\varphi \approx 180^o$ (Figure B.7f). Thus, the magnitude of the vertical eddy diffusivity, and thus the shear between the current and the lake water, at the interface k_{zi} tend to be larger for southward pointing inflows (Figure B.7g and Figure B**.7**h). For example, the average

differences between the vertical diffusivity at the interface for two extreme inflow angles (i.e. $\varphi \approx 0$ and $\varphi \approx 180^o$) are 45% higher when the river enters toward the south, and the average differences of the river-lake area of contact are also 30% higher for $\varphi > 120^o$ (Table B.4). As a result, maximal mixing ratios are simulated for $\varphi > 120$.

The intrusion depths of the river plumes, and hence, the fate of river-borne substances, as simulated in lake models, might differ depending on the inflow angle used and hence, on the initial mixing rate between lake and river water. Given that river inflows represent one of the major sources of nutrients to river valley reservoirs [*Kennedy*, 1999], inflow angles might also be important in determining the ecosystem response. In the uncertainty analysis conducted by *Ayala et al.* [2014] in Lake Béznar with a one-dimensional lake model [*Rueda et al.*, 2007, *Chung et al.*, 2008], the initial mixing ratio was allowed to vary randomly within the range of values reported in the literature, from 1 to 4 [*Ayala et al.*, 2014]. The model in that work was used to simulate the fate of river inflows and the loads of river-borne nutrients (phosphorus, in particular) in the surface mixed-layer SML during a period of 180 days in 2010. From those experiments, a set of $i = 300$ pairs of simulations were selected, with Γ in each pair (Γ_1, Γ_2) differing in 0.5 (i.e. $\Gamma_2(i) = \Gamma_1(i) + 0.5$), as found above for different inflow angles. The intrusion depths were, on average, 10% smaller and the phosphorous loads into the SML were 11% bigger in the simulations conducted with the biggest initial mixing ratios. The maximum differences in P loads could be of up to 100%, at times with peak loading rates. These maximal loads tended to occur, either at the start or the end of the stratification period [*Ayala et al.*, 2014]. These differences in P loads were significant in

Table B.3 ε_p (%) of the streamwise velocity profiles near the inflow section (section a), at the centre of the channel (section b) and near the outflow section (section c) for solutions with the SC approach. A- and B- simulations. Grid resolution 0.1×0.1×0.12 m.

Section	C_d	A	B
a	0.002	0.11	1.07
	0.02	0.95	1.84
	0.2	5.16	8.32
b	0.002	0.10	1.03
	0.02	0.16	1.19
	0.2	0.25	1.24
c	0.002	0.92	1.03
	0.02	1.91	1.75
	0.2	1.74	3.87

the statistical sense (at the 95% confidence level), and could be important from a water quality modeling perspective, depending on the sensitivity of the phytoplankton growth to nutrient concentration, and depending on the availability of nutrients in the SML. In any case, these results suggest that inflow angles should be accurately represented, at least when dealing with simulations of laterally-unconfined inflows in reservoirs. The SC-boundary method, in these cases, provides a simple and straightforward approach to account for the inflow angel in Cartesian grids.

B.4 Summary and Conclusions

Sources and sinks (SC) in the governing equations defined along flow boundaries can be used in 3D hydrodynamic and transport models to simulate the effects of inflows-outflows. This is an alternative and more flexible approach to define flow-boundary conditions in Cartesian grid models compared to the most commonly used approach (NF) in which velocities that are normal to the boundary faces are prescribed. Using the SC-approach, not only inflow magnitude, but also its direction (whether it is aligned or not with the grid axis) can be correctly represented. The approach was applied to simulate flows along a straight rectangular channel not aligned to the Cartesian axes. The error, when using a second-order space-centered method to discretize momentum advection terms together with the SC-boundary method, is comparable with that existing in the

Table B.4 Mean modeled values of the area of contact S_c and vertical eddy diffusivities at the interface k_{zi} for different sections ant two different inflow angles φ in Lake Béznar.

	K_{zi} ($\times 10^{-4}$) ($m^2\ s^{-1}$)		S_c (m^2)	
x_s(m)[2] \ φ[1]	14º (N)	166º (S)	14º (N)	166º (S)
20	0.522	0.704	0.7	0.8
30	0.688	1.414	1.0	2.6
40	0.046	3.038	1.6	4.6
50	0.302	3.713	2.2	4.6
60	0.025	1.737	2.8	6.2
70	0.019	6.514	2.8	5.8
80	0.605	7.458	3.2	6.6
90	1.075	5.107	3.0	8.6
100 (X-1)	1.615	5.271	5.0	6.0

[1] N = northward and S = southward;

[2] x_S = Distance from the inflow section.

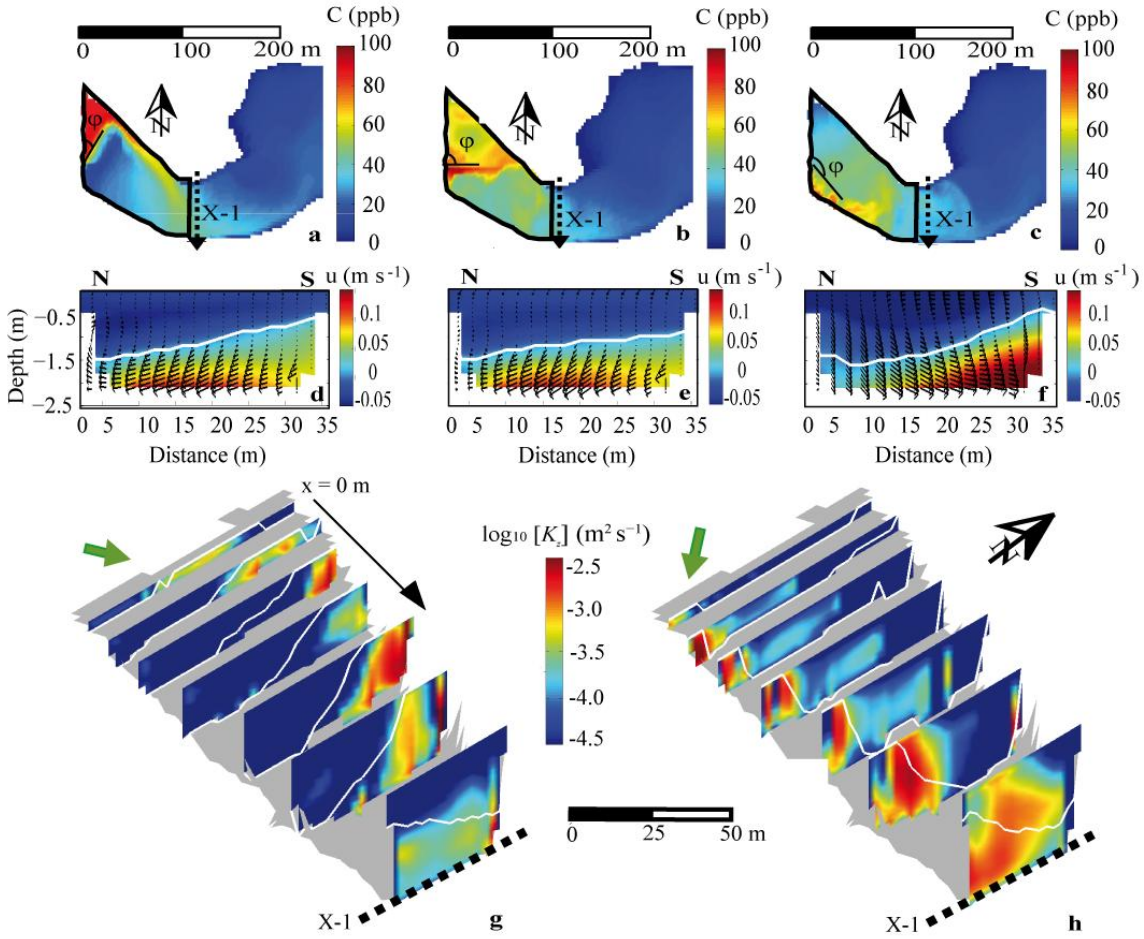

Figure B.7 Lake Béznar simulation results averaged during the 3 hr of tracer injection (t = 10-13 hr). [a,b,c] Tracer concentration field at the bottom layer of the inflow basin; it describes the pathways of the density current at the inflow basin as a function of the inflow angle, where (a) φ = 14º; (b) φ = 90º; (c) φ = 166º. [d,e,f] Cross sectional X-1 longitudinal velocities (u) field, where the arrows mark the tangential-vertical (v-w) velocity field, considering different inflow angles (d) φ = 14º; (e) φ = 90º; (f) φ = 166º. The white line marks the interface of the density current according to a velocity criterion. [g,h] Cross sectional decimal logarithmic vertical eddy diffusivity ($\log_{10}$ [K_z]) field along 6 different cross-sections from the inflow to X-1 (x = 100 m) for two extreme inflow angles (g) φ = 14º (north); and (h) φ = 166º (south). The green arrows correspond to the inflow jet

simulations conducted in a channel aligned with the Cartesian axis and using the NF-boundary method. Only near the boundaries, the SC- and the NF-approaches diverge.

In a series of simulations of a small scale negatively buoyant inflow into a reservoir, initial mixing rates between the river and the lake water in the inflow basin appeared sensitive to direction of the inflows. Mixing rates varied up to 20% depending on the inflow angle φ. As a result of the changes in the inflow direction, significant differences in intrusion depth, the timing of entrainment of the intrusions in the surface

mixed layer, and consequently, the fate of river-borne substances in the reservoir are likely to occur. Hence, being able to represent inflow inertia and direction in laterally-unconfined inflows is required for accurate predictions of the fate of river-borne substances.

Bibliography

Abad, J., Rhoads, B., Güneralp, İ., García, M., 2008. Flow Structure at Different Stages in a Meander-Bend with Bendway Weirs. J. Hydraul. Eng. 134, 1052–1063. doi:10.1061/(ASCE)0733-9429(2008)134:8(1052)

Abrahams, A.D., Updegraph, J., 1987. Some Space-Filling Controls on the Arrangement of Tributaries in Dendritic Channel Networks. Water Resour. Res. 23, 489–495. doi:10.1029/WR023i003p00489

Abrahams, At.D., Campbell, R.N., 1976. Source and Tributary-Source Link Lengths in Natural Channel Networks. Geol. Soc. Am. Bull. 87, 1016–1020.

Acosta, M., Anguita, M., Rueda, F.J., Fernández-Valdomero, F., 2010. Parallel implementation of a semi-implicit 3D lake hydrodynamic model, in: Proceedings of the International Conference on Computational and Mathematical Methods in Science and Engineering, Add/link/COMSOL. Almería, Spain, pp. 1026–1037.

Ahlfeld, D., Joaquin, A., Tobiason, J., Mas, D., 2003. Case Study: Impact of Reservoir Stratification on Interflow Travel Time. J. Hydraul. Eng. 129, 966–975. doi:10.1061/(ASCE)0733-9429(2003)129:12(966)

Allen, J.I., Somerfield, P.J., Gilbert, F.J., 2007. Quantifying Uncertainty in High-Resolution Coupled Hydrodynamic-Ecosystem Models. J. Mar. Syst. 64, 3–14. doi:http://dx.doi.org/10.1016/j.jmarsys.2006.02.010

Appt, J., Imberger, J., Kobus, H., 2004. Basin-Scale Motion in Stratified Upper Lake Constance. Limnol. Oceanogr. 49, 919–933. doi:10.4319/lo.2004.49.4.0919

Arneborg, L., Fiekas, V., Umlauf, L., Burchard, H., 2007. Gravity Current Dynamics and Entrainment—A Process Study Based on Observations in the Arkona Basin. J. Phys. Oceanogr. 37, 2094–2113. doi:10.1175/JPO3110.1

Ashmore, P., Parker, G., 1983. Confluence Scour in Coarse Braided Streams. Water Resour. Res. 19, 392–402. doi:10.1029/WR019i002p00392

Ashmore, P.E., 1982. Laboratory Modelling of Gravel Braided Stream Morphology. Earth Surf. Process. Landforms 7, 201–225. doi:10.1002/esp.3290070301

Ashmore, P.E., Ferguson, R.I., Prestegaard, K.L., Ashworth, P.J., Paola, C., 1992. Secondary Flow in Anabranch Confluences of a Braided, Gravel-Bed Stream. Earth Surf. Process. Landforms 17, 299–311. doi:10.1002/esp.3290170308

Ayala, A.I., Cortés, A., Fleenor, W.E., Rueda, F.J., 2014. Seasonal Scale Modeling of River Inflows in Stratified Reservoirs: Structural vs. Parametric Uncertainty in Inflow Mixing. Environ. Model. Softw. 60, 84–98. doi:http://dx.doi.org/10.1016/j.envsoft.2014.06.011

Benda, L., Poff, N.L., Miller, D., Dunne, T., Reeves, G., Pess, G., Pollock, M., 2004. The Network Dynamics Hypothesis: How Channel Networks Structure Riverine Habitats. Biosci. 54 , 413–427. doi:10.1641/0006-3568(2004)054[0413:TNDHHC]2.0.CO;2

Benda, L., Veldhuisen, C., Black, J., 2003. Debris flows as Agents of Morphological heterogeneity at Low-Order Confluences, Olympic Mountains, Washington. Geol. Soc. Am. Bull. 115, 1110–1121. doi:10.1130/B25265.1

Berger, M.J., Oliger, J., 1984. Adaptive Mesh Refinement for Hyperbolic Partial Differential Equations. J. Comput. Phys. 53, 484–512. doi:http://dx.doi.org/10.1016/0021-9991(84)90073-1

Best, J., Reid, I., 1984. Separation Zone at Open-Channel Junctions. J. Hydraul. Eng. 110, 1588–1594. doi:10.1061/(ASCE)0733-9429(1984)110:11(1588)

Best, J.L., 1987. Flow Dynamics at River Channel Confluences, in: Recent Developments in Fluvial Sedimentology. SEPM Society for Sedimentary Geology, pp. 27–35. doi:10.2110/pec.87.39.0027

Best, J.L., Rhoads, B.L., 2008. Sediment Transport, Bed Morphology and the Sedimentology of River Channel Confluences, in: River Confluences, Tributaries and the Fluvial Network. John Wiley & Sons, Ltd, pp. 45–72. doi:10.1002/9780470760383.ch4

Best, J.L., Roy, A.G., 1991. Mixing-Layer Distortion at the Confluence of Channels of Different Depth. Nature 350, 411–413.

Bettess, R., 1999. Flow resistance equations for gravel bed rivers, in: Proceedings of the XXVIII IAHR Congress. Graz, Austria, p. (CD–rom).

Bever, A.J., MacWilliams, M.L., 2015. Factors Influencing the Calculation of Periodic Secondary Circulation in a Tidal River: Numerical Modelling of the Lower Sacramento River, USA. Hydrol. Process. doi:10.1002/hyp.10690

Bigelow, P.E., Benda, L.E., Miller, D.J., Burnett, K.M., 2007. On debris flows, river networks, and the spatial structure of channel morphology. For. Sci. 53, 220–238. doi:10.1016/j.neuroimage.2011.08.082

Biron, P., Best, J., Roy, A., 1996a. Effects of Bed Discordance on Flow Dynamics at Open Channel Confluences. J. Hydraul. Eng. 122, 676–682. doi:10.1061/(ASCE)0733-9429(1996)122:12(676)

Biron, P., De Serres, B., Roy, A.G., Best, J.L., 1993. Shear layer turbulence at an unequal depth channel confluence, in: Clifford, N.J., French, J.R., Hardisty, J. (Eds.), Turbulence: Perspectives on Flow and Sediment Transport. John Wiley & Sons, Chichester, pp. 197–213.

Biron, P., Lane, S.N., 2008. Modelling hydraulics and sediment transport at river confluences, in: Rice, S.P., Roy, A.G., Rhoads, B.L. (Eds.), River Confluences, Tributaries and the Fluvial Network. John Wiley & Sons, Chichester, pp. 17–44.

Biron, P., Ramamurthy, A., Han, S., 2004. Three-Dimensional Numerical Modeling of Mixing at River Confluences. J. Hydraul. Eng. 130, 243–253. doi:10.1061/(ASCE)0733-9429(2004)130:3(243)

Biron, P., Roy, A., Best, J.L., Boyer, C.J., 1993. Bed Morphology and Sedimentology at the Confluence of Unequal Depth Channels. Geomorphology 8, 115–129. doi:http://dx.doi.org/10.1016/0169-555X(93)90032-W

Biron, P., Roy, A.G., Best, J.L., 1996b. Turbulent Flow Structure at Concordant and Discordant Open-Channel Confluences. Exp. Fluids 21, 437–446. doi:10.1007/BF00189046

Bladé i Castellet, E., Arbat, M., Sánchez-Juny, M., Dolz, J., Cobos, G., Polanco, L., 2010. Dinámica Sedimentaria del Extremo Aguas Arriba del Embalse de Ribarroja (río Ebro), in: Proceedings of the 24th Congreso Latinoamericano de Hidráulica. Punta del Este, Uruguay.

Blake, A., Burau, J.R., Adams, N.S., 2012. Outmigration Behavior of Juvenile Chinook Salmon in a River Bend in the Sacramento River At Clarksburg California, in: Fisheries Networks: Building Ecological, Social, and Professional Relationships. 142nd Annual Meeting of the American Fisheries Society. Minneapolis.

Blake, A., Horn, M.J., 2004. Acoustic Tracking of Juvenile Chinook Salmon Movement in the Vicinity of the Delta Cross Channel, Sacramento River, California - 2001 Study Results. U.S. Geological Survey Open-File Report.

Blanckaert, K., DeVriend, H.J., 2004. Secondary flow in sharp open-channel bends. J. Fluid Mech. 498, 353–380.

Bouchez, J., Lajeunesse, E., Gaillardet, J., France-Lanord, C., Dutra-Maia, P., Maurice, L., 2010. Turbulent Mixing in the Amazon River: The Isotopic Memory of Confluences. Earth Planet. Sci. Lett. 290, 37–43. doi:http://dx.doi.org/10.1016/j.epsl.2009.11.054

Bournet, P., Dartus, D., Tassin, B., Vinçon-Leite, B., 1999. Numerical Investigation of Plunging Density Current. J. Hydraul. Eng. 125, 584–594. doi:10.1061/(ASCE)0733-9429(1999)125:6(584)

Boxall, J.B., Guymer, I., 2001. Estimating transverse mixing coefficients. Proc. Inst. Civ. Eng. - Water Marit. Eng. 148, 263–275. doi:10.1680/wame.2001.148.4.263

Boyer, C., Roy, A.G., Best, J.L., 2006. Dynamics of a River Channel Confluence with Discordant Beds: Flow Turbulence, Bed Load Sediment Transport, and Bed Morphology. J. Geophys. Res. Earth Surf. 111, n/a–n/a. doi:10.1029/2005JF000458

Boyle, E., Collier, R., Dengler, A.T., Edmond, J.M., Ng, A.C., Stallard, R.F., 1974. On the Chemical Mass-Balance in Estuaries. Geochim. Cosmochim. Acta 38, 1719–1728. doi:http://dx.doi.org/10.1016/0016-7037(74)90188-4

Bradbrook, K., Lane, S., Richards, K., Biron, P., Roy, A., 2001. Role of Bed Discordance at Asymmetrical River Confluences. J. Hydraul. Eng. 127, 351–368. doi:10.1061/(ASCE)0733-9429(2001)127:5(351)

Bradbrook, K.F., Lane, S.N., Richards, K.S., 2000. Numerical simulation of three-dimensional, time-averaged flow structure at river channel confluences. Water Resour. Res. 36, 2731–2746. doi:10.1029/2000WR900011

Bramblett, R.G., Bryant, M.D., Wright, B.E., White, R.G., 2002. Seasonal Use of Small Tributary and Main-Stem Habitats by Juvenile Steelhead, Coho Salmon, and Dolly Varden in a Southeastern Alaska Drainage Basin. Trans. Am. Fish. Soc. 131, 498–506. doi:10.1577/1548-8659(2002)131<0498:SUOSTA>2.0.CO;2

Brandes, P.L., Mclain, J.S., 2001. Juvenile Chinook Salmon Abundance, Distribution, and Survival in the Sacramento–San Joaquin Estuary, in: Brown, R.L. (Ed.), Contributions to the Biology of Central Valley Salmonids, Volume 2. California Department of Fish and Game, Fish Bulletin 179, Sacramento, pp. 39–138.

Bruns, D.A., Minshall, G.W., Cushing, C.E., Cummins, K.W., Brock, J.T., Vannote, R.L., 1984. Tributaries as Modifiers of the River Continuum Concept: Analysis by Polar Ordination and Regression Models. Arch. für Hydrobiol. 99, 208–220.

Cairns, M.A., Ebersole, J.L., Baker, J.P., Jr., P.J.W., Lavigne, H.R., Davis, S.M., 2005. Influence of Summer Stream Temperatures on Black Spot Infestation of Juvenile Coho Salmon in the Oregon Coast Range. Trans. Am. Fish. Soc. 134, 1471–1479. doi:10.1577/T04-151.1

Campodonico, V.A., García, M.G., Pasquini, A.I., 2015. The Dissolved Chemical and Isotopic Signature Downflow the Confluence of Two Large Rivers: The Case of the Parana and Paraguay Rivers. J. Hydrol. 528, 161–176. doi:http://dx.doi.org/10.1016/j.jhydrol.2015.06.027

Casulli, V., Cheng, R.T., 1992. Semi-implicit finite difference methods for three-dimensional

shallow water flow. Int. J. Numer. Methods Fluids 15, 629–648. doi:10.1002/fld.1650150602

Causon, D.M., Ingram, D.M., Mingham, C.G., Yang, G., Pearson, R. V, 2000. Calculation of Shallow Water Flows Using a Cartesian Cut Cell Approach. Adv. Water Resour. 23, 545–562. doi:http://dx.doi.org/10.1016/S0309-1708(99)00036-6

Cavallo, B., Gaskill, P., Melgo, J., Zeug, S.C., 2015. Predicting Juvenile Chinook Salmon Routing in Riverine and Tidal Channels of a Freshwater Estuary. Environ. Biol. Fishes 98, 1571–1582. doi:10.1007/s10641-015-0383-7

Chant, R.J., 2002. Secondary circulation in a region of flow curvature: Relationship with tidal forcing and river discharge. J. Geophys. Res. 107, 3131. doi:10.1029/2001JC001082

Chao, X., Jia, Y., Wang, S., 2009. 3D Numerical Simulation of Turbulent Buoyant Flow and Heat Transport in a Curved Open Channel. J. Hydraul. Eng. 135, 554–563. doi:10.1061/(ASCE)0733-9429(2009)135:7(554)

Chapman, E.D., Hearn, A.R., Michel, C.J., Ammann, A.J., Lindley, S.T., Thomas, M.J., Sandstrom, P.T., Singer, G.P., Peterson, M.L., MacFarlane, R.B., Klimley, A.P., 2013. Diel Movements of Out-Migrating Chinook Salmon (Oncorhynchus tshawytscha) and Steelhead Trout (Oncorhynchus mykiss) Smolts in the Sacramento/San Joaquin Watershed. Environ. Biol. Fishes 96, 273–286. doi:10.1007/s10641-012-0001-x

Chaudhry, M.H., 1993. Open-Channel Flow. Prentice-Hall, Englewood Cliffs, New Jersey.

Chen, C.-T.A., Millero, F.J., 1986. Thermodynamic Properties for Natural Waters Covering Only the Limnological Range. Limnol. Oceanogr. 31, 657–662. doi:10.4319/lo.1986.31.3.0657

Chen, C.Y.-J., Wu, S.-C., Lee, B.-S., Hung, C.-C., 2006. Behavior of Storm-Induced Suspension Interflow in Subtropical Feitsui Reservoir, Taiwan. Limnol. Oceanogr. 51, 1125–1133. doi:10.4319/lo.2006.51.2.1125

Christensen, H.B., Gislason, K., Fredsøe, J., 1999. Secondary turbulent flow in an infinte bend. I.A.H.R. Symp. River, Coast. Estuar. Morphodynamics.

Chu, V., Babarutsi, S., 1988. Confinement and Bed Friction Effects in Shallow Turbulent Mixing Layers. J. Hydraul. Eng. 114, 1257–1274. doi:10.1061/(ASCE)0733-9429(1988)114:10(1257)

Chua, V.P., Fringer, O.B., 2011. Sensitivity Analysis of Three-Dimensional Salinity Simulations in North San Francisco Bay Using the Unstructured-Grid SUNTANS Model. Ocean Model. 39, 332–350. doi:http://dx.doi.org/10.1016/j.ocemod.2011.05.007

Chung, E., Schladow, S.G., Perez-Losada, J., Robertson, D., 2008. A Linked Hydrodynamic and

Water Quality Model for the Salton Sea. Hydrobiologia 604, 57–75. doi:10.1007/s10750-008-9311-6

Chung, S., Gu, R., 1998. Two-Dimensional Simulations of Contaminant Currents in Stratified Reservoir. J. Hydraul. Eng. 124, 704–711. doi:10.1061/(ASCE)0733-9429(1998)124:7(704)

Cohen, A.N., Carlton, J.T., 1998. Accelerating Invasion Rate in a Highly Invaded Estuary. Science (80-.). 279, 555–558.

Constantinescu, G., Miyawaki, S., Rhoads, B., Sukhodolov, A., 2012a. Numerical analysis of the effect of momentum ratio on the dynamics and sediment-entrainment capacity of coherent flow structures at a stream confluence. J. Geophys. Res. Earth Surf. 117, n/a–n/a. doi:10.1029/2012JF002452

Constantinescu, G., Miyawaki, S., Rhoads, B., Sukhodolov, A., 2012b. Numerical analysis of the effect of momentum ratio on the dynamics and sediment-entrainment capacity of coherent flow structures at a stream confluence. J. Geophys. Res. 117, F04028. doi:10.1029/2012JF002452

Constantinescu, G., Miyawaki, S., Rhoads, B., Sukhodolov, A., Kirkil, G., 2011. Structure of turbulent flow at a river confluence with momentum and velocity ratios close to 1: Insight provided by an eddy-resolving numerical simulation. Water Resour. Res. 47, W05507. doi:10.1029/2010WR010018

Constantinescu, G., Sukhodolov, A., McCoy, A., 2009. Mass exchange in a shallow channel flow with a series of groynes: LES study and comparison with laboratory and field experiments. Environ. Fluid Mech. 9, 587–615. doi:10.1007/s10652-009-9155-2

Cook, C.B., Richmond, M.C., Titzler, S.P., Dibrani, B., Bleich, M.D., Fu, T., 2006. Hydraulic Characteristics of the Lower Snake River During Periods of Juvenile Fall Chinook Salmon Migration. Report PNNL-15532. Pacific North West National Laboratory. Prepared for the Bonneville Power Administration, U.S. Department of Energy.Richland, Washington. pp. 176.

Corney, R.K.T., Peakall, J., Parsons, D.R., Elliott, L., Amos, K.J., Best, J.L., Keevil, G.M., INGHAM, D.B., 2006. The Orientation of Helical Flow in Curved Channels. Sedimentology 53, 249–257. doi:10.1111/j.1365-3091.2006.00771.x

Corney, R.K.T., Peakall, J., Parsons, D.R., Elliott, L., Best, J.L., Thomas, R.E., Keevil, G.M., Ingham, D.B., Amos, K.J., 2008. Reply to Discussion of Imran et al. on "The orientation of helical flow in curved channels" by Corney et al., Sedimentology, 53, 249–257. Sedimentology 55, 241–247. doi:10.1111/j.1365-3091.2007.00925.x

Cortés, A., Fleenor, W.E., Wells, M.G., de Vicente, I., Rueda, F.J., 2014a. Pathways of River Water to the Surface Layers of Stratified Reservoirs. Limnol. Oceanogr. 59, 233–250. doi:10.4319/lo.2014.59.1.0233

Cortés, A., Rueda, F.J., Wells, M.G., 2014b. Experimental Observations of the Splitting of a Gravity Current at a Density Step in a Stratified Water Body. J. Geophys. Res. Ocean. 119, 1038–1053. doi:10.1002/2013JC009304

Cossu, R., Wells, M.G., 2010. Coriolis Forces Influence the Secondary Circulation of Gravity Currents Flowing in Large-Scale Sinuous Submarine Channel Systems. Geophys. Res. Lett. 37, L17603. doi:10.1029/2010GL044296

Cruzado, A., Velásquez, Z., Pérez, M. del C., Bahamón, N., Grimaldo, N.S., Ridolfi, F., 2002. Nutrient fluxes from the Ebro River and subsequent across-shelf dispersion. Cont. Shelf Res. 22, 349–360. doi:http://dx.doi.org/10.1016/S0278-4343(01)00060-7

Dallimore, C., Imberger, J., Ishikawa, T., 2001. Entrainment and Turbulence in Saline Underflow in Lake Ogawara. J. Hydraul. Eng. 127, 937–948. doi:10.1061/(ASCE)0733-9429(2001)127:11(937)

De Serres, B., Roy, A.G., Biron, P.M., Best, J.L., 1999. Three-dimensional Structure of Flow at a Confluence of River Channels with Discordant Beds. Geomorphology 26, 313–335. doi:http://dx.doi.org/10.1016/S0169-555X(98)00064-6

DeVriend, H.J., 1979. Flow Measurements in a Curved Rectangular Channel. Internal report no. 9-79, TU Delft, Department of Hydraulic Engineering,Delft, The Netherlands.

Dinehart, R.L., Burau, J.R., 2005a. Repeated Surveys by Acoustic Doppler Current Profiler for Flow and Sediment Dynamics in a Tidal River. J. Hydrol. 314, 1–21. doi:http://dx.doi.org/10.1016/j.jhydrol.2005.03.019

Dinehart, R.L., Burau, J.R., 2005b. Averaged indicators of secondary flow in repeated acoustic Doppler current profiler crossings of bends. Water Resour. Res. 41, n/a–n/a. doi:10.1029/2005WR004050

Duan, J., 2004. Simulation of Flow and Mass Dispersion in Meandering Channels. J. Hydraul. Eng. 130, 964–976. doi:10.1061/(ASCE)0733-9429(2004)130:10(964)

Durran, D.R., 1999. Numerical Methods for Wave Equations in Geophysical Fluid Dynamics, 1st Editio. ed. Springer-Verlag, New York.

Elder, R.A., Wunderlich, W.., 1978. Inflow Density Currents in TVA Reservoirs, in: Proceedings of the International Symposium on Stratified Flows. Novosibirsk, pp. 221–236.

Ferguson, R.I., Parsons, D.R., Lane, S.N., Hardy, R.J., 2003. Flow in meander bends with

recirculation at the inner bank. Water Resour. Res. 39, n/a–n/a. doi:10.1029/2003WR001965

Fernandes, C.C., Podos, J., Lundberg, J.G., 2004. Amazonian Ecology: Tributaries Enhance the Diversity of Electric Fishes. Sci. 305 , 1960–1962. doi:10.1126/science.1101240

Fernandez, R.L., Imberger, J., 2006. Bed roughness induced entrainment in a high Richardson number underflow. J. Hydraul. Res. 44, 725–738. doi:10.1080/00221686.2006.9521724

Finger, D., Schmid, M., Wüest, A., 2006. Effects of Upstream Hydropower Operation on Riverine Particle Transport and Turbidity in Downstream Lakes. Water Resour. Res. 42, W08429. doi:10.1029/2005WR004751

Fischer, H.B., List, E.J., Koh, R.C.Y., Imberger, J., Brooks, N.H., 1979. Mixing in Inland and Coastal Waters. Academic Press, New York.

Fischer, H.B., Smith, R.D., 1983. Observations of Transport to Surface Waters from a Plunging Inflow to Lake Mead. Limnol. Oceanogr. 28, 258–272.

Fleenor, W.E., 2001. Effects and Control of Plunging in Flows on Reservoir hydrodynamics and downstream releases. Ph.D. thesis, University of California, Davis.

Fleenor, W.E., Schladow, S.G., 2000. Mixing in the Plunge Zone of Lake Inflows, in: Proceedings of the 5th International Symposium on Stratified Flows. Vancouver, B.C.

Flint, J.J., 1980. Tributary Arrangements in Fluvial Systems. Am. J. Sci. 280, 26–45.

Flumen-Group, 2009. Estudio de la dinámica sedimentaria y batimetría de precisión del embalse de Ribarroja.

Fong, D.A., Geyer, W.R., 2001. Response of a River Plume During an Upwelling Favorable Wind Event. J. Geophys. Res. Ocean. 106, 1067–1084. doi:10.1029/2000JC900134

Ford, D.E., Johnson, M.C., 1983. An Assessment of Reservoir Density Currents and Inflow Processes. Tech. Rep. E-83-7, U.S. Army Corps of Eng. Waterways Exp. Station, Vicksburg, Miss.

Franks, C.A., Rice, S.P., Wood, P.J., 2002. Hydraulic Habitat in Confluences: An Ecological Perspective on Confluence Hydraulics, in: Dyer, F.J., Thoms, M.C., Olley, J.M. (Eds.), The Structure, Function and Management Implications of Fluvial Sedimentary Systems. International Association Hydrological Sciences Publication 276, Wallingford, UK, pp. 61–67.

Fraser, D.F., Gilliam, J.F., Yip-Hoi, T., 1995. Predation as an Agent of Population Fragmentation in a Tropical Watershed. Ecology 76, 1461–1472. doi:10.2307/1938148

Fringer, O.B., Gerritsen, M., Street, R.L., 2006. An unstructured-grid, finite-volume,

nonhydrostatic, parallel coastal ocean simulator. Ocean Model. 14, 139–173. doi:http://dx.doi.org/10.1016/j.ocemod.2006.03.006

García Berdeal, I., Hickey, B.M., Kawase, M., 2002. Influence of wind stress and ambient flow on a high discharge river plume. J. Geophys. Res. Ocean. 107, 13–24. doi:10.1029/2001JC000932

Gaudet, J.M., Roy, A.G., 1995. Effect of Bed Morphology on Glow Mixing Length at River Confluences. Nature 373, 138–139.

Geyer, W.R., 1993. Three-Dimensional Tidal Flow Around Headlands. J. Geophys. Res. Ocean. 98, 955–966. doi:10.1029/92JC02270

Gibou, F., Min, C., Ceniceros, H.., 2007. Non-Graded Adaptive Grid Approaches to the Incompressible Navier-Stokes Equations. Fluid Dyn. Mater. Process. 3, 37–48. doi:10.3970/fdmp.2007.003.037

Gleichauf, K.T., Wolfram, P.J., Monsen, N.E., Fringer, O.B., Monismith, S.G., 2014. Dispersion Mechanisms of a Tidal River Junction in the Sacramento–San Joaquin Delta, California. San Fr. Estuary Watershed Sci. 12.

Godin, G., 1972. The analysis of tides. University of Toronto Press, Toronto, Canada.

González, O., 2007. Modelització de la Hidrodinàmica d'un Embassament, Aplicació al Cas de l'Embassament de Riba-roja al Riu Ebre. Degree thesis, Escola Técnica Superior d'Enginyers de Camins, Canals i Ports, Tech. Univ. of Catalonia, Barcelona.

Goodwin, R., Nestler, J., Loucks, D., Chapman, R., 2001. Simulating Mobile Populations in Aquatic Ecosystems. J. Water Resour. Plan. Manag. 127, 386–393. doi:10.1061/(ASCE)0733-9496(2001)127:6(386)

Goodwin, R.A., Nestler, J.M., Anderson, J.J., Weber, L.J., Loucks, D.P., 2006. Forecasting 3-D fish Movement Behavior Using a Eulerian–Lagrangian–Agent Method (ELAM). Ecol. Modell. 192, 197–223. doi:http://dx.doi.org/10.1016/j.ecolmodel.2005.08.004

Gooseff, M.N., Bencala, K.E., Wondzell, S.M., 2008. Solute transport along stream and river networks, in: Rice, S.P., Roy, A.G., Rhoads, B.L. (Eds.), River Confluences, Tributaries and the Fluvial Network. John Wiley & Sons, Chichester, pp. 395–418.

Goudsmit, G.-H., Burchard, H., Peeters, F., Wüest, A., 2002. Application of k-ϵ Turbulence Models to Enclosed Basins: The Role of Internal Seiches. J. Geophys. Res. Ocean. 107, 13–23. doi:10.1029/2001JC000954

Gross, E., Koseff, J., Monismith, S., 1999. Three-Dimensional Salinity Simulations of South San Francisco Bay. J. Hydraul. Eng. 125, 1199–1209. doi:10.1061/(ASCE)0733-

9429(1999)125:11(1199)

Gualtieri, C., 2008. Numerical Simulation of Flow Patterns and Mass Exchange Processes in Dead Zones, in: Proceedings of the 4th Biennial Meeting of iEMSs. Barcelona, Spain, pp. 150–161.

Gualtieri, C., López Jiménez, P.A., Mora Rodríguez, J., 2009. A comparison among turbulence modelling approaches in the simulation of a square dead zone, in: Proceedings of the 33rd IAHR Congress: Water Engineering for a Sustainable Environment. Vancouver, B.C.

Gurram, S., Karki, K., Hager, W., 1997. Subcritical Junction Flow. J. Hydraul. Eng. 123, 447–455. doi:10.1061/(ASCE)0733-9429(1997)123:5(447)

Ham, F.E., Lien, F.S., Strong, A.B., 2002. A Fully Conservative Second-Order Finite Difference Scheme for Incompressible Flow on Nonuniform Grids. J. Comput. Phys. 177, 117–133. doi:http://dx.doi.org/10.1006/jcph.2002.7006

Hardy, R.J., Lane, S.N., Ferguson, R.I., Parsons, D.R., 2003. Assessing the credibility of a series of computational fluid dynamic simulations of open channel flow. Hydrol. Process. 17, 1539–1560. doi:10.1002/hyp.1198

Hauenstein, W., Dracos, T., 1984. Investigation of Plunging Density Currents Generated by Inflows in Lakes. J. Hydraul. Res. 22, 157–179. doi:10.1080/00221688409499404

He, Y.Y., Fu, Y.F., Li, F.T., Jiang, J.Y., Fu, D.C., 1992. Preliminary Experimental Investigation on the Properties of the Thermal Density Flow in Open Channel Bend, in: Proceedings of the Second National Symp. Environmental Hydraulics. Beijing, China, pp. 199–205.

Heard, S., Gienapp, C., Lemire, J., Heard, K., 2001. Transverse mixing of transported material in simple and complex stream reaches. Hydrobiologia 464, 207–218. doi:10.1023/A:1013918122117

Hebbert, B., Patterson, J., Loh, I., Imberger, J., 1979. Collie River Underflow into the Wellington Reservoir. J. Hydraul. Div. 105, 533–545.

Hickey, B.M., Pietrafesa, L.J., Jay, D.A., Boicourt, W.C., 1998. The Columbia River Plume Study: Subtidal variability in the velocity and salinity fields. J. Geophys. Res. Ocean. 103, 10339–10368. doi:10.1029/97JC03290

Hodges, B.R., Imberger, J., Saggio, A., Winters, K.B., 2000. Modeling basin-scale internal waves in a stratified lake. Limnol. Oceanogr. 45, 1603–1620. doi:10.4319/lo.2000.45.7.1603

Hollan, E., 1998. Large Inflow-Driven Vortices in Lake Constance, in: Imberger, J. (Ed.), Physical Processes in Lakes and Oceans. American Geophysical Union, Washington, D.C., pp. 123–136. doi:10.1029/CE054p0123

Horne, A.J., Goldman, C.R., 1994. Limnology. McGraw-Hill, New York.

Hoyer, A.B., Schladow, S.G., Rueda, F.J., 2015. A Hydrodynamics-Based Approach to Evaluating the Risk of Waterborne Pathogens Entering Drinking Water Intakes in a Large, Stratified Lake. Water Res. 83, 227–236. doi:http://dx.doi.org/10.1016/j.watres.2015.06.014

Hoyer, A.B., Wittmann, M.E., Chandra, S., Schladow, S.G., Rueda, F.J., 2014. A 3D Individual-Based Aquatic Transport Model for the Assessment of the Potential Dispersal of Planktonic Larvae of an Invasive Bivalve. J. Environ. Manage. 145, 330–340. doi:http://dx.doi.org/10.1016/j.jenvman.2014.05.011

Imboden, D.M., Wüest, A., 1995. Mixing Mechanisms in Lakes, in: Lerman, A., Imboden, D.M., Gat, J.R. (Eds.), Physics and Chemistry of Lakes. Springer-Verlag, Berlin, pp. 83–138.

Jia, Y., Blanckaert, K., Wang, S.S.Y., 2001. Simulation of secondary flow in curved channels, in: Roceedings of the FMTM2001 International Conference. Tokyo, Japan.

Jia, Y., Wang, S.S.Y., 2009. Physical Process Validation, in: Wang, S.S.Y., Roche, P.J., Schmalz, R.A., Jia, Y., Smith, P.E. (Eds.), Verification and Validations of 3D Free-Surface Flow Models. ASCE, Reston, Virginia, pp. 153–247.

Johannesson, H., Parker, G., 1988. Theory of river meanders. St. Anthony Falls Hydraulic Laboratory, Minneapolis. Retrieved from the University of Minnesota Digital Conservancy, http://purl.umn.edu/114112.

Johnson, T., Farrell, G., Ellis, C., Stefan, H., 1987. Negatively Buoyant Flow in a Diverging Channel. I: Flow Regimes. J. Hydraul. Eng. 113, 716–730. doi:10.1061/(ASCE)0733-9429(1987)113:6(716)

Johnson, T.R., Stefan, H.G., 1988. Experimental Study of Density Induced Plunging into Reservoirs and Coastal Regions. St. Anthony Falls Hydraulics Laboratory, University of Minnesota (Report245).

Kaeding, L.R., 1996. Summer Use of Coolwater Tributaries of a Geothermally Heated Stream by Rainbow and Brown Trout, Oncorhynchus mykiss and Salmo trutta. Am. Midl. Nat. 135, 283–292. doi:10.2307/2426711

Kalkwijk, J.P.T., Booij, R., 1986. Adaptation of secondary flow in nearly-horizontal flow. J. Hydraul. Res. 24, 19–37. doi:10.1080/00221688609499330

Kantha, L.H., Clayson, C.A., 1994. An improved mixed layer model for geophysical applications. J. Geophys. Res. Ocean. 99, 25235–25266. doi:10.1029/94JC02257

Kassem, A., Imran, J., Khan, J., 2003. Three-Dimensional Modeling of Negatively Buoyant Flow in Diverging Channels. J. Hydraul. Eng. 129, 936–947. doi:10.1061/(ASCE)0733-

9429(2003)129:12(936)

Kawahara, Y., Tamai, N., 1988. Note on turbulence modelling for secondary flows in passages of non-circular cross-section, in: Proc. Japanese Soc. Civ. Eng., 399(II-10),. pp. 247–250.

Keevil, G.M., Peakall, J., Best, J.L., 2007. The Influence of Scale, Slope and Channel Geometry on the Flow Dynamics of Submarine Channels. Mar. Pet. Geol. 24, 487–503. doi:http://dx.doi.org/10.1016/j.marpetgeo.2007.01.009

Keevil, G.M., Peakall, J., Best, J.L., Amos, K.J., 2006. Flow Structure in Sinuous Submarine Channels: Velocity and Turbulence Structure of an Experimental Submarine Channel. Mar. Geol. 229, 241–257. doi:http://dx.doi.org/10.1016/j.margeo.2006.03.010

Kennedy, R.H., 1999. Reservoir Design and Operation: Limnological Implications and Management Opportunities, in: Tundisi, J.G., Straškraba, M. (Eds.), Theoretical Reservoir Ecology and Its Applications. Backhuys Publishers, Leiden, pp. 1–28.

Kiffney, P.M., Greene, C.M., Hall, J.E., Davies, J.R., 2006. Tributary streams create spatial discontinuities in habitat, biological productivity, and diversity in mainstem rivers. Can. J. Fish. Aquat. Sci. 63, 2518–2530. doi:10.1139/f06-138

Kimmerer, W.J., 2008. Losses of Sacramento River Chinook Salmon and Delta Smelt to Entrainment in Water Diversions in the Sacramento–San Joaquin Delta. San Fr. Estuary Watershed Sci. 6.

Kimura, I., Hosoda, T., 1997. Fundamental Properties of Flows in Open Channels with Dead Zone. J. Hydraul. Eng. 123, 98–107. doi:10.1061/(ASCE)0733-9429(1997)123:2(98)

Kneller, B.C., Bennett, S.J., McCaffrey, W.D., 1999. Velocity Structure, Turbulence and Fluid Stresses in Experimental Gravity Currents. J. Geophys. Res. Ocean. 104, 5381–5391. doi:10.1029/1998JC900077

Knispel, S., Castella, E., 2003. Disruption of a Longitudinal Pattern in Environmental Factors and Benthic Fauna by a Glacial Tributary. Freshw. Biol. 48, 604–618. doi:10.1046/j.1365-2427.2003.01030.x

Komar, P.D., 1969. The Channelized Flow of Turbidity Currents with Application to Monterey Deep-Sea Fan Channel. J. Geophys. Res. 74, 4544–4558. doi:10.1029/JC074i018p04544

Konsoer, K., Rhoads, B., 2014. Spatial–Temporal Structure of Mixing Interface Turbulence at Two Large River Confluences. Environ. Fluid Mech. 14, 1043–1070. doi:10.1007/s10652-013-9304-5

Kupferberg, S.J., 1996. Hydrologic and Geomorphic Factors Affecting Conservation of a River-Breeding Frog (Rana Boylii). Ecol. Appl. 6, 1332–1344. doi:10.2307/2269611

Lacy, J.R., Monismith, S.G., 2001. Secondary Currents in a Curved, Stratified, Estuarine Channel. J. Geophys. Res. Ocean. 106, 31283–31302. doi:10.1029/2000JC000606

Lane, S.N., Parsons, D.R., Best, J.L., Orfeo, O., Kostaschuk, R.A., Hardy, R.J., 2008. Causes of Rapid Mixing at a Junction of Two Large Rivers: Río Paraná and Río Paraguay, Argentina. J. Geophys. Res. Earth Surf. 113, F02024. doi:10.1029/2006JF000745

Laraque, A., Guyot, J.L., Filizola, N., 2009. Mixing Processes in the Amazon River at the Confluences of the Negro and Solimões Rivers, Encontro das Águas, Manaus, Brazil. Hydrol. Process. 23, 3131–3140. doi:10.1002/hyp.7388

Latif, M., Stockdale, T., Wolff, J., Burgers, G., Maier-Reimer, E., Junge, M.M., Arpe, K., Bengtsson, L., 1994. Climatology and Variability in the ECHO Coupled GCM. Tellus A 46, 351–366. doi:10.1034/j.1600-0870.1994.t01-3-00003.x

Laval, B., Imberger, J., Findikakis, A., 2005. Dynamics of a Large Tropical Lake: Lake Maracaibo. Aquat. Sci. 67, 337–349. doi:10.1007/s00027-005-0778-1

Leopold, L.B., Maddock, T., 1953. The Hydraulic Geometry of Stream Channels and Some Physiographic Implications, US Geological Survey Professional Paper 252.

Leschziner, M.A., Rodi, W., 1979. Calculation of Strongly Curved Open Channel Flow. J. Hydraul. Div. 105, 1297–1314.

Leupi, C., Altinakar, M., 2005. 3D Finite Element Modeling of Free-Surface Flows with Efficient k – ε Turbulence Model and Non-hydrostatic Pressure, in: Sunderam, V., van Albada, G., Sloot, P.A., Dongarra, J. (Eds.), Computational Science – ICCS 2005 SE - 5, Lecture Notes in Computer Science. Springer Berlin Heidelberg, pp. 33–40. doi:10.1007/11428862_5

Lewis, Q.W., Rhoads, B.L., 2015. Rates and Patterns of Thermal Mixing at a Small Stream Confluence Under Variable Incoming Flow Conditions. Hydrol. Process. 29, 4442–4456. doi:10.1002/hyp.10496

Liang, Q., Zang, J., Borthwick, A.G.L., Taylor, P.H., 2007. Shallow Flow Simulation on Dynamically Adaptive Cut Cell Quadtree Grids. Int. J. Numer. Methods Fluids 53, 1777–1799. doi:10.1002/fld.1363

Llebot, C., Rueda, F.J., Solé, J., Artigas, M.L., Estrada, M., 2014. Hydrodynamic States in a Wind-Driven Microtidal Estuary (Alfacs Bay). J. Sea Res. 85, 263–276. doi:http://dx.doi.org/10.1016/j.seares.2013.05.010

Low, A.F., White, J., Chappel, E., 2006. Relationship of Delta Cross Channel Gate Operations to Loss of Juvenile Winter-Run Chinook Salmon at the CVP/SWP Delta Facilities. California Department of Fish and Game. Available:

http://science.calwater.ca.gov/pdf/ewa/EWA_delta_cross_channel_closures_06_111406.pdf, pp. 19.

Lung, W., O'Connor, D., 1984. Two Dimensional Mass Transport in Estuaries. J. Hydraul. Eng. 110, 1340–1357. doi:10.1061/(ASCE)0733-9429(1984)110:10(1340)

Lynch, D.R., 1986. Basic Hydrodynamic Equations for Lakes, in: Gray, W.G. (Ed.), Physics-Based Modeling of Lakes, Reservoirs, and Impoundments. American Society of Civil Engineers, New York, pp. 17–53.

Lyubimova, T., Lepikhin, A., Konovalov, V., Parshakova, Y., Tiunov, A., 2014. Formation of the Density Currents in the Zone of Confluence of Two Rivers. J. Hydrol. 508, 328–342. doi:http://dx.doi.org/10.1016/j.jhydrol.2013.10.041

Mackay, J.R., 1970. Lateral Mixing of the Liard and Mackenzie Rivers Downstream from their Confluence. Can. J. Earth Sci. 7, 111–124. doi:10.1139/e70-008

Macnab, K., Jacobson, C., Brierley, G., 2006. Spatial Variability of Controls on Downstream Patterns of Sediment Storage: a Case Study in the Lane Cove Catchment, New South Wales, Australia. Geogr. Res. 44, 255–271. doi:10.1111/j.1745-5871.2006.00388.x

Madsen, P.A., Rugbjerg, M.Y., Warren, I.R., 1988. Subgrid Modeling in Depth Integrated Flows, in: Proceedings of the 21st Coastal Engineering Conference, ASCE, Vol. 1. New York, pp. 505–511.

Markham, A.J., Thorne, C.R., 1992. Geomorphology of Gravel-Bed Rivers, in: Billi, P., Hey, r. D., Thorne, C.R., Tacconi, P. (Eds.), Dynamics of Gravel-Bed Rivers. John Wiley & Sons, Chichester, pp. 433–450.

Marti, C.L., Mills, R., Imberger, J., 2011. Pathways of Multiple Inflows into a Stratified Reservoir: Thomson Reservoir, Australia. Adv. Water Resour. 34, 551–561. doi:http://dx.doi.org/10.1016/j.advwatres.2011.01.003

Maurice-Bourgoin, L., Quemerais, B., Moreira-Turcq, P., Seyler, P., 2003. Transport, Distribution and Speciation of Mercury in the Amazon River at the Confluence of Black and White Waters of the Negro and Solimões Rivers. Hydrol. Process. 17, 1405–1417. doi:10.1002/hyp.1292

McLelland, S.J., Ashworth, P.J., Best, J.L., 1996. The Origin and Downstream Development of Coherent Flow Structures at Channel Junctions, in: Ashworth, P.J., Bennett, S.J., Best, J.L., S.J., M. (Eds.), Coherent Flow Structures in Open Channels. John Wiley & Sons, Chichester, pp. 459–490.

Mellor, G.L., Yamada, T., 1974. A Hierarchy of Turbulence Closure Models for Planetary

Boundary Layers. J. Atmos. Sci. 31, 1791–1806. doi:10.1175/1520-0469(1974)031<1791:AHOTCM>2.0.CO;2

Milner, A.M., Petts, G.E., 1994. Glacial Rivers: Physical Habitat and Ecology. Freshw. Biol. 32, 295–307. doi:10.1111/j.1365-2427.1994.tb01127.x

Mockmore, C.A., 1944. Flow around Bends in Stable Channels. Trans. Am. Soc. Civ. Eng. 109, 593–618.

Morillo, S., Imberger, J., Antenucci, J., Woods, P., 2008. Influence of Wind and Lake Morphometry on the Interaction between Two Rivers Entering a Stratified Lake. J. Hydraul. Eng. 134, 1579–1589. doi:10.1061/(ASCE)0733-9429(2008)134:11(1579)

Mosley, M.P., 1976. An Experimental Study of Channel Confluences. J. Geol. 84, 535–562.

Murphy, A.H., Epstein, E.S., 1989. Skill Scores and Correlation Coefficients in Model Verification. Mon. Weather Rev. 117, 572–582. doi:10.1175/1520-0493(1989)117<0572:SSACCI>2.0.CO;2

Muto, Y., Baba, Y., Aya, S., 2002. Velocity Measurements in Open Channel Flow with Rectangular Embayments Formed by Spur Dikes. Annu. Disaster Prev. Res. Inst. 45B-2.

Muto, Y., Imamoto, H., Ishigaki, T., 2000. Velocity measurements in a straight open channel with a rectangular embayment, in: Proceedings of the 12th APD-IAHR: Sustainable Water Resources Management: Issues and Future Challenges for the Next Millenium. Bangkok, Thailand.

Navarro, E., Bacardit, M., Caputo, L., Palau, T., Armengol, J., 2006. Limnological Characterization and Flow Patterns of a Three-coupled Reservoir System and Their Influence on Dreissena polymorpha Populations and Settlement During the Stratification Period. Lake Reserv. Manag. 22, 293–302. doi:10.1080/07438140609354363

Nelson, W.R., Freidenburg, L.K., Rondorf, D.W., 1994. Swimming Performance of Subyearling Chinook Salmon, in: Rondorf, D.W., Miller, V.H. (Eds.), Identification of the Spawning, Rearing, and Migratory Requirements of Fall Chinook Salmon in the Columbia River Basin. Bonneville Power Administration, Annual Report 1992, Portland, Oregon, pp. 39–62.

Newman, K.B., 2003. Modelling Paired Release-Recovery Data in the Presence of Survival and Capture Heterogeneity with Application to Marked Juvenile Salmon. Stat. Modelling 3, 157–177. doi:10.1191/1471082X03st055oa

Newman, K.B., Brandes, P.L., 2010. Hierarchical Modeling of Juvenile Chinook Salmon Survival as a Function of Sacramento–San Joaquin Delta Water Exports. North Am. J. Fish. Manag. 30, 157–169. doi:10.1577/M07-188.1

Newman, K.B., Rice, J., 2002. Modeling the Survival of Chinook Salmon Smolts Outmigrating Through the Lower Sacramento River System. J. Am. Stat. Assoc. 97, 983–993. doi:10.1198/016214502388618771

Nichols, F.H., Cloern, J.S.E., Luoma, S.N., Peterson, D.H., 1986. The Modification of an Estuary. Science (80-.). 231, 567–573.

NMFS, 1997. NMFS Proposed Recovery Plan for the Sacramento River Winter-Run Chinook Salmon. NMFS (National Marine Fisheries Service), Southwest Regional Office, Long Beach, California.

Okely, P., Imberger, J., 2007. Horizontal Transport Induced by Upwelling in a Canyon-Shaped Reservoir. Hydrobiologia 586, 343–355. doi:10.1007/s10750-007-0706-6

Otero, P., Ruiz-Villarreal, M., Peliz, A., 2008. Variability of River Plumes off Northwest Iberia in Response to Wind Events. J. Mar. Syst. 72, 238–255. doi:http://dx.doi.org/10.1016/j.jmarsys.2007.05.016

Parsons, D.R., Best, J.L., Lane, S.N., Kostachuk, R.A., Hardy, R.J., Orfeo, O., Amsler, M.L., Szupiany, R.N., 2008. Large river channel confluences, in: Rice, S.P., Roy, A.G., Rhoads, B.L. (Eds.), River Confluences, Tributaries and the Fluvial Network. John Wiley & Sons, Chichester, pp. 73–92.

Parsons, D.R., Best, J.L., Lane, S.N., Orfeo, O., Hardy, R.J., Kostaschuk, R., 2007. Form Roughness and the Absence of Secondary Flow in a Large Confluence–Diffluence, Rio Paraná, Argentina. Earth Surf. Process. Landforms 32, 155–162. doi:10.1002/esp.1457

Parsons, D.R., Jackson, P.R., Czuba, J.A., Engel, F.L., Rhoads, B.L., Oberg, K.A., Best, J.L., Mueller, D.S., Johnson, K.K., Riley, J.D., 2013. Velocity Mapping Toolbox (VMT): a processing and visualization suite for moving-vessel ADCP measurements. Earth Surf. Process. Landforms 38, 1244–1260. doi:10.1002/esp.3367

Parsons, D.R., Peakall, J., Aksu, A.E., Flood, R.D., Hiscott, R.N., Beşiktepe, Ş., Mouland, D., 2010. Gravity-Driven Flow in a Submarine Channel Bend: Direct Field Evidence of Helical Flow Reversal. Geology 38, 1063–1066.

Pawlowicz, R., 2008. Calculating the Conductivity of Natural Waters. Limnol. Oceanogr. Methods 6, 489–501. doi:10.4319/lom.2008.6.489

Peng, Y.-F., Mittal, R., Sau, A., Hwang, R.R., 2010. Nested Cartesian Grid Method in Incompressible Viscous Fluid Flow. J. Comput. Phys. 229, 7072–7101. doi:http://dx.doi.org/10.1016/j.jcp.2010.05.041

Perry, R.W., 2010. Survival and Migration Dynamics of juvenile Chinook salmon (Oncorhynchus

tshawytshcha) in the Sacramento-San Joaquin River Delta. PhD Thesis. School of Aquatic & Fishery Sciences. University of Washington, Seattle, Washington.

Perry, R.W., Brandes, P.L., Burau, J.R., Klimley, A.P., MacFarlane, B., Michel, C., Skalski, J.R., 2013. Sensitivity of Survival to Migration Routes Used by Juvenile Chinook Salmon to Negotiate the Sacramento-San Joaquin River Delta. Environ. Biol. Fishes 96, 381–392. doi:10.1007/s10641-012-9984-6

Perry, R.W., Brandes, P.L., Burau, J.R., Sandstrom, P.T., Skalski, J.R., 2015. Effect of Tides, River Flow, and Gate Operations on Entrainment of Juvenile Salmon into the Interior Sacramento–San Joaquin River Delta. Trans. Am. Fish. Soc. 144, 445–455. doi:10.1080/00028487.2014.1001038

Perry, R.W., Romine, J.G., Adams, N.S., Blake, A.R., Burau, J.R., Johnston, S. V, Liedtke, T.L., 2014. Using a Non-Physical Behavioural Barrier to Alter Migration Routing of Juvenile Chinook Salmon in the Sacramento–San Joaquin River Delta. River Res. Appl. 30, 192–203. doi:10.1002/rra.2628

Perry, R.W., Romine, J.G., Brewer, S.J., LaCivita, P.E., Brostoff, W.N., Chapman, E.D., 2012. Survival and Migration Route Probabilities of Juvenile Chinook Salmon in the Sacramento-San Joaquin River Delta During the Winter of 2009–10. U.S. Geological Survey Open-File Report 2012-1200. pp. 30.

Perry, R.W., Skalski, J.R., Brandes, P.L., Sandstrom, P.T., Klimley, A.P., Ammann, A., MacFarlane, B., 2010. Estimating Survival and Migration Route Probabilities of Juvenile Chinook Salmon in the Sacramento–San Joaquin River Delta. North Am. J. Fish. Manag. 30, 142–156. doi:10.1577/M08-200.1

Peskin, C.S., 2002. The Immersed Boundary Method. Acta Numer. 11, 479–517.

Peskin, C.S., 1972. Flow Patterns Around Heart Valves: A Numerical Method. J. Comput. Phys. 10, 252–271. doi:http://dx.doi.org/10.1016/0021-9991(72)90065-4

Petts, G.E., Greenwood, M., 1985. Channel changes and invertebrate faunas below Nant-Y-Moch dam, River Rheidol, Wales, UK. Hydrobiologia 122, 65–80. doi:10.1007/BF00018961

Plumb, J.M., Adams, N.S., Perry, R.W., Holbrook, C.M., Romine, J.G., Blake, A.R., Burau, J.R., 2015. Diel Activity Patterns of Juvenile Late Fall-run Chinook Salmon with Implications for Operation of a Gated Water Diversion in the Sacramento–San Joaquin River Delta. River Res. Appl. doi:10.1002/rra.2885

Pollock, D.W., 1988. Semianalytical Computation of Path Lines for Finite-Difference Models. Ground Water 26, 743–750. doi:10.1111/j.1745-6584.1988.tb00425.x

Power, M.E., Dietrich, W.E., 2002. Food Webs in River Networks. Ecol. Res. 17, 451–471.

Prats, J., 2011. El Règim Tèrmic del Tram Inferior de l'Ebre i les seues Alteracions. Ph.D. thesis, Escola Te`cnica Superior d'Enginyers de Camins, Canals i Ports de Barcelona, Inst. Flumen,Tech. Univ. Catalonia.

Prats, J., Arbat-Bofill, M., Martí-Cardona, B., Dolz, J., Armengol, J., 2013. Utilidad de los Sensores Térmicos Aerotransportados en Estudios de Hidrodinámica de Embalses y Ríos, in: III Jornadas de Ingeniería Del Agua. Valencia, Spain.

Prats, J., Armengol, J., Marcé, R., Sánchez-Juny, M., Dolz, J., 2010. Dams and Reservoirs in the Lower Ebro River and Its Effects on the River Thermal Cycle, in: Barceló, D., Petrovic, M. (Eds.), The Ebro River Basin SE - 68, The Handbook of Environmental Chemistry. Springer Berlin Heidelberg, pp. 77–95. doi:10.1007/698_2010_68

Ramón, C.L., 2011. Circulación y Mezcla en la Confluencia de los Ríos Ebro y Segre a su Entrada al Embalse de Ribarroja. M.S. thesis, Escuela Técnica Superior de Ingenieros de Caminos Canales y Puertos, Inst. de Hidráulica Ambiental (IH Cantabria), Univ. de Cantabria, Santander.

Ramón, C.L., Armengol, J., Dolz, J., Prats, J., Rueda, F.J., 2014. Mixing Dynamics at the Confluence of Two Large Rivers Undergoing Weak Density Variations. J. Geophys. Res. Ocean. 119, 2386–2402. doi:10.1002/2013JC009488

Ramón, C.L., Hoyer, A.B., Armengol, J., Dolz, J., Rueda, F.J., 2013. Mixing and circulation at the confluence of two rivers entering a meandering reservoir. Water Resour. Res. 49, 1429–1445. doi:10.1002/wrcr.20131

Ramón, C.L., Prats, J., Rueda, F.J., 2015. Simulation of Turbulent Flows in River Confluences and Meandering Channels with a Cartesian 3D Free Surface Hydrodynamic Model. Int. J. Comput. Methods 1550035. doi:10.1142/S0219876215500358

Rastogi, A.K., Rodi, W., 1978. Predictions of Heat and Mass Transfer in Open Channels. J. Hydraul. Div. 104, 397–420.

Reckinger, S., Vasilyev, O., Fox-Kemper, B., 2012. Adaptive Volume Penalization for Ocean Modeling. Ocean Dyn. 62, 1201–1215. doi:10.1007/s10236-012-0555-3

Rhoads, B.L., 1996. Mean Structure of Transport-Effective Flows at an Asymmetrical Confluence when the Main Stream is Dominant, in: Ashworth, P., Bennett, S.J., Best, J.L., McLelland, S. (Eds.), Coherent Flow Structures in Open Channels. John Wiley & Sons, New York, pp. 491–517.

Rhoads, B.L., Kenworthy, S.T., 1998. Time-Averaged Flow Structure in the Central Region of a

Stream Confluence. Earth Surf. Process. Landforms 23, 171–191. doi:10.1002/(SICI)1096-9837(199802)23:2<171::AID-ESP842>3.0.CO;2-T

Rhoads, B.L., Kenworthy, S.T., 1995. Flow Structure at an Asymmetrical Stream Confluence. Geomorphology 11, 273–293. doi:http://dx.doi.org/10.1016/0169-555X(94)00069-4

Rhoads, B.L., Sukhodolov, A.N., 2004. Spatial and Temporal Structure of Shear Layer Turbulence at a Stream Confluence. Water Resour. Res. 40, n/a–n/a. doi:10.1029/2003WR002811

Rhoads, B.L., Sukhodolov, A.N., 2001. Field Investigation of Three-Dimensional Flow Structure at Stream Confluences: 1. Thermal Mixing and Time-Averaged Velocities. Water Resour. Res. 37, 2393–2410. doi:10.1029/2001WR000316

Rice, S.P., Ferguson, R.I., Hoey, T.B., 2006. Tributary Control of Physical Heterogeneity and Biological Diversity at River Confluences. Can. J. Fish. Aquat. Sci. 63, 2553–2566. doi:10.1139/f06-145

Rice, S.P., Greenwood, M.T., Joyce, C.B., 2001. Tributaries, sediment sources, and the longitudinal organisation of macroinvertebrate fauna along river systems. Can. J. Fish. Aquat. Sci. 58, 824–840. doi:10.1139/f01-022

Rice, S.P., Rhoads, B.L., Roy, A.G., 2008. Introduction: River Confluences, Tributaries and the Fluvial Network, in: Rice, S.P., Roy, A.G., Rhoads, B.L. (Eds.), River Confluences, Tributaries and the Fluvial Network. John Wiley & Sons, Chichester, pp. 1–9.

Richardson, W.R., Thorne, C.R., Mahmood, S., 1996. Secondary Currents and Channel Changes Around a Bar in the Brahmaputra River Bangladesh, in: Ashworth, P.., Best, J.L., Bennett, S.J., McLelland, S.J. (Eds.), Coherent Flow Structures in Open Channels. John Wiley & Sons, Chichester, pp. 519–544.

Riley, J.D., Rhoads, B.L., 2012. Flow structure and channel morphology at a natural confluent meander bend. Geomorphology 163–164, 84–98. doi:http://dx.doi.org/10.1016/j.geomorph.2011.06.011

Riley, J.D., Rhoads, B.L., Parsons, D.R., Johnson, K.K., 2015. Influence of junction angle on three-dimensional flow structure and bed morphology at confluent meander bends during different hydrological conditions. Earth Surf. Process. Landforms 40, 252–271. doi:10.1002/esp.3624

Robson, B.J., Hamilton, D.P., 2004. Three-dimensional modelling of a Microcystis bloom event in the Swan River estuary, Western Australia. Ecol. Modell. 174, 203–222. doi:http://dx.doi.org/10.1016/j.ecolmodel.2004.01.006

Rodi, W., 2010. Large eddy simulation of river flows, in: Proceedings of the Int. Conf. Fluvial Hydraulics (River Flow). Graunschweig, Germany, pp. 23–32.

Roe, P.L., 1984. Generalized formulation of TVD Lax-Wendroff schemes. ICASE Rep, 84–53, NASA CR-172478, NASA Langley Res. Cent. Hampton, VA, USA.

Roe, P.L., 1984. Generalized formulation of TVD Lax-Wendroff schemes. ICASE Rep, 84–53, NASA CR-172478, NASA Langley Res. Cent. Hampton, VA, USA.

Rohr, J.J., Itsweire, E.C., Helland, K.N., Atta, C.W. Van, 1988. Growth and Decay of Turbulence in a Stably Stratified Shear Flow. J. Fluid Mech. 195, 77–111.

Roura, M., 2004. Incidència de l'Embassament de Mequinensa en el Transport de Sòlids en Suspensió i la Qualitat de l'Aigua del Riu Ebre. Ph.D. thesis, Fac. de Biología, Univ. of Barcelona, Barcelona.

Roy, A., Bergeron, N., 1990. Flow and Particle Paths at a Natural River Confluence with Coarse Bed Material. Geomorphology 3, 99–112. doi:http://dx.doi.org/10.1016/0169-555X(90)90039-S

Roy, A.G., Roy, R., Bergeron, N., 1988. Hydraulic Geometry and Changes in Flow Velocity at a River Confluence with Coarse Bed Material. Earth Surf. Process. Landforms 13, 583–598. doi:10.1002/esp.3290130704

Rozovskii, I.L., 1961. Flow of Water in Bends of Open Channels: Israel Program for Scientific Translation. OTS 60-51133, US Department of Commerce, Washington, DC (Originally published by Acad. of Sci. of the Ukrainian SSR, 1957, pp. 233).

Rueda, F.J., Cowen, E.A., 2005. Residence time of a freshwater embayment connected to a large lake. Limnol. Oceanogr. 50, 1638–1653. doi:10.4319/lo.2005.50.5.1638

Rueda, F.J., Fleenor, W.E., de Vicente, I., 2007. Pathways of River Nutrients Towards the Euphotic Zone in a Deep-Reservoir of Small Size: Uncertainty Analysis. Ecol. Modell. 202, 345–361. doi:http://dx.doi.org/10.1016/j.ecolmodel.2006.11.006

Rueda, F.J., MacIntyre, S., 2010. Modelling the Fate and Transport of Negatively Buoyant Storm–River Water in Small Multi-Basin Lakes. Environ. Model. Softw. 25, 146–157. doi:http://dx.doi.org/10.1016/j.envsoft.2009.07.002

Rueda, F.J., Schladow, S.G., Clark, J.F., 2008. Mechanisms of Contaminant Transport in a Multi-Basin Lake. Ecol. Appl. 18, A72–A87. doi:10.1890/06-1617.1

Rueda, F.J., Schladow, S.G., Pálmarsson, S.Ó., 2003. Basin-scale internal wave dynamics during a winter cooling period in a large lake. J. Geophys. Res. Ocean. 108, n/a–n/a. doi:10.1029/2001JC000942

Rueda, F.J., Vidal, J., 2009. Currents in the Upper Mixed Layer and in Unstratified Water Bodies, in: Likens, G.E.B.T.-E. of I.W. (Ed.), . Academic Press, Oxford, pp. 568–582. doi:http://dx.doi.org/10.1016/B978-012370626-3.00083-1

Rutherford, V.J.C., 1994. River mixing. John Wiley & Sons, Chichester.

Ryan, P.J., Harleman, D.R., 1971. Prediction of the Annual Cycle of Temperature Changes in a Stratified Lake or Reservoir: Mathematical Model and User's manual. Parsons,R.M. Laboratory for Water Resources and Hydrodynamics, Massachusetts (Report137).

Saiki, E.M., Biringen, S., 1996. Numerical Simulation of a Cylinder in Uniform Flow: Application of a Virtual Boundary Method. J. Comput. Phys. 123, 450–465. doi:http://dx.doi.org/10.1006/jcph.1996.0036

Schräder, T., 1958. Thermische Verhältnisse in Talsperren. Gewässer und Abwässer 21, 68–87.

Scrivener, J.C., Brown, T.G., Andersen, B.C., 1994. Juvenile Chinook Salmon (Oncorhynchus tshawytscha) Utilization of Hawks Creek, a Small and Nonnatal Tributary of the Upper Fraser River. Can. J. Fish. Aquat. Sci. 51, 1139–1146. doi:10.1139/f94-113

Seim, H.E., Gregg, M.C., 1997. The Importance of Aspiration and Channel Curvature in Producing Strong Vertical Mixing Over a Sill. J. Geophys. Res. Ocean. 102, 3451–3472. doi:10.1029/96JC03415

Sequeiros, O., Spinewine, B., Beaubouef, R., Sun, T., García, M., Parker, G., 2010. Characteristics of Velocity and Excess Density Profiles of Saline Underflows and Turbidity Currents Flowing over a Mobile Bed. J. Hydraul. Eng. 136, 412–433. doi:10.1061/(ASCE)HY.1943-7900.0000200

Shao, X., Wang, H., Chen, Z., 2003. Numerical modeling of turbulent flow in curved channels of compound cross-section. Adv. Water Resour. 26, 525–539. doi:http://dx.doi.org/10.1016/S0309-1708(03)00008-3

Shen, Y.-M., Ng, C.-O., Ni, H.-Q., 2003. 3D Numerical Modeling of Non-Isotropic Turbulent Buoyant Helicoidal Flow and Heat Transfer in a Curved Open Channel. Int. J. Heat Mass Transf. 46, 2087–2093. doi:http://dx.doi.org/10.1016/S0017-9310(02)00501-X

Sherman, F.S., Imberger, J., Corcos, G.M., 1978. Turbulence and Mixing in Stably Stratified Waters. Annu. Rev. Fluid Mech. 10, 267–288. doi:10.1146/annurev.fl.10.010178.001411

Shintani, T., de la Fuente, A., de la Fuente, A., Niño, Y., Imberger, J., 2010. Generalizations of the Wedderburn Number: Parameterizing Upwelling in Stratified Lakes. Limnol. Oceanogr. 55, 1377–1389. doi:10.4319/lo.2010.55.3.1377

Singer, G., Hearn, A., Chapman, E., Peterson, M., LaCivita, P., Brostoff, W., Bremner, A.,

Klimley, A.P., 2013. Interannual variation of Reach Specific Migratory Success for Sacramento River Hatchery Yearling Late-Fall Run Chinook Salmon (Oncorhynchus tshawytscha) and Steelhead trout (Oncorhynchus mykiss). Environ. Biol. Fishes 96, 363–379. doi:10.1007/s10641-012-0037-y

Singleton, V.L., Rueda, F.J., Little, J.C., 2010. A Coupled Bubble Plume–Reservoir Model for Hypolimnetic Oxygenation. Water Resour. Res. 46, n/a–n/a. doi:10.1029/2009WR009012

Smith, P., 2006. A Semi-Implicit, Three-Dimensional Model of Estuarine Circulation. Open File Report 2006-1004, USGS, Sacramento, USA.

Smith, P., Donovan, J., Wong, H., 2005. Applications of 3D Hydrodynamic and Particle Tracking Models in the San Francisco Bay-Delta Estuary, in: Impacts of Global Climate Change. American Society of Civil Engineers, pp. 1–8. doi:doi:10.1061/40792(173)393

Smith, R., Daish, N.C., 1991. Dispersion far Downstream of a River Junction. Phys. Fluids A 3, 1102. doi:10.1063/1.858091

Steel, A., Sandstrom, P., Brandes, P., Klimley, A.P., 2013. Migration Route Selection of Juvenile Chinook Salmon at the Delta Cross Channel, and the Role of Water Velocity and Individual Movement Patterns. Environ. Biol. Fishes 96, 215–224. doi:10.1007/s10641-012-9992-6

Stevens, C., Hamblin, P., Lawrence, G., Boyce, F., 1995. River-Induced Transport in Kootenay Lake. J. Environ. Eng. 121, 830–837. doi:10.1061/(ASCE)0733-9372(1995)121:11(830)

Straškraba, M., 1999. Retention Time as a Key Variable of Reservoir Limnology, in: Tundisi, J.G., Straškraba, M. (Eds.), Theoretical Reservoir Ecology and Its Applications. International Institute of Ecology, Brazilian Academy of Sciences and Backhuys Publishers, pp. 385–410.

Straškraba, M., Mauersberger, P., 1988. 9 - Some Simulation Models for Water Quality Management of Shallow Lakes and Reservoirs and a Contribution to Ecosystem Theory, in: William J. Mitsch, M.S. and S.E.J.B.T.-D. in E.M. (Ed.), Wetland Modelling. Elsevier, pp. 153–175. doi:http://dx.doi.org/10.1016/B978-0-444-42936-0.50014-6

Strayer, D.L., 2008. Twenty years of zebra mussels: lessons from the mollusk that made headlines. Front. Ecol. Environ. 7, 135–141. doi:10.1890/080020

Sukhodolov, A., Uijttewaal, W.S.J., Engelhardt, C., 2002. On the correspondence between morphological and hydrodynamical patterns of groyne fields. Earth Surf. Process. Landforms 27, 289–305. doi:10.1002/esp.319

Sukhodolov, A.N., Rhoads, B.L., 2001. Field investigation of three-dimensional flow structure at stream confluences: 2. Turbulence. Water Resour. Res. 37, 2411–2424.

doi:10.1029/2001WR000317

Sukhodolov, A.N., Sukhodolova, T., 2007. Coherent Structures in River Flows over Submerged Vegetation, in: Cowen, E.A. (Ed.), Hydraulic Measurements and Experimental Methods. ASCE, Lake Placid, N. Y., pp. 172–177.

SWRCB, 1995. Water Quality Control Plan for the San Francisco Bay/Sacramento–San Joaquin Delta Estuary. State Water Resources Control Board. Available: http://www.waterboards.ca.gov/waterrights/water_issues/programs/bay_delta/wq_control_plans/1995wqcp/docs/1995wqcpb.pdf.

Szupiany, R., Amsler, M., Best, J., Parsons, D., 2007. Comparison of Fixed- and Moving-Vessel Flow Measurements with an aDp in a Large River. J. Hydraul. Eng. 133, 1299–1309. doi:10.1061/(ASCE)0733-9429(2007)133:12(1299)

Szupiany, R.N., Amsler, M.L., Parsons, D.R., Best, J.L., 2009. Morphology, flow structure, and suspended bed sediment transport at two large braid-bar confluences. Water Resour. Res. 45, n/a–n/a. doi:10.1029/2008WR007428

Tao, F., Aucour, A.M., Sheppard, S., Benedetti, M., Guyot, J.L., 1999. Mixing at the Negro/Solimões Confluence: Isotopic Constraints and Major Element Redistribution, in: Proceedings of the International Symposium on Hydrological and Geochemical Processes in Large Scale River Basins. IRD-HiBam Publications, Manaus, Brazil, p. CDRom.

Torgersen, C.E., Gresswell, R.E., Bateman, D.S., Burnett, K.M., 2008. Spatial Identification of Tributary Impacts in River Networks, in: Rice, S.P., Roy, A.G., Rhoads, B.L. (Eds.), River Confluences, Tributaries and the Fluvial Network. John Wiley & Sons, Chichester, pp. 159–182.

Trevethan, M., Martinelli, A., Oliveira, M., Ianniruberto, M., Gualtieri, C., 2015. Fluid Mechanics, Sediment Transport and Mixing about the Confluence of Negro and Solimões Rivers, Manaus, Brazil, in: Proceedings of the 36th IAHR World Congress. The Hague, the Netherlands.

Tundisi, J.G., 1984. Estratificação Hidráulica em Reservatórios e suas Consequências Ecológicas. Cienc. Cult. 36, 1489–1496.

Uijttewaal, W.S.J., Booij, R., 2000. Effects of Shallowness on the Development of Free-Surface Mixing Layers. Phys. Fluids 12.

van Balen, W., 2010. Curved Open-Channel Flows. A Numerical Study. PhD Thesis. Department of Environmental Fluid Mechanics, Delft University of Technology, Delft, the Netherlands.

van Leer, B., 1974. Towards the Ultimate Conservative Difference Scheme. II. Monotonicity and

Conservation Combined in a Second-Order Scheme. J. Comput. Phys. 14, 361–370. doi:http://dx.doi.org/10.1016/0021-9991(74)90019-9

van Rijn, L.C., 1987. Mathematical Modelling of Morphological Processes in the Case of Suspended Sediment Transport. Ph.D. thesis, Delft Hydraul. Commun. 382. Delft Hydraul. Lab., Delft, Netherlands.

Vidal, J., Rueda, F.J., Casamitjana, X., 2007. The seasonal evolution of high vertical-mode internal waves in a deep reservoir. Limnol. Oceanogr. 52, 2656–2667. doi:10.4319/lo.2007.52.6.2656

Vowinckel, B., Schnauder, I., Sukhodolov, A.N., 2007. Spectral Dynamics of Turbulence in Shallow Mixing Layers at a Confluence of Two Parallel Stream, in: Cowen, E.A. (Ed.), Hydraulic Measurements and Experimental Methods. ASCE, Lake Placid, N. Y., pp. 635–630.

Wang, B., Fringer, O.B., Giddings, S.N., Fong, D.A., 2009. High-Resolution Simulations of a Macrotidal Estuary Using SUNTANS. Ocean Model. 28, 167–192. doi:http://dx.doi.org/10.1016/j.ocemod.2008.08.008

Wang, B., Giddings, S.N., Fringer, O.B., Gross, E.S., Fong, D.A., Monismith, S.G., 2011. Modeling and Understanding Turbulent Mixing in a Macrotidal Salt Wedge Estuary. J. Geophys. Res. Ocean. 116. doi:10.1029/2010JC006135

Weber, L., Schumate, E., Mawer, N., 2001. Experiments on Flow at a 90° Open-Channel Junction. J. Hydraul. Eng. 127, 340–350. doi:10.1061/(ASCE)0733-9429(2001)127:5(340)

Weitbrecht, V., Jirka, G., 2001. Flow Patterns and Exchange Processes in Dead Zones of Rivers, in: Proceedings of the IAHR Congress. Beijing.

Weitbrecht, V., Socolofsky, S., Jirka, G., 2008. Experiments on Mass Exchange between Groin Fields and Main Stream in Rivers. J. Hydraul. Eng. 134, 173–183. doi:10.1061/(ASCE)0733-9429(2008)134:2(173)

Wells, M., Nadarajah, P., 2009. The Intrusion Depth of Density Currents Flowing into Stratified Water Bodies. J. Phys. Oceanogr. 39, 1935–1947. doi:10.1175/2009JPO4022.1

Wells, M.G., Wettlaufer, J.S., 2007. The Long-Term Circulation Driven by Density Currents in a Two-Layer Stratified Basin. J. Fluid Mech. 572, 37–58.

Wipfli, M.S., Gregovich, D.P., 2002. Export of Invertebrates and Detritus from Fishless Headwater Streams in Southeastern Alaska: Implications for Downstream Salmonid Production. Freshw. Biol. 47, 957–969. doi:10.1046/j.1365-2427.2002.00826.x

Wolfram, P.J., 2013. Secondary Flows and Dispersion in Channel Junctions. PhD Thesis.

Department of Civil and Environmental Engineering, Stanford University, Stanford, California.

Wolfram, P.J., Fringer, O.B., 2013. Mitigating horizontal divergence "checker-board" oscillations on unstructured triangular C-grids for nonlinear hydrostatic and nonhydrostatic flows. Ocean Model. 69, 64–78. doi:http://dx.doi.org/10.1016/j.ocemod.2013.05.007

Zajanc, D., Kramer, S.H., Nur, N., Nelson, P.A., 2013. Holding Behavior of Chinook Salmon (Oncorhynchus tshawytscha) and Steelhead (O. mykiss) Smolts, as Influenced by Habitat Features of Levee Banks, in the Highly Modified Lower Sacramento River, California. Environ. Biol. Fishes 96, 245–256. doi:10.1007/s10641-012-0060-z

Zamani, K., Bombardelli, F., Wuertz, S., Smith, P., 2010. Toward a 3-Dimensional Numerical Modeling of Tidal Currents in San Francisco Bay, in: World Environmental and Water Resources Congress 2010. American Society of Civil Engineers, pp. 1385–1394. doi:doi:10.1061/41114(371)147